

# Potential Applications of Quantum Computing at Los Alamos National Laboratory

v0.1.0

Andreas Bäertschi, Francesco Caravelli, Carleton Coffrin<sup>1</sup>, Jonhas Colina, Stephan Eidenbenz, Abhijith Jayakumar, Scott Lawrence, Minseong Lee, Andrey Y. Lokhov, Avanish Mishra, Sidhant Misra, Zachary Morrell, Zain Mughal, Duff Neill, Andrei Piryatinski, Allen Scheie, Marc Vuffray, Yu Zhang

LA-UR-24-24966  
May 2024

Distribution Statement A – Approved for Public Release, Distribution Unlimited

---

<sup>1</sup>Corresponding author [cjc@lanl.gov](mailto:cjc@lanl.gov)

**Contents**

<b>1</b>	<b>Overview</b>	<b>1-1</b>
1.1	Introduction	1-1
1.1.1	Report Structure	1-2
1.2	Quantum Physics Research at Los Alamos National Laboratory	1-3
1.2.1	Quantum Physics Simulation	1-3
1.2.2	Quantum Physics Experimentation	1-4
1.3	Utility Estimation Methods	1-5
1.3.1	Method 1: Offsetting current computational investments	1-6
1.3.2	Method 2: Enabling successful completion of a research project	1-6
1.4	Quantum Computational Kernels	1-7
1.4.1	Hamiltonian Simulation	1-7
1.4.2	Open quantum systems	1-11
1.4.3	Finding ground states	1-12
1.4.4	Preparation of thermal states	1-13
<b>2</b>	<b>Experimental analysis of magnetic materials at the MAGLAB user facility</b>	<b>2-1</b>
2.1	Application area overview	2-2
2.1.1	High-level description of the application area	2-2
2.1.2	Utility estimation	2-2
2.2	Problem and computational workflows: Kitaev QSLs	2-3
2.2.1	Detailed background for Kitaev QSLs	2-3
2.2.2	Application category 1: Hamiltonian search for spin liquids	2-5
2.3	Requirements summary	2-13
2.4	Supplementary material for Kitaev quantum spin liquids	2-15
2.5	Quantum implementation	2-16
<b>3</b>	<b>Exploring exotic phases of magnetic materials near instabilities</b>	<b>3-1</b>
3.1	Application area overview	3-2
3.1.1	High-level description of the application area	3-2
3.1.2	Utility estimation	3-2
3.2	Problem and computational workflows	3-3
3.2.1	Detailed background of the application area	3-3
3.2.2	Classical methods	3-5
3.3	Requirements summary	3-12
<b>4</b>	<b>Driven-dissipative Dicke model in the ultrastrong coupling regime</b>	<b>4-1</b>
4.1	Application area overview	4-2
4.1.1	High-level description of the application area	4-2
4.1.2	Utility estimation	4-2
4.2	Problem and computational workflows	4-3
4.2.1	Detailed background of the application area	4-3
4.2.2	Application 1: Low energy spectrum of Dicke and Tavis-Cummings models	4-4
4.2.3	Application 2: Phase diagram of the driven-dissipative Dicke model	4-5
4.3	Requirements summary	4-9

## Contents

<b>5</b>	<b>High-temperature superconductivity and exotic properties of Fermi-Hubbard models</b>	<b>5-1</b>
5.1	Application area overview	5-2
5.1.1	High-level description of the application area	5-2
5.1.2	Role of Fermi-Hubbard physics in the investigations of HTC	5-4
5.1.3	Utility estimation	5-6
5.2	Problem formulation and computational workflows	5-7
5.2.1	Methods used to derive the model Hamiltonians	5-8
5.2.2	Phases of the model via observables, and their properties	5-12
5.3	Computational applications	5-15
5.4	Models instantiations	5-19
5.4.1	Two dimensional lattice models	5-19
5.4.2	Two band superconductivity via transverse Ising mapping	5-20
5.4.3	Iron-based models	5-21
5.5	Requirements summary	5-22
5.6	Supplementary material for Fermi-Hubbard models	5-25
5.6.1	More on the underlying Fermi-Hubbard	5-25
5.6.2	Methods to derive the parameters of the Fermi-Hubbard models	5-26
5.6.3	Numerical methods used to study the Fermi-Hubbard model	5-27
5.6.4	D-Wave superconductivity	5-30
5.6.5	Statics vs Dynamics in superconductivity	5-30
<b>6</b>	<b>Computational catalysis for artificial photosynthesis</b>	<b>6-1</b>
6.1	Application area overview: computational catalysis in quantum chemistry	6-2
6.1.1	High-level description of the application area	6-2
6.1.2	Utility estimation	6-3
6.2	Problem and computational workflows	6-3
6.2.1	Application 1: Energetics of reaction pathways for down selection of catalysts for artificial photosynthesis	6-6
6.2.2	Application 2: Reaction dynamics through quantum molecular dynamics simulations	6-14
6.3	Requirements summary	6-21
6.4	Quantum implementation	6-22
<b>7</b>	<b>Simulations of quantum chromodynamics and nuclear astrophysics</b>	<b>7-1</b>
7.1	Application area overview	7-2
7.2	Problem and computational workflows	7-2
7.2.1	Application 1: Supernova neutrinos	7-2
7.2.2	Application 2: Hydrodynamics of hot and dense matter	7-8
7.3	Requirements summary	7-14
<b>8</b>	<b>End Notes</b>	<b>8-1</b>
8.1	Author Contributions	8-1
8.2	Acknowledgements	8-1
8.3	Change Log	8-1

Figures

1-1 For the majority of modern history the scientific discovery process has been characterized by a feedback loop between experimental observation and hypothesis development. The emergence of physics simulation on digital computers in the 20th century introduced a new layer in the scientific discovery process, which has dramatically increased research productivity. . . . . 1-1

1-2 A summary of the application topics that were studied using 500 million core-hours of computing workload on LANL’s Chicoma supercomputer in 2022. The workloads in Materials Science, Chemistry and Particle Physics focused on simulations of quantum physics, indicating that around 33% of this computing has the potential to benefit from quantum computation. . . . . 1-4

2-1 Each color indicates  $K_x, K_y, K_z$  bonds [350] . . . . . 2-4

2-2 Workflow for Hamiltonian search using magnetization experimental data. The red box (Hamiltonian Simulation) contains the hard computational task/kernel. . . . . 2-9

2-3 The inverse of magnetization divided by external magnetic field ( $1/\chi$ ) as a function of temperature with magnetic field along two different directions are shown [344]. . . . . 2-9

2-4 Field vs. time profiles of superconducting dc magnet (a) and 65 T short pulse magnet (b) [175]. Note that the time scale difference between dc magnet and pulsed field magnet. . . . . 2-10

2-5 The magnetization measurements (solid green lines) with field along in-plane with larger magnetization and out-of-plane with smaller magnetization [202]. The red and blue solids lines are from exact diagonalization simulations [442]. . . . . 2-10

2-6 Workflow for Hamiltonian search using experimental ground state. The red box contains the hard computational task/kernel. . . . . 2-13

2-7 List of parameters for  $\alpha$ -RuCl<sub>3</sub> suggested by different theoretical approaches. . . . . 2-16

2-8 The spin structure of the magnetic ground state of  $\alpha$ -RuCl<sub>3</sub> . . . . . 2-16

3-1 Computational workflow for ground state calculation. . . . . 3-7

3-2 Experimental neutron scattering on KYbSe<sub>2</sub> at three different temperatures (a)-(c). The  $y$  axis gives energy transfer, the  $x$ -axis gives different scattering directions in reciprocal space units, and the color scale indicates the scattered neutron intensity. Panel (d) shows the Quantum Fisher Information (d) computed from the spectra in panels (a)-(c) via Eq. 18. Here  $n\text{QFI} = f_Q/(12S^2)$  gives a lower bound on entanglement depth. . . . . 3-9

3-3 Fourier-transforming neutron scattering from frequency and reciprocal space to time and distance. Panel (a) shows the experimental neutron spectrum of KCuF<sub>3</sub>. Panel (b) shows the spectra transformed into real space on the  $x$  axis and time on the  $y$  axis [370], which corresponds to a lattice-averaged time-evolved spin correlation. . . . . 3-10

3-4 Workflow for Hamiltonian dynamics to compare with neutron scattering data. The red boxes contain the hard computational task/kernel. . . . . 3-10

4-1 Schematic of driven-dissipative Dicke model: An ensemble of  $\mathcal{N}_o$  two-level quantum emitters with transition energy  $\hbar\omega_o$  and cavity photon mode of energy  $\hbar\omega_c$  interact via coherent quantum exchange rate  $\lambda$ . The quantum emitters are subject to the incoherent pump and internal relaxation processes whereas the cavity leakage results in the photon emission outside the cavity. . . . . 4-4

## Contents

4-2	Phase diagram of generalized Dicke model accounting for the coherent and dissipative coupling. [321] (a)-(c): Mean-field phase diagrams marking the normal (NS), superradiant (SR), lasing without inversion (LWI), and regular lasing (RL) states. (d)-(f) The steady state projection on the quantum emitter population inversion $s_z = \sum_{n=1}^{N_o} \langle \hat{\sigma}_n^z \rangle / 2N_o$ and (g)-(i) reduced cavity mode population (the order parameter) $\mathcal{N}_{sp} = \langle \hat{a}^\dagger \hat{a} \rangle$ normalized per total number of quantum emitters $N_o$ calculated for the driven dissipative Dicke model with the coherent $\bar{\lambda} = \lambda/\omega_o$ and dissipative $\bar{\eta} = \eta/\omega_o$ couplings. The left and central columns represent quantum emitters below population inversion and the right one above. The diagram segments for $\sqrt{N_o \bar{\lambda}} > 0$ and $\bar{\eta} > 0$ are attributed to the USC regime. . . . .	4-7
5-1	Evolution of the superconductivity critical temperature over the years for various materials. The gap between low-temperature superconductors and HTC is over a hundred of Kelvin. . . . .	5-2
5-2	The crystal structure of $\text{La}_2\text{CuO}_4$ (or $\text{Sr}_2\text{CuO}_4$ ), a high temperature superconductor, and its reduction to a single band effective model by the progressive elimination of degrees of freedom until the square lattice of Fig. 5-4 is reached. In the two dimensional sublattice, Cu has four nearby O atoms. . . . .	5-5
5-3	The Fermi-Hubbard model originates from the hopping of electrons between the orbitals of the crystal's atoms in a copper oxide. In the case of the two dimensional Fermi-Hubbard model on the square lattice, the hopping parameters $t_{ij}$ originate from the overlap of the orbitals of oxygen and copper. . . . .	5-6
5-4	A graphical representation of the Fermi-Hubbard model. The parameter $t$ is the energy associated with the hopping between sites, while the parameter $U$ represents the energy associated to the particle remaining on the same site. . . . .	5-8
5-5	Pseudo-phase diagram for the Fermi-Hubbard model in two dimensions. The pseudogap phase is often measured via the spectral function as a pronounced dip in the spectral function. The other phases have a well defined combinations of the order parameters, as highlighted above. . . . .	5-11
5-6	Asymmetry in the couplings along the x- and y- direction of eqn. (49). . . . .	5-20
5-7	The lattice considered in graphene-based superconductors of [209]. . . . .	5-21
5-8	The 2- and 3- orbital Hamiltonians of Dagotto et al. [100]. . . . .	5-22
6-1	Flowchart of selecting catalysts for different reaction mechanisms of artificial photosynthesis using computational modeling. . . . .	6-9
6-2	(a) One proposed $\text{CO}_2$ reduction mechanisms with CoPc catalyst [265]. (b) One possible water oxidation reaction pathway with the cobalt dimer catalyst [125]. . . . .	6-12
6-3	Flowchart of selecting catalysts for different reaction mechanisms of artificial photosynthesis using QMD. . . . .	6-17

## Contents

- 7-1 We plot the evolution of the difference in flavor occupation,  $N_{\nu_e} - N_{\nu_\mu}$ , for neutrino in momentum mode  $i = 1$  compared to the prediction utilizing the grand-canonical partition function (black dotted line), which represents the equilibrated long-time answer. The calculation is performed for a toy model of the full neutrino problem where the number of momentum modes equals the number of neutrinos, with an unphysically small number of neutrinos. The momentum modes are not allowed to change, only the flavor occupation in the simplified model. Thus each neutrino is labeled by its specific fixed momentum mode  $i = 1, \dots, 16$ , and  $N_{\nu_e}(i) - N_{\nu_\mu}(i)$  captures the flavor distribution of that mode. The line and arrow indicate when the time-averaging begins for comparison against the grand canonical prediction. *Inset:*  $N_e(i) - N_\mu(i)$  as a function of time for every neutrino on the entire considered time domain. Adapted from [277]. . . . . 7-5

## Tables

- 3-1 Well-studied examples of interacting quantum spin systems where classical methods fail, and quantum simulation is necessary. . . . . 3-4
- 3-2 Examples of nontrivial quantum magnetic materials with well-measured properties but poorly understood quantum ground states. . . . . 3-4
- 6-1 Molecular information of CO<sub>2</sub> reduction and water oxidation. . . . . 6-13

# 1 Overview

## 1.1 Introduction

Since the scientific revolution in the 16th and 17th centuries, the process of scientific discovery has followed an iterative feedback process of observation, hypothesis development and testing with physical experiments, which is widely referred to as the scientific method. This process remained largely unchanged until the middle of the 20th century, when the emergence of digital computers empowered scientist to build and inspect detailed simulations of physical phenomena. Over the last century, computational tools have transformed modern approaches to scientific discovery by enabling fast and affordable hypothesis testing before physical experiments are conducted, shown in Figure 1-1. Some notable examples include: global climate forecasts to understand how the environment may change over decades [119]; modeling the behavior of plasma to design fusion reactors [56]; and understanding the behavior of molecules in biological processes [148, 205].

Due to the transformational impact of computing technology for accelerating scientific discovery, the United States National Laboratories were some of the first developers of High-Performance Computing (HPC) facilities going back as far as the 1950's [252]. These facilities leverage so-called supercomputers to solve large and complex physics simulation tasks. Modern supercomputers often take the form of large clusters of general purpose commodity computers with specifications that are tailored to the requirements for physics simulations [121]. However, for most of the 20th century, it was common for National Laboratories to develop computing hardware that was specialized to physics simulation, such as the *vector machines* developed by Cray Research [252, 113]. These large-scale computing facilities continue to be an essential component of the modern scientific discovery process with the Department of Energy investing over one billion dollars annually to provision, operate and maintain a range of cutting edge computing facilities across more than ten national laboratories [120].

There is no doubt that physics simulation with computing technology is a key component of the scientific discovery process for many important subject areas. However, physics regimes that exhibit quantum mechanical effects largely have not benefited from this computational transformation in scientific discovery. The foundational challenge is that each quantum mechanical particle that is added to the simulation roughly doubles the amount of traditional (i.e., classical) computing resources that are required to perform this simulation. Consequently, the amount of classical computing resources needed to simulate quantum physics grows exponentially with the size of the quantum system, dramatically limiting the types of quantum systems that can be studied through computational simulation. Over the years many classical algorithm designers have worked to reduce these requirements and have been successful in a variety of specific cases, such as simulations where limited entanglement is required. However, a breakthrough method for *general purpose* quantum

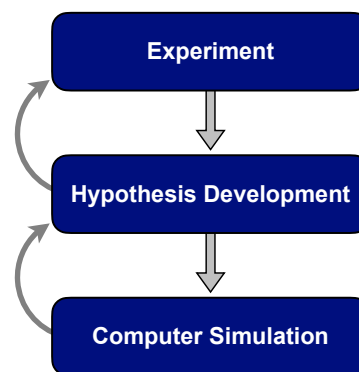


Figure 1-1: For the majority of modern history the scientific discovery process has been characterized by a feedback loop between experimental observation and hypothesis development. The emergence of physics simulation on digital computers in the 20th century introduced a new layer in the scientific discovery process, which has dramatically increased research productivity.

## Overview

physics simulation on classical computers has resisted over fifty years of exploration.

The lack of flexible, scalable and accurate simulation tools for quantum mechanical physics has been holding back the understanding of important foundational topics such as super conductivity, chemistry and magnetism, for at least four decades. This challenge motivated Feynman's proposal to develop a quantum mechanical computer for the study of quantum physics in the 1980's [129]. The last decade has seen the emergence of the first generation of such devices, widely referred to as Noisy Intermediate Scale Quantum (NISQ) computers [331], to recognize the challenges that noise and limited scalability present to conducting computations of interest. It is anticipated that the next generation of quantum computers will leverage error correction protocols to provide a fault tolerant quantum computation, which addresses many of the challenges faced by current NISQ devices [331, 60, 426, 58, 59]. Regardless of the specific trajectory of quantum technological development, the emergence of this technology suggests the possibility for science in quantum mechanical systems to experience the same computer-accelerated discovery that classical physics has experienced over the last century.

The development of quantum computing technology naturally leads to the following questions:

1. *If a sufficiently large and performant quantum computer existed, what would National Laboratories (and other large research intuitions) use it for?*
2. *What are the capability requirements for a quantum computer to meet the simulation needs of the application?*
3. *How much would these types of institutions be willing and able to pay for improved quantum simulation capabilities?*

The primary objective of this report to develop initial answers to these questions and provide details of how quantum computing technologies could impact scientific discovery. This is accomplished by conducting a broad investigation of quantum physics research activities at Los Alamos National Laboratory (LANL), one of the Department of Energy's seventeen laboratories. This report includes both a survey of how LANL currently uses classical computers for scientific discovery and develops a collection of detailed use cases for the kinds of quantum simulations that LANL scientist would like to conduct, if a sufficient computing technology was available. While the report strives to provide a broad portfolio of possible use cases, our investigation also suggests that many additional use cases could be documented with sufficient time and effort.

### 1.1.1 Report Structure

The remainder of this report is structured as follows. It begins with a brief overview of the current methods for conducting quantum physics research at LANL (Section 1.2). This section highlights the need for quantum simulation capabilities at this type of intuition and introduces how improved quantum simulation capabilities would support the scientific discovery process, in broad terms. The next section (Section 1.3) introduces the methodical foundations for estimating the value of quantum simulation capabilities. These methods are used throughout the document for developing concrete value estimates for specific science applications. The last in component of the overview chapter (Section 1.4) provides a broad introduction to the well-established algorithmic tools for quantum computers that could benefit quantum simulation applications. Through these sections, this overview chapter provides a foundation for understanding the remaining *application instance* chapters.



Each subsequent chapter conducts a deep-dive on a specific application topic. These chapters focus on documentation of the application requirements needed for a quantum simulation capability to have a transformational impact on the subject area. These application examples tend to focus on grand challenge tasks that can serve as guiding stars as quantum computational capabilities develop over time. A subset of application chapters also include references to external resources that provide implementations of the proposed quantum computational tasks using established quantum algorithms. Such transformational workloads are too challenging for existing NISQ devices but are valuable as a tool for conducting quantum computer *resource estimates*, which quantify the computational requirements of future quantum computers to address these applications. As the field of quantum computer algorithms is nascent, it is expected that the implementation details in these external resources will see consistent improvements over the next several years.

This document follows a three digit version numbering the convention vX.Y.Z, which is inspired by the Semantic Versioning standard [332]. A leading zero in this version number system indicates that this document is still under active development. Improved subsequent versions are expected until v1.0.0 is released.

## 1.2 Quantum Physics Research at Los Alamos National Laboratory

Los Alamos National Laboratory's (LANL) interest in quantum physics dates back to the inception of laboratory, with a wide variety of research continuing on to present day in areas such as nuclear physics, high energy physics, condensed matter and chemistry. All of these research areas include theoretical, experimental and computational components, which work together to produce scientific insights and discoveries. This section highlights a few examples of how computation and experimental capabilities support this kind of research. This is not a comprehensive list of LANL's capabilities in quantum physics research.

### 1.2.1 Quantum Physics Simulation

LANL hosts a variety supercomputers that support a wide collection of computational needs. Based on the performance specifications of the Trinity supercomputer [240], one can estimate that LANL's total classical computational capability is on the order of 10 billion core hours per year. Around 1 billion of these annual core hours are provided by a system called Chicoma, which is dedicated to supporting basic scientific research needs. The Chicoma supercomputer includes around 1800 compute nodes, each with two AMD EPYC 7H12 processors (64 cores at 2.6 GHz clock) and 512 GB RAM. Throughout this document the value of computations that are executed on Chicoma are estimated using the a value of \$4.00 to \$8.00 USD per node hour. This is based on the costs required to provision similar resources on established cloud computing providers. The large capital investments in specialized HPC hardware at National Laboratories dramatically reduces the cost of these computations, however detailed information about the costs of specific computational capabilities at National Laboratories is not readily available.

To better understand the needs for quantum physics simulation at LANL, this project analysed the workloads conducted on Chicoma in 2022 to understand how much of this compute might benefit from quantum computation. In 2022 the Chicoma computer supported around 500 million core-hours of research spanning more than 100 individual research projects. However, the bulk of total capacity (75%) of the system was consumed by approximately 30 flagship projects. These 30 flagship projects spanned a range of subject areas including: Plasma Physics, Chemistry, Biology,

## Overview

Materials Science, Earth Science, Astrophysics, and Particle Physics. The relative breakdown of the total compute into these subject areas is shown in Figure 1-2. Plasma physics and Material Science were the clear leading workloads followed by significant contributions from Astrophysics, Chemistry and Earth Science models.

Given this project's interest in quantum computation, the specific types of physics simulation that were conducted in each of these 30 flagship projects was also investigated. This investigation identified that the majority of computations conducted in the Chemistry, Materials Science and Particle Physics subjects were simulations of quantum physics. These workloads included both exact methods for quantum simulation (e.g., diagonalization) and approximate methods such as Density Function Theory (DFT), Tensor Network Methods (e.g., DMRG) and Quantum Monte Carlo methods; all of which have notable limitations in scalability or accuracy. Overall, these results indicate that 33% of Chicoma's workload in 2022 were quantum physics simulations, which are natural candidates to benefit from quantum computation. There is an ongoing debate in the research community whether quantum computers will be able to improve classical physics simulation, such as the Plasma Physics, Biology, Earth Science and Astrophysics workloads identified in this study. If this turns out to be the case, then it reasonable to assume that a quantum computer might benefit more than 75% of Chicoma's workloads.

Based on this analysis, it is clear that there is a significant demand at LANL for quantum physics simulations, which would likely benefit from quantum computing technology. However, note that computing capability of Chicoma is less than 1% of the total compute resource in the Department of Energy. If similar demand for quantum simulation exists broadly across the entire department, that would represent a large demand for computing technology that specializes in quantum simulation tasks.

### 1.2.2 Quantum Physics Experimentation

In scientific research topics where computer simulation is inadequate for hypothesis testing, laboratory experiments are the sole method for testing theories and making new discoveries. In the context of quantum physics, the Large Hadron Collider (LHC) stands out as a widely known example. This experimental facility was provisioned to investigate the properties of subatomic particles, including but not limited to confirming the existence of the Higgs-Boson particle. This experimental facility cost more than \$4 Billion USD and has been producing scientific insights in particle physics since 2010.

The LHC is one example of an experimental user facility, where capital investments in extreme technologies enable experimental scientists to make unique observations of physical systems. However, a wide range of smaller scale facilities exist to provide insights into a variety different aspects of physics. Two examples of such facilities at LANL that are particularly interested in quantum

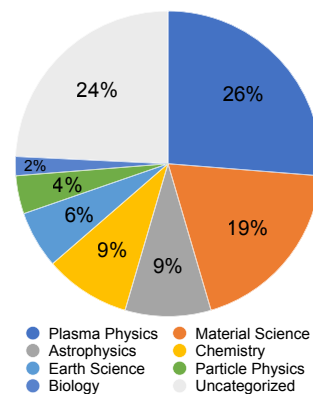


Figure 1-2: A summary of the application topics that were studied using 500 million core-hours of computing workload on LANL's Chicoma supercomputer in 2022. The workloads in Materials Science, Chemistry and Particle Physics focused on simulations of quantum physics, indicating that around 33% of this computing has the potential to benefit from quantum computation.

physics are the National High Magnetic Field Laboratory (MAGLAB) [241], which specializes in exposing materials to extremely strong magnetic fields (up to 100 Tesla) to probe the quantum limits of materials and the Center for Integrated Nanotechnologies (CINT) [355], which specializes in the fabrication and characterization of materials at nanoscales, including those exhibiting quantum mechanical properties. The productivity of both of these facilities would be increased by improved computer simulation capabilities of quantum mechanical systems. Indeed, these experimental physics facilities are a significant source for the quantum simulations workloads that are run on LANL's HPC facilities.

In the context of experimental physics, computer simulations provide valuable insights in several ways. First, using a computer simulation to reproduce observations that have been made in an experimental facility confirms an understanding of the specific physics that are driving the observed phenomena. Second, once a simulation can reproduce experimental data it can be inspected in a variety of ways that are not feasible in the laboratory, providing deeper insights into underlying mechanisms. Third, computer simulations can be used to automate the search through a large collection of physical systems, to identify the most promising candidates for experimental validation. This report includes several examples of how a quantum computer could be used to provide these kinds of insights to experimental quantum research being conducted at LANL.

### 1.3 Utility Estimation Methods

In this section, we provide an introduction to the various approaches to estimating the utility of a given set of computational tasks. Each computational task of value is termed an *application* in this document and are presented in the subsequent area-specific chapters. Broadly, the set of applications can be divided into two categories; (i) scientific utility, and (ii) commercial utility. The scientific utility category contains applications that are of value to researchers in a research facility such as national laboratories, universities and other research organizations. The commercial utility category contains applications with direct economic value to various industries such as the chemical manufacturing and drug-design, among others. All the applications presented in this document belong to the scientific utility category. Although many of them are expected to have commercial utility, we do not pursue commercial utility estimation. Regardless of the category, the added value provided by a fault-tolerant quantum computer with appropriate specifications can be attributed to one or more of its following capabilities.

- *Speed*: Solve a computational task much faster than current methods.
- *Accuracy*: Find a solution with higher accuracy than current methods.
- *Scalability*: Solve a problem at a larger scale than is possible with current methods.

Although scalability and speed are both a consequence of faster computational capability, it is natural from an application perspective to make a distinction between them by comparison to current (classical computing) approaches to the problem. For an application where a faster solution time is desired, for example to solve a larger number of instances of the problem, we attribute it to the *speed* feature. If instead, a larger problem instance is desired, for example to eliminate finite-size effects, then we attribute it to the *scalability* feature.

Two main approaches are employed in this document for scientific utility estimation. Our goal is to use them to provide a numerical monetary value to each application instance (orange highlighted

## Overview

boxes in subsequent chapters) while maintaining a bias towards under-estimating these values. These approaches are described in the following sections, along with the estimation methods, and the caveats and uncertainties inherent to them.

### 1.3.1 Method 1: Offsetting current computational investments

In many research projects, it is necessary to obtain solutions to highly complex models. Consequently, a significant fraction of the research budget is dedicated to affording computational capabilities ranging from individual computing nodes to high performance computing (HPC) platforms. Suppose that in a given research project, an average of  $D$  dollars per application instance is spent on computing capabilities. We determine that a quantum computer can provide utility for this research project because it can solve these instances *at least as well as the currently utilized computing capabilities*, because of one or more of its *speed*, *accuracy* and *scalability* features. Then we can conclude that the value of a quantum computation  $U$  for this application is at least  $D$  per application instance on average, i.e.

$$U \geq D. \quad (1)$$

Method 1 is employed to estimate the numerical utility value of the application instance provided in Chapter 5 for studying phase diagrams of Fermi-Hubbard models in the context of high-temperature superconductivity, in Chapter 6 for quantum chemistry applications in catalyst design.

### 1.3.2 Method 2: Enabling successful completion of a research project

A research project is funded with the goal of producing answers to a specific set of project-defining research questions. Some examples of such project-defining questions are: “determine if a given material has a spin liquid phase”, or “find the optimal reaction pathway for a given chemical reaction”. If the project has a total budget of  $B$  dollars, we can then assign a value of  $B$  dollars for answering the set of research questions. Depending on the project area, achieving this goal can require a combination of experimental, theoretical and computational capabilities and efforts. Ideally, the fraction  $\alpha_{comp}$  of the budget required for computational efforts is accurately estimated and allocated. Suppose that a set of  $N_Q$  application instances cover the computational part of the project-defining research questions, then each application instance has an average utility of

$$U = \frac{\alpha_{comp}B}{N_Q}. \quad (2)$$

While the number of required application instances  $N_Q$  can be accurately determined, the total budget  $B$  and the fraction dedicated to computational tasks  $\alpha_{comp}$  may or may not be available. In certain cases, a project is part of an ongoing effort and is expected to continue for several more years in the future with the project-defining research questions remaining unchanged. In this case, we determine the total budget of the project by multiplying the expenditure of the project thus far by an estimated constant greater than one to account for the total duration of the project.

In many projects the fraction  $\alpha_{comp}$  is not specified or allocated and is determined on-the-fly using the best judgement of the performers in the project. Therefore,  $\alpha_{comp}$  must be estimated and this estimate is subject to significant uncertainty. A particularly challenging scenario occurs when the application instances are well beyond the capabilities of classical computing hardware often due

to their scaling requirements. In this case, researchers use alternative approaches such as approximation algorithms, heuristics, reduced models and experimental protocols, thus leading to  $\alpha_{comp}$  being excessively underestimated when using historical data. However, although these alternative approaches provide scientific progress, a quantum computer with the appropriate specifications will be the most efficient and therefore the preferred choice owing to its *scalability* feature. In such scenarios, we provide estimates of  $\alpha_{comp}$  by direct communication with project performers and by comparing to other projects where this data is available.

Method 2 is used to provide numerical utility value of application instances in Chapter 2 for the study of magnetic materials in the MAGLAB user facility, Chapter 3 for the study of exotic phases in spin systems and Chapter 4 for analyzing the ultra-strong coupling regime in optical cavities.

### 1.4 Quantum Computational Kernels

The promise of quantum computing is to develop algorithms and methods for solving problems more efficiently than classical computers. Among the multiple quantum algorithms developed over the past decades, we have selected those that solve tasks that we believe have the highest chances to be implemented in the near future. In agreement with Feynman’s insight [127], the tasks that we have identified as the most promising for quantum computers to solve pertain to scientific computation. The general concept is that quantum computers are efficient tools for finding properties of quantum systems. Four general tasks, which we call Quantum Computational Kernels, were found to be central for speeding-up current scientific computations. These four tasks are *Hamiltonian Simulation*, *Open Quantum System Simulation*, *Ground-state Preparation* and *Thermal State Preparation*. The goal of the first two kernels is to simulate the time evolution of an isolated and open quantum system respectively, while the goal of the last two is to prepare the lowest energy state or a thermal mixed state of a quantum system respectively.

In what follows, we expand in more detail about the nature of these quantum kernels and provide a list of developed quantum algorithms that achieve these tasks based on our current literature survey, quantum algorithms reviews [102, 260, 452] and [300]. The main strengths and weaknesses of each method are briefly reviewed as well as their computational complexity. Note that in addition to these algorithms, there are two main hidden computational costs that need to be considered based on specific applications. Namely, *initial state preparation* and *information extraction*. While preparing the initial state of the register is usually considered a separate task in literature, it can come with a prohibitive cost, see for instance [1]. Similarly, computing observables can be a challenging task as reconstructing the full final state of a quantum system is an inherently inefficient procedure [159]. However, several strategies exist for constructing highly efficient procedures to obtain estimations of a large numbers of few-qubit observables [92, 449, 181].

#### 1.4.1 Hamiltonian Simulation

Hamiltonian simulation is the fundamental computational primitive that can be performed efficiently on a quantum computer. The general task on a  $n$ -qubit system can be stated as follows; given a Hamiltonian operator  $H \in \mathbb{C}^{2^n \times 2^n}$  and a time  $t$  apply the unitary time evolution operator,  $\exp(-iHt)$  to the  $n$ -qubit register.

The relevance of this task comes from the fact that this time evolution operator is the solution to the Schrödinger equation that governs how a quantum system with a Hamiltonian  $H(t)$  evolves

## Overview

in time,

$$\frac{\partial |\psi(t)\rangle}{\partial t} = -iH(t) |\psi(t)\rangle. \quad (3)$$

The solution to this equation for a given initial state tells us how the quantum state of a system evolves in time. If the Hamiltonian is not a function of time (i.e.  $H(t) = H$ ), it can be shown that the state of a quantum system, initially in a state  $|\psi\rangle$ , evolves to the state  $\exp(-iHt) |\psi\rangle$  after time  $t$  [300]. This time independence assumption on the Hamiltonian does not hold for some systems, and relaxing this assumption leads to time-dependent Hamiltonian simulation problem. Simulating time-dependent systems is a more complex algorithmic task.

The Hamiltonian for an  $n$ -qubit system is a  $2^n \times 2^n$  matrix. The task in time-independent simulation is simply to apply the operator  $e^{-iHt}$  to a quantum register. For physically relevant systems, the Hamiltonian often has several features that makes this task feasible in time that scales at worst as a polynomial in the number of qubits of the system and the evolution time  $t$ . For Hamiltonians of locally interacting systems, there is strong theoretical evidence that the complexity of this task in the worst case cannot scale sub-linearly i.e. scaling slower than  $nt$  [28, 77]. However for a certain subsets of Hamiltonians this evolution can be simulated faster [155].

- **Common features of the Hamiltonian.** A commonly assumed feature of the Hamiltonian is *locality*, i.e. it only contains terms that describe interactions between qubits/particles that are close to each other in space. The most favorable assumption that one can make in this context is strict geometric locality, i.e. qubits/particles only interact with their nearest neighbors in a  $D$ -dimensional lattice. This assumption is true for many Hamiltonians that come up frequently in condensed matter or high-energy physics. Another assumed feature of Hamiltonians is *sparsity*, i.e. the number of non-zero elements in each row of the matrix is significantly smaller than  $2^n$ . Locality can often be shown to imply sparsity.

Physical systems can also have interactions that whose strength decay as an inverse polynomial of distance between particles (e.g. Coulomb interactions). Hamiltonians of such systems are harder to simulate compared to the strictly local systems.

- **Specification of Hamiltonian.** The Hamiltonian is an exponentially large matrix, so for efficient quantum simulation it is necessary that there exists a way to efficiently compute the elements of this matrix. The most common way to represent Hamiltonians in this way is to write them as a sum of Pauli terms, where each term contains only Pauli-matrices on only a few qubits,

$$H = \sum_{l=1}^L H_l. \quad (4)$$

For instance, in the well studied Heisenberg model Hamiltonian in 1D,  $H_l$  would be a term of the form  $X_l X_{l+1} + Y_l Y_{l+1} + Z_l Z_{l+1}$  which is supported on a nearest neighbour pair of qubits.

Some quantum simulation algorithms assume a different access model based on an oracle (i.e. a black box function) that can compute in coherent superposition the matrix entries of the Hamiltonian given the corresponding indices [73]. Such an oracle can be constructed with polynomial overhead from the representation in Equation (4).

- **Error definitions.** The runtime complexity of Hamiltonian simulation algorithms is often specified in terms of an error guarantee  $\epsilon$ . This error is measured in terms of operator norm,

which is defined as the largest eigenvalue of an operator in absolute value. Simulation algorithms give a method to efficiently implement an operator  $U$  such that  $\|U - e^{-iHt}\| \leq \epsilon$ .

**Algorithms for time-independent Hamiltonians** An extensive amount of work has been done on the problem of time-independent Hamiltonian simulation. Often, complexity bounds in literature are stated in terms of the operator norm  $\|H\|$ . Keep in mind that in many physical systems this quantity is linear (or of higher-order) in the number of particles in the system.

- **Trotter product formulas.** Product formulas give simple ways to simulate the time evolution of  $H$  using time evolution of few-body interaction terms (i.e. the  $H_l$  in Equation (4)), which make up the full Hamiltonian. For the simplest case of simulation  $H = H_1 + H_2$  for time  $t$ , the second order Trotter product formula gives the following recipe for simulation,

$$e^{-iHt} = (e^{-i(H_1+H_2)\Delta t})^N \approx (e^{-iH_1\Delta t/2} e^{-iH_2\Delta t} e^{-iH_1\Delta t/2})^N, \quad (5)$$

Here the evolution is broken up into  $N$  time steps of time  $\Delta t$  and the evolution in each time step is approximated using the second-order Trotter formula. Higher-order product formulas are more accurate but a single step requires more overhead to implement. It can be shown that achieving a final error of  $\epsilon$  in the simulation using a  $(2k)$ -th order formula for a physical Hamiltonian requires a circuit with a gate-count that scales as  $O(\alpha_{k,comm}^{1/2k} 5^{2k} n L \frac{t^{1+1/2k}}{\epsilon^{1/2k}})$ . Here  $\alpha_{k,comm}$  is a quantity that captures the commutativity of the terms in the Hamiltonian [75, 102]. In theory and in practice, the performance of these algorithms can be improved if the Hamiltonian has many terms that commute with each other.

Trotter product formulas are simple to implement and work well in practice. These methods do not require ancilla qubits or extra control operations. These features make them ideal for implementation in near-term quantum computers. However, there are two main drawbacks: higher order product formulas lead to higher circuit depth and they do not scale well in terms of the error  $\epsilon$ .

- **Randomization and qDRIFT.** It has been observed that randomizing the order in which terms are applied in a Trotter formula can improve its performance [74]. A popular algorithm that uses randomization is *qDRIFT*. This method has a scaling that is independent of the number of terms in the Hamiltonian ( $L$ ) [49]. The downside is that the complexity scales quadratically in  $t$ . This might be useful for cases where the Hamiltonian is dominated by a few terms, refer to [69] for details.
- **HHKL algorithm for simulation on lattices.** For Hamiltonians defined on a  $D$ -dimensional lattice with geometric locality, the algorithm described in [158] can achieve  $\tilde{O}(nt \log(\frac{1}{\epsilon}))$  scaling. The algorithm is similar to a product formula and exploits locality of quantum evolution to optimally break it up into smaller pieces. This gives a circuit complexity that is asymptotically optimal with much improved dependence on error compared to Trotter product formulas. However, the algorithm is not applicable to more complex geometries.
- **LCU series expansion method.** For general sparse Hamiltonians, a method based on series expansion can give better asymptotic scaling compared to product formulas. These algorithms exploit various expansions (Taylor series, Dyson series etc..) to write  $e^{-iHt}$  as a weighted sum of easily implementable unitary operations [234, 29]. Such a series can be

## Overview

implemented on a quantum computer using a technique known as Linear Combination of Unitaries (LCU). The complexity of this method for simulating an  $s$ -sparse Hamiltonian is  $O(s^2 nt \|H\|_{max} \log(1/\epsilon))$  given Oracle access to such a Hamiltonian ( $\|H\|_{max}$  scales with  $n$  for physical systems). This algorithm only succeeds with a certain probability and hence requires an amplitude amplification step at the end to boost this success probability to an acceptable level. The main drawback of this method is identified as the potentially large number of ancillas required for implementation [76].

- **Qubitization and QSVT.** These are related techniques that work by manipulating the so-called *block encoding* of the Hamiltonian, which is a larger unitary matrix that has a matrix proportional to  $H$  as a submatrix. Such a block encoding necessarily requires ancillary qubits but fewer ancillas are required compared to LCU. The complexity of these methods depend heavily on the various input models assumed [268]. For simulation on lattices the complexity is seen to scale with  $n^2 t$  [158]. Quantum Singular Value Transformation (QSVT) is a generalization of qubitization and some related techniques [269] These allow for implementing any function  $f(H)$  of the Hamiltonian, given an appropriate block encoding of  $H$  [146, 147]. These techniques are not as simple to implement as product formulas, but they have asymptotically better complexities.

**Time-dependent Hamiltonians** Time-dependent Hamiltonian simulation is a strictly harder task than time-independent simulation. However, many ideas from the time-independent case carry over. Using ideas from Trotterization, product formulas have been developed that can be used in the time dependent case [434]. The main issue with this approach is the strong dependence of the complexity on the rate of change of the Hamiltonian. This issue can be mitigated by using a randomization approach [330]. The HHKL algorithm [158] also works natively for time-dependent geometrically local time-dependent Hamiltonians.

Time-dependent evolution can also be approximated using a Dyson series and simulated using the LCU technique discussed above [270, 215]. These methods lead to improved dependence in the rate of change of the Hamiltonian but are more difficult to implement. Developing a time-dependent equivalent of QSVT type techniques is an open problem [102].

**Simulating Fermionic Hamiltonians** A large fraction of Hamiltonians seen in areas such as quantum chemistry or condensed matter physics describe the physics of fermions. Fermionic Hamiltonians require some overhead to be mapped to Hamiltonians that describe interactions between qubits. The main reason for this overhead is the following fact: Fermionic operators that have disjoint supports anti-commute and this constraint is highly non-trivial to satisfy for a system of qubits. Following are some techniques used in literature to map fermionic problems to qubits.

- **Jordan-Wigner:** This is the standard conversion that is used between fermions and qubits. However for Hamiltonians that are not one-dimensional, this will turn a local Fermionic Hamiltonian into a highly non-local qubit Hamiltonian. This produces high-weight Pauli terms in the qubit Hamiltonian that can be challenging for simulation algorithms [410].
- **Bravyi-Kitaev:** This is similar to Jordan-Wigner and produces a non-local Hamiltonian. But the mapping itself is more efficient in theory. Both Jordan-Wigner and Bravyi-Kitaev does not require ancillary qubits to do the mapping [41].



- **Techniques using auxiliary fermions:** These preserve locality of the Hamiltonian but require ancillary qubits. Key idea is to use extra fermions to mediate interactions so as to preserve locality. Refer [417] and the corresponding section in [158] for one such technique.
- **First quantization:** For electronic Hamiltonians the issue of anti-commutation can be avoided if the simulation is performed in the first-quantized representation [396, 270]. These approaches require that the initial state be prepared to respect the exchange symmetry of electronic wave functions. While this is a very promising approach for quantum chemistry problems, it is under-explored in other areas like QCD.

### 1.4.2 Open quantum systems

Consider a more general version of Hamiltonian simulation that applies to an open quantum system that is interacting with an environment. The dynamics of an open quantum system under Markovian assumptions is governed by the Lindblad master equation [276]. The Lindblad equation describes a non-unitary dynamics and this makes it more challenging to simulate on a closed quantum computer. The dynamics of the system qubits alone (now given as a density matrix  $\rho$ ), can be described by a *Lindblad master equation*:

$$\frac{\partial \rho(t)}{\partial t} = \mathcal{L}\rho(t) := \underbrace{-i[H, \rho]}_{\substack{\text{coherent part} \\ \text{(Schrödinger equation)}}} + \underbrace{\sum_{j=1}^m \overbrace{\left(L_j \rho L_j^\dagger\right)}^{\text{transition}} - \frac{1}{2} \overbrace{\left(L_j^\dagger L_j \rho + \rho L_j^\dagger L_j\right)}^{\text{decay}}}_{\text{dissipative part}} \quad (6)$$

The operators  $L_i$  define the interaction between the system and the environment and have to be specified as part of the input to the algorithm. Many ideas from Hamiltonian simulation can be generalized to the case of open quantum systems.

- **Simulation of environment:** Simulation of open quantum systems can be mapped to the Hamiltonian simulation problem by using ancilla qubits to represent the environment and then simulating the system and ancilla qubits together as the larger closed system. Then any property of the system can be estimated by measuring the system qubits alone [84, 401]. This technique has a large overhead in terms of ancillas.
- **Trotterization for Lindbladians:** The solution of the Lindblad master equation can be given by the super operator (i.e. a linear operator acting on the space of operators)  $e^{t\mathcal{L}}$ . Trotter product formulas can be developed for this operator. Reference [78] gives a Trotterization framework for such open evolutions improving on [227]. An experimental implementation can be found in [169]. Going beyond second-order trotter formulas for such evolutions is an open problem.
- **Series expansion:** A generalized LCU technique can be used to simulate the Lindblad equation [84]. Just like for closed quantum system, this technique can improve asymptotic scaling of the algorithm but requires ancillary control to be implemented.

## Overview

### 1.4.3 Finding ground states

The ground state of a system is the quantum state with the lowest energy. Given the system Hamiltonian, the ground state is also the eigenstate with the lowest eigenvalue. In terms of worst-case complexity, finding the ground state is thought of as a harder problem than simulating the Hamiltonian [214]. But it is far less clear if the Hamiltonians found in nature correspond to worst-case instances for this problem. Quantum simulation is often used as a subroutine in algorithms that aim to find the ground state. The main quantum algorithms for finding ground states are the following:

1. **Quantum Phase Estimation (QPE):** Given an  $n$ -qubit Hamiltonian with the spectral decomposition,  $H = \sum_i E_i |\lambda_i\rangle \langle \lambda_i|$  with  $E_i \in [0, 1]$  and an initial state  $|\psi\rangle = \sum_i \psi_i |\lambda_i\rangle$ , the QPE algorithm essentially implements the following transformation,

$$\sum_i \psi_i \underbrace{|0\rangle}_{t \text{ ancillas}} \underbrace{|\lambda_i\rangle}_{n \text{ qubit system}} \xrightarrow{QPE} \sum_i \psi_i |\tilde{E}_i\rangle |\lambda_i\rangle \quad (7)$$

Here  $\tilde{E}_i$  is a  $t$  bit approximation of the energy eigenvalue  $E_i$ . For physical systems, the constraint  $E_i \in [0, 1]$  can be satisfied by scaling the Hamiltonian. The QPE circuit consists of a sequence of quantum simulation steps controlled on the ancilla register followed by quantum Fourier transform. Measuring the ancilla register then gives us the state  $|\tilde{E}_i\rangle |\lambda_i\rangle$  with probability  $|\psi_i|^2$ . Thus, if the initial state  $|\psi\rangle$  is prepared such that it has a significant overlap with the ground state, then this measurement will have a correspondingly large probability to prepare the ground state. The smaller this overlap the more number of times the QPE circuit will have to be run to guarantee the preparation of the ground state. Also notice that the number of ancillary qubits ( $t$ ) sets the ability of the algorithm to resolve different eigenstates, hence the number of ancillas required will depend on the energy gap between the ground state and the first excited states. The number of ancillas required to have  $\epsilon$  accuracy in eigenvalues with a success probability of  $1 - \delta$  is  $t = \lceil \log(\frac{1}{\epsilon}) \rceil + \lceil \log(2 + \frac{1}{2\delta}) \rceil$  [300, 260].

Additional errors can be incurred in QPE due to errors coming from the Hamiltonian simulation steps in QPE. For Hamiltonian simulation using Trotterization, this error is studied in Ref. [225]. The cost of Hamiltonian simulation can be offset by using QPE directly with the qubitized version of the Hamiltonian [329]. A recent efficient implementation of QPE can be found in [110]. The key issue in using QPE is finding a good initial state which has a significant overlap with the ground state. Existing classical approaches like Hartree-Fock can help here and QPE can be used to further refine them [412].

2. **Adiabatic theorem.** The adiabatic theorem is a result that converts the problem of ground state preparation to one of time-dependent Hamiltonian simulation [6, 3]. For  $t \in [0, T]$ , consider the following time dependent Hamiltonian,  $H(t) = (1 - \frac{t}{T})H_i + \frac{t}{T}H_f$  and a system whose dynamics is governed by this Hamiltonian via (3). If the initial state of this system is prepared to be ground state of  $H_i$ , then for large enough  $T$ , the state at time  $T$  can be shown to have a large overlap with the ground state of  $H_f$ .  $H_i$  is often taken to be Hamiltonian whose ground state is easy to prepare and  $H_f$  is taken to be the Hamiltonian whose ground state we are interested in preparing. The interpolation between these two Hamiltonians can be a general non-linear function and in some cases this is advantageous [352]. There is a theoretical characterization of how large  $T$  should be based on some properties of the interpolation

used and hence cannot be generally bounded. Ref. [429] gives an end-to-end description of an adiabatic approach for the Hubbard model. The adiabatic theorem can also be used in conjunction with QPE to prepare ground states [36].

3. **Variational approaches [61, 404].** Variational approaches work constructing by a quantum circuit with variational parameters which are then optimized to minimize the energy of the system. These techniques usually have a hybrid quantum-classical nature. The energy of the ansatz is first estimated by measuring an observable by repeatedly applying this circuit to a register and then measuring it. Then the variational parameters of the circuit are updated using an optimization algorithm running on a classical computer. The promise of these methods come from the fact that variational quantum circuits have enough expressibility to represent highly entangled states efficiently. It is impossible to give theoretical guarantees for these types of methods as the quality of their solution depends on the the choice of the variational circuit. Just like for classical variational methods, an effective ansatz would be one which can represent the ground state with only a few variational parameters.

### 1.4.4 Preparation of thermal states

Preparation of thermal states is an important algorithmic task that can be seen as a generalization of finding ground states. The state of a quantum system with Hamiltonian  $H$  at thermal equilibrium with a bath of inverse temperature  $\beta$  is given by the mixed state  $\rho = \exp(-\beta H)/Z$ . Here  $Z$  is known as partition function which is an important thermodynamic quantity that also fixes the normalization of the state. The ability to prepare copies of such states or compute observable from them is crucial in studying quantum systems in thermal equilibrium. We can see that in the  $\beta \rightarrow \infty$  limit the thermal state reduces to the ground state of  $H$ . In practice, this problem is often harder for higher values of  $\beta$  than for lower values. The exact algorithmic task here is to compute observables from the state  $\rho \propto \exp(-\beta H)$  given access to a Hamiltonian  $H$ . A more technical overview of the algorithms known for this task can be found in Reference [70].

- **Series expansion:** Reference [80] shows the application of the LCU technique to the problem of thermal state preparation. The key innovation is a cleverly constructed series approximation (a discretized Hubbard-Stratonovich transform) for the exponential function. The complexity of this algorithm scales as  $O(\sqrt{\frac{2^{n/2}\beta}{Z}} \text{poly}(\log(\frac{1}{\epsilon})))$ . This is very inefficient in the worst case.
- **Using Quantum Singular Value Transforms (QSVT):** QSVT is meta-algorithm that can be seen as a generalization of the qubitization procedure. For a given function  $f$  and a Hamiltonian  $H$ , this technique allows us to construct operators proportional to  $f(H)$ . QSVT techniques can also be used with a polynomial approximation for the exponential function to achieve this task (see Section 5 in Reference [147] for detailed discussion on complexities).
- **Quantum Gibbs sampling:** Classically thermal state distributions are most easily prepared by Monte-Carlo-Markov-Chain (MCMC) samplers (Glauber dynamics, Metropolis-Hastings etc.). At a high level these methods exploit the physical fact that a carefully constructed open system evolution eventually converges to a thermal state (i.e by cooling/heating by a thermal bath). This opens the possibility of using open quantum system evolution to prepare quantum thermal states. These algorithms are most closely related to how thermal states are prepared by natural processes [70, 68, 337]. Just like for classical MCMC samplers, the time

## Overview

taken for such algorithms to converge to the thermal states cannot be tightly upper bounded in general. However, each step of the algorithm can be implemented efficiently. We should note that these class of algorithms are very recent and as of writing this it is not clear which proposal will be the most useful one in practice.

- **QPE-based methods:** Another way to leverage classical MCMC to prepare quantum thermal states is to run MCMC directly in the energy eigenbasis of the Hamiltonian [400, 328]. These methods use the QPE transform to achieve this task. The disadvantage of this method compared to quantum Gibbs sampling is the large overhead of the QPE procedure which needs to be repeated many times here. There are also complications arising from the rejection step that is used in the MCMC sampler (refer [70] for a detailed discussion on these issues).

## **2 Experimental analysis of magnetic materials at the MAGLAB user facility**

This chapter presents several applications relevant to the MAGLAB user facility. The MAGLAB is an experimental facility that analyzes several magnetic materials of interest. These include Kitaev quantum spin liquids (KQSLs), multi-ferroic materials for memory and high temperature superconductivity. We focus on the applications of quantum computing in the study of KQSLs, where the broad research goal is to identify the effective spin Hamiltonian and search for the existence of the KQSL phase in the phase space. The computational capabilities required are methods for quantum Hamiltonian simulation and computation of ground states for spin Hamiltonians on given regular two-dimensional lattices. Current classical approaches cannot be scaled to sufficiently large system sizes ( $> 10000$  sites) that are required to avoid significant errors from finite size effects. Consequently, the primary potential benefit of a quantum computer is the ability to perform these computations at a scale where the results accurately represent experimental observables and properties of the material. The following table summarizes the computational requirements that must be met to be of value to research at the MAGLAB.

**Hamiltonian Type:** Spin Kitaev/Heisenberg Hamiltonian.

**Quantum Computational Kernels:** Ground State Preparation, Hamiltonian simulation.

# Experimental analysis of magnetic materials at the MAGLAB user facility

## 2.1 Application area overview

### 2.1.1 High-level description of the application area

Materials that exhibit strong spin-spin interactions typically manifest long-range magnetic order. When subjected to a magnetic field, these materials undergo a spin structure evolution that is reflected in distinct magnetization curves. Analyzing these curves enables the deduction of the spin Hamiltonian governing the magnetic systems. The recent identification of potential quantum spin liquid (QSL) candidates has generated considerable excitement in the condensed matter community [471, 222, 411, 363, 43]. However, the intricate magnetization behavior, stemming from purely quantum mechanical origins, poses challenges in interpreting experimentally measured magnetization and thermodynamic properties [267]. Consequently, the advent of scalable quantum computers holds great promise for efficiently deciphering complex spin Hamiltonians, facilitating a deeper understanding of quantum effects.

The quest for materials featuring a robust coupling between spin and electrical degrees of freedom is pivotal for realizing ultra-low-power devices compatible with existing industrial technology [141, 71]. This is because current-based electronic devices inevitably dissipate heat, whereas controlling spin-based devices does not. The coupling between spin and electrical degrees of freedom is achieved through a robust spin-orbit coupling, which induces spin-dependent charge motion and vice versa. While current studies often rely on symmetry arguments [116], the absence of simulations considering both spin and charge degrees of freedom hinders the discovery of ideal magnetoelectric materials capable of operating at room temperature with minimal magnetic and electric fields. A crucial imperative lies in formulating a Hamiltonian that encompasses both charge and spin degrees of freedom, utilizing extensive magnetization and electric polarization data accumulated over the years. Identifying key parameters that enhance operational temperatures to room temperature is paramount for guiding materials design in this pursuit.

Aforementioned studies are actively pursued in The National High Magnetic Field Laboratory (NHMFL), which operates seven user facilities spread across three campuses in the United States [175]. The headquarters is situated in Tallahassee, Florida, and specializes in ultra-high 'dc' magnetic fields. It boasts numerous Guinness World Records, including the most potent dc magnet capable of reaching up to 45 T [176]. Another branch is located in Gainesville, Florida, where ultra-low temperatures down to 300  $\mu\text{K}$  can be combined with a 20 T dc magnet. The final branch is situated at Los Alamos National Laboratory, which operates pulsed magnets reaching up to 100.75 T [176], making it the most powerful pulsed magnet globally. Annually, more than 1,800 researchers utilize these facilities, with most incurring no cost, and collectively, they produce over 400 peer-reviewed publications studying magnetic materials. NHMFL supports a diverse range of experimental techniques, including various magnetometry methods, torque magnetometry, electrical property measurements, and thermodynamic measurements.

### 2.1.2 Utility estimation

**Overview of the value of the application area** The accurate identification of a spin Hamiltonian for a Quantum Spin Liquid (QSL) phase is a critical task, as it provides insights into the quasi-particle excitations that the QSL phase can accommodate. Some quasi-particle excitations within certain QSL phases exhibit valuable physical properties, paving the way for fault-tolerant topological quantum computations [220]. These computations hold the promise of mitigating the noise issues inherent in quantum computations [242].

# Experimental analysis of magnetic materials at the MAGLAB user facility

Furthermore, the realization and identification of devices with ultra-low energy consumption, leveraging magnetoelectric coupling, are indispensable for sustaining Moore's Law [228]. The conventional trajectory of Moore's Law is impeded by heat generation [381], and the pursuit of reduced energy consumption without compromising computational capabilities is paramount.

Hence, a fundamental goal is to comprehend the magnetic and electric properties of materials, propelling our society toward smaller, faster, smarter, and more robust technology. This endeavor not only addresses the challenges posed by issues we are facing but also has the potential to usher in innovative technologies that will reshape the way we perceive and experience the world.

**Concrete utility estimation** The MAGLAB receives a budget of \$40M per year [135] which is utilized to cover labor costs, the cost of experimental equipment and materials. On average a total of 20 materials are studied within one fiscal year [333], thus resulting in a budget of \$2M per year per material. A given material, especially the more promising ones, are studied for multiple years in a row with the goal of answering a given set of questions. The research goals for the specific material will be complete once these set of questions are answered. Following this argument, if a material is studied for  $N_Y$  years with the goal of answering  $N_Q$  questions, then the allocated budget for answering each question on average is  $\$2M \times \frac{N_Y}{N_Q}$ .

In Section 2.2, we consider the Kitaev Quantum Spin Liquid candidate materials using  $\alpha$ -RuCl<sub>3</sub> as the concrete example. A set of four applications, of which two are presented in the chapter, cover the set of questions that constitute the current research goals. These set of questions are currently unanswered due to the computational bottlenecks of classical approaches, and the applications presented will be able to resolve this problem thus successfully achieving the research goals for  $\alpha$ -RuCl<sub>3</sub>. Consequently, we assign a cumulative value for the four applications equal to the total budget for the current research goals. The material  $\alpha$ -RuCl<sub>3</sub> has been studied in the MAGLAB for at least 5 years. Therefore, we estimate the value of each of the four applications presented to be  $\$2M \times 5/4 = \$2.5M$ .

## 2.2 Problem and computational workflows: Kitaev QSLs

### 2.2.1 Detailed background for Kitaev QSLs

We first define some notation that we will use for the rest of the chapter regarding the bonds and coordinates. We use  $(\mathcal{X}, \mathcal{Y}, \mathcal{Z})$  to denote the set of edges in the lattice in Figure 2-1 corresponding to the  $X, Y$  and  $Z$  bonds respectively. Each site  $i$  has a magnetic spin  $S_i$  which can be decomposed in the Pauli basis as  $S_i = (S_i^x, S_i^y, S_i^z)$  denoting the component of the spin along the orthogonal  $(\hat{x}, \hat{y}, \hat{z})$  directions shown in Figure 2-8.

Note this is different from the capitalized letters  $(X, Y, Z)$  used to denote bond types. An alternative orthogonal coordinate system  $(\hat{a}, \hat{b}, \hat{c})$  that is relevant to the experimental protocols and observables is shown in Figure 2-8, where  $\hat{c}$  is the out of plane component. The relationship between the two orthogonal coordinate systems is given as

$$\begin{bmatrix} \hat{a} \\ \hat{b} \\ \hat{c} \end{bmatrix} = D \begin{bmatrix} \hat{x} \\ \hat{y} \\ \hat{z} \end{bmatrix}, \quad \text{where } D = \begin{bmatrix} 1/\sqrt{6} & 1/\sqrt{6} & -2/\sqrt{6} \\ 1/\sqrt{2} & -1/\sqrt{2} & 0 \\ 1/\sqrt{3} & 1/\sqrt{3} & 1/\sqrt{3} \end{bmatrix} \quad (8)$$

Therefore, the decomposition of the spin  $S_i = (S_i^a, S_i^b, S_i^c)$  along the  $(\hat{a}, \hat{b}, \hat{c})$  coordinates and along

## Experimental analysis of magnetic materials at the MAGLAB user facility

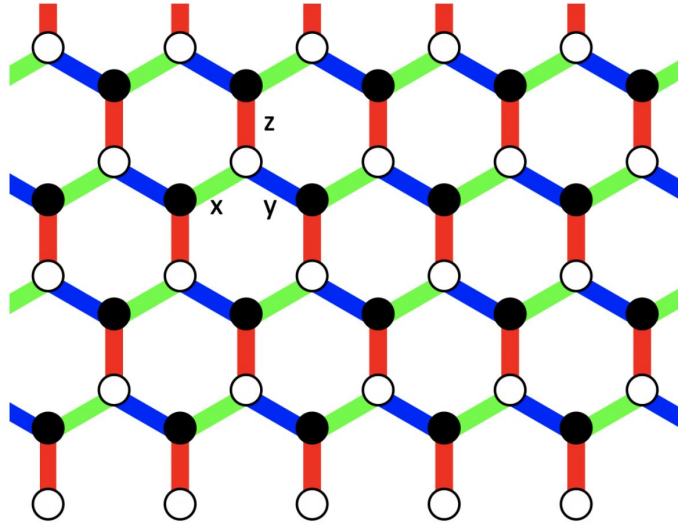


Figure 2-1: Each color indicates  $K_x, K_y, K_z$  bonds [350]

the  $(\hat{x}, \hat{y}, \hat{z})$  coordinates are given by

$$(S_i^x, S_i^y, S_i^z) = (S_i^a, S_i^b, S_i^c) D, \quad (S_i^a, S_i^b, S_i^c) = (S_i^x, S_i^y, S_i^z) D'. \quad (9)$$

The quantum spin liquid phase is a magnetic state that lacks magnetic long-range ordering even at the lowest temperatures, despite strong spin-spin interactions [363]. Although the ground state appears genuinely chaotic without any discernible local structure, the long-range quantum entanglement among spins enables the emergence of exotic excitations [431]. These excitations are topologically protected, providing a foundation for fault-tolerant quantum computations. One prominent example of a quantum spin liquid phase predicted to host such topologically protected excitations is the Kitaev quantum spin liquid phase, proposed by Alexey Kitaev in 2003 [220, 222]. He examined the honeycomb lattice, where each vortex with a spin-1/2 is linked to its nearest neighbor spin through a bond-dependent spin interaction as shown in 2-1.

The spin Hamiltonian is expressed as follows.

$$\mathcal{H} = K_x \sum_{ij \in \mathcal{X}} S_i^x S_j^x + K_y \sum_{ij \in \mathcal{Y}} S_i^y S_j^y + K_z \sum_{ij \in \mathcal{Z}} S_i^z S_j^z, \quad (10)$$

This Hamiltonian emerged as a rare instance of an exactly solvable model for a two-dimensional system. In its ground state, it was established that only very short-range spin-spin correlations exist at zero temperature, indicating the absence of magnetic long-range ordering [222]. Additionally, two types of Majorana Fermions were identified as excitations: local flux excitations and itinerant Majorana Fermions. Initially serving as a useful toy model for physics exploration, subsequent theoretical investigations [192, 341, 217] demonstrated that  $\alpha$ -RuCl<sub>3</sub> could realize this Hamiltonian. However, further investigations revealed that while  $\alpha$ -RuCl<sub>3</sub> indeed captures the bond-dependent interactions, other unwanted terms such as Heisenberg exchange interactions up to third nearest neighbors and symmetric off-diagonal terms are also permissible [340]. The presence of these terms in the spin Hamiltonian leads to undesirable magnetic long-range ordering [249].

It was discovered that the magnetic field destabilizes the magnetic long-range ordering and gives rise to an intermediate phase before saturating the system [211]. In this intermediate state, a



# Experimental analysis of magnetic materials at the MAGLAB user facility

disordered configuration is observed, marked by the presence of half-quantized thermal Hall conductivity—a characteristic feature of a topologically nontrivial state and chiral spin liquid states [211]. Nevertheless, the debate surrounding the nature of the intermediate phase persists, and the features of this state remain considerably uncertain, despite extensive experimental studies [267], including magnetization measurements in various configurations. The absence of an appropriate spin Hamiltonian capable of describing the magnetic properties of the compound adds to the complexity in comprehending the nature of the intermediate state.

## 2.2.2 Application category 1: Hamiltonian search for spin liquids

In this category of applications, we pose the problem of determining the accurate spin Hamiltonian of candidate Kitaev QSLs using various experimental data such as net magnetization, specific heat, etc. The computational workflow will be different for the various applications in this category depending on the type of experimental data being utilized.

We will use the compound  $\alpha$ -RuCl<sub>3</sub> as an example for this section. A similar description is relevant for several other candidate spin liquid materials. The permitted terms in the spin Hamiltonian for  $\alpha$ -RuCl<sub>3</sub> are determined by its local and global symmetry. Through symmetry arguments, researchers have derived the most general form of the spin Hamiltonian for  $\alpha$ -RuCl<sub>3</sub> [340]. This includes: 1) Heisenberg-type exchange interactions up to the third nearest neighborhood, 2) Kitaev exchange interactions up to the third nearest neighborhood, 3) Off-diagonal symmetric interactions between nearest neighbor exchange interactions, and 4) Single-ion anisotropy with the Zeeman term. The most generic spin Hamiltonian possesses a number of parameters as shown in Eq. (11).

$$\begin{aligned}
 \mathcal{H} = & K_x \sum_{ij \in \mathcal{X}} S_i^x S_j^x + K_y \sum_{ij \in \mathcal{Y}} S_i^y S_j^y + K_z \sum_{ij \in \mathcal{Z}} S_i^z S_j^z \\
 & + J \sum_{ij} \mathbf{S}_i \cdot \mathbf{S}_j \\
 & + \Gamma_z \sum_{ij \in \mathcal{Z}} (S_i^x S_j^y + S_i^y S_j^x) + \Gamma_y \sum_{ij \in \mathcal{Y}} (S_i^z S_j^x + S_i^x S_j^z) + \Gamma_x \sum_{ij \in \mathcal{X}} (S_i^y S_j^z + S_i^z S_j^y) \\
 & + A \sum_i (S_i^c)^2 + \sum_i \mathbf{S}_i \cdot \mathbf{H}
 \end{aligned} \tag{11}$$

The term  $\mathbf{H}$  denotes the external magnetic field applied during experimental protocols. A tabulated list of potential spin Hamiltonian terms has been compiled based on these considerations and is given in Figure 2-7.

To elucidate the properties of Kitaev quantum spin liquid candidates such as  $\alpha$ -RuCl<sub>3</sub>, we conduct a series of experiments. The initial investigation involves magnetization measurements, wherein we assess magnetization as a function of temperature with magnetic fields at various angles, primarily along and perpendicular to the bond within the plane and out-of-plane directions. We explore potential distinctions between zero-field-cooled conditions—where we cool the compound to its lowest temperature without a magnetic field—and field-cooled magnetization, where we cool the compound with a magnetic field before conducting measurements. Given that a QSL is anticipated to lack long-range ordering, we scrutinize magnetization versus temperature curves for any anomalies. Additionally, we examine magnetic anisotropy by comparing the magnitude of magnetization along different directions as a function of magnetic field, aiming to deduce interaction types embedded in the spin Hamiltonian. Sweeping the magnetic field allows us to observe the evolution of the

## Experimental analysis of magnetic materials at the MAGLAB user facility

spin structure. In the case of  $\alpha$ -RuCl<sub>3</sub>, the role of the magnetic field is pivotal, as it destabilizes long-range magnetic ordering, leading the system into the putative Kitaev QSL phase.

Another commonly conducted measurement involves magnetic specific heat measurement for the Kitaev QSL phase. The magnetic specific heat is anticipated to exhibit two distinctive broad anomalies at certain temperatures. These anomalies are attributed to the release of entropy from itinerant Majorana fermions and  $Z_2$  flux excitations. The precise locations of these two anomalies serve to pinpoint the energy scale of the Kitaev exchange interactions [296, 443].

Furthermore, we explore how the magnetic specific heat evolves with varying magnetic fields to gain insights into the stabilization of the long-range ordered phase and the scaling of the spin gap with magnetic field strength. In the Kitaev QSL phase, the magnetic gap is expected to exhibit a cubic scaling relationship with the magnetic field [399].

A crucial final measurement involves thermal conductivity assessments. The Kitaev Quantum Spin Liquid (KQSL) phase is topologically distinct from the vacuum, and the presence of charge-neutral particles at the edge state is imperative. Given that these carriers lack charge, their detection is possible solely through the flow of thermal energy. The KQSL phase under a magnetic field is expected to exhibit half-integer quantization of the thermal Hall conductance [211].

### **Application 1.1 - Seeking the accurate spin Hamiltonian for $\alpha$ -RuCl<sub>3</sub> using experimental data on magnetization.**

**Specific background of the application - magnetization experimental protocol** The measurable parameter is the net magnetization denoted as  $g\mu_B \sum_i \langle \psi | \mathbf{S}_i | \psi \rangle$ . For dc field experiment, we employ vibrating sample magnetometry for its determination. This technique involves oscillating a sample around a coil and measuring the induced voltage across the coil, directly proportional to the net magnetization of the sample. Through meticulous calibration against a standard sample, we can obtain the absolute value of magnetization. Our typical temperature scan ranges from 0.5 K to 400 K under a small magnetic field of up to 14 T. An example data is shown in Fig. 2-3. During the temperature scan, we discern whether the sample exhibits spontaneous magnetic ordering.

Furthermore, we perform a field scan to detect spin flip or spin flop phase transitions, providing insights into the energy scale of magnetic anisotropy. Moreover, the saturation field aids in determining the energy scale of spin interactions. For pulsed field measurements, we utilize extraction magnetometry, measuring the change in magnetization over time ( $dM/dt$ ). Subsequently, we integrate the signal with time to derive the magnetization. The pulsed field profile as a function of time is depicted in Figure 2-4 and typical data of magnetization are shown in Fig. 2-5.

**Objective** The objective is to discern which candidate Hamiltonians are the most accurate predictors of existing magnetization data as a function of external magnetic fields.

### **End-to-end computational workflow**

- **Inputs:**

1. List of candidate Hamiltonians  $\{H_i, i \in [m]\}$ .
2. External magnetic field settings  $\{B_k, k \in [K]\}$  and simulation times  $\{t_{sim}^k, k \in [K]\}$ .
3. For each tuple of candidate Hamiltonian  $H_i$ , external field setting  $B_k$  and simulation time  $t_{sim}^k$ , the full description of the resulting time-varying Hamiltonian in the magnetic field sweep experimental protocol  $\{H_i^k(t), t \in [0, t_{sim}^k]\}$ .

# Experimental analysis of magnetic materials at the MAGLAB user facility

4. Initial state  $\rho_0$ .
5. Experimental data on magnetization  $\{M_k^d, k \in [K]\}$ .

- **Outputs**

1. Net in-plane magnetization perpendicular to the bond direction :  $g_a \mu_B \sum_i \mathbf{S}_i \cdot \hat{a}$ , where  $\hat{a}$  is perpendicular to one of the bond directions shown in Fig. 2-1, where  $g_a$  is  $g$ -factor anisotropy that is close to 2.3 and  $\mu_B$  is Bohr magneton.
2. Net in-plane magnetization along the bond direction:  $g_b \mu_B \sum_i \mathbf{S}_i \cdot \hat{b}$ , where  $\hat{b}$  is one of the bond directions shown in Fig. 2-1, where  $g_b$  is  $g$ -factor anisotropy that is close to 2.3.
3. Net out-of-plane magnetization  $g_c \mu_B \sum_i \mathbf{S}_i \cdot \hat{c}$ , where  $\hat{c}$  is perpendicular direction to the honeycomb plane, where  $g_c$  is  $g$ -factor anisotropy that is close to 1.3.

- **Workflow:** The flowchart showing the *end to end workflow* is given in Figure 2-2. The *hard computational module* is the *Hamiltonian simulation*. For the the lattice sizes relevant to study this problem, the exponential dimension of the Hilbert space makes the simulation classically intractable.

## Why classical methods are not sufficient to perform the hard computational module

Classical methods to solve the hard computational module of Hamiltonian simulation include *exact diagonalization* and heuristics such as *density matrix renormalization group (DMRG)* and *quantum monte carlo (QMC)*. These methods are either too limited in size, not sufficiently accurate or not applicable in some situations. The details and limitations of these methods are given in the supplementary material Section 2.4.

**Concrete problem instantiations** Our focus is on  $\alpha$ -RuCl<sub>3</sub>, a key compound anticipated to exhibit a quantum spin liquid phase under a magnetic field. Researchers have compiled potential spin Hamiltonians through simulations on classical computers.

*Input 1:* The list of candidate Hamiltonians is given in the table in Figure 2-7. The size of the Hamiltonian is  $100 \times 100$  and is chosen to avoid finite size effects.

In experiments, the sample is cooled to an extremely low temperature of approximately 2 K, applying a magnetic field to establish a single magnetic domain. We anticipate observing the anti-ferromagnetic phase transition around 6.5 K. During this process, we gradually sweep the magnetic field between 0 and 60 Tesla while measuring the magnetization. A suitable spin Hamiltonian should be capable of capturing: 1) the magnitude of the magnetization within 5% of the experimentally measured magnetization, 2) the critical magnetic field between magnetically long-range ordering and the intermediate phase, as well as between the intermediate phase and the saturated phase, within 5%, 3) magnetic anisotropy between in-plane and out-of-plane magnetization, and 4) the magnetic anisotropy within the plane, specifically the subtle magnetization difference between the magnetic field along the bond and perpendicular to the bond. In the magnetization data shown in Figure 2-5, quantum critical fields are evident, marking the transitions from the antiferromagnetic phase to the intermediate phase and from the intermediate phase to the fully saturated phase. It is imperative that these quantum critical fields are reproduced within a 5% accuracy. Additionally, the ratio between in-plane and out-of-plane magnetizations should be faithfully reproduced, as it

## Experimental analysis of magnetic materials at the MAGLAB user facility

provides insight into the energy scale of off-diagonal terms and single ion anisotropy.

Based on the above discussion, a resolution of 0.5 Tesla is chosen for the external magnetic field settings, with a finer resolution of 0.1 Tesla in the region believed to contain the phase transitions. This specifies the list of external field set points.

*Input 2:* The external field set points are  $B_k \in 0 : 0.5 : 60$  Tesla, with an increased resolution in the critical range  $B_k \in 7 : 0.1 : 9$  Tesla. The simulation times  $t_{sim}^k$  are given by the x-axis values in Figure 2-4 corresponding to the  $B_k$  values specified above.

The time varying form of the Hamiltonian can be obtained by incorporating the external field with the chosen candidate Hamiltonian  $H_i$  among the list given in Input 1.

*Input 3:* The time varying Hamiltonian is given by

$$H_i^k(t) = H_i + f(t) \sum_j S_j^a, \quad \text{for } t \in [0, t_{sim}^k], \quad (12)$$

The time dependent magnetic field profiles  $f(t)$  of both dc and pulsed magnets are shown in Figure 2-4.

The initial state of the sample can be inferred from experimental data. See supplementary material section for more details.

*Input 4:* The initial state  $\rho_0$  is given in Section 2.4.

*Input 5:* The experimental data on net magnetization is given in Figure 2-5.

*Output precision requirement:* The magnetization measurements  $M_k^i$  from the Hamiltonian simulation must be computed to 1% relative accuracy. Given that a candidate Hamiltonian is considered suitable if it can predict experimental observables  $M_k^d$  within 5% accuracy, and the experimental measurement precision is less than 1%.

*Output wall-clock time limit:* Finding a suitable Hamiltonian by comparing with the existing experimentally measured magnetization data requires lots of iteration and we need to scan many possible form of Hamiltonian. To this end, therefore, we need to simulate a spin Hamiltonian with a couple minutes. For the entire workflow, less than two weeks time scale is acceptable.

**List of candidate systems where similar process is relevant** Numerous quantum spin liquid candidates face a common challenge: determining their spin Hamiltonians is challenging with current computational power and methods. This set of candidates includes iridates compounds such as  $\text{Na}_2\text{IrO}_3$ ,  $\alpha\text{-Li}_2\text{IrO}_3$ , and  $A'_3\text{LiIr}_2\text{O}_6$  ( $A' = \text{H, Cu, and Ag}$ ) [341]. Recently, certain cobaltites have garnered interest from researchers, including  $\text{Na}_2\text{Co}_2\text{Te}_2\text{O}_6$  [460] and  $\text{BaCo}_2(\text{AsO}_4)_2$  [464].

## Experimental analysis of magnetic materials at the MAGLAB user facility

For each candidate Hamiltonian  $H_i$ ,  $i = 1, \dots, m$

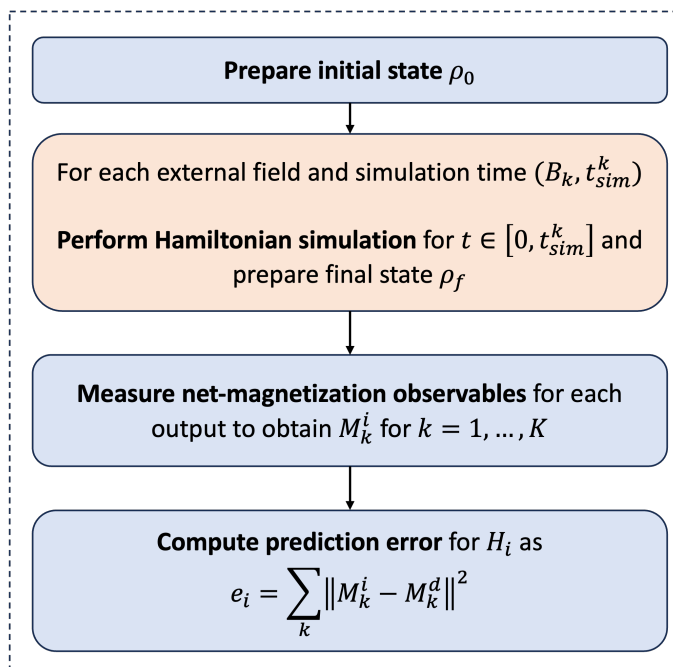


Figure 2-2: Workflow for Hamiltonian search using magnetization experimental data. The red box (Hamiltonian Simulation) contains the hard computational task/kernel.

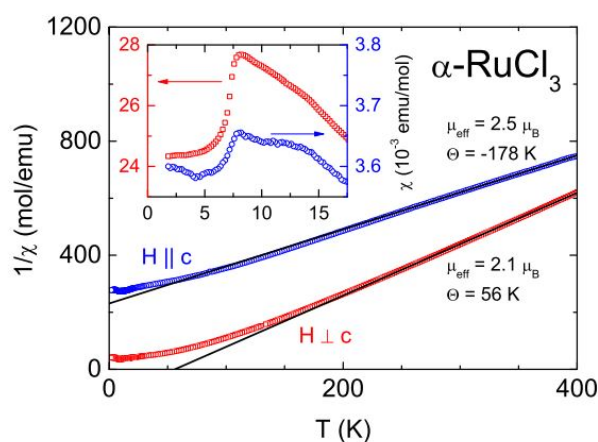


Figure 2-3: The inverse of magnetization divided by external magnetic field ( $1/\chi$ ) as a function of temperature with magnetic field along two different directions are shown [344].

## Experimental analysis of magnetic materials at the MAGLAB user facility

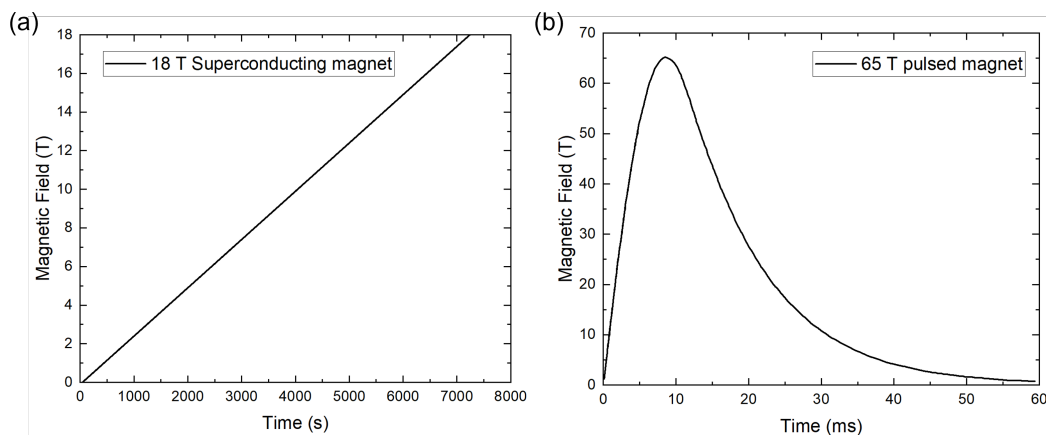


Figure 2-4: Field vs. time profiles of superconducting dc magnet (a) and 65 T short pulse magnet (b) [175]. Note that the time scale difference between dc magnet and pulsed field magnet.

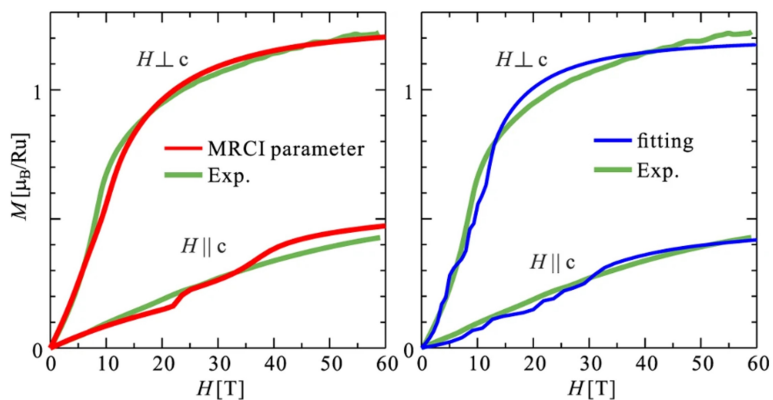


Figure 2-5: The magnetization measurements (solid green lines) with field along in-plane with larger magnetization and out-of-plane with smaller magnetization [202]. The red and blue solids lines are from exact diagonalization simulations [442].

# Experimental analysis of magnetic materials at the MAGLAB user facility

## Application 1.2 - Testing candidate Hamiltonians for $\alpha$ -RuCl<sub>3</sub> using ground state prediction.

**Specific background of the application - Experimental protocol to determine the ground state** The spin structure of the ground state at *zero external magnetic field* can be inferred from magnetization-temperature and magnetic field measurements. Initially, we categorize whether a system exhibits magnetic long-range ordering, discernible through singularities such as divergences or kinks in the magnetization measurement, indicative of a symmetry-breaking phase transition.

Subsequently, we ascertain if the magnetic ordering possesses a net magnetization. In the presence of a net magnetic component, particularly a ferromagnetic one, distinctions often arise between zero field cooled and field cooled states owing to magnetic domain effects. The direction of the ferromagnetic component can be deduced from the magnitude of magnetization.

In the case of antiferromagnetism, understanding how spins counterbalance is achieved by analyzing magnetization against temperature and magnetic field in various orientations. When the magnetic field aligns with spin directions, the net magnetization approaches zero in the limit of zero temperature; however, when perpendicular to the spins, a temperature-independent finite magnetization is observed. The magnetization-field curve illustrates spin flip or flop transitions, marked by sudden changes when the field aligns with spin directions and gradual increases when perpendicular. Symmetry-sensitive techniques, such as electric polarization, are also employed. Depending on the spin structure's symmetry, linear magnetoelectric coupling or second-order magnetoelectric coupling may be allowed.

Finally, we validate the symmetry through neutron diffraction experiments. In the presence of magnetic ordering, magnetic Bragg peaks emerge in momentum space, aligning with the wave vector of the spin ordering. Analyzing these magnetic Bragg peaks allows us to infer the spin arrangement and magnetic interactions within the material. The intensity of the peaks serves as an indicator of the magnetic order's strength, while the positions of the peaks unveil the spatial distribution of magnetic moments.

**Objective** The objective is to identify which of the candidate Hamiltonians in Figure 2-7 is able to predict the experimentally observed ground state in Figure 2-8 at *zero external magnetic field*. This procedure serves as a screening process for the proposed candidate Hamiltonians.

### End-to-end computational workflow

- **Inputs:**

1. List of candidate Hamiltonians  $\{H_i, i \in [m]\}$ .
2. A set  $\mathcal{P}$  of  $m$  points  $\mathbf{p}_1, \dots, \mathbf{p}_m$  in the two dimensional momentum space for which the Fourier transform is desired.
3. The experimentally observed intensities  $y^d$  of the Fourier transform of the ground state  $\rho_0$  at zero (near-zero) external field.
4. (Optional) Use classical methods such as DMRG for initialization.

- **Outputs**

## Experimental analysis of magnetic materials at the MAGLAB user facility

1. The Fourier transform of the spin ground state at the  $m$  points specified in  $\mathcal{P}$ . This can be obtained by computing the quantities for each  $k = 1, \dots, m$ ,

$$F(\mathbf{p}_k) = \frac{1}{N} \sum_j \exp(i\mathbf{r}_j \cdot \mathbf{p}_k) S_j, \quad (13)$$

and the intensities can be computed as  $I(\mathbf{p}_k) = F^*(\mathbf{p}_k)F(\mathbf{p}_k)$ . In the above  $N$  is the total number of magnetic moments,  $\mathbf{r}_j$  is the position vector in real space of spin vector  $S_j$ .

- **Workflow:** The flowchart showing the *end to end workflow* is given in Figure 2-6. The *hard computational module* is the *ground state preparation*.

**Why classical methods are not sufficient to perform the hard computational module** Same as Application 1.1.

**Concrete problem instantiations** The compound in consideration is  $\alpha$ -RuCl<sub>3</sub>.

*Input 1:* The list of candidate Hamiltonians is given in the table in Figure 2-7. The size of the Hamiltonian is  $100 \times 100$  and is chosen to avoid finite size effects.

*Input 2:* We select  $100 \times 100$  uniformly spaced data points in two dimensional reciprocal space within the first Brillouin zone.

*Input 3 :* The experimentally observed ground state is given in Figure 2-8.

*Output precision requirement:* We should be able to resolve the momentum space less than  $\frac{2\pi}{100a}$ , where  $a$  is one of the lattice constant.

*Output wall-clock time limit:* Finding a suitable Hamiltonian by comparing with the existing experimentally measured magnetization data requires lots of iteration and we need to scan many possible form of Hamiltonian. To this end, therefore, we need to simulate a spin Hamiltonian with a couple minutes. For the entire workflow, finding the proper ground state within two weeks is acceptable.

**List of candidate systems where similar process is relevant** Same as Application 1.1.



# Experimental analysis of magnetic materials at the MAGLAB user facility

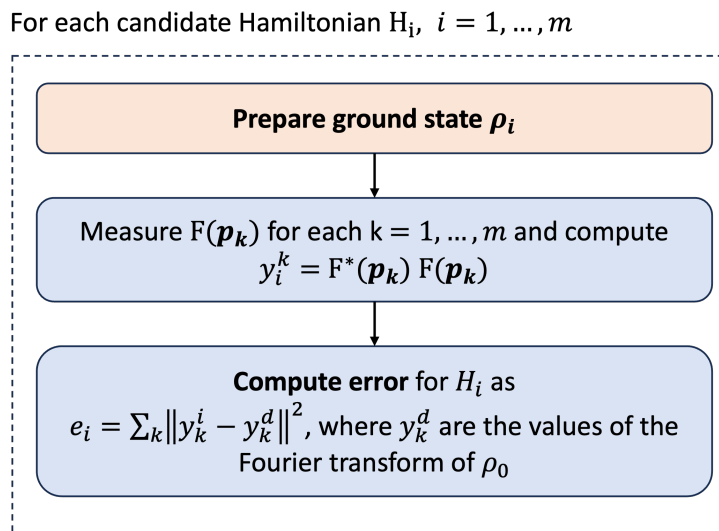


Figure 2-6: Workflow for Hamiltonian search using experimental ground state. The red box contains the hard computational task/kernel.

## 2.3 Requirements summary

This section summarizes the application requirements for all the applications described in this chapter.

### Application 1.1: Seeking the accurate spin Hamiltonian for $\alpha\text{-RuCl}_3$ using experimental data on magnetization

<b>Workload:</b>	Total time limit	2 weeks - 1 month
	Number of subroutine calls required	$140 \times 15$
	Maximum subroutine time limit	2 weeks - 1 month
<b>Problem specifications:</b>	Model type	Kitaev/Heisenberg spin hamiltoninan
	Size	minimum $30 \times 30$ sites target $100 \times 100$ sites
	Interaction Structure	Sparse regular (2-D Hexagonal lattice)
	Computational target	Net magnetization after time evolution
	Accuracy requirement	1% relative on net magnetization

## Experimental analysis of magnetic materials at the MAGLAB user facility

### Application 1.2: Testing candidate Hamiltonians for $\alpha$ - $\text{RuCl}_3$ using ground state prediction

<b>Workload:</b>	Total time limit	2 weeks - 1 month
	Number of subroutine calls required	$100 \times 100 \times 15$
	Maximum subroutine time limit	2 weeks - 1 month
<b>Problem specifications:</b>	Model type	Kitaev/Hiesenberg spin hamiltoninan
	Size	minimum $30 \times 30$ sites target $100 \times 100$ sites
	Interaction Structure	Sparse regular (2-D Hexagonal lattice)
	Computational target	Fourier transform of ground state on a specified lattice
	Accuracy requirement	$0.01 * (2 * \pi/a)$ where $a$ is lattice constant

## 2.4 Supplementary material for Kitaev quantum spin liquids

### Classical methods

1. Exact diagonalization (ED) faces computational challenges beyond a certain lattice size. While ED accurately captures quantum effects, the spin Hamiltonian matrix grows exponentially with the number of spin sites, making it impractical for lattices exceeding 50-60 sites. The need for a  $2^{60} \times 2^{60}$  matrix, even with high-performance computing (HPC), renders ED time-consuming and impossible for the sizes of problems presented in this chapter. Our objectives involve exploring numerous parameter combinations, making ED unfeasible despite its insights into quantum effects.

The resulting finite size effects can make the predictions too inaccurate to be relevant. The intermediate phase in spin liquids that is topologically distinct from the vacuum entails edge states. To model edge states effectively, a large lattice is essential, as closely situated edge states can interact, obscuring their properties. ED, limited to small lattices, is unsuitable for detecting critical properties like edge states in the topologically distinct quantum spin liquid phase. The small lattice size also fails to capture long-range quantum entanglement, another distinctive feature of the quantum spin liquid phase.

2. Heuristic methods like density matrix renormalization group (DMRG) and quantum Monte Carlo (QMC) simulations have been devised for simulating quantum magnetism. Regrettably, these methods are not readily applicable to the quantum spin liquid phase. The Kitaev quantum spin liquid, characterized by magnetic frustration resulting from bond frustration due to competing bond interactions, presents challenges for both QMC and DMRG. In QMC simulations, the presence of magnetic frustrations gives rise to an unsolvable sign problem. Additionally, when a system exhibits significant magnetic anisotropy, as evidenced by a large magnetic gap in the magnon band structure, studying the impact of quantum fluctuations becomes challenging, limiting the analysis to the classical ground state. While DMRG method is a highly effective tool for one-dimensional systems, it is not suitable for investigating quantum long-range entanglement.

**List of Hamiltonians** The table in Figure 2-7 is a list of candidate Hamiltonians proposed for  $\alpha$ -RuCl<sub>3</sub> based on symmetry and other theoretical arguments.

**Experimental ground state** Symmetries inferred from experimental observations in  $\alpha$ -RuCl<sub>3</sub> can be used to conclude that its ground state can be one of three equivalent states. This symmetry can be broken and one among the three is chosen in the presence of an external magnetic field. The ground state of  $\alpha$ -RuCl<sub>3</sub> is called a zigzag spin structure and it is given in Fig. 2-8. From the figure, we see that there are two categories of nodes distinguished by arrows colored blue and red. The spin configuration of the ground states are given by

$$S_{blue}^a = \sqrt{1 - \epsilon^2}, S_{blue}^b = 0, S_{blue}^c = \epsilon, \quad \text{and} \quad S_{red} = -S_{blue}. \quad (14)$$

Here  $\epsilon = 0.1$ . There is some uncertainty about the value of the out-of-plane component quantified by  $\epsilon$  based on currently available experimental observations. However, we deem it will be consequential to the result of the Hamiltonian simulation.

# Experimental analysis of magnetic materials at the MAGLAB user facility

**Table 1.** The spin Hamiltonians for  $\alpha$ -RuCl<sub>3</sub> considered in this work.

Reference	Method	$J_1$	$K_1$	$\Gamma_1$	$\Gamma'_1$	$J_2$	$K_2$	$J_3$	$K_3$	BA
1 Winter et al. PRB <sup>47a</sup>	Ab initio (DFT + exact diag.)	-1.7	-6.7	+6.6	-0.9	-	-	+2.7	-	*
2 Winter et al. NC <sup>27</sup>	Ab initio-inspired (INS fit)	-0.5	-5.0	+2.5	-	-	-	+0.5	-	
3 Wu et al. <sup>40</sup>	THz spectroscopy fit	-0.35	-2.8	+2.4	-	-	-	+0.34	-	
4 Cookmeyer and Moore <sup>52</sup>	Magnon thermal Hall (sign)	-0.5	-5.0	+2.5	-	-	-	+0.1125	-	
5 Kim and Kee <sup>46</sup>	DFT + $t/U$ expansion	-1.53	-6.55	+5.25	-0.95	-	-	-	-	*
6 Suzuki and Suga <sup>53,79</sup>	Magnetic specific heat	-1.53	-24.4	+5.25	-0.95	-	-	-	-	*
7 Yadav et al. <sup>48b</sup>	Quantum chemistry (MRCI)	+1.2	-5.6	+1.2	-0.7	+0.25	-	+0.25	-	
8 Ran et al. <sup>26</sup>	Spin wave fit to INS gap	-	-6.8	+9.5	-	-	-	-	-	
9 Hou et al. <sup>49c</sup>	Constrained DFT + $U$	-1.87	-10.7	+3.8	-	-	-	+1.27	+0.63	*
10 Wang et al. <sup>50d</sup>	DFT + $t/U$ expansion	-0.3	-10.9	+6.1	-	-	-	+0.03	-	
11 Eichstaedt et al. <sup>44,81e</sup>	Fully ab initio (DFT + cRPA + $t/U$ )	-1.4	-14.3	+9.8	-2.23	-	-0.63	+1.0	+0.03	*
12 Eichstaedt et al. <sup>44,81e</sup>	Neglecting non-local Coulomb	-0.2	-4.5	+3.0	-0.73	-	-0.33	+0.7	+0.1	*
13 Eichstaedt et al. <sup>44,81e</sup>	Neglecting non-local SOC	-1.3	-13.3	9.4	-2.3	-	-0.67	+1.0	+0.1	*
14 Banerjee et al. <sup>21</sup>	Spin wave fit	-4.6	+7.0	-	-	-	-	-	-	
15 Kim et al. <sup>45,80</sup>	DFT + $t/U$ expansion	-12	+17	+12	-	-	-	-	-	
16 Kim and Kee <sup>46f</sup>	DFT + $t/U$ expansion	-3.5	+4.6	+6.42	-0.04	-	-	-	-	
17 Winter et al. PRB <sup>47g</sup>	Ab initio (DFT + exact diag.)	-5.5	+7.6	+8.4	+0.2	-	-	+2.3	-	
18 Ozel et al. PRB <sup>82</sup>	Spin wave fit/THz spectroscopy	-0.95	+1.15	+3.8	-	-	-	-	-	
19 Ozel et al. PRB <sup>82</sup>	Spin wave fit/THz spectroscopy	+0.46	-3.50	+2.35	-	-	-	-	-	

Dashes (-) indicate that the value is unavailable or negligible. The bolded models are considered in the main text, and results for the other models are given in the Supplementary Information. Asterisks in the 'BA' column signify that the full Hamiltonian has different values for the  $XY$  bonds compared with the  $Z$  bonds, and that the parameter values given in the row have been bond averaged.  
<sup>a</sup>Using the proposed minimal model, which is bond averaged and neglects small  $\Gamma'_1 = -0.9$  meV. Values for the monoclinic ( $C2/m$ ) crystal structure.  
<sup>b</sup>We use the sign convention in refs. <sup>53,80</sup>  
<sup>c</sup>This work gives values for several values of  $U$ . Here we use the  $U = 3.5$  eV parameters  
<sup>d</sup>Values for the  $C2$  structure  
<sup>e</sup>These are the parameters from the preprint version in ref. <sup>81</sup>. They were revised in the published version, ref. <sup>44</sup>. In Supplementary Note 4 we show that this slight modification does not affect our conclusions  
<sup>f</sup>Case 0, corresponding to  $P3$  structure and weaker Hund's coupling than in Model 15  
<sup>g</sup>Values for the  $P3$  structure

Figure 2-7: List of parameters for  $\alpha$ -RuCl<sub>3</sub> suggested by different theoretical approaches.

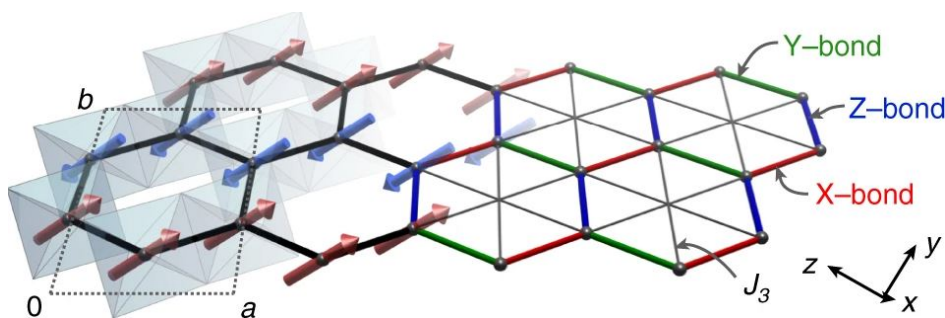


Figure 2-8: The spin structure of the magnetic ground state of  $\alpha$ -RuCl<sub>3</sub>

## 2.5 Quantum implementation

The fully specified Hamiltonians in Figure 2-7 and quantum implementation and resource estimation can be found in [289].

### **3 Exploring exotic phases of magnetic materials near instabilities**

This chapter presents applications related to the study of exotic phases in magnetic materials. For many Hamiltonians, either of theoretical importance or those proclaimed to be effective models for certain compounds, there are regions in the parameter space of the exchange interactions that defy classical or semi-classical description. This phenomenon often arises from the presence of long range entanglement that prevents understanding and prediction of properties of such phases. The computational capabilities required to enable the study of these exotic phases is the ability to compute specified observables either from the ground state or after simulating simulate the time-dynamics for a spin Hamiltonian defined on a lattice. Existing classical methods cannot be scaled to large lattice sizes, where a fault tolerant quantum computer can provide utility by computing these observables at the desired scale and accuracy. The following table provides a condensed summary of the computational requirements of the applications.

**Hamiltonian Type:** Heisenberg spin Hamiltonian.

**Quantum Computational Kernels:** Ground State Preparation, Hamiltonian simulation.

# Exploring exotic phases of magnetic materials near instabilities

## 3.1 Application area overview

### 3.1.1 High-level description of the application area

In 1964, Richard Feynman wrote, “given a lot of electron spins in a regular lattice, interacting with such and such a law, what do they do? It is simply stated, but it has defied complete analysis for years.”[128] Now, in 2024, this basic physics problem remains unsolved. Despite tremendous efforts over the decades, we have no universal way to calculate and predict interacting magnetic atoms in a crystal lattice.

By and large, physics can predict and explain magnetic behavior if materials “behave” classically or semiclassically [132], but these methods fail when the system is tuned to an instability and becomes “highly quantum.” And, unfortunately, such regions are where the most exciting properties exist. For all but a few such cases, we cannot actually calculate or simulate their behavior, because the state involves such a large number of entangled spins. Thus, their study is riddled with speculation, uncertainty, and controversy.

Quantum spin liquids are a high-profile example of a magnetic state beyond the reach of classical simulation, but there are in fact a large number of unstable regions where current algorithms fail. This has three consequences: (i) Many exotic magnetic states have been proposed to exist, but there is often no way to calculate or verify whether these predictions are correct. (ii) Many quantum materials have been found which act strange, but their underlying physics is unknown because their behavior cannot be compared with simulations. (iii) Many unstable regions are known to exist in theory, but there is no robust way to calculate what actually happens at these unstable points, and whether there is an exotic phase. As a result, the study of quantum magnets is awash in speculation and unanswered questions. In our opinion, this is a prime application for quantum computers.

### 3.1.2 Utility estimation

**Overview of the value of the application area** The motivation for this research is both for fundamental physics and technology. On the fundamental side, interacting quantum spin systems are some of the simplest models in many-body quantum physics. The problem of interacting quantum spins dates back to the origin of quantum mechanics, attracting such brilliant minds as Hans Bethe [31], Lars Onsager [308], Phil Anderson [8], and Duncan Haldane [164]; and it has been the subject of four Nobel prizes in physics (1970, 1977, 2007, 2016). Their study has produced foundational physics concepts like spontaneous symmetry breaking [8] and quantum criticality [362]. Meanwhile, on the technology side, real materials with interacting magnetic atoms can give unique and useful properties like giant magnetoresistance (used in magnetic sensing and computer memory) [154], atomically thin electronic switches [108], or—looking to the future—topological qubits [297]. On a basic level, quantum magnetic materials offer the ability to harness quantum mechanics at higher temperatures and longer length-scales than is possible with other quantum devices. Indeed, if physicists could reliably predict the behavior of materials, this could yield a veritable technology revolution [408].

**Concrete utility estimation** The three applications presented in this chapter provide a comprehensive list of computational tasks that will enable completion of the short-term research goals for a given material and set of models. We calculate the total budget used for the study of the models and materials presented in this chapter. The Department of Energy’s budget request for running the neutron facilities for FY24 was \$373M which includes a total of 33 instruments. For the

## Exploring exotic phases of magnetic materials near instabilities

neutron scattering experiments for a given material (KYbSe<sub>2</sub>) presented in this chapter, 2.5 weeks of beamtime were utilized out of a total annual up-time of 8 months. From this we compute the experimental expenditure to be  $\frac{373}{33} \times \frac{2.5}{0.66 \times 52} \approx 1\text{M}$  dollars. The time and labor costs are funded by the quantum science center and is estimated to be  $\approx \$0.5\text{M}$  for four years for a total of  $\$2\text{M}$ . We assign a equal value to each of the applications presented resulting in per application resulting in a value of  $\$0.75\text{M}$  per application.

### 3.2 Problem and computational workflows

#### 3.2.1 Detailed background of the application area

The basic scientific problem is simple: we assume a lattice of interacting spins with the overall Hamiltonian

$$\mathcal{H} = \sum_{i,j} \mathbf{S}_i \mathbb{J}_{ij} \mathbf{S}_j \quad (15)$$

where  $\mathbf{S}_i$  are quantum spin operators and  $\mathbb{J}_{ij}$  is a second rank tensor governing the interactions between spins. In most cases of interest, the interactions are nonzero only for the nearest few neighbors on the lattice. Also, for many classic theoretical models,  $\mathbb{J}_{ij}$  is isotropic, meaning it is replaced by a scalar  $J_{ij}$  and the spins interact via a dot product:

$$\mathcal{H} = \sum_{i,j} J_{ij} \mathbf{S}_i \cdot \mathbf{S}_j \quad (16)$$

which is commonly called “Heisenberg exchange”.

After the Hamiltonian is defined, the computational challenge is to calculate the ground state and excitation spectrum. In trivial cases, such as long range magnetic order, the quantum ground state is the same as the classical ground state. However, there are many cases where the quantum ground state involves nontrivial superpositions which are impossible classically, and the full quantum ground state must be computed. This is trivial for a small number ( $< 10$ ) of spins; but the real problems of interest are in the thermodynamic limit, where the lattice has Avogadro’s number of spins. Because this is impractical, the usual approach is to assume a “large enough” lattice (often  $\sim 10^2$  sites along each dimension) and calculate the properties based on this. Thus for a two-dimensional lattice,  $\sim 10^4$  spins would be required to simulate the thermodynamic limit. The size of the Hamiltonian matrix scales as  $2^n$  (where  $n$  is the number of spins), so such a lattice would have a  $10^{300} \times 10^{300}$  Hamiltonian matrix, far beyond the reach of a classical computer!

Because the general solution of Eq. 15 is computationally hard, classical or semiclassical approximations are usually employed. If we choose to completely ignore quantum effects, the spin dynamics and ground state can be simulated with classical Monte Carlo and Landau Lifschitz dynamics [457]. Also, semiclassical dynamics can be calculated with spin wave theory [132] which assumes the excitations can be described by a boson quasiparticle effective field theory. These approaches work well when the system is “well-behaved,” which means quantum effects are small and the system can indeed be described by boson quasiparticles. However, there are many models (and correspondingly many materials) where these assumptions break down (see Table 3-1 for models and Table 3-2 for materials), and the full quantum solution is necessary.

## Exploring exotic phases of magnetic materials near instabilities

Model	References
2D square lattice antiferromagnet, with second neighbor $J_2$ over first neighbor $J_1$ tuned to $J_2/J_1 = \frac{1}{2}$	[263, 64, 99, 64, 131, 360, 327, 81, 378, 191, 117, 379, 469, 387, 52, 53, 456, 398, 388, 375, 275, 104, 10, 190, 293, 23, 347, 453, 198, 285, 424, 179, 112, 334, 150, 79, 288, 348, 425, 325, 423, 161, 264, 326, 126, 301]
2D triangular lattice antiferromagnet, with second neighbor $J_2$ over first neighbor $J_1$ tuned to $J_2/J_1 = \frac{1}{8}$	[475, 178, 189, 359, 435, 149, 177]
3D pyrochlore lattice with anisotropic nearest neighbor exchange	[26, 444]
2D Kagome lattice antiferromagnet	[26, 444]
3D pyrochlore Heisenberg antiferromagnet	[188, 162, 13, 365, 324]
2D honeycomb anisotropic $\Gamma$ antiferromagnet	[271]
2D Shastry Sutherland lattice	[262]
Hyperkagome antiferromagnet	[472, 45]
Hyper-hyperkagome antiferromagnet	[72]
$S = 1$ spins with biquadratic exchange on various lattices	[180, 323]

Table 3-1: Well-studied examples of interacting quantum spin systems where classical methods fail, and quantum simulation is necessary.

Compound	Description
Herbertsmithite	A kagome quantum spin liquid candidate [170, 302]
$A\text{YbSe}_2$	A family of triangular quantum spin liquid candidates, where $A$ is an Alkalai metal [101, 440, 368, 367]
$\text{NaCaNi}_2\text{F}_7$	A nearly isotropic pyrochlore magnet with exchange disorder [322, 462]
$\text{Yb}_2\text{Ti}_2\text{O}_7$	A pyrochlore a well-studied Hamiltonian [403, 444] but a puzzling excitation spectrum [369]
$\text{YbMgGaO}_4$	An intrinsically disordered triangular lattice quantum magnet [256, 309, 382], with great controversy over the excitations [218, 338].
$\text{RuCl}_3$	A candidate Kitaev spin liquid candidate with a well-measured neutron spectrum [19, 18]

Table 3-2: Examples of nontrivial quantum magnetic materials with well-measured properties but poorly understood quantum ground states.



## Exploring exotic phases of magnetic materials near instabilities

### 3.2.2 Classical methods

In the case of the full quantum treatment, there are some quantum methods for classical computers that work with limited success. Some of the most popular are:

- Exact Diagonalization (ED), wherein a system of interacting spins is diagonalized using Lanczos techniques [193]. Current state of the art is around 32 spins [437]. This is a far cry from an extended system, and finite size effects can severely affect the calculations (especially for non-local long-range entangled states).
- Matrix Product methods, most notably density matrix renormalization group (DMRG). This method is numerically accurate in one dimension [377], able to simulate lattices of  $\approx 100$  spins [366]. Recent advances have applied this to simulate two-dimensional systems by wrapping the spins along a cylinder [114, 383]. However the limited dimensionality around the cylinder ( $\sim 6$  sites) means that this method too is severely limited by finite size effects in two dimensions, and cannot be used for three-dimensional lattices.
- Quantum Monte Carlo is a stochastic variational wave-function approach to calculating quantum systems [134]. This technique is extremely powerful, easily able to simulate  $\sim 10,000$  spins, but it suffers from a so-called “sign problem” which prevents numerical convergence for frustrated lattices [187] — which is precisely where some of the most interesting physics lies.

None of these methods are able to calculate the ground state of the most interesting problems. Going beyond these methods requires a radically new approach, such as a quantum computer.

#### **Application 1: Ground state of systems near instabilities**

Computing the magnetic ground state of interacting magnetic spins where entanglement becomes long ranged and semiclassical methods fail.

**Specific background of the application** Spin ground states can be calculated by classical and semiclassical methods, but these methods fail when the exchange interactions are tuned to an instability: either an exotic magnetic phase which defies semiclassical description, or a phase boundary between two types of magnetic order. In such cases, it is often unclear what the ground state is and where the phase boundaries lie.

**Objectives** There are two objectives: (1) To compute the magnetic ground state of spins at or near an instability, and determine whether an additional non-trivial magnetic phase exists at this point; and (2) compute the extent in parameter space that this ground state is stabilized (i.e., where the phase boundaries lie).

**End-to-end computational workflow** For a Hamiltonian of the form in Eq. (15) with values defined from regions where semiclassical methods fail or a proposed exotic quantum phase, the goal is to compute the spin correlation functions of the ground state. The most commonly used is the lattice-averaged two-spin correlation  $\langle S_i \cdot S_j \rangle$ , but depending on the geometry of the lattice and the postulated order, this can include three, four, or six spin correlators as a means of identifying distinct phases among the ground states. In many cases, the unstable region is already known from where semi-classical methods break down, and the range will be well-defined.

## Exploring exotic phases of magnetic materials near instabilities

- **Inputs:**
  - A Hamiltonian of the form in Eq. (15) with values defined from regions where semiclassical methods fail or a proposed exotic quantum phase (Fig. 3-1) exists.
- **Outputs**
  - Spin correlations of the ground state.
- **Workflow:** The flowchart showing the *end to end workflow* is given in Figure 3-1. The *hard computational module* is the *ground state preparation*.

### Why classical methods are not sufficient to perform the hard computational module

As explained in Section 3.2.2, approximating the behavior of a thermodynamic quantum spin system requires diagonalizing huge matrices, often greater than  $10^{300} \times 10^{300}$ .

**Concrete problem instantiations** For the input, the workflow is applicable to all the listed systems in Table 3-1. We choose two especially long-standing problems.

*Input Option 1:* 2D square lattice tuned to instability, with second neighbor  $J_2$  over first neighbor  $J_1$  tuned to instability  $J_2/J_1 = \frac{1}{2}$  (see Table 3-1 for references). The key question to answer for this model is: what is the nature of the intermediate phase? Is it a valence bond solid, or quantum spin liquid [335, 263]?

*Input Option 2:* 2D triangular lattice antiferromagnet, with second neighbor  $J_2$  over first neighbor  $J_1$  near  $J_2/J_1 = \frac{1}{8}$ . In the quantum limit, there is a quantum spin liquid phase between approximately  $0.07 < J_2/J_1 < 0.16$  [475, 178, 189, 359, 435, 149, 177]. The key questions for this model are: what is the exact range of this phase in  $J_2/J_1$ ? Is it a resonating valence bond liquid, or another type of spin liquid?

*Discretization of parameter space:* The range of the parameter values  $J_1$  is discretized into  $\approx 100$  points to provide sufficient accuracy for mapping out the local phase diagram around an instability or quantum phase.

*Output precision:* The ground state must be evaluated to an energy accuracy  $\approx |J_1|/1000$  where  $J_1$  is the largest exchange in the Hamiltonian.

## Exploring exotic phases of magnetic materials near instabilities

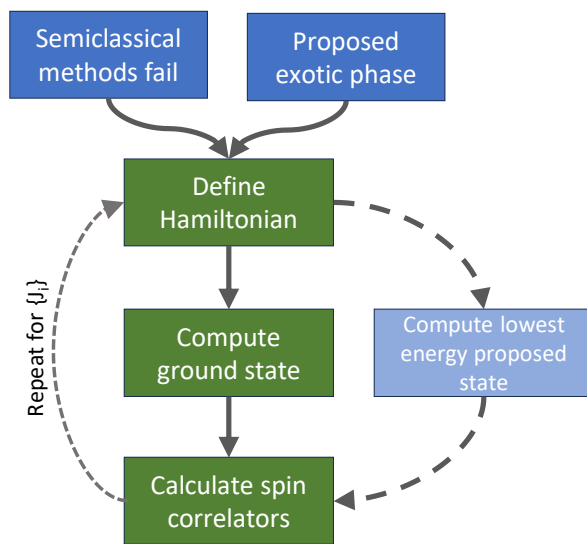


Figure 3-1: Computational workflow for ground state calculation.

### **Application 2: Validating the spin Hamiltonian of a compound and predicting the dynamics of an exotic quantum phase**

Computing the magnetic dynamics of model spin systems for comparison with experimental data from neutron scattering experiments.

**Specific background of the application** For quantum magnetic materials, a standard measurement to study the magnetic dynamics is inelastic neutron scattering. This measures the lattice-averaged two-point spin correlation function  $\langle S_i \cdot S_j \rangle$ , Fourier transformed in time and space [39]. For a given magnetic Hamiltonian, in the case where the magnetic excitations act like boson quasiparticles, the inelastic neutron spectrum can be modeled by spin wave theory [132] and can be efficiently predicted using current computing hardware. This prediction can be used to fit the parameters of the magnetic Hamiltonian by comparing with experimental data. However, for more exotic quantum materials, such analysis tools break down.

A central goal in experimental condensed matter is understanding why certain materials act the way they do, and this requires understanding both the interactions between spins and the nature of the excitations. However without the ability to compare with a theoretical model, the underlying magnetic interactions (the spin exchange Hamiltonian) and magnetic dynamics (the type of quasiparticles) are extremely hard to determine.

**Objectives** The objective is to calculate the time-evolved two-point quantum spin correlation function of a particular lattice Hamiltonian in eq. (15) after a local spin flip corresponding to a scattered neutron. The purpose of this is to compare with experimental neutron scattering data to verify or rule out a particular Hamiltonian, a parameter range in the Hamiltonian or type of dynamics to describe a particular material (e.g., whether the boson quasiparticle description matches the full quantum simulation).

## Exploring exotic phases of magnetic materials near instabilities

**End-to-end computational workflow** We begin with a specific Hamiltonian, initially obtained by an educated guess at a compound's interactions (for an example in KYbSe<sub>2</sub>, see below). From this, there are two possible routes in the computational workflow with the same goal: compute the two-point spin correlation  $\langle S_i \cdot S_j \rangle$  as a function of time/energy. The first route is to calculate the spin correlations as a function of time by simulating the time dynamics corresponding to a neutron scattering experiment. The second is to calculate the spin correlations as a function of energy by calculating the correlations corresponding to the low energy wavefunctions of the Hamiltonian. For the first route, we begin from a sufficiently low energy state, randomly flip a spin corresponding to a scattered neutron in experiment, and allow the system to time-evolve with quantum interactions. After a specified time, an observation is made correlating the flipped spin to the rest of the lattice. The whole process is repeated for many different flipped spins and many different times to gain a complete, lattice-averaged picture. The second route involves obtaining a low energy state and computing the corresponding spin correlation and repeating the process sufficiently many times until a complete picture of the energy dependence of the correlation is obtained. In the following we only consider the first route and present its inputs, outputs and specifications.

- **Inputs:**

1. A list of candidate Hamiltonians  $\mathcal{H}$ . This is usually obtained by an educated guess at a compound's interactions.
2. Time length of the simulation  $t_{sim}$  and time resolution  $dt$ .
3. Total number of samples  $M$  required to obtain a good lattice averaged picture of the time evolution.

- **Outputs**

1. For each of the  $M$  samples, the lattice averaged two point spin correlation  $\langle S_i \cdot S_j \rangle$  as a function of time.

- **Workflow:** The flowchart showing the *end to end workflow* is given in Figure 3-4. The *hard computational modules* are the *ground state preparation* and *Hamiltonian simulation* as highlighted by the red boxes.

### Why classical methods are not sufficient to perform the hard computational module

Simulating quantum dynamics on large system sizes requires matrices beyond the reach of classical methods, see above.

**Concrete problem instantiations** This workflow is applicable to many systems, see Table 3-2. We present specifications for two specific compounds KYbSe<sub>2</sub> [368, 367] and a sister material NaYbSe<sub>2</sub> [101, 367].

The material KYbSe<sub>2</sub> has a triangular lattice of magnetic Yb atoms, and behaves in a way that suggests it is close to a quantum instability, specifically a quantum spin liquid phase [368]. The exchange Hamiltonian is the 2D Heisenberg triangular model, with empirically determined  $J_2/J_1 = 0.044 \pm 0.005$  [367]. However, NaYbSe<sub>2</sub>, has much larger uncertainty with  $J_2/J_1 = 0.071 \pm 0.015$  [367], and appears to be a quantum spin liquid at low temperatures [101].

## Exploring exotic phases of magnetic materials near instabilities

*Input 1:* Two dimensional triangular lattice with a range of  $J_2/J_1$  values between 0.035 and 0.09 in steps of 0.001 chosen to be able to address both the compounds. The size of the lattice to avoid finite size effects is chosen to be  $100 \times 100$ .

The experimental neutron scattering spectra for KYbSe<sub>2</sub> are shown in Fig. 3-2. The data were collected at very low temperatures with  $k_B T/J_1 = 0.06, 0.20,$  and  $0.39$ , where  $J_1 = 0.438 \pm 0.008$  meV. The total timescale over which the inelastic spectra are probed is  $\approx 10^{-10}$  s. The energy resolution used in the experiment is 0.04 meV (corresponding to  $10^{-10}$  s) compared to a bandwidth of 1.5 meV (corresponding to  $2.8 \times 10^{-12}$  s). Therefore, the experiment is equivalent to a quantum system simulation with a time-resolution of  $2.8 \times 10^{-12}$  s and a total time of  $10^{-10}$  s corresponding to 37 time steps. This suggests that the system is being probed in a phase far from thermal equilibrium. For the application specification we conservatively suggest a higher resolution than the experiment.

*Input 2:* Total simulation time  $t_{sim} = 10^{-10}$  s and time resolution  $dt = 2 \times 10^{-12}$  s.

*Input 3:* We choose the total number of samples  $M = 10000$  chosen to be the same as the lattice size to get sufficient spatial averaging.

*Output precision requirement:* The energy precision of the final state of the Hamiltonian simulation is chosen to be  $\frac{|J_1|}{100}$  and a 1% precision is chosen on the two-point correlation.

*Output wall-clock time limit:* One month

Constraining the exchange Hamiltonian in NaYbSe<sub>2</sub> (and other members of the chemical series) would be an important role of simulating the inelastic neutron spectrum. What is more, an accurate simulation of  $S(q, \omega)$  could be compared with different quasiparticle simulations [459], and would give great confidence that the observed behavior is indeed from this non-trivial quantum liquid phase.

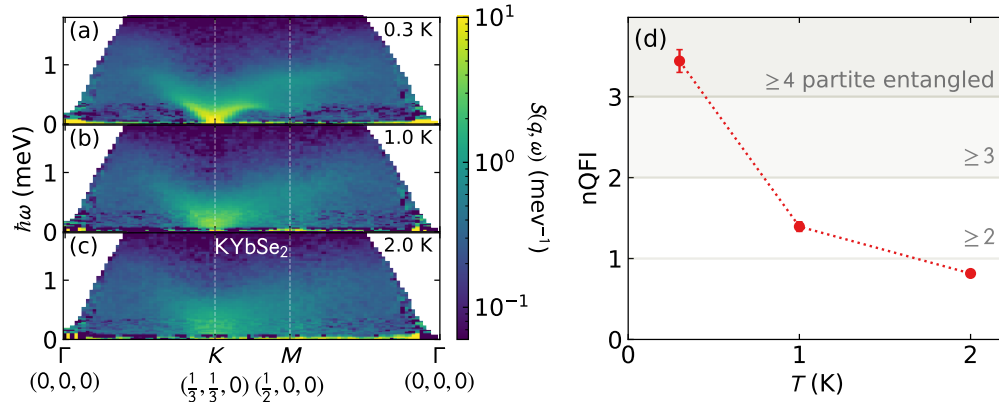


Figure 3-2: Experimental neutron scattering on KYbSe<sub>2</sub> at three different temperatures (a)-(c). The  $y$  axis gives energy transfer, the  $x$ -axis gives different scattering directions in reciprocal space units, and the color scale indicates the scattered neutron intensity. Panel (d) shows the Quantum Fisher Information (d) computed from the spectra in panels (a)-(c) via Eq. 18. Here  $n\text{QFI} = f_Q/(12S^2)$  gives a lower bound on entanglement depth.

## Exploring exotic phases of magnetic materials near instabilities

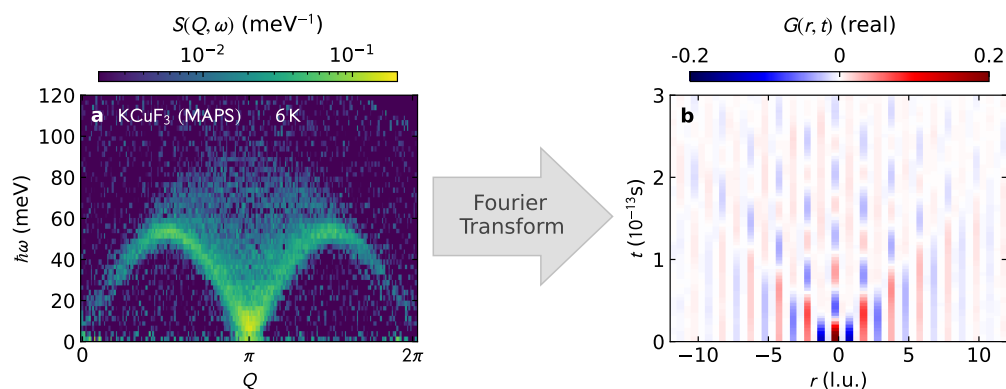


Figure 3-3: Fourier-transforming neutron scattering from frequency and reciprocal space to time and distance. Panel (a) shows the experimental neutron spectrum of  $\text{KCuF}_3$ . Panel (b) shows the spectra transformed into real space on the  $x$  axis and time on the  $y$  axis [370], which corresponds to a lattice-averaged time-evolved spin correlation.

For each candidate Hamiltonian and each sample

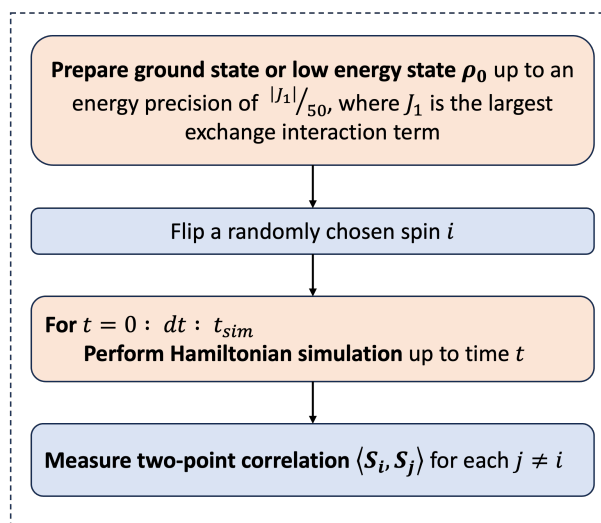


Figure 3-4: Workflow for Hamiltonian dynamics to compare with neutron scattering data. The red boxes contain the hard computational task/kernel.

### Application 3: Using quantum correlations and quantum information to certify the existence and extent of exotic phases

Calculate quantum correlation functions for given spin Hamiltonians to understand their quantum ground state and compare with theory.

**Specific background of the application** Although computing total correlation functions like  $\langle S_i \cdot S_j \rangle$  can reveal much about a system, even more can be revealed by **quantum correlation functions**. For example, quantum Fisher information, which for a pure state is expressed as

$$F_Q = 4(\langle \psi | \hat{S}(-\vec{Q}) \hat{S}(\vec{Q}) | \psi \rangle - \langle \psi | \hat{S}(\vec{Q}) | \psi \rangle^2) \quad (17)$$

Potential Applications of Quantum Computing at Los Alamos National Laboratory

## Exploring exotic phases of magnetic materials near instabilities

[172] gives a lower bound on entanglement depth [185]. Here  $\vec{Q}$  is the translation vector in the reciprocal space and  $\hat{S}(\vec{Q}) = \sum_i \hat{S}_i e^{i\vec{r}_i \cdot \vec{Q}}$  where  $\vec{r}_i$  refers to the position of the spin in the 2-D lattice. In fact, there are a large number of experimentally accessible quantum correlation functions [356, 137, 138], which have distinct meaning in terms of entanglement witnesses (akin to Bell’s theorem), and can be used to diagnose quantum entanglement transitions [246]. Simulating highly entangled spin Hamiltonians using a quantum computers offers the possibility to study the entanglement structure and dynamics in far larger systems than is possible to study with classical computers.

In the last few years it has been demonstrated that quantum correlations, and correspondingly quantum entanglement, can be extracted from the spin correlations  $S(\mathbf{Q}, \omega)$  measured by neutron scattering via the equation

$$f_{\mathcal{Q}}[\mathbf{Q}] = 4 \int_0^{\infty} d(\hbar\omega) \tanh\left(\frac{\hbar\omega}{2k_B T}\right) \left(1 - e^{-\hbar\omega/k_B T}\right) S(\mathbf{Q}, \omega), \quad (18)$$

[366, 246, 370, 245, 282, 371], also see Fig. 3-2(d) where  $n\text{QFI} = f_{\mathcal{Q}}/(12S^2)$ . This allows simulations to be compared to experiment in new ways, and to establish the entanglement structure of experimental quantum materials—which are not guaranteed to be the same as a simplified theoretical model [397].

**Objectives** The first objective is to understand the fundamental quantum properties of exotic quantum phases of matter. We do this by calculating quantum correlation functions of exotic quantum spin phases (see Table 3-1) to distinguish between their quantum properties [255]. The second objective is to compare the entanglement structure of simulated lattices to real materials. This is important to discern, e.g., whether infinitesimal amounts of spin exchange disorder (which can be theoretically controlled but not experimentally controlled) destroy a given quantum phase [397].

**End-to-end computational workflow** This workflow is identical to Application 1, but instead of simplistic spin correlation functions, we calculate quantum correlation functions. The quantum correlation function most straightforward to calculate and interpret is Quantum Fisher Information (QFI, eq. 17), which can be extracted from experimental data [366]. This is then used to analyze the entanglement structure of a given phase (where QFI is analyzed in real space, looking for the pattern of highly entangled bonds), or for comparison with experimental data (where QFI is analyzed in Fourier space). The input and output of the workflow are as follows:

- **Inputs:**

1. A list of Hamiltonians  $\mathcal{H}$  around a quantum phase or quantum instability (see Table 3-1), with sufficient granularity in the parameters to distinguish phase boundaries.
2. A specified set of points for  $\vec{Q}$  in the two-dimensional reciprocal space.

- **Outputs**

1. Quantum Fisher Information of the ground state, calculated via Eq. 17 for pure states.
2. Optionally, other quantum correlation functions as defined in Ref. [371].

- **Workflow:** The flowchart showing the *end to end workflow* is given in Figure 3-1, but with “calculate spin correlators” indicating the quantum correlation functions discussed above. The *hard computational module* is the *ground state preparation*.

## Exploring exotic phases of magnetic materials near instabilities

**Why classical methods are not sufficient to perform the hard computational module**  
Simulating quantum dynamics on large system sizes requires matrices beyond the reach of classical methods, see above.

**Concrete problem instantiations** Any of the phases in Table 3-1 would be relevant to this application, as would the [Na,K]YbSe<sub>2</sub> compound described above.

For a concrete example, let us take the 2D square lattice antiferromagnet with  $J_1$  nearest neighbor exchange (along square edges) and  $J_2$  second neighbor exchange (along square diagonals). In this case, the region of interest would be between

*Input 1:* Two dimensional triangular lattice with a range of  $J_2/J_1$  values between 0.5 and 0.65 in steps of 0.002. The size of the lattice to avoid finite size effects is chosen to be  $100 \times 100$ .

*Input 2:* A grid of  $100 \times 100$  uniformly spaced points in the region  $\vec{Q} \in [0, 1/2] \times [0, 1/2]$ .

*Input 3 (Optional):* random Gaussian noise to the  $J_1$  exchange interactions, with FWHM  $\delta_J$  between 0 and  $J_1$  in steps of  $J_1/50$ .

*Output- precision requirement:* The energy precision of the ground state is chosen to be  $\frac{|J_1|}{1000}$ .

*Output wall-clock time limit:* One month.

Obtaining quantum correlation/entanglement as the lattice is tuned through nontrivial quantum points will allow the underlying quantum state to be rigorously characterized, and studying the quantum phase as a function of exchange disorder will give a picture of disorder in real materials might affect the stability of the quantum phase.

### 3.3 Requirements summary

This section summarizes the application requirements for all the applications described in this chapter.

#### Application 1: Ground state of systems near instabilities

<b>Workload:</b>	Total time limit	1 month
	Number of subroutine calls required	100
	Maximum subroutine time limit	1 month
<b>Problem specifications:</b>	Model type	Hiesenberg spin hamiltoninan
	Size	minimum $30 \times 30$ sites target $100 \times 100$ sites
	Interaction Structure	Sparse regular (2-D square or triangular lattice)
	Computational target	2, 4, 6-point spin correlations of ground state
	Accuracy requirement	$ J_1 /1000$ for ground state energy and 1% relative on correlations



## Exploring exotic phases of magnetic materials near instabilities

### **Application 2: Validating the spin Hamiltonian of a compound and predicting the dynamics of an exotic quantum phase**

<b>Workload:</b>	Total time limit	1 month
	Number of subroutine calls required	$\# \text{spin-flips} \times \text{parameter resolution} \times \text{time-steps}$ $= 100 \times 100 \times 55 \times 50$
	Maximum subroutine time limit	1 month
<b>Problem specifications:</b>	Model type	Hiesenberg spin hamiltoninan
	Size	minimum $30 \times 30$ sites target $100 \times 100$ sites
	Interaction Structure	Sparse regular (2-D triangular lattice)
	Computational target	2-point correlations after time evolution
	Accuracy requirement	$ J_1 /100$ for energy of the final state and 1% relative on correlations

### **Application 3: Using quantum correlations and quantum information to certify the existence and extent of exotic phases**

<b>Workload:</b>	Total time limit	1 month
	Number of subroutine calls required	$\# \text{ parameters} = 75$
	Maximum subroutine time limit	1 month
<b>Problem specifications:</b>	Model type	Hiesenberg spin hamiltoninan
	Size	minimum $30 \times 30$ sites target $100 \times 100$ sites
	Interaction Structure	Sparse regular (2-D square or triangular lattice)
	Computational target	Quantum correlation functions (Fischer information) computed from the ground state
	Accuracy requirement	$ J_1 /1000$ for ground state energy and 1% relative on quantum correlation functions

## 4 Driven-dissipative Dicke model in the ultrastrong coupling regime

The interaction between light and matter is at the core of most our nanotechnologies. Using atoms to produce highly coherent sources of light , i.e., lasers, that in turns can be used to control particles at the individual level is one of the most remarkable success of quantum optics. Even though the nature of the interactions between light and matter are well-understood, the consequences of these interactions are not, in particular when matter and light are highly entangled. The Dicke model is one of the simplest example of light-matter coupling, realizable experimentally, that exhibits such exotic behavior in what is called the ustrastrong coupling regime. While being proposed more than fifty years ago, the analysis of this model is still elusive due to its difficult highly quantum nature. In this chapter, we introduce the Dicke model and its connection to quantum optic. We then describe the computational workflow needed to understand the propriety of this model and how quantum computing resources can help in portraying its phase diagram.

**Hamiltonian Type:** Spins + multi-level state Hamiltonian.

**Quantum Computational Kernels:** Ground State Preparation, Open Quantum System Simulation.

# Driven-dissipative Dicke model in the ultrastrong coupling regime

## 4.1 Application area overview

### 4.1.1 High-level description of the application area

Recent advances in the development of optical functional materials and the fabrication of complex nanostructures incorporating these materials have unlocked broad opportunities for designing on-chip photonic circuits. These circuits hold vast potential for applications, including tunable coherent light sources, optoelectronics, light harvesting and energy conversion devices, and the development of solid state devices for quantum communication and computation. The functionality of these nanostructures relies on our capacity to control the interaction between light (photons) and optically active nanoparticles (quantum emitters). For the sake of technological advances to achieving this control, fundamental physical aspects governing various regimes of coupled photons and quantum emitter excitations should be understood. The coupling strength, which quantifies the rate of energy exchange between photons and quantum emitters is a key parameter governing the emergence of novel states in the composite light-matter excitations known as polaritons. When the coupling is weaker than any rate of energy losses in the quantum emitters and the confining optical cavity, this regime is identified as the weak coupling regime. Conversely, the strong coupling regime characterizes the opposite situation with distinct features in polariton physics. The ultra-strong coupling (USC) regime is defined by a coupling rate that constitutes a significant fraction (0.1 or larger) of the photon energy that the quantum emitters can absorb or emit. This regime manifests distinctly different quantum properties than those observed in the weak and strong coupling regimes. Theoretical analysis and modeling of such properties encounter considerable challenges, even with substantially simplified light-matter interaction models.

### 4.1.2 Utility estimation

**Overview of the value of the application area** Addressing the challenges in USC theory promises to yield new fundamental insights into emergent phenomena, laying the groundwork for experimental investigations. Together, these efforts will expand our fundamental understanding of the behavior of light and matter. Moreover, exploring the USC regime in various nanostructures holds the potential for technological advancements, this includes the design of new photonic circuits for the use in telecommunication and optoelectronics. As detailed below, USC has been demonstrated not only in the optical spectrum but also in microwave superconducting circuits and magnetic materials, unlocking technological possibilities for designing novel information storage and processing devices, potentially including ultrafast quantum computers.

**Concrete utility estimation** Three projects were identified at LANL that are connected with the study USC regime. These projects were or are funded internally, each for a duration of three years, and include both an experimental and a theoretical component. The first research project entitled "Hybrid Photonic-Plasmonic Materials: Toward Ultimate Control Over the Generation and Fate of Photons" took place in FY 2017-2019 with a total budget of \$4.8M, for which 30% = \$0.5M per year was allocated in labour cost to theoretical investigations of the USC regime. The two other projects, "Complementary Metal-oxide-semiconductor (CMOS)-Compatible Exploitation of Emergent Nanoplasmonic Phenomena in the Near-Infrared" and "Paired Exciton-Polariton Condensates and Bloch Surface Waves as Neurons and Synapses in Photonic Neuromorphic Computers" are currently undergoing from FY 2023 to FY 2025 and have each a total budget of approximately \$750K, The part of this budget allocated in labour cost to the study of USC regime represents \$95K

## **Driven-dissipative Dicke model in the ultrastrong coupling regime**

per year and \$90K per year respectively. Therefore, the total investment made by these projects on answering this particular scientific question is approximately \$2M. It is worth recalling that the approximation methods used in these projects for producing phase diagrams, such as depicted latter in this chapter, are insufficient to accurately describe and predict the physics of the problem.

### **4.2 Problem and computational workflows**

#### **4.2.1 Detailed background of the application area**

Over the last decade, the USC regime has undergone extensive theoretical and experimental investigations. Comprehensive reviews of this topic can be found in Refs. [139, 133]. According to these reports, the USC has been experimentally realized across diverse quantum systems, including semiconductor quantum wells, molecules within optical and plasmonic cavities, microcavity exciton-polaritons, magnons in microwave cavities, optomechanical systems, and superconducting circuits. It is noteworthy that some of the experimental implementations have served as a hardware platform for quantum simulations, validating theoretical predictions of various USC models. [244, 272, 318] Consequently, the applications of quantum systems in the USC regime span from low-threshold solid-state lasers and efficient quantum photon sources to quantum spectroscopies, control of chemical reactions, ultrafast quantum computing, and optomechanics. [139, 133]

Understanding the complex cavity quantum electrodynamics in the USC regime relies on theoretical methods developed in the past decade as reviewed in Ref. [248]. The review outlines efforts to investigate the spectral properties (eigenstates and eigenenergies) of coupled quantum emitters and a cavity mode forming closed quantum system under USC. Using the Rabi model describing a single two-level quantum emitter interacting with the cavity mode, the importance of accounting for the effect of counter-rotating terms breaking standard rotating-wave approximation (RWA) has been demonstrated. Yet, the interpretation of the experimentally studied quantum systems calls for treating both the quantum emitters and the photonic cavity as an open quantum system, accounting for dissipation and energy supply through various driving mechanisms. Ref. [248] underscores the challenges posed by the USC when applying two key theoretical approaches to open quantum systems—the reduced density matrix master equation and quantum Langevin equations in conjunction with the input-output formalism. Among these considerations, it is necessary to introduce common bath degrees of freedom for the coupled quantum emitters and cavity photons. The dissipation rates should be treated as time-dependent, necessitating the inclusion of non-Markovian effects. Finally, ensuring the fulfillment of gauge invariance is crucial for models describing quantum systems in the USC regime [248]. These constraints impose restrictions on conventional quantum optics approximations. For example, the use of a two-level approximation for quantum emitters in certain cases yields inconsistent outcomes in the Coulomb and multipolar gauges. Additionally, the diamagnetic contribution of the photon fields cannot be neglected.

Theoretical challenges outlined above impose significant limitations on the analytical and computational techniques developed for studying ensembles of quantum emitters coupled to cavity photons in the strong coupling regime while extending them to the USC. Within this framework, we explore a representative generalization of the Rabi model to the driven-dissipative Dicke model. In the strong coupling regime the driven-dissipative Dicke model predicts different non-equilibrium phases of polariton state [219]. However, the extension of such phase diagrams to the USC is yet to be done. We argue that the utilization of noiseless quantum computers should enhance our modeling capabilities and offer insights into non-equilibrium polariton states under the USC regime beyond

## Driven-dissipative Dicke model in the ultrastrong coupling regime

the constraints imposed by classical computing.

### 4.2.2 Application 1: Low energy spectrum of Dicke and Tavis-Cummings models

**Specific background of the application** The Dicke model's schematic, illustrated in Fig. 4-1, shows the photonic cavity mode of energy  $\hbar\omega_c$ , described by the Bose annihilation and creation operators  $\hat{a}$  and  $\hat{a}^\dagger$ , respectively. Identical two-level quantum emitters with energy  $\hbar\omega_o$  positioned at sites  $n = \overline{1, \mathcal{N}_o}$  and characterized by the Pauli SU(2) operators  $\hat{\sigma}_n^\pm = \hat{\sigma}_n^x \pm i\hat{\sigma}_n^y$ ,  $\sigma_n^z$ , interact with the cavity mode. The strength of this interaction is defined by the coherent quantum exchange rate,  $\lambda$ . Consequently, we describe the system through the following Dicke Hamiltonian

$$\hat{H}_D = \hbar\omega_c \hat{a}^\dagger \hat{a} + \frac{\hbar\omega_o}{2} \sum_{n=1}^{\mathcal{N}_o} (\hat{\sigma}_n^z + 1) + \hbar\lambda (\hat{a} + \hat{a}^\dagger) \sum_{n=1}^{\mathcal{N}_o} (\hat{\sigma}_n^- + \hat{\sigma}_n^+), \quad (19)$$

which is invariant under  $\mathbb{Z}_2$  symmetry transformations.

The Dicke Hamiltonian gives the most general account of the quantum-emitter-cavity-mode interactions including the rotating terms  $\hat{a}^\dagger \hat{\sigma}_n^- + \hat{\sigma}_n^+ \hat{a}$  and the counter rotating terms  $\hat{a}^\dagger \hat{\sigma}_n^+ + \hat{\sigma}_n^- \hat{a}$  standing for simultaneous (de)excitation of the quantum emitters and cavity mode. In the Rotating Wave Approximation (RWA), neglecting the later terms, the Dicke model becomes the Tavis-Cummings model with the Hamiltonian

$$\hat{H}_{TC} = \hbar\omega_c \hat{a}^\dagger \hat{a} + \frac{\hbar\omega_o}{2} \sum_{n=1}^{\mathcal{N}_o} (\hat{\sigma}_n^z + 1) + \hbar\lambda \sum_{n=1}^{\mathcal{N}_o} (\hat{a}^\dagger \hat{\sigma}_n^- + \hat{\sigma}_n^+ \hat{a}). \quad (20)$$

Notice, that dropping the counter-rotating terms lifts symmetry of the Tavis-Cummings model to U(1). Finally, the single quantum emitter ( $n=1$ ) limit of the Dicke and Tavis-Cummings models is referred to as the Rabi and Jaynes-Cummings models, respectively.

**Objectives** Our initial goal is to conduct a spectral analysis of the Dicke Hamiltonian (19) within the USC regime to specifically identify the parameter range where the inclusion of the counter-rotating terms becomes important. Achieving this will need a comparative analysis involving the solution of the spectral problem for the Tavis-Cummings Hamiltonian (20). Additionally, we will explore variations in the number of quantum emitters, ranging from  $N = 1$  to anticipated order of  $10^2 - 10^3$ . This investigation aims to examine the evolution of the eigenspectra comparing with the well-established spectra of the Rabi and Jaynes-Cummings models.

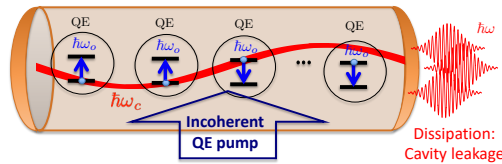


Figure 4-1: Schematic of driven-dissipative Dicke model: An ensemble of  $\mathcal{N}_o$  two-level quantum emitters with transition transition energy  $\hbar\omega_o$  and cavity photon mode of energy  $\hbar\omega_c$  interact via coherent quantum exchange rate  $\lambda$ . The quantum emitters are subject to the incoherent pump and internal relaxation processes whereas the cavity leakage results in the photon emission outside the cavity.

## Driven-dissipative Dicke model in the ultrastrong coupling regime

**End-to-end computational workflow** The input to the workflow are the Hamiltonians in (19) and (20) and the parameter ranges. The trial ground state should be prepared in the form of squeezed vacuum state.

```
set N0 in range 100 to 1000
  for omega_0: 0.7 omega_c to 1.3 omega_c, step domg = 0.05 omega_c
    for lambda: 0.5 omega_0 to 1.5 omega_0, step dlmb = 0.01 omega_0
      # Find first 100 eigenenergies of the Hamiltonians (1) and (2)
      # with precision in range 0.01 omega_0 to 0.001 omega_0
    end
  end
end
output: array of eigenenergies vs corresponding omega_0 and lambda values
```

### Why classical methods are not sufficient to perform the hard computational module

The capacity of classical hardware introduces constraints on the number of quantum emitters and bosonic degrees of freedom that can be accommodated in the simulations. The bottleneck in this computational process is the limitation on the number of bosonic quanta of the cavity mode. For instance, simulations using the QuTiP package [201] allow for numerically exact handling of approximately 10 quantum emitters coupled to about 50 bosonic quanta. Classical methods can be employed to diagonalize the Hamiltonians (19) and (20) using the Lanczos algorithm that enables the extraction of a few, 1 to 10, lowest energy eigenstates. For larger number of eigenstates quantum algorithms must be employed. Pushing the boundaries to incorporate 1000 quantum emitters and hundreds of bosonic quanta becomes crucial when dealing with USC regime, however, these scenarios become challenging to realize using the classical hardware.

**Concrete problem instantiations** The eigenenergies obtained in the workflow outlined above will be plotted against coupling strength for a fixed number of quantum emitters and various values of detuning  $\omega_c - \omega_o$ . This graphical analysis should facilitate the identification of coupling parameters beyond which the Dicke spectrum diverges from that of the Tavis-Cummings model due to the effect of the counter-rotating terms. In addition, by comparison with the lowest eigenstates obtained using the classical hardware, one will identify the limitations of this approach. Conversely, the case of a single quantum emitter will be compared with the outcomes of the Rabi and Jaynes-Cummings models found in the existing literature [139] and the evolution of the spectra for the increasing number of quantum emitters analyzed.

**List of other candidate instances** The Dicke Hamiltonians (19) of interest have identical coupling rates  $\lambda$  for quantum emitters with both rotating and counter-rotating terms. Nevertheless, these parameters can be varied, leading to what is known as the asymmetric Dicke model [219, 248]. The numerical examination of the interplay between these parameters and their impact on spectral properties is a worthwhile investigation.

### 4.2.3 Application 2: Phase diagram of the driven-dissipative Dicke model

**Specific background of the application** By taking into account that the cavity and quantum emitters form an open quantum system, we introduce the associated reduced density operator  $\hat{\rho}$

## Driven-dissipative Dicke model in the ultrastrong coupling regime

whose time evolution is described by the Liouville-Lindblad master equation

$$\partial_t \hat{\rho} = -\frac{i}{\hbar} [\hat{H}, \hat{\rho}] + \frac{\gamma_c}{2} \hat{\mathcal{D}}_{\hat{a}}[\hat{\rho}] + \frac{\gamma_{\uparrow}}{2} \sum_{n=1}^{N_o} \hat{\mathcal{D}}_{\hat{\sigma}_n^+}[\hat{\rho}] + \frac{\gamma_{\downarrow}}{2} \sum_{n=1}^{N_o} \hat{\mathcal{D}}_{\hat{\sigma}_n^-}[\hat{\rho}] + \gamma_{\phi} \sum_{n=1}^{N_o} \hat{\mathcal{D}}_{\hat{\sigma}_n^z}[\hat{\rho}] + \eta \sum_{n=1}^{N_o} \hat{\mathcal{D}}_{\hat{a}, \hat{s}_n^{\pm}}[\hat{\rho}]. \quad (21)$$

Here, the first term in the right-hand side accounts for coherent dynamics governed by the Hamiltonian  $\hat{H}$  which is given by either Eq. (19) or (20) and the rest of the terms account for the incoherent energy pump and the dissipation processes using the Lindblad superoperator  $\hat{\mathcal{D}}_{\hat{O}}[\hat{\rho}] = 2\hat{O}\hat{\rho}\hat{O}^{\dagger} - \hat{O}^{\dagger}\hat{O}\hat{\rho} - \hat{\rho}\hat{O}^{\dagger}\hat{O}$ . Specifically, we care about the cavity leakage with the rate  $\gamma_c$ , the quantum emitter population (pump) decay with the rate  $(\gamma_{\uparrow}) \gamma_{\downarrow}$ , and the quantum emitter pure dephasing processes with the rate  $\gamma_{\phi}$ . The last term in Eq. (21) represents the dissipative interaction via common bath degrees of freedom between the cavity mode and quantum emitters characterized by the rate  $\eta$ . The associated Lindblad operator is  $\hat{\mathcal{D}}_{\hat{a}, \hat{s}_n^{\pm}}[\hat{\rho}] = 2\hat{a}\hat{\rho}\hat{s}_n^{\pm} - \hat{s}_n^{\pm}\hat{a}\hat{\rho} - \hat{\rho}\hat{s}_n^{\pm}\hat{a} + 2\hat{s}_n^{\mp}\hat{\rho}\hat{a}^{\dagger} - \hat{a}^{\dagger}\hat{s}_n^{\mp}\hat{\rho} - \hat{\rho}\hat{a}^{\dagger}\hat{s}_n^{\mp}$ . We introduced this term into a generalized version of the Dicke model in Ref. [321].

By tuning the quantum emitter and cavity mode frequencies in resonance,  $\omega_o \approx \omega_c$ , distinct coupling regimes can be distinguished. The strong coupling regime occurs when the coupling strength, scaling as  $\sqrt{N_o}\lambda$ , exceeds any of the relaxation rates listed above. In this regime, excitations of quantum emitters can form hybrid states with the cavity mode known as polariton states. These states exhibit emergence of spontaneous coherence between quantum emitters and cavity mode beyond the critical coupling rate, i.e., for  $\lambda > \lambda_c$ . In the framework of the Dicke model, spontaneous coherence can be associated with the nonequilibrium phase transition to the superradiant state, breaking  $\mathbb{Z}_2$  symmetry. In contrast, the Tavis-Cummings model allows for a lasing phase transition associated with  $U(1)$  symmetry breaking. Conventional approach to explore the phase diagram involves a two-step process: initially, stability analysis is conducted in the mean-field approximation, which holds in the thermodynamic limit. Subsequently, long-range correlations are incorporated, e.g., via the second cumulant approximation which works well for relatively large  $N_o \gtrsim 10^2$  finite-size ensembles of quantum emitters.[219]

An example of the phase diagram, depicted in Fig. 4-2, shows results obtained using both the mean-field (a-c) and the second cumulant (d-i) approximations.[321] In the left and central columns of Fig. 4-2, corresponding to the quantum emitter populations below inversion, we predict the coexistence of superradiant (SR) and lasing without inversion (LWI) polariton phases. In the right column of Fig. 4-2, presenting the population inversion regime, only the regular lasing (RL) phase is observed. Of particular interest is the scenario where the coupling rates are  $N_o\lambda^2/\omega_o^2 \gtrsim 0.3$  and  $\eta/\omega_o \gtrsim 0.3$ , indicative of the USC. In this instance, our phase diagram shows the overlap of the SR and LWI phases. This ‘‘gray’’ region warrants further in-depth investigation, holding the potential for identifying novel polariton phases. Investigating the USC phase diagram, we should consider the higher-order cumulants, given that the second-order approximation may break down. Additionally, incorporating common bath conditions and accounting for potential non-Markovian effects in the calculations, as outlined earlier, is important. While other examples of Dicke model phase diagrams exist [219], extending these diagrams to the USC regime remains an open research problem, awaiting resolution. We foresee the utilization of noiseless quantum computers as a reliable tool for overcoming aforementioned problems and gaining deeper insights into this intriguing class of problems.

**Objectives** According to the discussion above, our objective is to investigate the phase diagram of the generalized driven-dissipative Dicke model, as defined by Eqs. (19) and (21) where the size of the

## Driven-dissipative Dicke model in the ultrastrong coupling regime

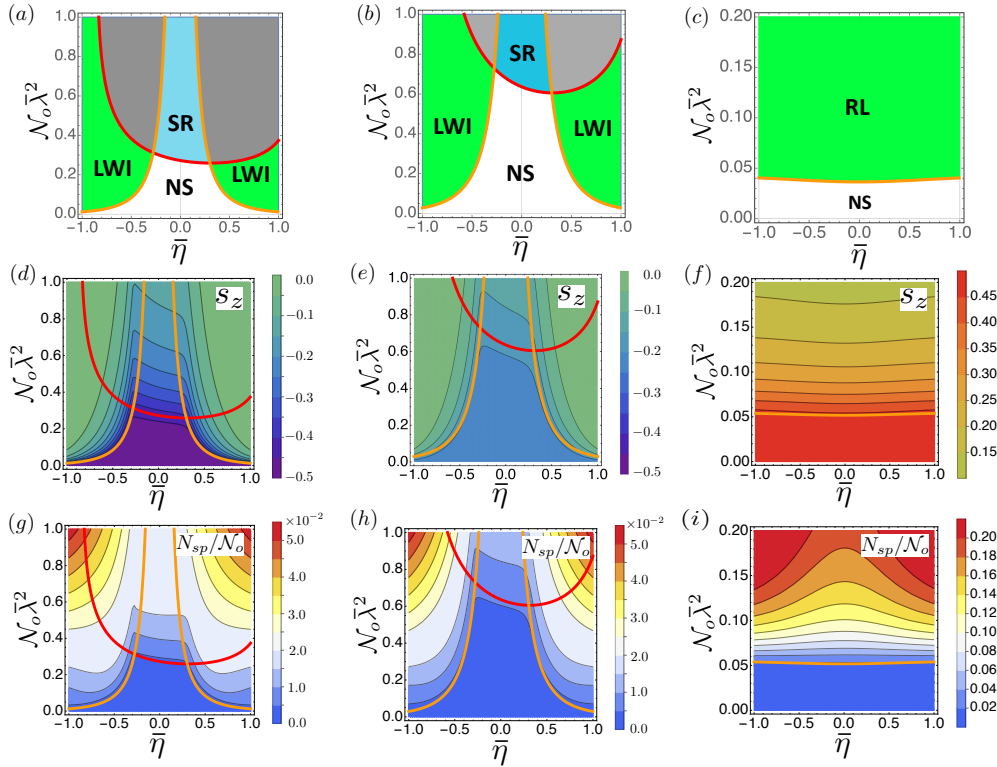


Figure 4-2: Phase diagram of generalized Dicke model accounting for the coherent and dissipative coupling. [321] (a)-(c): Mean-field phase diagrams marking the normal (NS), superradiant (SR), lasing without inversion (LWI), and regular lasing (RL) states. (d)-(f) The steady state projection on the quantum emitter population inversion  $s_z = \sum_{n=1}^{\mathcal{N}_o} \langle \hat{\sigma}_n^z \rangle / 2\mathcal{N}_o$  and (g)-(i) reduced cavity mode population (the order parameter)  $\mathcal{N}_{sp} = \langle \hat{a}^\dagger \hat{a} \rangle$  normalized per total number of quantum emitters  $\mathcal{N}_o$  calculated for the driven dissipative Dicke model with the coherent  $\bar{\lambda} = \lambda/\omega_o$  and dissipative  $\bar{\eta} = \eta/\omega_o$  couplings. The left and central columns represent quantum emitters below population inversion and the right one above. The diagram segments for  $\sqrt{\mathcal{N}_o \bar{\lambda}} > 0$  and  $\bar{\eta} > 0$  are attributed to the USC regime.

ensemble of quantum emitter and the coherent and dissipative coupling parameters are varied. To understand the influence of the counter-rotating terms (reflecting different spontaneous symmetry breaking) in the emergence of phases, we aim to conduct a comparative analysis with the driven-dissipative Tavis-Cummings model described by Eqs. (20)-(21) within the same parameter range. Furthermore, exploring variations in the number of quantum emitters will be helpful in identifying emergent signatures of phase transitions and their deviations from the thermodynamic limit.

**End-to-end computational workflow** Solution of Lindblad Eq. (3) with the Hamiltonians (1) and (2)

```

set N0 in range 100 to 1000
set omega_0 = delta omega_c with delta in range 0.7 to 1.3
set dissipative parameters [gamma_c, gamma_uo, gamma_down, gamma_phi]
in Eq. (3) in range 0.01 omega_c to 0.1 omega_c
for lambda: 0.5 omega_c to 1.5 omega_c, step dlambda = 0.01 omega_c
  for eta: 0.5 omega_c to 1.5 omega_c, step deta = 0.01 omega_c
    # Initialize reduced density operator as direct product of
    # density operator for photon vacuum and quantum emitters

```



## Driven-dissipative Dicke model in the ultrastrong coupling regime

```
# in certain population state rho(0) = rho_photon_vacuum rho_QE
# Run time dependant quantum trajectories with timestep
# dt = 0.01/omega_c for rho until reaching steady state
# with precision 0.01
# Measure order parameters such as QE population inversion sigma_z
# and cavity photon population a^dag a
# Store measured values in array vs corresponding lambda
# and eta values
end
end
output: array of order parameter values vs corresponding lambda and eta values
```

### Why classical methods are not sufficient to perform the hard computational module

State of the art numerically exact simulations meant to explore the phase diagram of the Dicke model in the strong coupling regime have been reported to handle ensembles of  $\mathcal{N}_o = 25$  quantum emitters.[219] This truncation of the interacting quantum emitter chain defines the scope of the physics we can accurately model. Although phase transitions are well-defined in the thermodynamic limit, we can detect them for relatively large but finite ensembles of quantum emitters by adopting the second-order cumulant approximation. Classical computations can handle scenarios with about  $10^3$  interacting quantum emitters using the second cumulant approximation.[321] However, extending these simulations to incorporate higher-order cumulants becomes impractical due to memory scaling limitations and the inherent complexity in deriving analytical expressions. The utilization of QPUs holds promise in overcoming these challenges, allowing for the natural incorporation of higher-order cumulants in the numerically exact modeling of the extended ensembles of quantum emitters entering the USC regime.

**Concrete problem instantiations** Using computational workflow outlined above explore the phase diagram similar to that depicted in Fig. 4-2 for an ensemble of quantum emitters of the size of  $N \sim 10^2 - 10^3$  where we suggest using  $N = 1, N = 50, N = 100, N = 500,$  and  $N = 1000,$  which will be helpful in identifying emergent signatures of phase transitions and their deviations from the thermodynamic limit. To understand the influence of the counter-rotating terms (reflecting different spontaneous symmetry breaking) in the emergence of phases, we aim to conduct a comparative analysis with the driven-dissipative Tavis-Cummings model described by Eqs. (20)-(21) within the same parameter range. Comparison to the second cumulant classical calculation in Fig. 4-2 will be performed to identify the limitations of this method.

**List of other candidate instances** Expanding the phase diagrams for different generalizations of the Dicke model [219, 254], for instance, the asymmetric variant, obtained in the strong coupling regime, into the USC range is of particular interest. Furthermore understanding the impact of non-Markovian effects requires further studies involving the modification of the Lindblad master equation (21) by incorporating the appropriate relaxation memory kernel, along with the implementation of suitable quantum algorithms. To ensure the fulfillment of the gauge invariance requirement, an augmentation of the Dicke Hamiltonian (19) to multi-level quantum emitters is necessary. Furthermore, a broadening of the Dicke Hamiltonian introducing multiple cavity modes could be relevant.

## Driven-dissipative Dicke model in the ultrastrong coupling regime

### 4.3 Requirements summary

This section summarizes the application requirements for all the applications described in this chapter.

#### **Application 1: Low energy spectrum of Dicke and Tavis-Cummings models**

<b>Workload:</b>	Total time limit	2 months
	Number of subroutine calls required	$13 \times 100 \times 100$
	Maximum subroutine time limit	NA
<b>Problem specifications:</b>	Model type	Multiple-spins with one multi-level state
	Size	minimum 100 spins + 100 levels, target 1000 spins + 500 levels
	Interaction Structure	Star Graph (the multi-level state is the center)
	Computational target	100 lowest energy values
	Accuracy requirement	Relative with respect to multi-level coupling, minimum $10^{-2}$ , target $10^{-3}$

#### **Application 2: Phase diagram of the driven-dissipative Dicke model**

<b>Workload:</b>	Total time limit	2 months
	Number of subroutine calls required	$13 \times 100 \times 100$
	Maximum subroutine time limit	NA
<b>Problem specifications:</b>	Model type	Multiple-spins with one multi-level state
	Size	minimum 100 spins + 100 levels, target 1000 spins + 500 levels
	Interaction Structure	Star Graph (the multi-level state is the center)
	Computational target	Average quantum emitter population Average cavity population (after reaching dynamical steady-state)
	Accuracy requirement	For averages: Relative to number of quantum emitters, $10^{-2}$  For considering dynamical steady-state: relative changes over time, $10^{-2}$

## **5 High-temperature superconductivity and exotic properties of Fermi-Hubbard models**

The design of new crystals and alloys is currently hindered by the lack of theoretical guidance and predictions for the so-called strongly correlated materials. The principal limitations are not believed to reside in the quality of the models but in the inherent classical constraints to simulate them. In this chapter, we describe applications of the Fermi-Hubbard model(s) for predicting high-temperature superconductivity and other exotic properties in materials. We briefly introduce how the Fermi-Hubbard model arises as an effective description of the behavior of strongly correlated electrons in crystals. We depict what the expected phases, or material's behavior, of the Fermi-Hubbard model look like and what physical observables are identified as key markers of these different phases. Finally, we show how these different phases can be computed using quantum computing resources and we provide a series of concrete use cases that are of relevant and important scientific value.

**Hamiltonian Type:** Fermionic Hamiltonians.

**Quantum Computational Kernels:** Ground State Preparation, Thermal State Preparation.

# High-temperature superconductivity and exotic properties of Fermi-Hubbard models

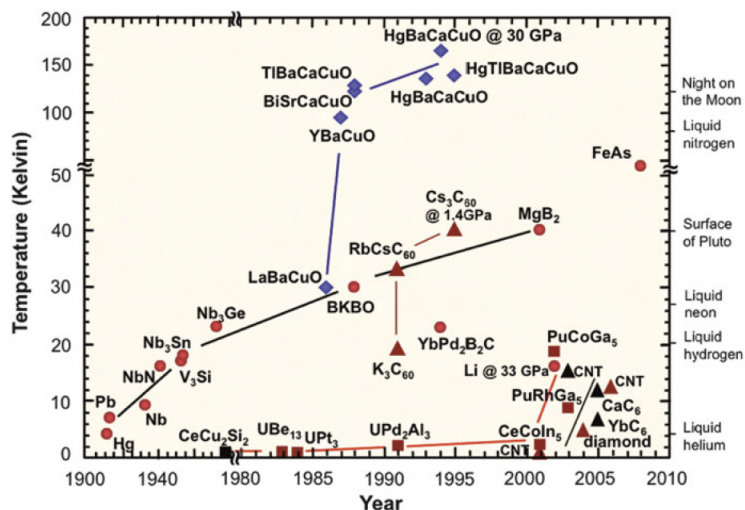


Figure 5-1: Evolution of the superconductivity critical temperature over the years for various materials. The gap between low-temperature superconductors and HTC is over a hundred of Kelvin.

## 5.1 Application area overview

### 5.1.1 High-level description of the application area

Superconductivity manifests itself physically as virtually zero electric resistance and the expulsion of magnetic fields from the bulk of the material (Meissner effect). Overall, there is a good understanding of low temperature superconductivity, which is due to the interaction between electrons and lattice phonons (quantized vibrations), leading to the Bardeen-Cooper-Schrieffer theory (BCS) of late 1950s. Above a certain temperature  $T_c$ , conventional superconductors behave as “regular” metals, and below their resistivity is virtually zero by the current testing methods. The basic insights that this theory provides is that electrons, naturally repelling each other because of their charge, become attracted as a result of the mediation of phonons. In contrast to the BCS theory of conventional superconductors, High Temperature Superconductors (HTC) requires grasping a variety of concomitant phenomena [97] and its understanding remains one of the biggest open scientific and technological problems. The goal of this review is to point out to some models that currently require intensive numerical methods to study and for which quantum computer may prove useful at removing computational barriers.

In Fig. 5-1, we see the evolution of superconductivity critical temperatures over the years, and the branching off in 1986 of HTC materials. In materials based on Lanthanide (La) compounds, pressure displaces lanthanum and induces high temperature superconductivity at higher critical temperatures [421]. This shows how the critical temperature is sensitive to the material structure and physical conditions. In what follows, we provide a review of some basic methods to probe the physics of various materials:

- Mercury Barium Calcium copper Oxide ( $\text{HgBa}_2\text{Ca}_2\text{Cu}_3\text{O}_8$  or sometimes simply Hg-1223) is an important cuprate (based on copper oxides) superconductor with a superconducting transition temperature that can exceed 138 Kelvin. Its complex structure, particularly the interactions within the  $\text{CuO}_2$  planes as we will see below, contributes to its high-temperature

## High-temperature superconductivity and exotic properties of Fermi-Hubbard models

superconducting properties. The reduction of this compound to layers of 2-dimensional lattices of copper and oxygen can be studied using the Fermi-Hubbard model. The cuprates are founded on two-dimensional planes comprising a square lattice of Cu ions connected by O ions at the links [98].

- Iron pnictides are a class of high-temperature iron-based superconductors with a layered crystal structure [384]. For instance, in Iron-Pnictide LaFeAsO (e.g.,  $\text{LaFeAsO}_{1-x}\text{F}_x$ ), superconductivity is observed with critical temperatures ( $T_c$ ) up to 26 K when doped with fluorine and is one of the materials believed to require a multi-band Fermi-Hubbard. Various compounds are reported to exhibit up to 150 Kelvin transitions. Iron-based superconductors are a class of high-temperature superconductors discovered in the late 2000s [206] in LaOFeP. Unlike traditional HTC, which often contain copper, these compounds feature iron atoms at their core. They exhibit superconducting behavior at relatively higher temperatures compared to conventional superconductors. LaOFeP represents a specific composition within this class. LaOFeP's structure consists of an intricate arrangement: it comprises alternating layers of lanthanum oxide (composed of  $\text{La}_3^+$  and  $\text{O}_2^-$  ions) and iron pnictide (made up of  $\text{Fe}_2^+$  and  $\text{P}_3^-$  ions) [199]. An illustrative instance of the family of Fe-based superconducting compounds is exemplified by  $\text{LaO}_{1-x}\text{F}_x\text{FeAs}$ , which is among the extensively studied pnictides. Notably, a remarkable superconducting critical temperature of approximately 55 K [468] has been achieved in a related compound,  $\text{SmO}_{1-x}\text{F}_x\text{FeAs}$ . These critical temperature values are surpassed only by those observed in the Cu-oxide family of high critical temperature superconductors. The physics of the new Fe-based superconductors exhibits several resemblances to the properties of cuprates, which are however much more studied in the literature.
- In some types of compounds based on lanthanides, a stripe phase is observed, e.g. a modulation of the charge density on top of antiferromagnetism [118]. This suggests the presence of ordered stripes or charge density waves within the material, that occur as a modulation of the strength of the magnetic field on top of the antiferromagnetic state. These stripes are believed to arise from a delicate interplay between charge, spin, and lattice degrees of freedom and are mostly observed in materials of the  $\text{La}_2\text{CuO}_4$  family [409, 438, 140]. An interesting fact is that in nickelates (which we do not discuss here at length) a charge density wave leads to insulators, while in cuprates it leads to superconductors [224];
- Graphene based superconductors are an old family of conventional superconductors that have been proposed to have a high temperature superconductive phase when properly doped. These types of compounds are currently under study, predicted but never observed experimentally [163, 294]. In addition to the physics of cuprate-based superconductors, a fresh area of research has emerged in the form of graphene-based superconductivity and iron-based superconductivity. For graphene based superconductivity, there have been a few proposals of superconductivity on honeycomb lattice systems [294, 295]. These are typically either hexagonal or triangular plaquette materials, inspired by the physics of graphene. Recently, a study introduced a single orbital Fermi-Hubbard model on a octagraphene lattice, which is a square-octagon lattice.

Below we will provide more background on the origin of superconductivity in Fermi-Hubbard models.

# High-temperature superconductivity and exotic properties of Fermi-Hubbard models

## 5.1.2 Role of Fermi-Hubbard physics in the investigations of HTC

As we discuss below, the physics of HTC is deeply intertwined with the theory of Mott insulators that was introduced to explain why some materials that would be conducting electricity according to band theory, are effectively insulators [55]. The Fermi-Hubbard model was central in predicting the physics of Mott insulators and the Mott transition [291, 11, 470, 250].

From an explanatory point of view, there are two global pictures in HTC physics, both connected to a Mott-Insulator transition but near two phases that, from a material perspective, are considered different: the stripe phase and the d-wave picture. The conventional d-wave superconductive picture refers to the symmetry of the superconducting order parameter in momentum space near a Mott transition, in the presence of an antiferromagnetic state. This picture emphasizes the d-wave nature of the superconducting pairing, where the order parameter changes sign along specific directions on the Fermi surface, on top of the antiferromagnetic state.

One of the reasons why there is so much effort and numerical studies in the study of the Fermi-Hubbard model to explain HTC is that it exhibits a large number of strongly competing orders observed in the cuprates, including both d-wave superconducting and charge/spin stripe order. Another physical picture which was very popular among HTC explanations, i.e. Anderson's resonating valence bond developed for  $La_2CuO_4$  [7] and topological order, while having an important role in physics as a theory of non-Landau symmetry breaking, is now considered an independent area of research which does not apply to "conventional" high-temperature superconductors or does not completely explain it. The physics of HTC is among the most important aspects of the more general field of strongly correlated materials. In general, it is also observed experimentally that the superconductive critical temperature can be increased at high pressure [151].

In the survey of applications below, we describe four models. In particular, we suggest instances based on cuprates and those based on iron-based materials for superconductors (with square plaquette), those based on graphene (honeycomb plaquette), and a particular choice of parameters for a 2D square lattice which is of academic interest. The model used to describe the hopping of electrons is the Fermi-Hubbard model, which describes electrons as particles (of spin up and down) hopping on a certain lattice or crystal structure. The two key quantities of interests are the onsite repulsion (due to the Coulomb energy in the Hamiltonian, and Pauli's principle at the wavefunction level) and the hopping energy. The hopping energy requires a deep knowledge of the crystal structure, the orbitals involved, and the overlaps between the orbitals, which all contribute to the hopping energy (later called more generically  $t_{ij}$  between sites  $i, j$ ). While the model is predominantly studied on square lattices or decorations thereof, the study of real materials thus requires a careful characterization of the crystal structure. However, models derived on certain sublattices of the original one are typically used to explain some aspects of the nature of the HTC phase. For instance, in Fig. 5-2,  $La_2CuO_4$  is reduced from a full crystal structure to three bands involving only O and Cu atoms, and subsequently reduced to a single band model with the O atoms integrated out<sup>2</sup>. Cuprates are the most studied materials from the point of view of conventional HTC. Generically, the important quantities which affect the physical behavior of the system are the number of electrons on the lattice (at most two per sites, later referred as electron filling), the temperature and the intrinsic parameters of the Hamiltonian (hopping energies and onsite repulsion, or ratios thereof). These three sets of parameter inputs that characterizes the Fermi-Hubbard physics from a computational perspective [470].

High temperature superconductivity can be studied, to some degree, using the Fermi-Hubbard

---

<sup>2</sup>In the literature, bands and orbitals are used interchangeably.

## High-temperature superconductivity and exotic properties of Fermi-Hubbard models

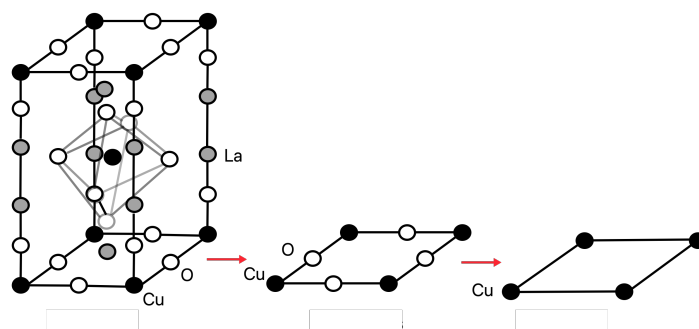


Figure 5-2: The crystal structure of  $\text{La}_2\text{CuO}_4$  (or  $\text{Sr}_2\text{CuO}_4$ ), a high temperature superconductor, and its reduction to a single band effective model by the progressive elimination of degrees of freedom until the square lattice of Fig. 5-4 is reached. In the two dimensional sublattice, Cu has four nearby O atoms.

model. The material's electron filling then can be modelled by the number of electrons in the model. The FH model incorporates the most important electronic interactions in a lattice structure, considering the hopping of electrons between lattice sites and their repulsive interactions. The cuprate-based single-band models primarily focus on the behavior of doped Mott insulators. Upon electron filling with charge carriers (holes or electrons), these materials undergo a transition from an antiferromagnetic insulating phase to a superconducting phase at relatively high temperatures compared to conventional superconductors [212].

As we will discuss below, from a numerical perspective evaluating the physical properties of these systems becomes challenging because of the necessity of analyzing the Fermi-Hubbard model numerically: this implies calculating ground and thermal states of a Hamiltonian with a large number of states. The phases of the Fermi-Hubbard model (FH) is rather complicated. It involves various phases and multiple order parameters that need to be evaluated. Classical methods can be pushed, with supercomputers of various generations, to systems with 20-25 spins at most.

In the following Section 5.1.3, we provide an overview of the utility of the applications. Section 5.2.1 contains a brief introduction of the derivation of the model from localized orbitals, with further basic background provided in Appendix. 5.6.2, while in Appendix 5.6.3 we survey a few classical methods used to analyze the FH model. In Section 5.2.2, we characterize the main observables used to describe each phase of the model, based on a consensus from a broad literature survey. In Section 5.3, we provide a pseudo-algorithmic approach to the study of superconductivity, with concrete examples drawn from the literature in Section 5.4.

## High-temperature superconductivity and exotic properties of Fermi-Hubbard models

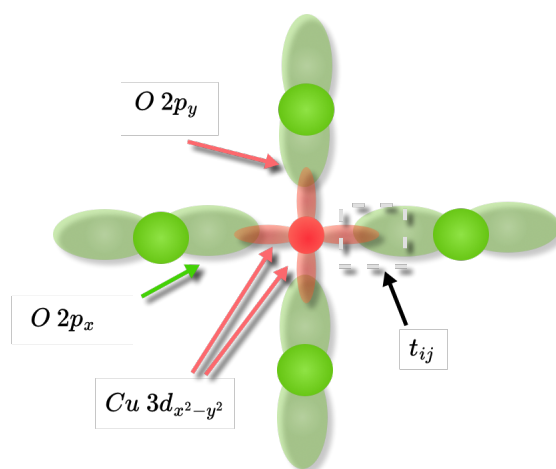


Figure 5-3: The Fermi-Hubbard model originates from the hopping of electrons between the orbitals of the crystal's atoms in a copper oxide. In the case of the two dimensional Fermi-Hubbard model on the square lattice, the hopping parameters  $t_{ij}$  originate from the overlap of the orbitals of oxygen and copper.

### 5.1.3 Utility estimation

**Overview of the value of the application area** Predictions of the phase diagram of Fermi-Hubbard models is an important scientific endeavour as it would provide guidance for the exploration and development of new strongly correlated materials. The exotic phases of these crystals are currently elusive to classical simulations precisely because they require to take into account the full quantum nature of a large multitude of interacting electrons. Having a better understanding of how the lattice geometry, interaction intensities and electron filling impact superconductivity at higher-temperature constitutes the flagship application and primary scientific motivation for doing Fermi-Hubbard simulations. The promise of high-temperature superconductors is the emergence of stronger, more compact and more sensitive magnets with applications in all sectors of our society: Transportation with smaller electric drives, Industry with kaolin/clay separation, Medical with stronger MEG coils, Communication with more sensitive antennas, Electric power with resilient auxiliary control equipment and Defense & Space with more sensitive satellite and submarine sensors [90, 89]. Therefore, it is not surprising that a considerable amount of effort and compute time is dedicated every year by the scientific community to understand and simulate Fermi-Hubbard models.

**Concrete utility estimation** In FY22, the total computing power at LANL is on the order of 10 billions core-hours. Open-science computations amount for 10% of the total load which represents 1 billion core-hours. The fraction of the open-science compute time dedicated to solving material science problem is around 20%, see Section 1.2. Approximately 50% of this later computational burden is focused on simulating Fermi-Hubbard models alone. In summary, on the order of 100 million core-hours are spent on solving Fermi-Hubbard models at LANL using different classical algorithms. Moreover, these simulations require access to large amount of RAM with the nodes in LANL Chicoma supercomputer possessing 128 cores and 512Gb of memory. For these specifications, the typical cloud computing cost is around \$0.03 per core-hour. Therefore, the open science Fermi-Hubbard simulations performed at LANL in 2022 would cost approximately \$3 million per



# High-temperature superconductivity and exotic properties of Fermi-Hubbard models

year at a commercial cloud computing vendor.

Unfortunately, the exact number and nature of the Fermi-Hubbard models that were studied is unknown. However, based on the 2022 list of publications involving these computations, we estimated that approximately 10 different models were studied. This would bring the cost of characterizing part of the phase diagram of small Fermi-Hubbard models with classical algorithms to \$300K per model within a time-frame of 1-2 months.

## 5.2 Problem formulation and computational workflows

As mentioned earlier, the Fermi-Hubbard model is a simplified, effective, theoretical model that describes the behavior of electrons in a strongly correlated crystal. This implies that a series of steps are necessary to select a Fermi-Hubbard model that can be representative of an actual material, the final goal being of testing predictions of the model against experimental results.

From a computational perspective, calculating the physical properties of a strongly correlated material, using a realistic parameter estimation procedure from the the knowledge of a crystal structure, obeys a particular workflow that reads at a high-level:

1. Pick a crystal structure representative of the material
2. Study the orbital overlap via atomic wave function or similar and equivalent methods
3. Derive a Fermi-Hubbard model
4. Choose the parameters of the model (electron filling, temperature)
5. Pick a method or approximation scheme to study the Fermi-Hubbard model
6. Investigate the properties of the Fermi-Hubbard model (phases, conductivity, etc)

In this workflow, quantum computing can help by replacing Step 5 with a quantum kernel (either ground state estimation or thermal sampling, as we will see later). The input and observables of this kernel are specified in Step 4 and Step 6 respectively.

The generic form of the Hamiltonian of the Fermi-Hubbard model reads for a single band [184, 157, 207]:

$$H = - \sum_{\substack{\langle i,j \rangle, \sigma \\ \langle i,j \rangle}} t_{ij} (c_{i,\sigma}^\dagger c_{j,\sigma} + h.c.) + U \sum_i n_{i,+} n_{i,-} \quad (22)$$

where the first term is a tight-binding Hamiltonian which leads to standard band theory of itinerant electrons, while the second term represents the repulsive interaction between the electrons. Another way of interpreting this Hamiltonian is to consider that the first term represents the kinetic energy of electrons hopping between neighboring lattice sites, while the second is an onsite interaction energy. The operators  $c_{i,\sigma}^\dagger$  and  $c_{j,\sigma}$  are the creation and annihilation ladder operators for an electron at site  $i$  and  $j$ , respectively, with spin  $\sigma \in \{-, +\}$ . They satisfy the (anti)commutator relationships  $\{c_{i,\sigma}, c_{j,\sigma'}^\dagger\} = \delta_{ij} \delta_{\sigma\sigma'} \hbar$ , but in numerical simulations it is often used the notation  $\hbar = 1$ . This choice is not restrictive, as we will explain in the applications section.

The summation  $\sum_{\langle i,j \rangle}$  runs over pairs of neighboring sites. The term  $n_{i,+} n_{i,-}$ , where  $n_{i,\sigma} = c_{i,\sigma}^\dagger c_{i,\sigma}$ , ensures that there is a repulsion between electrons. A graphical representation of the meaning of the parameters  $t_{ij}$ , and  $U$  are shown in Fig. 5-4.

## High-temperature superconductivity and exotic properties of Fermi-Hubbard models

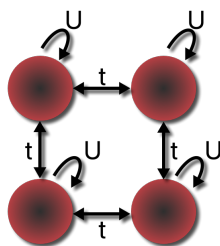


Figure 5-4: A graphical representation of the Fermi-Hubbard model. The parameter  $t$  is the energy associated with the hopping between sites, while the parameter  $U$  represents the energy associated to the particle remaining on the same site.

The complex behavior of the Fermi-Hubbard model arises from the competition between localization and itinerancy: it captures the interplay between electron hopping and on-site interactions, which can give rise to interesting phenomena like metal-insulator transitions, magnetic ordering, and, in certain cases, superconductivity. The Fermi-Hubbard model is expected to display a broad set of distinct behavior, or phases, for different values of electron filling and temperature. The phases of interest are the superconductive, pseudogap, Fermi Liquid, strange metal and antiferromagnetic phases which we will describe in more detail later. In addition, the Fermi-Hubbard Hamiltonian can be generalized to different bands, as we discuss below. The number of bands in the model refers to the energy bands that the particles can occupy as they move through the lattice. This makes the problem to study computationally even more complicated.

It is worth stressing at this point a difference between conventional superconductivity and the type of superconductivity predicted by the Fermi-Hubbard model. In both cases, it is the formation of Cooper pairs, which are pairs of electrons with opposite spin and momentum that experience an effective attractive interaction, that leads to superconductivity. For conventional superconductors, this effective attractive interaction is mediated by the lattice vibrations (phonons) and appears explicitly in the Hamiltonian.

We would like to point out that the Fermi-Hubbard hamiltonian of eqn. (22) is closely related to the t-J model, which is mapped via the Schrieffer-Wolff transformation in the limit  $U \gg t$  with  $J = 4t^2/U$  [65, 306]. Thus, many of the comments below will be valid for the t-J models as well in the limit described above.

### 5.2.1 Methods used to derive the model Hamiltonians

The Fermi-Hubbard hamiltonian of eqn. (22) is a generic description of a system of fermions. To make concrete predictions about physical systems, however, it is paramount that the parameters  $t_{ij}, U_{ij}$  are estimated from first principles, as it is the case in *ab initio* methods such as DFT. For instance, the first effective Hamiltonian introduced for the study of cuprate oxides was the single band Zhang-Rice hamiltonian [455]. It is commonly believed that multi-band models are necessary to describe the superconductive phase. However, certain properties such as antiferromagnetism can be understood from fewer band models.

To see the origin of the Fermi-Hubbard Hamiltonian, let us start by considering the many-body Hamiltonian that fully describes the interactions between electrons and nuclei. This is of the form

# High-temperature superconductivity and exotic properties of Fermi-Hubbard models

[473],

$$\mathcal{H} = \underbrace{\sum_i \frac{p_i^2}{2m_e}}_{\text{electron kinetic energy}} - \underbrace{\sum_{i,a} \frac{Z_a e^2}{|r_i - R_a|}}_{\text{electron-nuclei interactions}} + \underbrace{\frac{1}{2} \sum_{ij} \frac{e^2}{|r_i - r_j|}}_{\text{electron-electron interaction}} + \underbrace{\sum_a \frac{P_a^2}{2M_a}}_{\text{nuclei kinetic energy}} + \underbrace{\frac{1}{2} \sum_{ab} \frac{Z_a Z_b e^2}{|R_a - R_b|}}_{\text{nuclei-nuclei interaction}} \quad (23)$$

Solving such Hamiltonian, e.g. eigenfunctions and respective energies, would imply knowing essentially everything about the solid state. Since this task is unreasonably ambitious, most of the results are typically obtained in some form of approximation. One of the first approximations that one encounters is the Born-Oppenheimer approximation, in which the wavefunction of the entire system is approximated as the product of wavefunctions for the nuclei and the electrons. Perturbations over the nuclei's interaction lead to phononic modes. In most cases, these interactions are neglected. In Sec. 5.6.1 we provide some details on the derivation of the Fermi-Hubbard model from eqn. (23), but the final result is a discrete Hamiltonian, much easier to handle, of the form:

$$H_{FH} = - \sum_{ij} t_{ij} \hat{c}_{i\sigma}^\dagger \hat{c}_{j\sigma} + \frac{1}{2} \sum_{i,\sigma} U_i n_{i\sigma} n_{i,-\sigma}. \quad (24)$$

The model above is the Fermi-Hubbard model, and describes the hopping of electrons on the orbitals of the atoms in the particular molecular structure of interest.

The coefficients  $t_{ij}, U$  are given by

$$t_{\langle i,j \rangle} = - \int dr \phi^*(\vec{r} - \vec{R}_i) h(\vec{r}) \phi^*(\vec{r} - \vec{R}_j) \quad (25)$$

$$U_i = e^2 \int dr dr' \frac{|\phi(r - R_i)|^2 |\phi(r' - R_i)|^2}{|r - r'|} \quad (26)$$

where  $\phi(r - R_i)$  are the atomic wavefunctions, associated with the probability  $|\phi(r - R_i)|^2$  of finding an electron at a distance  $|r - R_i|$  from atom  $i$ . The key assumption is that these are localized, and thus only  $t_{ij}$  for neighboring atoms are effectively nonzero, inducing a local graph structure. Depending on the orbitals involved, and how extended they are, one can have not only nearest neighbors (N.N.) but also next-to-nearest neighbors interactions (N.N.N.). However, if the orbital wavefunctions are localized, they overlap only for nearby sites  $\langle i, j \rangle$  and thus  $t_{ij}$  can be represented by a local Hamiltonian, e.g. a graph representing the interactions. Also, if the system is translational invariant, then  $U_i \equiv U$ . The question is then how to obtain representative numbers for  $t_{ij}$  and  $U$ . These parameters  $U, t_{ij}$  can be obtained by computing the so-called exchange integrals (25) and (26) directly from first principles and using prior knowledge about the crystal structure. Alternatively, one can choose  $t_{ij}$  as free parameters, possibly reducing it to a smaller number by symmetries, and then fit the Fermi surface of the model to the experiment. For materials that are two-dimensional, the Fermi surface can be obtained via Angle-Resolved photoemission spectroscopy (ARPES). One can fix the number of particles by looking at a subspace of the Hilbert space with fixed number of particles,  $N = 2Lf$  where  $L$  is the number of sites and  $f$  is the total fraction ( $0 < f < 1$ ) of electrons, or electron filling. The interesting case is typically near half filling,  $f = 1/2$ . One can solve for the system fixing this number, e.g. summing over all possible states  $|n\rangle$  where  $\frac{\langle n | \hat{N} | n \rangle}{2L} = f$ , where  $\hat{N}$  is the number operator, defined as  $\hat{N} = \sum_i \hat{c}_i^\dagger \hat{c}_i$ .

# High-temperature superconductivity and exotic properties of Fermi-Hubbard models

The Hamiltonian of eqn. (24) is a four-body interaction, which cannot be treated with analytical methods. One of the key approximations in the study of superconductors and superfluids is, for the sake of tractability, to replace the four body term associated to the term

$$n_{i\sigma}n_{i,-\sigma} = c_{i\sigma}^\dagger c_{i\sigma} c_{i,-\sigma}^\dagger c_{i,-\sigma} \quad (27)$$

with a mean field, to a two body approximation.

As a last comment, it is often useful to work in momentum space, by working with operators defined in terms of the momentum  $\vec{k}$

$$d_{\vec{k}\sigma} = \frac{1}{\sqrt{L}} \sum_{\vec{r}} e^{-i\vec{k}\cdot\vec{r}} c_{\vec{r}\sigma}, \quad (28)$$

which satisfy  $\{d_{k\sigma}, d_{k'\sigma'}^\dagger\} = \delta_{kk'}\delta_{\sigma\sigma'}$ , again in units  $\hbar = 1$ . In momentum space, the Fermi-Hubbard Hamiltonian becomes

$$H_{FM} = \sum_{\vec{k},\sigma} \xi_{\vec{k}} d_{\vec{k},\sigma}^\dagger d_{\vec{k},\sigma} + \frac{U}{L} \sum_{\vec{k},\vec{k}',\vec{q}} d_{\vec{k}+\vec{q},+}^\dagger d_{\vec{k}'-\vec{q},-}^\dagger d_{\vec{k}',-} d_{\vec{k},+} \quad (29)$$

Using the Bogoliubov-de Gennes mean field theory [473], the Hamiltonian above is reduced to a quadratic and numerically treatable Hamiltonian of the form:

$$H_{BdG} = \sum_{\vec{k},\sigma} \xi_{\vec{k}} d_{\vec{k},\sigma}^\dagger d_{\vec{k},\sigma} + \sum_{\vec{k}} (\Delta_{\vec{k}} d_{\vec{k},+}^\dagger d_{-\vec{k},-}^\dagger + h.c.) \quad (30)$$

where  $\Delta_{\vec{k}}$  is the superconducting order parameter. In the literature, the insertion by hand of a non-zero superconducting order parameter allows to study the phases of the model, but this relies on a series of approximations. This form is typically used when trying to fit the Fermi surface from the ARPES experiments. We provide more details on how to derive the coefficients  $t_{ij}$  and  $U_i$  from the molecular structure in Appendix 5.6.2.

It is common to consider, in addition to the hopping, also an exchange interaction between the spins of the electrons. The spin operators are defined, on each site, as

$$S_i^* = \frac{\hbar}{2} \sigma_i^* \quad (31)$$

where  $\sigma^x, \sigma^y, \sigma^z$  are the Pauli operators. On a lattice, it is also common to introduce the notation for the site indices  $\mathbf{i} = (i_x, i_y)$ , which label the lattice sites on a square lattice. An important remark, as it will be important later, is that an anti-ferromagnetic phase is also often described by the Heisenberg-like Hamiltonian on the spin degrees of freedom:

$$H_{AF} = \tilde{J} \sum_{\langle \mathbf{i}, \mathbf{j} \rangle} \mathbf{S}_i \cdot \mathbf{S}_j, \quad (32)$$

where  $J$  represents the antiferromagnetic exchange coupling between neighboring spins indexed by the vectors  $\mathbf{i}, \mathbf{j}$ . The total Hamiltonian is then given by

$$\mathcal{H} = H_{FH} + H_{AF}. \quad (33)$$

Although in the following the second term will be neglected, the anti-ferromagnetic phase can arise from the second term alone.

## High-temperature superconductivity and exotic properties of Fermi-Hubbard models

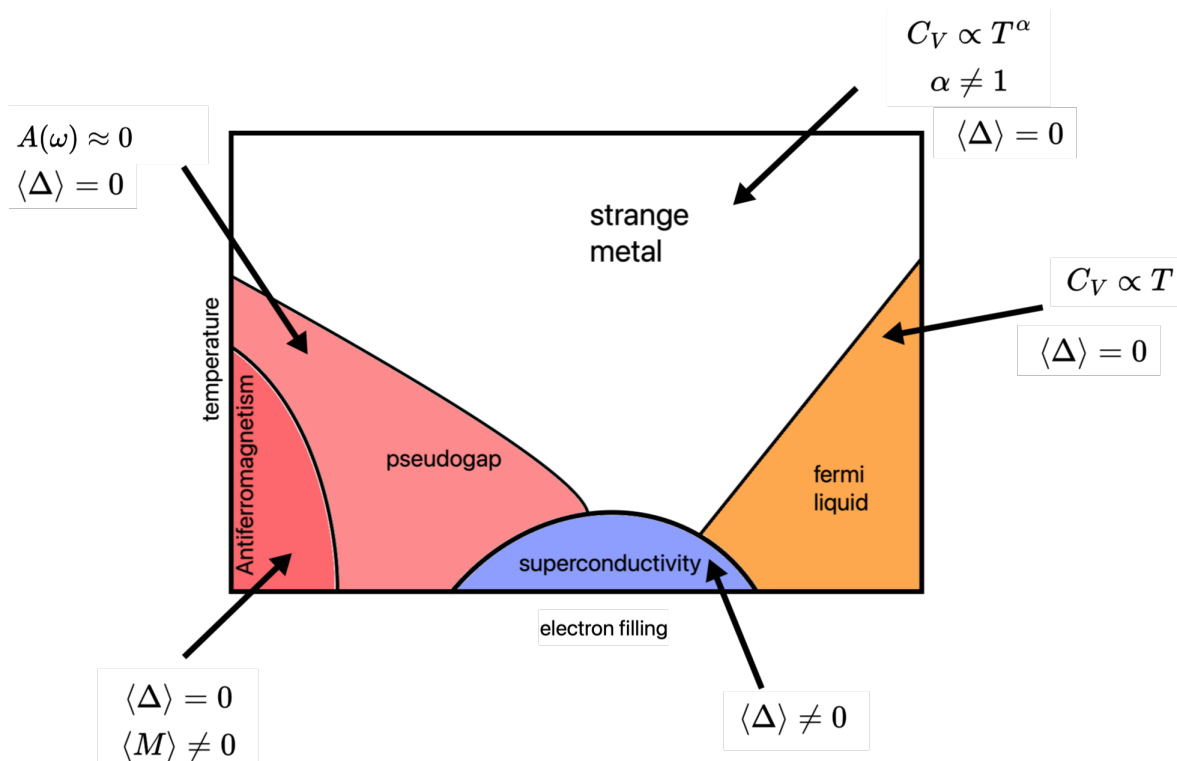


Figure 5-5: Pseudo-phase diagram for the Fermi-Hubbard model in two dimensions. The pseudogap phase is often measured via the spectral function as a pronounced dip in the spectral function. The other phases have a well defined combinations of the order parameters, as highlighted above.

# High-temperature superconductivity and exotic properties of Fermi-Hubbard models

## 5.2.2 Phases of the model via observables, and their properties

Although there is still a fair amount of debate [213] on the exact location of the transitions lines between different phases of the model, there is a consensus on the existing phases. A pictorial representation of such diagram is shown in Fig. 5-5. One of the unfortunate feature however is that there are well-established and agreed upon order parameters only for few of these phases, in the sense that various different order parameters and methods can be used to study the problems. Another important comment is that fixing the electron filling is sometimes complicated from a numerical standpoint. There is a workaround however, which is to fix the average electron density via a chemical potential  $\mu$ , e.g.  $H \rightarrow H - \mu N$  where  $N$  is the number operator for the species (electron spin up, spin down) of interest. For this reason, often in the literature ones sees instead of the electron filling (or doping), a function of the energy and chemical potential in the phase space.

An important aspect to clarify is that conductivity, the ultimate quantity that one wishes to understand, is not a static property, but a dynamical one. This aspect is clarified in Sec. 5.6.5. However, static observables as the ones described below provide key insights into the state of the system. Let us make some clarifying comment on how these quantities are calculate at zero vs finite temperature. Let us denote the ground state  $|0\rangle$ . We refer to the the zero temperature expectation value of a generic observable  $\hat{O}$  as

$$\langle \hat{O} \rangle_0 = \langle 0 | \hat{O} | 0 \rangle. \quad (34)$$

In the finite temperature setting, one simply extends the formula above to the thermal state average,

$$\langle \hat{O} \rangle_T = \text{Tr}(\rho \hat{O}) = \sum_n \frac{e^{-\beta E_n}}{Z} \langle n | \hat{O} | n \rangle. \quad (35)$$

where  $Z = \sum_n e^{-\beta E_n}$  and  $E_n$  are the energies of the  $|n\rangle$  eigenstate of the target Hamiltonian. We will often drop the explicit  $T$  dependence in what follows as it is understood that either the ground state or thermal average is used.

Here we present some options given in the literature.

- **Antiferromagnetic Phase (AFM):** The antiferromagnetic phase of the Fermi-Hubbard model is characterized by a staggered pattern in the spin density ( $\langle S_i^z \rangle$ ) with adjacent spins aligning antiparallel to each other [103]. The mean staggered magnetization

$$M = \frac{1}{L^2} \sum_i \langle (-1)^{i_x+i_y} \hat{S}_{i_x, i_y}^z \rangle \quad (36)$$

is an order parameter, which is non zero in this phase. This phase shows no superconductivity ( $\langle \Delta \rangle = 0$ , see below).

- **Fermi Liquid Phase:** The Fermi liquid phase of the Fermi-Hubbard model is characterized by well-defined quasiparticles near the Fermi surface [44], e.g. a theory of free fermions with an effective fermion mass. From a computational and non-perturbative perspective, diagonalizing the Hamiltonian is important, as  $C_V(T)$  can be calculated from the derivatives of the free energy [183],  $F = -\kappa_B T \log Z$  with  $\log Z = \text{Tr}(e^{-\beta H})$ . Then, one can look at  $\lim_{T \rightarrow 0} C_V(T)/T$  to understand in which phase the system is in [361]. If the energy states

## High-temperature superconductivity and exotic properties of Fermi-Hubbard models

of the Hamiltonians are known, then one can calculate  $C_V$  at a certain temperature  $T$  from basic statistical mechanics as

$$C_V = \kappa_B \beta^{-2} \partial_\beta^2 \log \sum_n e^{-\beta E_n} = \frac{\partial}{\partial T} \bar{E} \quad (37)$$

where  $E_n$  are the energy of the state  $|n\rangle$  of the Fermi-Hubbard Hamiltonian, while  $\beta = (\kappa_B T)^{-1}$ , and where

$$\bar{E} = \frac{1}{Z} \sum_n e^{-\beta E_n} E_n = \text{Tr}(\rho \hat{H}). \quad (38)$$

Another formula for the calculation of  $C_V$  is given by the thermal expectation value

$$C_V = \frac{1}{\kappa_B T^2 Z} \sum_n e^{-\beta E_n} (E_n^2 - \bar{E}^2) = \frac{1}{\kappa_B T^2} \text{Tr}((\hat{H}^2 - \bar{E}^2 \hat{I})\rho) \quad (39)$$

where  $\hat{I}$  is the identity operator.

From a computational perspective, the difference between the two is that eqn. (37) is evaluated in terms of second order derivatives, while the second formula is a thermal expectation value.

The Fermi-Liquid phase is characterized by the conductivity scaling as  $\rho(T) \propto T^2$ . It can be measured from  $C_V$ , in particular observing a linear scaling in temperature in the heat capacity, typical of metals

$$C_V \propto T. \quad (40)$$

- **Strange Metal Phase:** The strange metal phase within the Fermi-Hubbard model does not possess a distinct order parameter [153]. It is characterized by anomalous transport properties, such as non-Fermi liquid behavior in the electrical resistivity  $\rho(T)$  or violation of conventional scaling laws in the specific heat  $C_V(T)$  at temperature ( $T$ ). For Fermi liquids, the theory establishes that  $\rho \propto T^2$ , while in the strange metal phase one expects  $\rho \propto T^\alpha$  with  $\alpha$  typically in the range  $[1, 2)$ . To study the transport properties, in numerical simulations the Boltzmann transport equation or the (perturbative) Kubo methods are often used. However, the easiest thing to calculate in numerical experiments is

$$C_V \propto T^{\alpha'} \quad (41)$$

and check that  $\alpha' \neq 1$ .

- **Superconducting Phase:** The prevailing belief is that the most promising approach to achieving high-Tc superconductivity involves generating robust spin fluctuations by closely associating with antiferromagnetic-ordered phases. Examples of this approach include the well-known cuprates and iron-based superconductors. However, as we see below, some proposals have investigated graphene-based superconductors, which is a fresh area of research. It is fair to say that there have been thousands of papers and hundreds of proposals of possible superconductive states. However, the two key proposals are the perturbations of the striped ground state, e.g. antiferromagnetic state arranged in stripes near the half filling electron

## High-temperature superconductivity and exotic properties of Fermi-Hubbard models

filling level (with pairs of holes behaving as Cooper's pairs), or longer chains of holes at lower electron filling.

From a computational perspective, in Fermi-Hubbard models with different number of bands is suggested to exhibit different type of superconductivity. This can be captured by combinations and observations of order parameters. For the superconductivity, typically, this is studied via the correlation function, and in particular via operators of the form

$$\hat{\Delta}_{ij} = (c_{i+}c_{j-} - c_{i-}c_{j+}) \quad (42)$$

adapted to the problem at hand, and the two observables

$$C_1 = \Delta_{ij} = \frac{1}{2} \langle \hat{\Delta}_{ij} + \hat{\Delta}_{ij}^\dagger \rangle \quad (43)$$

$$C_2 = P_{ab,ij} = \langle \hat{\Delta}_{ab}^\dagger \hat{\Delta}_{ij} \rangle \quad (44)$$

to understand the scaling of the correlation, for instance power laws as a function of the distance  $d = |i - j|$ . In two or higher dimensions, this can be replaced by the Manhattan distance on the lattice. In particular, the numerical calculation can be simplified by looking at  $i = j$  in  $C_1$  and  $a = b, i = j$  in  $C_2$ . In the literature, it is often observed that superconductivity is due to spin fluctuations near an antiferromagnetic order, which is measured by  $C_1$ . Power law correlations, symptoms of a critical phase, are measured by  $C_2$  [274]. The observable  $C_1$  and  $C_2$  can be used as an indicator of d-wave superconductivity [364] in the 2D Fermi-Hubbard model. In fact, in d-wave superconductivity the order parameter  $\Delta_{ij}$  has a specific modulation in the angle (See Appendix).

- **Pseudogap:** The pseudogap phase in the Fermi-Hubbard model lacks a universally agreed-upon order parameter, and it can be measured experimentally [405] via ARPES in the spectral function. This phase is characterized by a substantial suppression or depletion of the electronic density of states (DOS  $N(E)$ ) near the Fermi level ( $N = 0$ ) without displaying any long-range order [213]. The spectral function, the Green function and the density of states are related. From an operational perspective, from the Lehmann representation one can obtain the following expression of the spectral density in the frequency domain [44] (pp 129, eq 8:50) reduced to a finite system:

$$A(i, \sigma, \omega) = \frac{4\pi}{Z(1 + e^{-\eta\omega})} \sum_n e^{-\beta E_n} \sum_{n'} \langle n | c_{i,\sigma} | n' \rangle \langle n' | c_{i,\sigma}^\dagger | n \rangle \delta(E_n - E_{n'} + \omega) \quad (45)$$

where  $|n\rangle$  are the eigenstates of the Hamiltonian. This quantity has to be scanned over the frequency  $\omega$  to observe a suppression  $A(\omega) \approx 0$ . Of all the phases above, the pseudo-gap is a dynamical phase as  $\omega$  arises from the Fourier transform in time. Thus, this phase requires an analysis of the dynamics of the system.

The reduction from a five bands to a single bands goes through various steps of integrations of degrees of freedom in the original crystal to a single atomic structure on a lattice sub-lattice. For instance, for  $\text{La}_2\text{CuO}_4$ , the reduction from the full crystal to a single layer and single atom and band (where La can be replaced for instance with Sr).



# High-temperature superconductivity and exotic properties of Fermi-Hubbard models

## 5.3 Computational applications

Below, we provide various concrete examples taken from the literature of relevant problems of interest for scientific discoveries. In all the Fermi-Hubbard models below, classical algorithms have a variety of shortcomings associated with the numerical evaluation of the ground state, as described in Sec. 5.6.3. It is important to stress that it is hard to imagine a self-contained algorithm which fully replaces the human eye and expertise. In many of the methods, it is necessary to look at a variety of order parameters to suggest a phase diagram and state of the system, as in Fig. 5-5. The range of the parameters is typically  $f = [0, 1]$  for the electron filling, while in principle the inverse temperature  $T \in [0, 300]$  Kelvin in physical units, this range can be restricted to observe a strange metal phase. The order parameters that one needs to look at in numerical simulations are of the form of Eqn. (45) for the pseudogap, and Eqn. (36) for the antiferromagnetic phase, Eqn. (40) or (41) for the Fermi liquid or strange metal phase, Eqn. (43),(44) for the superconducting phase.

Let us now describe the units of the parameters of the Fermi-Hubbard model in adimensional units. The FH is the sum of two terms

$$H_{FH} = \bar{t} \times H_{Kin} + \bar{U} \times H_{int}, \quad (46)$$

where  $\bar{t}$  is a scale, satisfying  $\bar{t} \geq \max_{ij} t_{ij}$  and  $\bar{U} \geq \max_i U_i$ . The onset of superconductivity in cuprates in the temperature range of 100 – 200 Kelvin, which corresponds to 8 – 16 milli electron Volts ( $\sim 10$  meV). The pseudo-gap phase is in the order of also tens of meV in temperature. The range of interesting physics for the parameter  $\chi = U/t$  is in the order of also 5 – 20. For instance, a common choice for the  $2d$  Fermi-Hubbard model is  $t = 1$  and  $\chi = 8$ . When computing the phase diagram, there is no time evolution, and it is not restrictive to also choose  $\hbar = 1$  and impose  $\{c_{i\sigma}^\dagger, c_{j\sigma'}\} = \delta_{ij}\delta_{\sigma\sigma'}$ .

In the following, one can set  $\bar{t} = 1$ , set  $\chi \in [0, 20]$  in adimensional units, and the temperature in adimensional units to range in the  $[0, 200]$  range, to make sure that it contains the strange metal phase. Using these adimensional units, we can introduce  $\kappa\mathcal{T}$  measured in meV,  $\bar{t}_{max} = 1$  and  $\chi = [0, 2]$ . The precision on the phase diagram variables varies. Typical choices are  $df_c = 0.1$ ,  $d\chi_c = 0.5$ ,  $d\mathcal{T}_c = 10$  with a refinement close to the phase diagram boundaries, with the underline  $c$  notation means coarser.

Thus, one way to think of the phase diagram in terms of discretization of the parameter space is as follows, in terms of coarser and finer phase diagrams. At a coarser level a homogeneous discretization for  $f$ ,  $\mathcal{T}$  respectively contained in the box  $[0, 1] \times [0, 50]$ . In this case, the half filling line is  $f = 1/2$ . Near the phase diagrams lines, it is common to pick a finer value of  $df_f = df_c/10$  and  $d\mathcal{T}_f = d\mathcal{T}_c/100$ , with the underline  $f$  notation means finer in the vicinity of phase lines.

We now present a list of concrete computational workflows and application by increasing order of complexity.

### **Application 1: Zero-Temperature Superconductivity**

The main goal of this application is to find signatures of superconductivity of a Fermi-Hubbard model at zero temperature. The core quantum capabilities required for this task is ground-state preparation. The zero temperature superconductivity is the simplest of all the tasks presented in this document, and is important to infer the exact critical density for the antiferromagnetic to superconductive phase.

## High-temperature superconductivity and exotic properties of Fermi-Hubbard models

**Specific background of the application** There are two different techniques for specifying the electron filling  $f$ . The first is to restrict computations with only states that are eigenvectors with eigenvalue  $f$  of the electron number operator  $N = \sum_{i,\sigma} c_{i\sigma}^\dagger c_{i,\sigma}$ . The second approach consists in modifying the original Hamiltonian by  $H \rightarrow H - \mu N$ , and vary the chemical potential  $\mu$  until the average electron filling of the ground state has the desired property  $\langle N \rangle = f$  on average.

**Objectives** For simplicity, we consider the superconductivity parameter (43) at a fixed location  $i = j = 0$  in the center of the lattice, i.e.,  $\Delta_0 = \frac{1}{2}(c_{0+}c_{0-} - c_{0-}c_{0+} + c_{0-}^\dagger c_{0+}^\dagger - c_{0+}^\dagger c_{0-}^\dagger)$ . The objective is to compute for a given ground state  $|\phi\rangle$ , the mean and fluctuation of the superconductivity parameter, i.e.,  $C_1 = \langle \phi | \Delta_0 | \phi \rangle$  and  $C_2 = \langle \phi | \Delta_0^2 | \phi \rangle$ . The precision required on the dimensionless quantities  $C_1$  and  $C_2$  is  $10^{-5}$ .

This computation is realized for different values of the electron filling  $f$  and potential to kinetic energy ratio  $\chi = U/t$ .

**End-to-end computational workflow** The inputs to the problem are the coupling parameters of the Fermi-Hubbard model and the required precision on the observables.

```
for chi : 0.5 to 20, step dchi=0.5
  for f : .1 to 1, step df=0.1
    (alternatively, loop over mu, mu=0... 100, dmu=1)
    # Set Hamiltonian (alternatively, with chemical potential)
    # Set Hilbert space with fixed number of electrons filling
    (skip this step with chemical potential)
    # Find ground state
    - Evaluate C1, C2 parameter up to prescribed precision
      (with chemical potential, report average electron filling)
    Is it nonzero?
    yes -> potential superconducting
    no -> no superconductivity
  end
end
```

As described earlier, the for loop in  $f$  can be replaced, alternatively, with a loop on the chemical potential  $\mu$ .

**Concrete problem instantiations** This workflow is applicable to all Hamiltonians described in Section 5.4.

### Application 2: High-Temperature Superconductivity

The main goal of this application is to find signatures of superconductivity of a Fermi-Hubbard model at non-zero temperature. The core quantum capabilities required for this task is thermal-state preparation.

**Specific background of the application** A thermal state, at the temperature  $T$ , is described by the density matrix  $\rho = \frac{e^{-H/T}}{Z}$ , where  $\text{Tr}(\rho) = 1$ .

There are again two different ways of specifying the electron filling  $f$ . The first is to con-

## High-temperature superconductivity and exotic properties of Fermi-Hubbard models

construct the density matrix only states that are eigenvectors with eigenvalue  $f$  of the electron number operator  $N = \sum_{i,\sigma} c_{i\sigma}^\dagger c_{i,\sigma}$ . The second approach consists in modifying the original Hamiltonian by  $H \rightarrow H - \mu N$ , and vary the chemical potential  $\mu$  until the average electron filling of the ground state has the desired property  $\text{Tr}(\rho N) = f$  on average.

**Objectives** The objective is to compute for a given thermal state  $\rho$ , the mean and fluctuation of the superconductivity parameter, i.e.,  $C_1 = \text{Tr}(\rho \Delta_0)$  and  $C_2 = \text{Tr}(\rho \Delta_0^2)$ . The precision required on the dimensionless quantities  $C_1$  and  $C_2$  is  $10^{-5}$ .

This computation is realized for different values of the electron filling  $f$ , potential to kinetic energy ratio  $\chi = U/t$  and temperature  $T$ .

**End-to-end computational workflow** The inputs to the problem are the coupling parameters of the Fermi-Hubbard model and the required precision on the observables.

```
for T : 1 to 200, step dT = 10
  for chi : 0.5 to 20, step dchi = 0.5
    for f : .1 to 1, step df = 0.1
      (alternatively, loop over mu, mu=0... 100, dmu=1)
        # Set Hamiltonian (alternatively, with chemical potential)
        # Set Hilbert space with fixed number of electrons filling
        (skip this step with chemical potential)
        # Find thermal state
          - Evaluate C1, C2 parameter up to prescribed precision
            (with chemical potential, report average electron filling)
          Is it nonzero?
            yes -> potential superconducting phase
            no -> return (see application 3)
    end
  end
end
```

In typical applications, if a critical line is observed in a particular interval, precision in  $df$  is increased and centered around the critical line by a factor or ten or more, e.g.  $df = 0.01$ .

Note that the loop on the in electron filling can be replaced by a loop on the chemical potential  $\mu$  as described earlier.

**Concrete problem instantiations** This workflow is applicable to all Hamiltonians described in Section 5.4.

### Application 3: Phase-Diagram of Fermi-Hubbard Models

The main goal of this application is to identify the full phase-diagram (Fermi-liquid, strange metal, AFM, superconductor) of the Fermi-Hubbard model. The core quantum capabilities required for this task is thermal-state preparation.

**Specific background of the application** A thermal state, at the temperature  $T$ , is described by the density matrix  $\rho = \frac{e^{-H/T}}{Z}$ , where  $\text{Tr}(\rho) = 1$ .

The two different ways of specifying the electron filling  $f$  in the range  $[0, 1]$  are: 1) Construct-

## High-temperature superconductivity and exotic properties of Fermi-Hubbard models

ing the density matrix only states that are eigenvectors with eigenvalue  $f$  of the electron number operator  $N = \sum_{i,\sigma} c_{i\sigma}^\dagger c_{i,\sigma}$ ; 2) modifying the original Hamiltonian by  $H \rightarrow H - \mu N$ , and vary the chemical potential  $\mu$  until the average electron filling of the ground state has the desired property  $\text{Tr}(\rho N) = f$  on average.

**Objectives** The objective is to compute for a given thermal state  $\rho$  the superconducting order parameters  $C_1$  from Eq. (43) and  $C_2$  from Eq. (44) at a given site  $i = j$ , the AFM order parameter  $M$  from Eq. (36) and  $C_v(T)$  from Eq. (39). This is done for different electron filling  $f$ , for different values of  $\chi = U/t$  and temperature  $T$ . The precision on  $C_1$  and  $C_2$  is  $10^{-5}$ , while on  $M$  is  $10^{-2}$ . The precision on the scaling exponent of  $C_v(T)$  is  $10^{-2}$ , (or alternatively choose a relative precision on  $C_v(T)$  of  $10^{-3}$ ).

**End-to-end computational workflow** The inputs to the problem are the coupling parameters of the Fermi-Hubbard model and the required precision on the observables.

A pseudo-code describing this procedure is provided below.

```
for T : 1 to 200, step dT = 10
  for chi : 0.5 to 20, step dchi = 0.5
    for f : .1 to 1, step df = 0.1
      (alternatively, loop over mu, mu=0... 100, dmu=1)
        # Set Hamiltonian (alternatively, with chemical potential)
        # Set Hilbert space with fixed number of electrons filling
        (skip this step with chemical potential)
        # Find thermal state
          - Evaluate C1, C2 parameter up to prescribed precision
            (with chemical potential, report average electron filling)
          Is it nonzero?
            yes -> potential superconducting phase
            no -> continue
          - Evaluate AFM order parameter
            # Is it AFM?
            yes -> return
            no -> continue
          - Evaluate Cv
            Does Cv scale as T?
              -> Fermi liquid?
            Does it scale as T^alpha, alpha>1?
              -> Strange metal
          - (Optional: calculate the pseudogap parameter A)
        end
      end
    end
  end
```

In typical applications, if a critical line is observed in a particular interval, precision in  $df$  is increased and centered around the critical line by a factor or ten or more, e.g.  $df = 0.01$ . Note that the loop on the in electron filling can be replaced by a loop on the chemical potential  $\mu$  as described earlier.

# High-temperature superconductivity and exotic properties of Fermi-Hubbard models

**Concrete problem instantiations** This workflow is applicable to all Hamiltonians described in Section 5.4.

## 5.4 Models instantiations

### 5.4.1 Two dimensional lattice models

The specific instance of interest is a low-electron filling superconductor model in 2-dimensions (lattice crystal) that was recently studied [467] but has been known for years [11] for the model of eqn. (22) with  $U=8t$  and at  $f = 1/8$ . A stripe phase was observed with different methods

$$H = -t \sum_{ij,\sigma} (\hat{c}_{i\sigma}^\dagger \hat{c}_{j\sigma} + \hat{c}_{j\sigma}^\dagger \hat{c}_{i\sigma}) + U \sum_i n_{i+} n_{i-} \quad (47)$$

for  $U = 8t$  and at  $1/8$  electron filling. Thus, for this particular instantiation, the parameter scan over  $f$  and  $\chi$  is omitted in the application boxes.

The Hamiltonian of interest is [213] for a 2-dimensional lattice

$$\hat{H} = - \sum_{(i,j)} \sum_{\sigma=\pm} t_{ij} c_{i\sigma}^\dagger c_{j,\sigma} + U \sum_i c_{i+}^\dagger c_{i-}^\dagger c_{i-} c_{i+} \quad (48)$$

with  $t_{ij} = t_{ij}^* = t \delta_{|\vec{i}-\vec{j}|,1}$ .

**Hamiltonian in momentum space** A similar phase diagram can be studied also for other models, in particular with different parametrizations and dimensionalities. A case of interest is given by the Hamiltonian on a 2-dimensional lattice written in Fourier space [303, 474], with the sum over  $i, j$  between 0 and  $L - 1$ , where  $L$  is the lattice size,  $\vec{k}(i, j) = (\frac{2\pi}{L}i, \frac{2\pi}{L}j)$ .<sup>3</sup> Then, the sum  $\sum_{\vec{k}} = \sum_{i,j=0}^{L-1}$ , and

$$H = \sum_{\vec{k},\sigma} \xi_{\vec{k}} d_{\vec{k},\sigma}^\dagger d_{\vec{k},\sigma} + \sum_{\vec{k}} (\Delta_{\vec{k}} d_{\vec{k},+}^\dagger d_{\vec{k},-}^\dagger + h.c.) \quad (49)$$

with

$$\begin{aligned} \xi_{\vec{k}} &= -2t_1(\cos k_x + \cos k_y) - 4t_2 \cos k_x \cos k_y - 2t_3(\cos 2k_x + \cos 2k_y) \\ &+ -4t_4(\cos 2k_x \cos k_y + \cos k_x \cos 2k_y) - 4t_5 \cos 2k_x \cos 2k_y - \mu \end{aligned} \quad (50)$$

with  $t_1 = 1$ ,  $t_2 = -0.2749$ ,  $t_3 = 0.0872$ ,  $t_4 = 0.0938$ ,  $t_5 = -0.0857$ ,  $\mu = -0.8772$ , and

$$\Delta_{\vec{k}} = \frac{\Delta_0}{2}(\cos k_x - \cos k_y) \quad (51)$$

with  $\Delta_0 = 0.1$ . The asymmetry between the x and y direction is due to the fact that the square lattice Hamiltonian is inherited from an original orthorombic symmetry [303], and in real space such asymmetry is shown Fig. 5-6. The quadratic Hamiltonian above can be converted to a full-

<sup>3</sup>In the Bogoliubov-de Gennes approximation, the linear size of the lattice can be also 100 or multiples thereof. However, when the quartic interactions are present, the state of the art of the literature is between 16-20 spins in total.

# High-temperature superconductivity and exotic properties of Fermi-Hubbard models

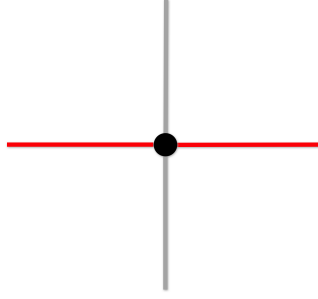


Figure 5-6: Asymmetry in the couplings along the x- and y- direction of eqn. (49).

fledged Fermi-Hubbard model by keeping the kinetic term identical term, and adding an interaction term:

$$H = \sum_{\vec{k}, \sigma} \xi_{\vec{k}} d_{\vec{k}, \sigma}^{\dagger} d_{\vec{k}, \sigma} + \frac{U}{L} \sum_{\vec{k}, \vec{k}', \vec{q}} d_{\vec{k}+\vec{q}, +}^{\dagger} d_{\vec{k}'-\vec{q}, -}^{\dagger} d_{\vec{k}', -} d_{\vec{k}, +} \quad (52)$$

This Hamiltonian has to be scanned in the parameter  $U$ .

**Graphene-based examples** We also report the graphene-based model in 2d [209] with a non-standard 2d lattice.

$$H = H_{TB} + U \sum_i n_{i+} n_{i-} \quad (53)$$

with  $U \approx 10$  eV, while

$$H_{TB} = -t_1 \sum_{\langle i, j \rangle, \sigma} (c_{i\sigma}^{\dagger} c_{j\sigma} + h.c.) \quad (54)$$

$$-t_2 \sum_{\langle i, j \rangle, \sigma} (c_{i\sigma}^{\dagger} c_{j\sigma} + h.c.) \quad (55)$$

where the first and second sum is intrasquare NN and intersquare NN hopping, with  $t_1 \approx 2.5$  eV while  $t_2 \approx 2.9$  eV, and  $U = 10$  eV. The lattice is shown in Fig. 5-7, with  $t_1$  for the black bonds and  $t_2$  for the red bonds.

## 5.4.2 Two band superconductivity via transverse Ising mapping

Although for the following example a set of parameters was not found which can be used to model a real material, we would like to point out a mapping in the strong coupling limit of a two band Fermi-Hubbard model to a transverse quantum Ising model [427]. The original Hamiltonian is a two-band model of the form

$$H = H_2 + H_4 \quad (56)$$

$$H_2 = \sum_{ij, \sigma} \left( (t_{ij}^c - \mu^c \delta_{ij}) c_{i\sigma}^{\dagger} c_{j\sigma} + (t_{ij}^d - \mu^d \delta_{ij}) d_{i\sigma}^{\dagger} d_{i\sigma} \right) \quad (57)$$

$$H_4 = \sum_{i, \sigma, \sigma'} \left( U_1 c_{i\sigma}^{\dagger} c_{i\sigma} d_{i\sigma'}^{\dagger} + \frac{U_2}{2} c_{i\sigma}^{\dagger} c_{i\sigma'}^{\dagger} d_{i\sigma} d_{i\sigma'} + h.c. \right) \quad (58)$$

## High-temperature superconductivity and exotic properties of Fermi-Hubbard models

where the operators  $c_{i\sigma}$  and  $d_{i\sigma}$  are ladder operators between electrons in bands  $c$  and  $d$  of a square lattice  $i$  with spin  $\sigma$ . The parameters  $U_1$  represents inter-band repulsion energy, while  $U_3$  is a pair hopping energy. In the strong coupling limit and for a particular choice of parameters  $U_1 = 4U(1 - \delta_{\sigma\sigma'})$ , and  $U_3 = 4U$  this model is interesting because it can be studied via QMC *without* sign problem. Also, the model can be mapped to a so called  $J_1$ - $J_2$  quantum Ising Hamiltonian of the form with a homogeneous transverse field if the  $\mu$ 's are homogeneous (after a rotation)

$$H = \sum_{ij} J_{ij} \sigma_i^z \sigma_j^z - h \sum_i \sigma_i^x \quad (59)$$

where  $h = \frac{(\mu^c - \mu)^2}{8U}$  and  $J_x = \frac{t_1^c t_1^d}{3U}$  and  $J_y = \frac{t_2^c t_2^d}{3U}$  where  $t_1$  represents horizontal couplings  $t_{ij}$  while  $t_2$  vertical couplings. QMC investigations has shown that this model has a paramagnetic to Neél transition. From a computational methodological perspective, the interesting properties of this model is the phase space in the plane  $a = h/J_2$  and  $b = J_1/J_2$  at zero temperature, and in three dimensions including temperature. The input is thus a Hamiltonian without well defined parameters but at zero temperature. One can either fix the electron filling or scan it. Contrarily to the previous examples, this is a case that can be studied efficiently using Quantum Monte Carlo [156]. Although Monte Carlo methods can be used in this case, in principle *the bottleneck of MC is the generation of random number and samples*. Interestingly, the problem of eqn. (59) can be studied using the current family of Ising annealers provided by D-Wave that can generate samples from the Hamiltonian of Eqn. (59).

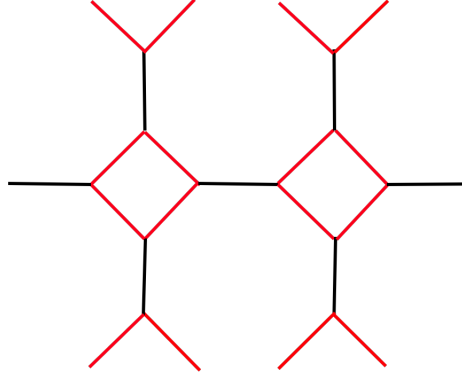


Figure 5-7: The lattice considered in graphene-based superconductors of [209].

### 5.4.3 Iron-based models

Aside from cuprates, there has been also interest in iron-based superconductors. The Hamiltonians presented below are obtained via the Slater-Koster approximation, with the extra parameters fitting experimentally observed Fermi surfaces. These are considered models of superconductivity, for which multi-orbital methods are needed. There are indications that the five 3d orbitals of the Fe should be included in a realistic model. A detailed analysis of the many possible hopping channels for electrons when only the two orbitals  $d_{xz}$  and  $d_{yz}$  are involved in the process, investigations based on the Slater-Koster approximation led to the construction of a tight-binding model Hamiltonian for this case [98].

# High-temperature superconductivity and exotic properties of Fermi-Hubbard models

The hamiltonian involves with only the  $3d_{xz}$  and  $3d_{yz}$  orbitals is given by the two-dimensional Hamiltonian shown in Fig. 5-8. The operators  $d_{i,\alpha,\sigma}^\dagger$  is a fermionic ladder operator which creates an electron at site  $i$  of the lattice, at the orbital  $\alpha$ , with spin (projection on the  $z$ -axis)  $\sigma$ . The hopping is both between nearest-neighbor (NN) atoms, and along the plaquette diagonals (NNN) [100].

The Hamiltonian is shown in Fig. 5-8 (top). The parameters fit using experimental data are  $t_1 = -1.0$ ,  $t_2 = 1.3$ ,  $t_3 = t_4 = -0.85$  in electronvolt units.

$$\begin{aligned}
H^{xz,yz} = & -t_1 \sum_{i,\sigma} (d_{i,x,\sigma}^\dagger d_{i+\hat{y},x,\sigma} + d_{i,y,\sigma}^\dagger d_{i+\hat{x},y,\sigma} + h.c.) \\
& -t_2 \sum_{i,\sigma} (d_{i,x,\sigma}^\dagger d_{i+\hat{x},x,\sigma} + d_{i,y,\sigma}^\dagger d_{i+\hat{y},y,\sigma} + h.c.) \\
& -t_3 \sum_{i,\hat{\mu},\hat{\nu},\sigma} (d_{i,x,\sigma}^\dagger d_{i+\hat{\mu}+\hat{\nu},x,\sigma} + d_{i,y,\sigma}^\dagger d_{i+\hat{\mu}+\hat{\nu},y,\sigma} + h.c.) \\
& +t_4 \sum_{i,\sigma} (d_{i,x,\sigma}^\dagger d_{i+\hat{x}+\hat{y},y,\sigma} + d_{i,y,\sigma}^\dagger d_{i+\hat{x}+\hat{y},x,\sigma} + h.c.) \\
& -t_4 \sum_{i,\sigma} (d_{i,x,\sigma}^\dagger d_{i+\hat{x}-\hat{y},y,\sigma} + d_{i,y,\sigma}^\dagger d_{i+\hat{x}-\hat{y},x,\sigma} + h.c.) \\
& -\mu \sum_i (n_i^x + n_i^y) \\
H^{xz,yz,xy} = & -t_7 \sum_{i,\sigma} [(-1)^{|i|} d_{i,xz,\sigma}^\dagger d_{i+\hat{x},xy,\sigma} + H.c.] - t_7 \sum_{i,\sigma} [(-1)^{|i|} d_{i,xy,\sigma}^\dagger d_{i+\hat{x},xz,\sigma} + H.c.] - t_7 \sum_{i,\sigma} [(-1)^{|i|} d_{i,yz,\sigma}^\dagger d_{i+\hat{y},xy,\sigma} + H.c.] \\
& -t_7 \sum_{i,\sigma} [(-1)^{|i|} d_{i,xy,\sigma}^\dagger d_{i+\hat{y},yz,\sigma} + H.c.] - t_8 \sum_{i,\sigma} [(-1)^{|i|} d_{i,xz,\sigma}^\dagger d_{i+\hat{x}+\hat{y},xy,\sigma} + H.c.] + t_8 \sum_{i,\sigma} [(-1)^{|i|} d_{i,xy,\sigma}^\dagger d_{i+\hat{x}+\hat{y},xz,\sigma} + H.c.] \\
& -t_8 \sum_{i,\sigma} [(-1)^{|i|} d_{i,xz,\sigma}^\dagger d_{i+\hat{x}-\hat{y},xy,\sigma} + H.c.] + t_8 \sum_{i,\sigma} [(-1)^{|i|} d_{i,xy,\sigma}^\dagger d_{i+\hat{x}-\hat{y},xz,y\sigma} + H.c.] - t_8 \sum_{i,\sigma} [(-1)^{|i|} d_{i,yz,\sigma}^\dagger d_{i+\hat{x}+\hat{y},xy,\sigma} + H.c.] \\
& + t_8 \sum_{i,\sigma} [(-1)^{|i|} d_{i,xy,\sigma}^\dagger d_{i+\hat{x}+\hat{y},yz,\sigma} + H.c.] + t_8 \sum_{i,\sigma} [(-1)^{|i|} d_{i,yz,\sigma}^\dagger d_{i+\hat{x}-\hat{y},xy,\sigma} + H.c.] - t_8 \sum_{i,\sigma} [(-1)^{|i|} d_{i,xy,\sigma}^\dagger d_{i+\hat{x}-\hat{y},yz,\sigma} + H.c.].
\end{aligned}$$

Figure 5-8: The 2- and 3- orbital Hamiltonians of Dagotto et al. [100].

**List of other candidate instances** A three orbital generalization of the two orbital model is presented in Fig. 5-8 (bottom) with  $t_1 = 0.02$ ,  $t_2 = 0.06$ ,  $t_3 = 0.03$ ,  $t_4 = 0.01$ ,  $t_5 = 0.2$ ,  $t_6 = 0.3$ ,  $t_7 = 0.2$ ,  $t_8 = -0.1$ , with all the parameters in eV. In this case, the orbitals  $d_{xz}$ ,  $d_{yz}$  and  $d_{xy}$  are involved in the hopping of the electrons.

In the case with five iron orbitals,  $3d_{xz}$ ,  $3d_{yz}$ ,  $3d_{x^2-y^2}$ ,  $3d_{xy}$ , and  $3d_{3z^2-r^2}$  a Hamiltonian of the type  $t - J_1 - J_2$  has been studied in [454], and obtained via an expansion of the five-orbital Fermi-Hubbard model with respect to the Mott transition point [152].

## 5.5 Requirements summary

This section summarizes the application requirements for all the applications described in this chapter.



# High-temperature superconductivity and exotic properties of Fermi-Hubbard models

## **Application 1: Zero-Temperature Superconductivity**

<b>Workload:</b>	Total time limit	1 month
	Number of subroutine calls required	$40 \times 10$
	Maximum subroutine time limit	NA
<b>Problem specifications:</b>	Model type	Fermionic Hamiltonian
	Size	minimum $20 \times 20$ lattice sites $\times$ 1 orbital target $100 \times 100$ lattice sites $\times$ 3 orbitals
	Interaction Structure	Sparse regular (2-D NNN square lattice)
	Computational target	Superconducting order parameters
	Accuracy requirement	minimum $10^{-3}$ , target $10^{-5}$

## **Application 2: High-temperature Superconductivity**

<b>Workload:</b>	Total time limit	1.5 month
	Number of subroutine calls required	$40 \times 10 \times 20$
	Maximum subroutine time limit	NA
<b>Problem specifications:</b>	Model type	Fermionic Hamiltonian
	Size	minimum $20 \times 20$ lattice sites $\times$ 1 orbital target $100 \times 100$ lattice sites $\times$ 3 orbitals
	Interaction Structure	Sparse regular (2-D NNN square lattice)
	Computational target	Superconducting order parameters
	Accuracy requirement	minimum $10^{-3}$ , target $10^{-5}$

# High-temperature superconductivity and exotic properties of Fermi-Hubbard models

## Application 3: Phase-Diagram of Fermi-Hubbard Models

<b>Workload:</b>	Total time limit	2 month
	Number of subroutine calls required	$40 \times 10 \times 20$
	Maximum subroutine time limit	NA
<b>Problem specifications:</b>	Model type	Fermionic Hamiltonian
	Size	minimum $20 \times 20$ lattice sites $\times$ 1 orbital target $100 \times 100$ lattice sites $\times$ 3 orbitals
	Interaction Structure	Sparse regular (2-D NNN square lattice)
	Computational target	Superconducting order parameters Specific heat scaling coefficient Mean staggered magnetization
	Accuracy requirement	minimum $10^{-3}$ , target $10^{-5}$

# High-temperature superconductivity and exotic properties of Fermi-Hubbard models

## 5.6 Supplementary material for Fermi-Hubbard models

### 5.6.1 More on the underlying Fermi-Hubbard

Let us mention some details on the derivation of the Fermi-Hubbard model of the main text. First of all, let us stress that the shortcomings of the tight-binding Hamiltonian is that this is only an approximation to the full problem, as this section shows. At the end of several of these approximations, one is left with a final many-body problem of the form

$$\left( -\frac{\hbar^2}{2m_e} \nabla_i^2 - \sum_{i,a} \frac{Z_a e^2}{|r_i - R_a|} + \frac{1}{2} \sum_{ij} \frac{e^2}{|r_i - r_j|} \right) \Psi_\alpha(\{r_i\}; \{R_a\}) = E_\alpha \Psi_\alpha(\{r_i\}; \{R_a\}) \quad (60)$$

where one uses the fact that the momentum operators become coordinate derivatives, and  $\Psi_\alpha(\{r_i\}; \{R_a\})$  is a fully symmetrized wave-function for the many-body problem. A common approach to solve it, is to use the Kohn-Sham density functional method, which is known to work well for static problems, but not for dynamic ones. To derive the Fermi-Hubbard model, one has to write the wavefunction in a second quantization scheme:

$$\mathcal{H} = \int dx \hat{\psi}^\dagger(x) \sum_i h_i(x) \hat{\psi}(x) + \frac{1}{2} \int dx dy \hat{\psi}^\dagger(x) \hat{\psi}^\dagger(y) v(x, y) \hat{\psi}(x) \hat{\psi}(y) \quad (61)$$

where

$$h_i(x) = -\frac{\hbar^2}{2m_e} \nabla_i^2 - \sum_a \frac{Z_a e^2}{|r_i - R_a|} \quad (62)$$

$$v(x, y) = \sum_{ij} \frac{e^2}{|r_i - r_j|} \quad (63)$$

It is very hard to study the continuous Hamiltonian if not using renormalization group method. This method is typically applied to strongly correlated systems to study the low-energy behavior of the Hamiltonian, directly at the level of the second quantized Hamiltonian of eqn. (61). Analytical techniques encompass both perturbative and functional techniques and require a parametrization of the Fermi surface [283] and nonetheless the integration of differential equations for the flow [46, 239].

The field operators are chosen to be the one of an electron gas (jellium model), e.g.

$$\psi_\sigma(r) = \frac{1}{\sqrt{L}} \sum_{\vec{k}} e^{i\vec{k} \cdot \vec{r}} \hat{c}_{\vec{k}, \sigma} \quad (64)$$

where  $\hat{c}_{\vec{k}, \sigma}, \hat{c}_{\vec{k}, \sigma}^\dagger$  are the creation operators of a plane wave. However, For a solid, the wavefunctions are written in terms of localized orbitals,

$$\psi_\sigma = \sum_a \phi(\vec{r} - \vec{R}_a) c_{a\sigma} \quad (65)$$

where  $\phi(\vec{r} - \vec{R}_a)$  are the localized orbitals for the atom at site  $a$ . Inserting this expression into the second quantized Hamiltonian, we get the Fermi Hubbard Hamiltonian of the main text, eqn ( 24).

# High-temperature superconductivity and exotic properties of Fermi-Hubbard models

## 5.6.2 Methods to derive the parameters of the Fermi-Hubbard models

In the main text we have mentioned fitting the Fermi surface via ARPES as a method to estimate the parameters. Another way of deriving the Fermi-Hubbard parameters is by performing the integrals knowing the lattice structure. There are various methods to do this. We briefly mention the Wannier functions and the Slater-Koster methods.

Wannier functions play an important role in the derivation of the hopping parameters for the Fermi-Hubbard model [279]. The Bloch theorem in solid state physics establishes that in a periodic potential, the wave function describing an electron can be written as a product of a periodic function and a plane wave [223, 12]. Their computational complexity can vary depending on the size of the basis set and the system under consideration. Often linear or slightly superlinear scaling with the number of basis functions or atoms ( $N$ ). Wannier functions are derived from Bloch states through a transformation, are localized electron wave functions (over one or more lattice sites to mimic hybridization).

The Wannier functions are used of an isolated band is defined as

$$w_n(\vec{r} - \vec{R}) = \frac{V}{(2\pi)^d} \int_{BZ} \int d^d k e^{-i\vec{k} \cdot \vec{R}} \psi_{n,k}(\vec{r}) \quad (66)$$

where  $\psi_{n,k}(\vec{r})$  are the localized Bloch functions, and BZ stands for Brillouin zone. Although it is not immediately obvious, it is important for what follows that Wannier functions are localized. For instance, see Fig. 5-3 for the cuprates. The overlap of the orbital  $3d$  and  $2p$  for copper and oxygen leads to a non-zero hopping  $t_{ij}$  between these two atoms. Let us briefly list the existing numerical methods that allow to construct the Wannier function. A method related to Wannier wavefunctions described above is the Maximally Localized Wannier Functions, whose aim is to maximize the localization of Wannier functions by minimizing the spread of the functions in real space [279]. The computational complexity can vary based on the algorithm used for optimization, based on the minimisation of the Marzari-Vanderbilt quadratic spread functional, often involving iterative optimization schemes. The computational complexity depends on the grid size and the accuracy required. Typically cubic scaling with the number of grid points or spatial resolution ( $N^3$ ) [418]. In scenarios where the Wannier functions are fewer than the Bloch bands there are entangled bands due to intricate mixing of electronic states [390]; in these case, some methods that work specifically for this case.

The Projector Augmented Wave (PAW) Method is an approach used in ab initio methods like density functional theory (DFT) to construct Wannier functions [35]. It involves the projection of Bloch functions onto atomic-like functions, which helps in obtaining localized Wannier functions. From a complexity standpoint, the scaling is often quadratic or slightly higher than linear, with respect to the number of atoms or basis functions.

There exist several software packages used to perform the calculations related to Wannier functions, facilitating the construction and analysis of these fundamental electronic states in solid-state materials. Wannier90 [290] is still the primary software designed explicitly for computing Wannier functions. Its functionality extends to interfacing with various electronic structure codes like Quantum ESPRESSO [145], VASP (Vienna Ab initio Simulation Package) [160], ABINIT [354], CRYSTAL [48], SIESTA [389], and OpenMolcas [9]. Among these first-principles codes, Quantum ESPRESSO is widely used and is known for its capabilities in electronic structure calculations.

The Slater-Koster approximation (or tight-binding), is a method used in solid-state physics to describe the electronic structure and properties of crystalline materials [310]. It is a simplified yet effective way to calculate the electronic band structure and electronic properties of a crystal

# High-temperature superconductivity and exotic properties of Fermi-Hubbard models

based on the interactions between neighboring atoms. In the Slater-Koster approximation, the electronic wavefunctions are expressed as linear combinations of atomic orbitals (LCAO) localized on individual atoms. To overcome the computational constraints, they proposed treating these integrals as adjustable parameters, to be determined based on results obtained from other, more efficient calculations. Similarly to the Wannier function method described above, the Slater-Koster approximation assumes that the interactions between atoms are predominantly due to the overlap of atomic orbitals and neglects other effects such as long-range electrostatic interactions. It provides a computationally efficient approach to calculate the electronic band structure and other electronic properties of materials. The method is used in one of the applications described below as a method to derive the hopping terms of the Hamiltonian of a Fermi-Hubbard model. The general form of the Hamiltonian matrix elements in the Slater-Koster approximation can be written as:

$$t_{ij}(\mathbf{k}) = \sum_{\mathbf{R}} e^{i\mathbf{k}\cdot\mathbf{R}} \sum_{\mu,\nu} [V_{\mu\nu}(\mathbf{R})S_{\mu\nu}(\mathbf{R}) + W_{\mu\nu}(\mathbf{R})] \quad (67)$$

In the equation above,  $t_{ij}(\mathbf{k})$  represents the matrix element between orbitals of the sites  $i$  and  $j$ , at wavevector  $\mathbf{k}$ . The sum over  $\mathbf{R}$  runs over the lattice vectors of the crystal, and  $e^{i\mathbf{k}\cdot\mathbf{R}}$  accounts for the phase factors associated with the periodicity of the crystal lattice. The terms  $V_{\mu\nu}(\mathbf{R})$  and  $W_{\mu\nu}(\mathbf{R})$  represent the overlap and exchange integrals, respectively. They depend on the specific form of the atomic orbitals  $\mu$  and  $\nu$  at atomic sites separated by the lattice vector  $\mathbf{R}$ . The overlap integral  $S_{\mu\nu}(\mathbf{R})$  quantifies the overlap between the orbitals.

The empirical parameters  $V_{\mu\nu}(\mathbf{R})$  and  $W_{\mu\nu}(\mathbf{R})$  in the Slater-Koster approximation are obtained through fitting to experimental data or other theoretical calculations. These parameters capture the essence of the orbital interactions and depend on the specific elements and crystal structure under consideration.

### 5.6.3 Numerical methods used to study the Fermi-Hubbard model

The study of Fermi-Hubbard hamiltonians is, as often for the case of quantum many body systems, plagued by the growth of the Hilbert space with the number of sites. Although there are a few mean field techniques mentioned below, exact analytical solutions can hardly be used in any realistic situation, except in 1D for a single band using the Bethe ansatz [257, 122, 136, 143], where it is known that the Mott transition is absent. Then, it is often necessary to use computational algorithms to study the behavior of the model [38]. Analytical methods are available in certain parameter regimes (see below).

- **Exact Diagonalization:** This method involves numerically diagonalizing the Hamiltonian matrix for small system sizes. For a system with  $N$  states or orbitals, the computational effort scales as  $O(N^3)$  for a dense matrix representation. However, in practice, the exact diagonalization method can become computationally expensive for large systems, because the size  $N$  of the Hamiltonian matrix grows exponentially with the number of sites. To mitigate this issue, various techniques such as Lanczos algorithm can be used to reduce the size of the Hamiltonian matrix and make the diagonalization process more efficient. The Lanczos algorithm starts with an initial vector  $\mathbf{v}_1$ , which is chosen randomly or with some prior knowledge about the system being studied. The first Krylov vector is then defined as  $\mathbf{w}_1 = \mathbf{H}\mathbf{v}_1$ , where  $\mathbf{H}$  is the matrix to be diagonalized. The Lanczos process then proceeds recursively as follows: a) Normalize the Krylov vector:  $\mathbf{v}_{k+1} = \frac{\mathbf{w}_k}{|\mathbf{w}_k|}$ . b) Apply the matrix to the Krylov

## High-temperature superconductivity and exotic properties of Fermi-Hubbard models

vector:  $\mathbf{w}_{k+1} = \mathbf{H}\mathbf{v}_{k+1}$ . c) Orthogonalize the new Krylov vector with respect to the previous ones:  $\mathbf{w}_{k+1} = \mathbf{w}_{k+1} - \sum_{i=1}^k \langle \mathbf{w}_{k+1} | \mathbf{v}_i \rangle \mathbf{v}_i$ . At each iteration, the resulting Krylov vectors form an orthonormal basis set of the Krylov subspace, which is a small subspace of the full vector space spanned by the original matrix. The Lanczos process can be truncated after a certain number of iterations or when the Krylov vectors stop improving the approximation to the eigenvalues. Once the Krylov subspace has been constructed, the matrix can be diagonalized using a smaller dense matrix that represents the matrix in this subspace.

- **Monte Carlo methods.** There are many Quantum Monte Carlo (QMC) methods, of which a few we list below. From a computational perspective, the issue with QMC is the so called sign problem which makes the convergence of the method very slow. *Variational Monte Quantum Carlo.* The Variational Quantum Monte Carlo (VQMC) algorithm involves the use of a trial wave function (WF) and the estimation of the expectation value of the energy of a quantum many body system. The algorithm involves the use of a trial WF  $|\Psi_T(\alpha)\rangle$ , the evaluation of the expectation Value of Energy via  $\langle E \rangle = \frac{\langle \Psi_T | H | \Psi_T \rangle}{\langle \Psi_T | \Psi_T \rangle}$  and then Monte Carlo sampling  $\langle O \rangle \approx \frac{1}{N} \sum_{i=1}^N O(x_i)$ . The key idea behind VQMC is to optimize the parameters of the trial wave function to minimize  $\langle E \rangle$  and consequently obtain an approximation to the ground state energy of the quantum system. This method can be used, for instance, for ground state preparation. The scaling behavior can range from linear to polynomial, depending on the complexity and quality of the trial wave function and the system being studied. *Quantum Monte Carlo (QMC) Methods.* For fermionic models, there are specific methods that take advantage of constraints due to properties of fermions in the partition function. We mention in particular the work [461] which is commonly used for strongly correlated fermions. *Continuous-time Quantum Monte Carlo (CTQMC):* This is an efficient method for studying equilibrium properties at finite temperatures [358] when the sign problem is absent, which is true for particular choices of parameters. *Auxiliary Field Quantum Monte Carlo (AFQMC)* is also particularly useful for ground state properties of the Fermi-Hubbard model. AFQMC is used to simulate systems with fermionic degrees of freedom by introducing auxiliary fields to represent the interaction terms (via the so called Hubbard-Stratonovich transformation). It involves decomposing the interactions into auxiliary fields and transforming the fermionic problem into a simpler bosonic problem [34]. *Determinantal Quantum Monte Carlo (DMC)* is a quantum Monte Carlo method specifically designed for systems of interacting fermions [62]. DMC represents the many-body wave function in terms of Slater determinants, which describe the configuration of occupied single-particle orbitals for fermions. These determinants capture the antisymmetric nature of fermionic wave functions. It involves an imaginary-time propagation of the system starting from a trial wave function. The system's ground state is approached by simulating the time evolution of the wave function in imaginary time using the Schrödinger equation. DMC employs importance sampling, another Monte Carlo technique, to sample configurations of particles according to their contributions to the total energy, focusing on more relevant configurations.
- **Analytical techniques and Mean-Field Theories.** Mean field theory has been very useful in analyzing the behavior of the Fermi-Hubbard model. The *Hartree-Fock Approximation* Simplifies the many-body problem by assuming a mean-field description of interactions for the terms of the form  $\hat{n}_i \hat{n}_j$  which are composed of four ladder operators, while keeping the rotational spin symmetry preserved and turning it effectively into a free (quadratic) model. HF is

## High-temperature superconductivity and exotic properties of Fermi-Hubbard models

often utilized as a starting point to describe the electronic band structure [124]. This method, which is analytical, is often used to infer the location of the transitions between paramagnetic, antiferromagnetic and ferromagnetic phases [317]. This method can be extended to study also dynamical mean fields to study the Mott transition [419, 314]. Also, another method is the Cellular dynamical mean-field theory (CDMFT) [236] which is obtained by including in the cluster Hamiltonian an external bath of uncorrelated electrons that mimics the rest of the lattice. The *Gutzwiller Approximation* introduces a variational wave function by projecting from a product state. The general idea behind the Gutzwiller and derivative methods is that electronic correlations impose constraints on reachable Hilbert space. this is particularly true in the Fermi-Hubbard model at large values of  $U$ , with the double occupations on the lattice sites suppressed. This method can be used to study the Fermi-liquid regime, and there are methods to extend it at finite  $U$  [235]. *Peculiar limits.* The behavior of the Fermi-Hubbard model can analyzed analytical in certain limits, for instance when  $U = 0$  we have a Fermi gas, and for  $t/U$  small [144].

- **Density Matrix Renormalization Group (DMRG)** Originally developed for 1D systems, DMRG is powerful for studying ground states and low-energy excitations of the Fermi-Hubbard model in one dimension [432]. DMRG can be used for capturing the ground state properties, low-energy excitations, and correlation functions of one-dimensional strongly correlated quantum systems. In DMRG, tensor networks play a crucial role in representing quantum states of many-body systems. The tensor network representation in DMRG, often in the form of Matrix Product States (MPS), provides an efficient way to encode and manipulate quantum states, particularly in one-dimensional systems. Leveraging on the Matrix Product States (MPS) representation, DMRG efficiently encodes intricate entanglement structures and correlations between particles within these 1D arrangements. The model is hardly usable beyond 2D, but in two dimensions it can be used in a variety of contexts [433]. DMRG's computational cost typically scales polynomially or sub-exponentially with the system size for one-dimensional systems. Specifically, it often exhibits a scaling of  $O(m^3 \cdot n)$  or  $O(m^3 \cdot n^2)$ , where  $m$  is the number of states kept in the matrix product state (MPS) approximation and  $n$  is the number of lattice sites. Another way of seeing this is that it scales linearly with the number of sites and in the number of tensorial legs. Thus, the method is efficient in 1D (2 legs) and in 2D the method can be reduced, using an approximation, to a 1D model (2 legs), while in principle one should use a 4 legged tensor representation.

As an example of how some of these methods are employed, let us consider the Fermi liquid theory. Parameters like the quasiparticle weight  $Z$  or the effective mass of the particles near the Fermi surface  $m^*$  serve as indicators of this phase, which follows Landau's theory of Fermi liquids. In numerical experiments and analytical methods, there are various methods that can be used to estimate these order parameters. For instance, in Dynamical Mean-Field Theory (DMFT) and in the Numerical Renormalization Group (NRG), the self-energy is evaluated directly  $\Sigma(\mathbf{k}, \omega)$ , which is the self-energy, describing the energy shift and damping of a quasiparticle excitation at momentum  $\mathbf{k}$  and frequency  $\omega$ . Quantum Monte Carlo (QMC) methods directly compute spectral functions, revealing information on the residue at the Fermi level, and therefore  $Z$  can be evaluated. In Density Matrix Renormalization Group (DMRG) calculations, especially in finite-size systems, provide spectral information near the Fermi surface, giving indications of  $Z$  and the effective mass renormalization. For the case of Exact Diagonalization (ED) techniques, applicable to smaller systems, the green function can be calculated via matrix inversion.

# High-temperature superconductivity and exotic properties of Fermi-Hubbard models

## 5.6.4 D-Wave superconductivity

D-Wave superconductivity is a modulation of the order parameter  $\langle \Delta_{ij} \rangle$ . To express the order parameter  $\Delta_{ij}$  in terms of momentum space variables  $k$ , we can first Fourier transform the lattice site indices  $i$  and  $j$ . We assume a simple square lattice for clarity. In the case of square lattice, we have  $i = (i_x, i_y)$  and  $j = (j_x, j_y)$ . The lattice constant is denoted by  $a$ . Then, the Fourier transform of the order parameter  $\Delta_{ij}$  is given by:

$$\langle \Delta(\mathbf{k}) \rangle = \sum_{i,j} e^{-i\mathbf{k} \cdot (\mathbf{R}_i - \mathbf{R}_j)} \langle \Delta_{ij} \rangle$$

where  $\mathbf{R}_i$  and  $\mathbf{R}_j$  are the position vectors corresponding respectively to lattice sites  $i$  and  $j$ , respectively, and  $\mathbf{k}$  is the momentum vector.

In momentum space, the lattice vectors are given by

$$\mathbf{R}_i = i_x \mathbf{a}_x + i_y \mathbf{a}_y$$

where  $\mathbf{a}_x$  and  $\mathbf{a}_y$  are the primitive lattice vectors.

Now we can substitute  $i$  and  $j$  into the Fourier transform expression:

$$\Delta(\mathbf{k}) = \sum_{i_x, i_y, j_x, j_y} e^{-i\mathbf{k} \cdot ((i_x - j_x)\mathbf{a}_x + (i_y - j_y)\mathbf{a}_y)} \Delta_{i_x, i_y, j_x, j_y}$$

We can express  $i$  and  $j$  in terms of momentum space variables. The momentum components  $k_x$  and  $k_y$  are related to the lattice vectors by  $k_x = \frac{2\pi}{a} n_x$  and  $k_y = \frac{2\pi}{a} n_y$ , where  $n_x$  and  $n_y$  are integers. Therefore, we can rewrite the sum as integrals over the Brillouin zone:

$$\Delta(\mathbf{k}) = \sum_{n_x, n_y} e^{-i\mathbf{k} \cdot ((n_x - n'_x)\mathbf{a}_x + (n_y - n'_y)\mathbf{a}_y)} \Delta_{n_x, n_y, n'_x, n'_y}$$

Now, to get the expression for  $\Delta(\mathbf{k})$ , we need to evaluate the sum over  $n_x$  and  $n_y$ , which will involve the lattice geometry and the specific form of  $\Delta_{ij}$ . The result will be a function of  $\mathbf{k}$ , giving us  $\Delta(\mathbf{k})$ , the Fourier transform of the order parameter.

D-Wave superconductivity is observed if  $\langle \Delta(\mathbf{k}) \rangle$  is modulated, e.g.

$$\langle \Delta(\mathbf{k}) \rangle = \Delta_0 (\cos(k_x a) - \sin(k_y a)), \quad (68)$$

where  $a$  is the lattice spacing, for a certain value  $\Delta_0$  which sets the energy scale.

## 5.6.5 Statics vs Dynamics in superconductivity

It is important to stress that conductivity is a dynamical and not static quantity. The phase diagram of the Fermi-Hubbard model provides indications of the physical states, via correlations, of the material. However, the key quantities that would be preferred to be studied in the context of conductors are dynamical quantities, such as the conductivity tensor, which we discuss briefly below in the context of FH for simplicity.

In the Fermi-Hubbard model, the current operator  $J_\alpha$  along the  $\alpha$ -direction on a lattice can be expressed in terms of creation and annihilation operators for electrons hopping between neighboring lattice sites:



## High-temperature superconductivity and exotic properties of Fermi-Hubbard models

$$J_\alpha = -\frac{e}{\hbar} \sum_{\langle i,j \rangle, \sigma} t_{ij} e^{i\mathbf{k}_{ij} \cdot \mathbf{r}_{ij}} c_{i\sigma}^\dagger c_{j\sigma}$$

The operator above measures the flow of charge in the FH model. Above  $t_{ij}$  is the hopping amplitude between sites  $i$  and  $j$  that we defined in the main text,  $\mathbf{k}_{ij}$  is the wavevector connecting the two sites, and  $\mathbf{r}_{ij} = a(\mathbf{i} - \mathbf{j})$  is the vector displacement between them. The first thing to note is that the current is connected to the kinetic term of the FH model. In turn, the conductivity can be written in terms of the current operator via linear response [44]. The Kubo formula, derived from perturbation theory, provides a framework for understanding electrical conductivity in materials operationally. It relates the dynamics of electrons under the influence of an external electric field. The Kubo formula expresses the electrical conductivity tensor  $\sigma_{\alpha\beta}$  (conductivity along the direction  $\alpha$  and  $\beta$ ) as:

$$\sigma_{\alpha\beta} = \lim_{\omega \rightarrow 0} \frac{i}{\omega} \left( \frac{e^2}{V} \right) \int_0^\infty dt e^{i\omega t} \langle J_\alpha(t) J_\beta(0) \rangle$$

We see that the expression above is the time Fourier transform of the quantity

$$\tilde{\sigma}_{\alpha\beta}(t) = \langle J_\alpha(t) J_\beta(0) \rangle$$

Above,  $e$  is the elementary charge,  $V$  is the volume of the system ( $L^d$  in the case of a lattice), and  $\langle J_\alpha(t) J_\beta(0) \rangle$  is the current-current correlation function. We see that conductivity in principle requires the knowledge of the time-evolved current operator,  $U^\dagger(t) J_\alpha(0) U(t)$ . The limit  $\omega \rightarrow 0$  implies that one focuses on long times (or rather equilibrium), but are derived from a dynamical quantity. By substituting the expression for the current operator into the Kubo formula and evaluating the relevant correlation functions, one can in principle calculate the conductivity of the Fermi-Hubbard model system. For Fermi-Hubbard, the expression above provides ultimate insights into the interplay between electron hopping, on-site interactions. However, since quantity depends on the expectation values, the state of the system is a key indicator of how the system is behaving.

## 6 Computational catalysis for artificial photosynthesis

This chapter discusses the identification of optimal catalysts in artificial photosynthesis, focusing on enhancing the efficiency of water oxidation and carbon dioxide reduction reactions. The preliminary phase of catalyst selection requires determining the reaction pathway and leveraging computational capabilities to estimate the ground state energies, thereby calculating the reaction barrier. Present-day classical computers fall short of accurately solving the Hamiltonians that encompass complex static and dynamic electronic correlations within molecular systems with trade-offs between accuracy and numerical efficiency. In contrast, a quantum computer's distinct advantage lies in its ability to handle huge Hilbert space, potentially enabling precise estimations of ground state energy and beyond efficiently without sacrificing accuracy. Subsequently, quantum molecular dynamics are employed on a subset of catalysts to understand the reaction's dynamics and further optimize the catalysts. This includes propagating classical Newton's equations for nuclei with ground state energies and the forces (the gradient of energy with respect to nuclear coordinates) calculated "on-the-fly" using a quantum computer.

**Hamiltonian Type:** Fermionic Hamiltonian.

**Quantum Computational Kernel:** Ground State Preparation.

# Computational catalysis for artificial photosynthesis

## 6.1 Application area overview: computational catalysis in quantum chemistry

### 6.1.1 High-level description of the application area

In this application area, we discuss an intriguing field where quantum chemistry and computational catalysis combine to address ever-growing energy challenges. Quantum chemistry is essential for understanding how natural processes, such as photosynthesis, function in plants [166], where sunlight is converted into energy. An in-depth understanding of photosynthesis requires a detailed examination of underlying chemical reactions, exploring how atoms and molecules interact at atomic and subatomic levels (electrons and protons). The gained insight is not only pivotal for photosynthesis but has broader applications in chemistry [281]. By applying these principles, we can revolutionize our approach to energy, climate, and material challenges in a sustainable and efficient manner [14].

Our aim to unravel the intricate mechanisms of photosynthesis directs us to computational quantum chemistry that predicts the electronic structures, response properties, chemical bonding, and nuclear dynamics by solving the Schrödinger equations from first-principles. It facilitates a fundamental understanding of chemical reactions, explaining reaction mechanisms, rates, and environmental influences without conducting costly and time-consuming experiments. Crucially, it helps predict reactions and identify superior catalysts [66], which are vital for enhancing processes like photosynthesis.

In this chapter, we specifically focus on how quantum chemistry can address the ever-growing energy demand and climate change challenges by understanding and developing the *artificial photosynthesis* process [446, 14]. Artificial photosynthesis aims to replicate the natural process of converting sunlight, water, and carbon dioxide into energy-rich fuels, revolutionizing how we generate and use energy [345]. By harnessing solar energy to produce clean fuels, artificial photosynthesis represents a transformative approach to generating energy, significantly reducing greenhouse gas emissions and advancing towards a carbon-neutral energy cycle [14, 216].

However, the efficiency of artificial photosynthesis systems needs improvement, primarily due to challenges in controlling the rate of involved chemical reactions due to the increased energy barrier for converting reactants to products. In this context, catalysts play a crucial role in accelerating reactions by reducing the energy barrier without being consumed in the process [91]. These catalysts are essential for facilitating and directing the specific reactions needed to efficiently convert solar energy into chemical energy, which can be easily stored and transported. The effectiveness of the process relies on the ability to design highly efficient but selective and stable catalysts. For instance, water ( $\text{H}_2\text{O}$ ) oxidation and carbon dioxide ( $\text{CO}_2$ ) reduction reactions are essential and often limiting steps in artificial photosynthesis [281, 105]. The ideal catalyst must selectively steer the reaction towards desirable products rather than other less valuable by-products.

To improve the efficiency of artificial photosynthesis, the fundamental focus is on designing catalysts for both reactions, i.e., water oxidation [450, 210] and  $\text{CO}_2$  reduction [123, 253, 27]. The scientific questions we ask here are complex and critical: How can we screen the highly selective and efficient catalysts that drive the necessary reactions? Can we accurately estimate the energies of involved molecules to identify favorable reaction pathways? How do we ensure the system favors producing desired products over unwanted ones? Answering these questions is vital as they affect artificial photosynthesis's feasibility, efficiency, selectivity, and environmental impact, enabling the transition from theory to a practical, scalable technology.

# Computational catalysis for artificial photosynthesis

## 6.1.2 Utility estimation

**Overview of the value of the application area** The development of artificial photosynthesis has immense utility value for both the scientific community and humanity. It enables us to better understand molecular interactions and solar energy conversion processes, leading to breakthroughs in catalyst design and the optimization of artificial photosynthesis processes [281, 105]. These advancements can unlock new ways to efficiently harness and store solar energy, potentially tapping into a multi-billion-dollar renewable energy market. Artificial photosynthesis has even more profound implications for humanity. It could offer a promising solution to climate change and fossil fuel shortage with its role in carbon capture and utilization, which could significantly impact the growing carbon credit market. Developing sustainable and eco-friendly alternatives to traditional energy sources can reduce our dependence on fossil fuels, significantly decrease greenhouse gas emissions, and combat global warming. In addition, the computational workflow used in designing catalysts for photosynthesis can be readily applied to other areas of catalyst development, such as energy production, automotive catalytic converters, chemical synthesis, pharmaceuticals, *etc.* (Note: the global Catalyst market size was estimated at about \$39 billion in 2021 [57]).

Artificial photosynthesis holds great promise for transforming our energy generation and usage approaches. If successful, we're looking at a future where energy could be clean and abundant, easily accessible to everyone. This could be a game-changer in global energy dynamics, significantly reducing energy deprivation and paving the way for impartial energy access worldwide. Such a shift would profoundly impact the health of our planet and improve the quality of life for people everywhere. But pursuing these questions goes beyond just expanding our knowledge. It's about contributing to a more sustainable future filled with hope for humanity. These scientific endeavors stretch far beyond labs and academic efforts, which are crucial to our environmental sustainability.

**Concrete utility estimation** Problems described in this chapter have a computational bottleneck beyond the reach of current computing methods. We expect quantum computers to provide utility for these quantum chemistry problems due to their scalable nature and exponentially larger expression capability. In the absence of those today, we can provide a loose lower bound on the cost of computations with existing approximate/heuristic methods on high-performance computing platforms. For the examples of the concrete applications presented in the following sections (Application 1), the hybrid DFT, CASSCF, or other classical many-body methods using the CC-PVDZ basis set takes at least 20 hours per state for a feasible size of an active space due to the geometry optimization. The inclusion of other effects (such as solvents, dispersion, periodic boundary, *etc.*) will further increase the computational cost. Application 2 focused on the quantum molecular dynamics (QMD) (explained in the subsequent sections below) is dominating the computational volume considered here. QMD with  $10^3$  steps and 100 initial conditions for 10 most promising screened catalyst candidates would require  $20 \times 10^3 \times 100 \times 10 = 20,000,000$  core-hours. Using a typical cloud computing cost available from commercial vendors of \$0.03 per core-hour, we obtain that the computations under Application 2 for one of the reactions involved in artificial photosynthesis would cost on the order of \$600,000 in terms of the classical compute-time using existing approximate/heuristic methods.

## 6.2 Problem and computational workflows

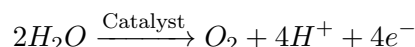
# Computational catalysis for artificial photosynthesis

## Detailed background of the application area: artificial photosynthesis

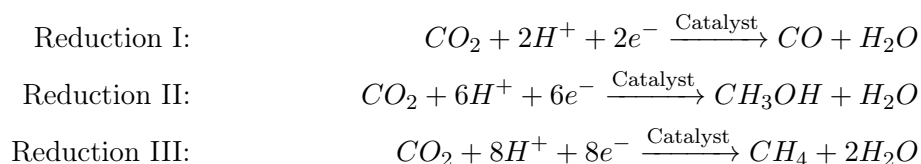
In nature, plants, algae, and some bacteria undergo this incredible transformation into energy-rich carbohydrates and oxygen through photosynthesis [166]. This process is fundamental to life on Earth, serving as the primary energy source for nearly all organisms. An essential step in photosynthesis is the charge separation through the absorption of photons, creating electron-hole pairs. This step is crucial as it generates energy and reduces the energy necessary for driving the reaction to synthesize carbohydrates. Drawing inspiration from this natural blueprint (photosynthesis), artificial photosynthesis aims to mimic and refine the process [284, 25, 20]. It focuses on generating renewable energy and capturing CO<sub>2</sub>, which is vital in addressing global energy and environmental challenges.

Artificial photosynthesis is a multi-step process that begins with the absorption of sunlight, followed by charge separation and the oxidation of water (H<sub>2</sub>O), producing oxygen (O<sub>2</sub>), protons (H<sup>+</sup>), and electrons (e<sup>-</sup>). These electrons and protons are utilized in the subsequent step for the CO<sub>2</sub> reduction to facilitate the production of fuels. This step involves reducing CO<sub>2</sub> into either CO, hydrocarbons like methane (CH<sub>4</sub>), or other carbohydrates such as glucose (C<sub>6</sub>H<sub>12</sub>O<sub>6</sub>) [428]. Water oxidation not only supplies the initial electron and proton necessary to drive the CO<sub>2</sub> reduction but also provides additional ones, facilitating the generation of various products during the reduction reaction. Alternatively, the hydrogen evolution reaction (HER) presents a pathway where the electrons and protons from water oxidation could be used to generate hydrogen gas (H<sub>2</sub>). However, due to the challenges associated with storing and transporting H<sub>2</sub> gas, artificial photosynthesis processes are designed to avoid HER. *Thus, water oxidation and subsequent CO<sub>2</sub> reduction reaction are core of artificial photosynthesis* [450, 210, 123, 253, 27].

### Water oxidation reaction:



### Example CO<sub>2</sub> reduction reactions:



All of these resulting chemicals from CO<sub>2</sub> reduction have a higher energetic content and can be used as fuel. These solar fuels circumvent the above-mentioned conventional challenges associated with hydrogen storage and transportation. Instead, CO<sub>2</sub> reduction focuses on creating fuels that can be more easily integrated into the existing energy infrastructure, offering a more practical and immediate application.

Although artificial photosynthesis offers a promising solution for global energy and environmental needs, its efficiency and scalability face significant challenges. Artificial photosynthesis requires the materials to a) efficiently absorb a broad spectrum of sunlight and b) effectively separate and transfer photo-excited electron holes to active sites for chemical reactions, which are often limited by the materials used. However, from a chemistry perspective, the significant challenges lie in identifying a catalyst that can effectively drive the water oxidation reaction by lowering the reaction barriers and selecting a catalyst tailored for the CO<sub>2</sub> reduction reaction. The catalyst for water oxidation

## Computational catalysis for artificial photosynthesis

must be highly active and stable over time to increase reaction kinetics, thus producing electrons and protons for CO<sub>2</sub> reduction. Meanwhile, the catalyst for the reduction reaction should exhibit selectivity and efficiency in converting CO<sub>2</sub> into valuable fuels with maximal yield. Therefore, an ideal catalyst needs to address efficiency, selectivity, and durability. Furthermore, these catalysts should be cost-effective and made from abundant materials to ensure the scalability and economic viability of the technology.

*The initial step involves carefully selecting potential catalyst candidates, focusing on those capable of efficiently driving the preferred reaction. This requires the characterization of energetically favorable reaction pathways and a calculation of activation energies. This assessment should focus on the catalyst's optimality, potential by-products, selectivity, and stability during the reaction.*

Experiments aimed at understanding the reaction mechanisms of artificial photosynthesis are often time-consuming and expensive [447, 14]. Moreover, capturing pathways opted during the reaction through in-situ [273] methods is challenging, given the timescale over which these reactions occur. Therefore, computational modeling offers a more comprehensive approach to gain in-depth insight into the reaction mechanisms. By using computational methods, such as ground state energy estimation, QMD, or advanced quantum nuclear dynamics methods, we can unravel the energetically favorable reaction pathways to select promising catalysts for water oxidation and CO<sub>2</sub> reduction. Additionally, computational modeling allows exploring a vast range of catalyst and reaction conditions, which might be impractical or unfeasible to test experimentally, leading to the discovery of efficient, sustainable, cost-effective catalysts with earth-abundant elements. Hence, this accelerates the development of energy solutions, bringing us closer to the practical implementation of sustainable energy production.

### Challenges of simulating chemical reactions on classical computers

Understanding the physical process of any chemical reactions generally requires the solutions to the Schrödinger equation of both electrons and nuclei,

$$i\hbar \frac{\partial \Theta(\mathbf{r}, \mathbf{R})}{\partial t} = H(\mathbf{r}, \mathbf{R})\Theta(\mathbf{r}, \mathbf{R}). \quad (69)$$

Where the molecular Hamiltonian is given as

$$\begin{aligned} \hat{H}(\mathbf{r}, \mathbf{R}) &= \hat{T}_n + \hat{T}_e + \hat{V}_{ee}(\mathbf{r}) + \hat{V}_{en}(\mathbf{r}, \mathbf{R}) + \hat{V}_{nn}(\mathbf{R}) \\ &= \hat{T}_n + \hat{H}_e(\mathbf{r}, \mathbf{R}). \end{aligned} \quad (70)$$

and  $\hat{T}_n = -\sum_A \frac{1}{2m_A} \nabla_{\mathbf{R}_A}^2$  is the nuclear kinetic energy operator. The electronic Hamiltonian  $\hat{H}_e(\mathbf{r}, \mathbf{R})$  contains the electronic kinetic energy operator as well as all the Coulomb operators involving electrons and nuclei. Since there is a large difference between nuclear and electronic mass, the Born-Oppenheimer approximation, which assumes that electrons adjust instantaneously to the slower motion of the nuclei so that a single adiabatic PES governs the motion of the latter, is used to factorize the total wavefunction as  $\Theta(\mathbf{r}, \mathbf{R}) \approx \Psi(\mathbf{r}; \mathbf{R})\chi(\mathbf{R})$ . Note that the Born-Oppenheimer approximation is a single decomposition approximation to the general Born-Huang representation. Such an approximation usually breaks down when two PESs are close, and the nonadiabatic effect becomes essential in these regimes [94]. Consequently, the Schrödinger equation can be divided into

## Computational catalysis for artificial photosynthesis

two equations for electrons and nuclei, respectively,

$$i\hbar \frac{\partial \Psi(\mathbf{r})}{\partial t} = \hat{H}_e(\mathbf{R})\Psi(\mathbf{r}, \mathbf{R}), \text{ or } \hat{H}_e(\mathbf{R})\Psi(\mathbf{r}, \mathbf{R}) = E(\mathbf{R})\Psi(\mathbf{r}; \mathbf{R}), \quad (71)$$

$$i\hbar \frac{\partial \chi(\mathbf{R})}{\partial t} = [\hat{T}_n + E(\mathbf{R})]\chi(\mathbf{r}, \mathbf{R}), \quad (72)$$

Where  $E(\mathbf{R})$  is the ground state of  $\hat{H}_e(\mathbf{R})$ , determining the potential energy surface (PES) for chemical reactions along certain reaction coordinates. Hence, in principle, two steps are required to simulate chemical reactions: (1) compute the energy  $E(\mathbf{R})$  from the electronic Hamiltonian  $\hat{H}_e(\mathbf{r}, \mathbf{R})$  for given nuclear coordinates (Eq. 71), (2) solve the *nuclear quantum dynamics* governed by Eq. 72 or *quantum molecular dynamics* which treats nuclei classically by taking the classical limit of Eq. 72 with quantum forces computed from ab initio PES  $E(\mathbf{R})$ . Unfortunately, neither of the two steps is trivial on classical computers due to the infeasible scaling of solving quantum many-body problems governed by Eqs. 71 and 72. Consequently, Density functional theory (DFT) or semi-empirical methods are widely used to solve Eq. 71. However, DFT or semi-empirical methods underestimate the electron correlations, particularly the dynamic correlations usually involved in chemical reactions, leading to inaccurate potential energy surface  $E(\mathbf{R})$ . Hence, the challenging nature of accurately simulating quantum systems led Richard Feynman to propose the development of quantum computers [130]. Today, quantum chemistry is recognized as one of the foremost applications of quantum computers [51, 22, 280].

**Current state-of-art in computational catalysis** Computational catalysis studies employ electronic structure methods to optimize stationary structures on Born-Oppenheimer potential energy surfaces (PES). This optimization identifies stable reactants, products, and intermediates essential to chemical processes. Optimizing first-order saddle points on these surfaces reveals transition state structures. Due to the computational challenges inherent in these studies, density functional theory (DFT) is widely used in the community. Significant efforts have been directed towards enhancing the accuracy and efficiency of DFT for catalyst screening. These improvements include the development of advanced solvent models, functionals beyond generalized gradient approximation (GGA), linear scaling methods, machine-learning potentials, and empirical models [67]. Additionally, first-principles-based kinetic methods have been developed to address kinetic effects in catalysis, such as Mean-Field Microkinetic Modeling, kinetic Monte Carlo, and quantum molecular dynamics. Further details are available in several reviews [67, 320]. Despite these advancements, the electronic structure remains a critical component of many models, and accurately computing this structure continues to pose significant challenges in classical computational catalysis.

### 6.2.1 Application 1: Energetics of reaction pathways for down selection of catalysts for artificial photosynthesis

**Specific background of the application** In artificial photosynthesis, optimizing the reaction mechanism is intrinsically linked to the design or identification of catalysts that can efficiently guide/accelerate reactions to yield desired products. For example, identifying catalysts for water oxidation and subsequent CO<sub>2</sub> reduction is vital. The down-selection of ideal catalysts for oxidation and reduction reactions depends on characterizing the energetically favorable reaction pathways with higher reaction rates for the desired product. For example, producing oxygen, electrons, and protons from water oxidation and useful fuels from CO<sub>2</sub> reduction. This involves accurately describing

## Computational catalysis for artificial photosynthesis

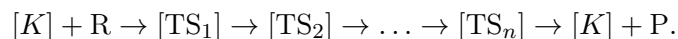
transition states and calculating activation energies. Transition states, as critical intermediates, are essential in mapping reaction pathways and understanding the energetics. They are the transformation step from reactants to products. In addition, activation energy, indicative of the energy barriers for reactions, is essential in assessing the feasibility and kinetics of a reaction and the efficiency of a catalyst.

Given the challenges and limitations of experimental methods in capturing these detailed aspects of catalyst, computational modeling becomes an essential tool. It allows for predicting catalyst behavior, describing transition state, and calculating activation energies. Through computational modeling, we can screen various catalyst candidates and identify the most effective one for driving the desired reactions. This approach is essential for both water oxidation and CO<sub>2</sub> reduction, where the choice of catalyst has a profound impact on the efficiency and practicality of the artificial photosynthesis process.

**Objectives** In this section, we explore the potential of quantum computers to enhance our understanding of reaction mechanisms involving catalysts [342]. By quantum computation of transition states and corresponding activation energies, we aim to significantly improve the accuracy and efficiency of catalyst design and optimization processes. Based on the challenges outlined above, the primary objective is to *down-select a pool of catalysts* for water oxidation and CO<sub>2</sub> reduction reaction. The catalysts for — water oxidation and CO<sub>2</sub> reduction — could either be the same or different. This objective entails identifying catalysts that can improve the efficiency of the reaction and are selective toward desired outcomes, such as water oxidation to produce electrons and protons or CO<sub>2</sub> reduction to produce CO, hydrocarbons, carbohydrates, etc.

The ultimate goal is precisely estimating the ground state electronic structure for transition states to calculate the energy barrier for the reaction pathway and select superior catalysts. Such calculations are usually non-trivial on classical computers because a) many catalysts involve transition metals with strong electronic correlations, and b) precise treatment of bond formation or breaking during the reactions. For identifying catalysts that enhance the efficiency of artificial photosynthesis, it is crucial to understand specific aspects of the reaction mechanisms for each catalyst, and reaction type (water oxidation or CO<sub>2</sub> reduction) is essential.

- **Reaction Pathway:** Identify the sequence of all intermediates or transition states (TS) characterizing the reaction pathways. Starting with a catalyst [K], we need to select the pathway.



This involves determining each intermediate stage, from the initial interaction of the catalyst with reactants ([K] + R) through various transition states (TS<sub>1</sub>, TS<sub>2</sub>, ..., TS<sub>n</sub>) to the final product ([K] + P).

- **Activation Energy :** For the established reaction pathway, *calculate the activation energy* ( $E_a$ ) that is crucial for determining rate constants. The Arrhenius equation defines the rate constants ( $k$ ):  $k \propto \exp(-E_a/RT)$ , where  $R$  is the gas constant and  $T$  is the temperature. We can predict the rate at which the reaction will proceed by estimating the activation energy of each reaction pathway and determining the rate-limiting step. However, these estimations are made under the approximation that nuclear dynamics can be neglected. This is an important and initial step for catalyst down-selection.



## Computational catalysis for artificial photosynthesis

These steps are critical for designing efficient and selective catalysts for desired products. Understanding these processes at a molecular level allows for precise modifications to the catalysts, enhancing their overall behavior and efficiency in artificial photosynthesis.

**End-to-end computational workflow Computational Workflow:** Figure 6-1 shows the computational workflow to down-select the most suitable catalyst for water oxidation and CO<sub>2</sub> reduction reactions from a pool of candidates by leveraging computational modeling. It begins by selecting the reaction mechanisms of artificial photosynthesis and evaluating a comprehensive pool of catalyst candidates ( $K_1$  through  $K_n$ ), followed by selecting the reactants (R) and the products (P) based on the chemical reaction (for example, H<sub>2</sub>O is the reactant and electrons and protons are the desired product in the water oxidation reaction). Next, potential reaction pathways are explored by identifying possible transition states ( $TS_1$  through  $TS_n$ ) with the nudged elastic band (NEB) or other counterparts [286], which are intermediate configurations leading from reactants to products. This exploration is facilitated using approximate quantum chemistry methods, such as DFT and CC methods, on classical computers. Such exploration of calculating energies for transition states is replaced by the quantum algorithms in the quantum computing workflow depicted in Figure 6-1.

The workflow considers the molecular structures of the reactant (R), product (P), and each transition state ( $TS_i$ ). Subsequently, a subset of these orbitals (active space) is selected for high-level electronic structure calculations, which is crucial for defining the electronic Hamiltonian's energy spectrum and balancing computational accuracy and efficiency. While molecular Hamiltonians are theoretically exact, they still depend on the wavefunction Ansatz to strike a balance between high accuracy and computational efficiency. The selected Hamiltonian within a certain active space is then used to estimate the ground state energy with the corresponding wavefunction Ansatz. Next, the wavefunction Ansatz is mapped onto a computational circuit, which can be executed on either classical computers for less demanding calculations or quantum computers for more complex problems. This encoding allows for estimating the ground state energies via either quantum phase estimation or other quantum algorithms [221]. The workflow then computes the energy for the reactant, product, and transition states, creating a potential energy surface along the reaction pathway (shown as inset in Figure 6-1). The workflow uses these energy values to estimate the activation energy ( $E_a$ ) and reaction barrier (reaction rates). These insights allow the workflow to characterize favorable pathways with the lowest barrier (highest reaction rate) for the selected catalyst, facilitating the identification of the most efficient catalyst based on the reaction rates through a down-selection process. This preferred catalyst is expected to improve the effectiveness and feasibility of artificial photosynthesis. As depicted in Figure 6-1, this workflow represents the integration of chemistry, quantum chemistry, and computational modeling to down-select effective catalysts for the different reaction mechanisms in artificial photosynthesis.

**Hard Computational Module:** The challenging aspect of the computational workflow is estimating the ground state energy. This involves complex calculations and optimization related to electronic correlations. The primary challenge in these calculations lies in accounting for all essential electronic configuration interactions (CIs) of a molecule in an exponentially large Hilbert (or CI) space, which becomes increasingly demanding with large numbers of electrons. This requires significant computational power, especially for catalysts with transition metals (that have strong electron correlations and spin polarization), where precision in calculating energy barriers is essential to determine the feasibility and rate of chemical reactions. Classical computational resources often fall short in processing these complex tasks due to their limitations in handling the huge CI space of large systems (curse of dimension). Quantum computing emerges as a solution to

## Computational catalysis for artificial photosynthesis

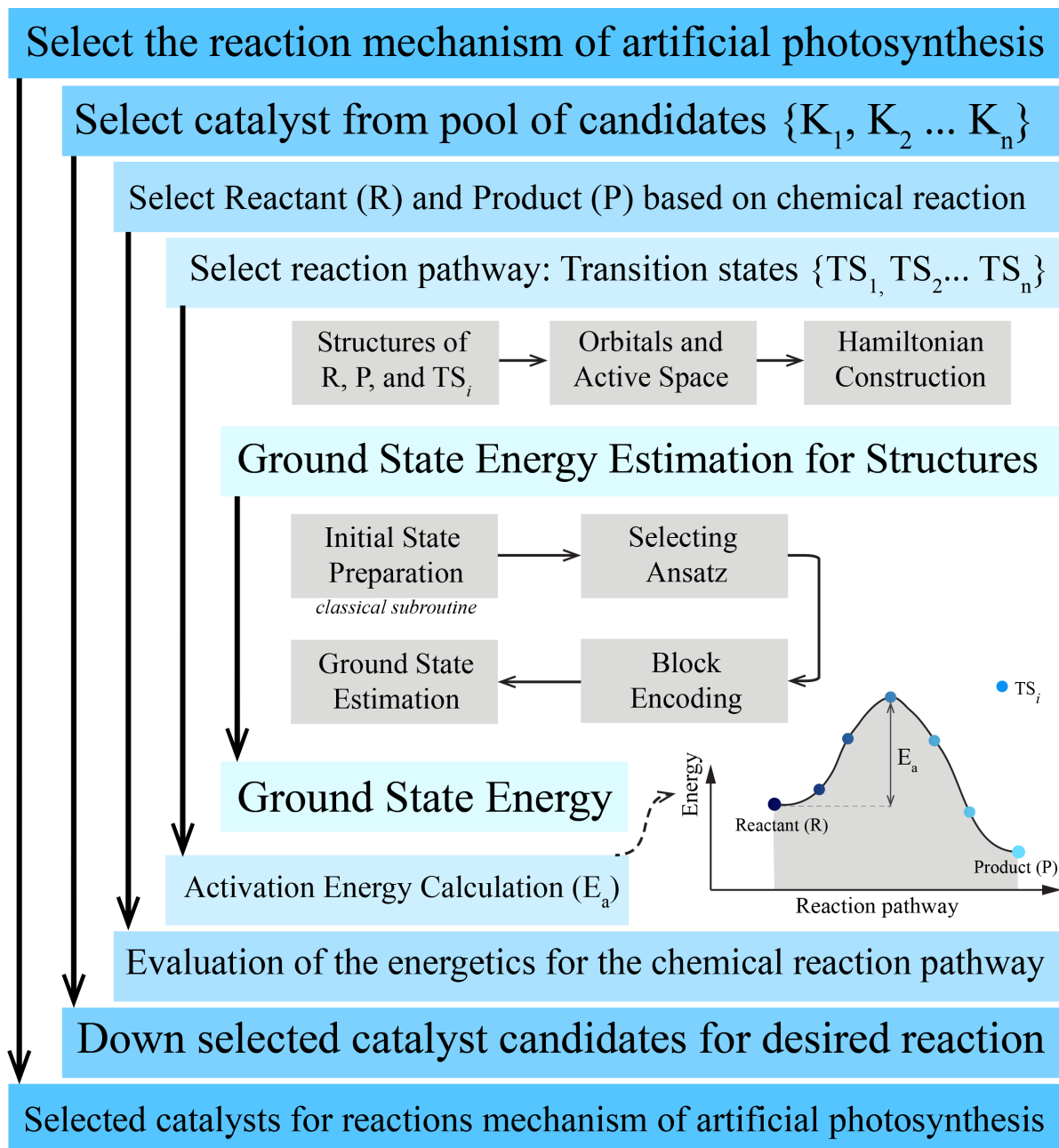


Figure 6-1: Flowchart of selecting catalysts for different reaction mechanisms of artificial photosynthesis using computational modeling.

## Computational catalysis for artificial photosynthesis

these challenges with its inherent exponentially large representation capability to encode quantum many-body wavefunction [130](or high-dimensional data), offering a much more efficient approach to these complex problems. They can handle the intricacies of quantum mechanics more naturally, potentially allowing for more accurate and economical solutions to problems. Integrating quantum computing into such workflows will significantly accelerate the research in quantum chemistry [47]. It enables the exploration of more complex molecular systems and reaction mechanisms that were previously inaccessible by classical computing, leading to more advanced and precise catalyst design.

The whole workflow shown in Figure 6-1 can be summarized as follows:

1. **Select Reaction Mechanism:** Begin by choosing the reaction mechanism involved in artificial photosynthesis, water oxidation reaction, or CO<sub>2</sub> reduction reactions.
2. **Select Catalyst from Pool of Candidates:** Accordingly choose the potential catalyst candidates,  $K_1, K_2, \dots, K_n$ .
3. **Select Reactant (R) and Product (P):** For the water oxidation reaction, H<sub>2</sub>O is the reactant, and O<sub>2</sub> (along with electrons and protons) is the product, and for the CO<sub>2</sub> reduction, CO<sub>2</sub> is the reactant and desired products are CO or other fuels.
4. **Select Reaction Pathway:** Identify possible transition states,  $TS_1, TS_2, \dots, TS_n$ , which are intermediate states between reactants and the products.
  - (a) **Structures of R, P, and  $TS_i$ :** Determine the molecular structures of the reactant, product, and each transition state.
  - (b) **Orbital and Active Space:** Determine the relevant orbital and select active space to define the scope of the Hamiltonian.
  - (c) **Hamiltonian Construction:** Construct the electronic Hamiltonian for these molecules.
    - i. **Quantum Ground State Estimation:** Employ quantum algorithms to approximate the ground state energies and eigenfunctions.
      - A. **Initial State Preparation:** Prepare initial states or wavefunctions for each molecular structure.
      - B. **Selecting Ansatz:** Selecting the initial quantum state to efficiently navigate the solution space of a problem on the computer.
      - C. **Block Encoding:** Encode the state Ansatz (including the initial states and unitaries for uncovering the correlations) of the molecules onto a computer.
      - D. **Ground State Measurement:** Perform the ground state energy measurements on computers, for example, on quantum computers, by measuring each individual Pauli string in the qubit Hamiltonian.
  - (d) **Ground State Energy for R, P, and  $TS_i$ :** Compute the energy levels for the reactant, product, and each transition state.
5. **Activation Energy Calculation ( $E_a$ ):** Calculate the activation energy required to convert reactants into products through the transition states.
6. **Energetic Pathway Evaluation:** Based on the calculated energies, identify an energetically favorable reaction pathway for the selected catalyst.

## Computational catalysis for artificial photosynthesis

7. **Catalyst Selection for Reactions:** From the initial pool of candidates, select the ideal catalyst that best facilitates the reaction.
8. **Selected Catalysts for Artificial Photosynthesis:** List all down-selected catalysts for water oxidation reaction and CO<sub>2</sub> reduction reactions.

### Why classical methods are not sufficient to perform the hard computational module

The hardness of classical computational methods in performing demanding tasks in quantum chemistry, particularly for down-selecting catalysts, can be attributed to system size, electronic structure complexity, and the inherent computational cost of these methods. Classical computational methods often struggle with large molecular systems or those with complex electronic structures. As the size of the system increases, the number of possible electronic CIs escalates, or an extended basis is needed to represent the wavefunctions, making the calculations more challenging.

The computational cost of DFT, a widely used method in quantum chemistry, scales cubically with the number of system electrons  $O(N^3)$  with density fitting technique [32]. Though DFT is efficient on classical computers, it has difficulty in accurately handling localized charges and strong electron correlation (a common scenario in catalysts) due to the lack of exact functional [24], leading to less reliable results. The coupled-cluster (CC) [21] method, which represents the wavefunction as an exponential of cluster operators and can be systemically improved by truncating at different orders ( $M$ ), is accurate for many systems, its steep computational scaling ( $O(N^{2(M+1)})$ ) makes it impractical for large systems. Moreover, CC is not particularly effective for strong static correlations [21]. For systems with strong electron interactions, the Density Matrix Renormalization Group (DMRG) [63] method offers significant advantages. DMRG approximates the wavefunction as a low-rank tensor product, enhancing its ability to capture strong electron correlations with greater accuracy, but it becomes less practical for higher-dimensional systems and is limited to small systems due to its computational complexity. Nevertheless, as the dimensions increase, the number of possible CIs grows exponentially, making classical calculations increasingly difficult and resource-heavy.

Given these limitations, classical computational methods often fall short in either computational efficiency or accuracy in capturing the challenging electron correlation problems in quantum chemistry, particularly for large or complex molecular systems. This is where quantum computing, with its different approach to handling calculations involving quantum states, offers a promising alternative capable of overcoming these limitations [50, 251, 22, 280].

**Concrete problem instantiations** Here, we use transition metal complexes as the example catalyst to demonstrate the application of quantum computation to computational catalysis.

**CO<sub>2</sub> Reduction:** Cobalt phthalocyanine (CoPc, molecular formula is CoC<sub>32</sub>N<sub>8</sub>H<sub>16</sub>) molecule is one of the high-performance CO<sub>2</sub> reduction catalysts [463]. The CoPc can also be used to make a metal-organic framework (MOF) for both high selectivity and CO<sub>2</sub> capture capability [253, 123]. Nevertheless, we use the basic unit, CoPc, as the sample to demonstrate the reaction pathway of CO<sub>2</sub> reduction. One of the proposed mechanisms of CO<sub>2</sub> reduction with the CoPc catalyst is shown in Figure 6-2(a).

**Water Oxidation with metal oxide catalyst:** The other sample application we consider is water oxidation to molecular oxygen mediated by model cobalt oxide. Cobalt oxide has recently gained wide popularity for its remarkable catalytic activity toward water splitting [208]. The structure of this molecular catalyst was also found to consist of Co<sub>4</sub>O<sub>4</sub> cubane-shaped metal oxide units.

## Computational catalysis for artificial photosynthesis

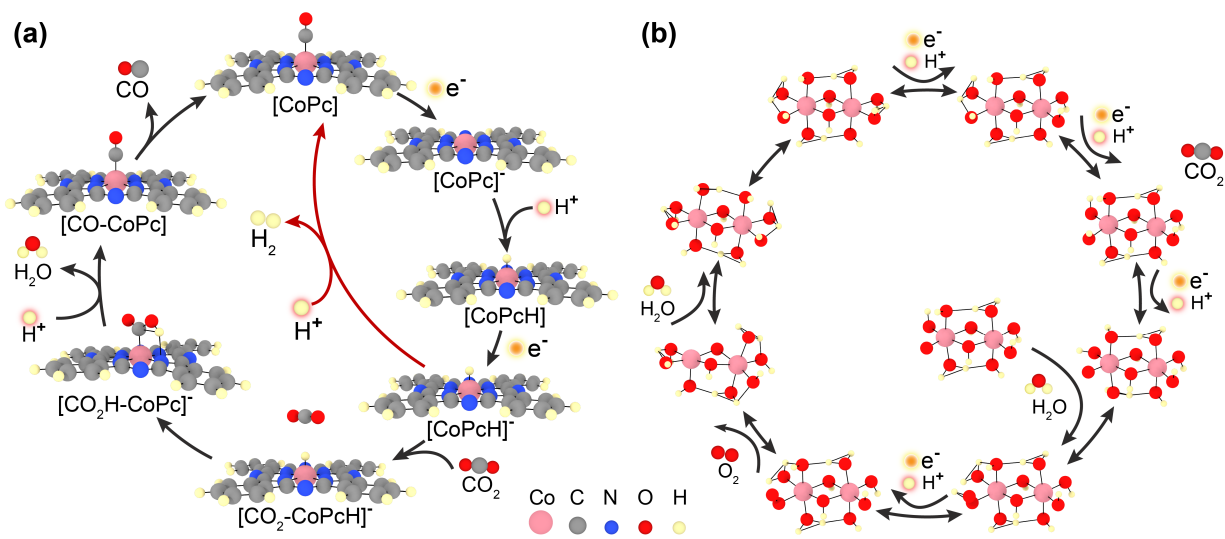


Figure 6-2: (a) One proposed CO<sub>2</sub> reduction mechanisms with CoPc catalyst [265]. (b) One possible water oxidation reaction pathway with the cobalt dimer catalyst [125].

Without losing generality, we consider a model cobalt oxide dimer Co<sub>2</sub>O<sub>9</sub>H<sub>12</sub> [125], which is a minimal unit of the cubane complex and serves as a typical model system for studying the paramagnetic intermediate in Cobalt-Catalyzed water oxidization, as shown in Figure 6-2(b). This cobalt dimer compound is characterized by two aqua ligands and two hydroxyl ligands attached to each cobalt center and Two  $\mu$ -hydroxo groups linking the two cobalt centers. The dimer compound can have many possible isomers with different positioning of these two aqua and hydroxyl ligands around the cobalt atoms.

It should be noted that both the water oxidation reactions pathways on the cobalt dimer and CO<sub>2</sub> reduction of CoPc catalyst are characterized by the proton-coupled charge transfer (PCET) as shown by experimental evidence [106], similar to PCET reactions in the oxygen-evolving complex of photosystem II in the nature. The PCET encompasses quantum nuclear effects such as quantum tunneling and quantum interference, which will be discussed in other applications.

**Molecular structure and classical hardness.** The molecular structures of the CO<sub>2</sub> reduction and water oxidation along one reaction pathway are shown in Figure 6-2(a) and (b), respectively. The number of atoms, total electrons, valence electrons, and the number of molecular orbitals with different basis sets are shown in Table 6-1. From the molecular structures, we are readily able to obtain electronic energies using quantum chemistry methods. However, the electronic structure of such transition metal compounds remains poorly understood due to the complexity of the multiple transition metal ions with their multiple charge states and complicated spin-couplings. The presence of a larger number of electrons/orbitals and strong correlation in *d* orbital electrons makes it hard to compute the energies with DMRG methods on classical computers if all the electrons and orbitals are considered. Even after removing the core electrons, there are still 92 valence electrons in 120 spatial orbitals for the water oxidization reaction. Hence, classical algorithms usually prune the number of orbitals/electrons further to construct small active valence electrons in the electronic structure calculations. However, even with this active space of 48 electrons in 32 orbitals (64 spin orbitals), i.e., (48e, 32o) as shown in Table 6-1, the dimension of the Full configuration interaction (FCI) is on the order of 10<sup>14</sup> (i.e.,  $\binom{32}{24} \times \binom{32}{24} \sim 10^{14}$ ) on classical computers. Even the efficient

## Computational catalysis for artificial photosynthesis

DMRG method has a complexity of  $O(ND^3)$  where  $N$  and  $D$  are the number of orbitals and bond dimensions, respectively. In the typical simulation of transition metal with a bond dimension of 5000, DMRG simulation requires a dimension of  $64 \times (5000)^3 \sim 10^{13}$ , which requires more than 80 TB RAM memory.

Table 6-1: Molecular information of CO<sub>2</sub> reduction and water oxidation.

System	Atoms	Total Electrons	Active space
CO <sub>2</sub> -CoPc	60	269	(45e, 35o)
H <sub>2</sub> O-CO <sub>2</sub> O <sub>9</sub> H <sub>12</sub>	26	148	(48e, 32o)

**Hamiltonian generation and encoding in quantum algorithms for artificial photosynthesis.** A good starting point for solving chemistry problems is the mean-field Hartree-Fock (HF) method. This method approximates the many-electron problem by effective one-body problems where each electron evolves in the mean field of the others. The HF method is very efficient on classical computers ( $O(N^3)$  scaling) and includes the exact exchange, but the electron correlations are missing. Therefore, the HF method is usually a good starting point for post-HF methods to include the missing correlations. With the HF method, we can rewrite the electronic Hamiltonian in the basis set of HF orbitals (namely, molecular orbitals (MOs)) in the second-quantization form (termed as molecular Hamiltonian). Since not all the electrons/orbitals contribute to the correlation energy, we usually only need to select a set of electrons/orbitals (namely active space) in the simulation. In the selection of active space, the key principle is that all strongly correlated orbitals must be identified and selected to active space, which can be accomplished by the so-called mutual information that measures the entanglement among orbitals [349, 406, 466]. With the selection of active space, we can effectively reduce the size of the molecular Hamiltonian and the subsequent qubit Hamiltonian described below.

However, the Fermionic operator in the molecular Hamiltonian cannot be directly simulated on quantum computers that work on qubits. The molecular Hamiltonian has to be mapped into its qubit counterpart by using either Jordan-Wigner (JW) [203], Bravyi-Kitaev (BK) [42], or parity [380] encoding. Hence, different encoding techniques lead to various numbers of qubits requirement and sparsity in the resulting qubit Hamiltonian [50] and consequently affect the gate complexity in the QPE. Nevertheless, the resulting qubit Hamiltonian can contain  $O(N^4)$  Pauli strings. Although the ultimate goal is to include all valence electrons and beyond (which requires hundreds of spin orbitals) in quantum simulations, we selected a restricted active space corresponding to orbitals near the Fermi energy surface, as shown in Table 6-1. This is due to the computational expense of generating two-body integrals and the associated mapping into qubit Hamiltonians. In fact, the large number of two-body integrals and Pauli strings in quantum chemistry problems stimulates the development of pre-processing techniques [351] and measurement reduction techniques [451, 182, 37]. For the specific cases of water oxidation and CO<sub>2</sub> reduction, we chose a small active space of (48e, 32o) and (45e, 35o), leading to 64 and 70 spin orbitals (qubits), respectively. But our target is to simulate a large active space ( $\sim 650$  spin-orbitals for the CoPc molecule) in order to treat either all electrons in a larger basis set (such as CC-PVQZ) or larger molecules. It should be noted that selecting the active space is a nontrivial task. In this context, the active space is determined by imposing an energy window that truncates according to the energy difference between the molecular orbital energies and the Fermi energy. This method represents one of the simplest approaches to

## Computational catalysis for artificial photosynthesis

select the active space. To enhance the quality of the active space, techniques inspired by quantum information theory [466, 109] or based on natural orbitals can be utilized [395]. The resulting qubit Hamiltonians have 1,542,149 and 930,650 Pauli strings, respectively.

**Initial state preparation.** The choice of initial states in quantum computation plays a pivotal role in achieving accurate results, particularly in capturing quantum systems' true ground state energies. In many cases, a single-determinant Hartree-Fock (HF) state is a good initial approximation, as it provides a reasonable starting point with a relatively large overlap with the actual ground state. However, in complex reactive systems like photosynthesis, which is characterized by bond breaking and formation, the static correlation effects become significant, and the single-determinant HF state usually has poorer overlap with the true ground states. In such instances, the wavefunction has a multireference nature, i.e., more than one electronic configuration contributes significantly to the ground state energies. Consequently, the low-complexity multireference can be employed, such as the linear combination of the HF state and selected configuration interaction singles (CIS) states [407]. Such multireference states can be easily prepared on quantum computers with rotation and entanglement gates [413], and it was found that such low-complexity multireference state can usually provide sufficient overlap with the true ground states, boosting the success probability of the phase estimation for the complex reactive systems [413].

**List of candidate systems where a similar process is relevant?** A similar workflow can be used for cases where ground-state energy estimation is required. For example,

- Oxygen Evolution Reaction on metal oxides, such as Cobalt Oxide [238] and titanium Oxide [316].
- Hydrogen Evolution Reaction or protonation for H<sub>2</sub> fuel generation and storage [357].
- In materials science: Defect migration within the crystal [200] and structural phase transitions [312, 287].

### 6.2.2 Application 2: Reaction dynamics through quantum molecular dynamics simulations

**Specific background of the application** The quantum computation of reaction energies in *Application 1* leverages pre-determined reaction pathways in reduced dimensions. Among the various strategies for identifying these pathways, the nudged elastic band (NEB) [286] method, supported by chemical intuition, stands out. Although proficient, the NEB method recognizes that it may not always determine the lowest barrier path. Such discrepancies arise because the method's success relies on the chemist's insight and experience, which guides the selection process but does not guarantee the most energetically favorable pathway. Furthermore, despite its effectiveness, the NEB method incorporates approximations to determine the reaction pathways, which may not fully capture the complexity of the quantum mechanical landscape [374].

Besides, *Application 1* primarily uses a static method to identify reaction barriers, but it doesn't provide detailed insights into reaction dynamics [374, 186, 88], such as kinetic effects and efficiencies of chemical reactions. These drawbacks, inherent in traditional static quantum chemistry methods for transition states, can be mitigated by the adiabatic Quantum Molecular Dynamics (QMD) [40, 54, 315, 278, 414] or nonadiabatic molecular dynamics (NAMM) [299, 94]. QMD allows the system

## Computational catalysis for artificial photosynthesis

to evolve from the reactant state to the product state via the “on-the-fly” update of the potential energy surfaces, involving extensive sampling of initial conditions and/or long simulation times [315]. This approach enables comprehensive analysis of reaction dynamics, capturing intricate details of electron interactions and molecular kinetics. Consequently, QMD’s ability to accurately simulate the evolution of transition states is fundamental for elucidating the chemical reaction mechanisms of complex structures. Furthermore, QMD also helps identify intermediates that impact product formation, allowing for optimization of reaction conditions to improve selectivity and yield in chemical processes.

Thus, QMD is a pivotal method in assessing catalysts for water oxidation and CO<sub>2</sub> reduction in artificial photosynthesis. For water oxidation, QMD can identify the most efficient pathways for breaking water molecules into oxygen and hydrogen, highlighting catalysts with higher reaction rates, efficiency, and speed. Similarly, for CO<sub>2</sub> reduction, QMD can reveal how catalysts can effectively convert CO<sub>2</sub> into useful carbon-based fuels or chemicals, pinpointing reactions with lower energy costs and higher selectivity. This detailed insight is important for designing effective, sustainable, and cost-effective catalysts, accelerating the development of artificial photosynthesis. Moreover, QMD allows the investigation of the role of temperature, pressure, and external stimuli on the reaction mechanism. This also provides the opportunity to comprehensively understand how these factors influence the reaction rate and mechanism. Additionally, QMD can mimic realistic chemical environments, extending the scope of the investigation to conditions that would be challenging to achieve in *Application 1* and experiments. *Application 2* provides the ability to explore a wide range of conditions, including

- **Effect of External Fields:** Dynamics electric or magnetic fields to enhance catalytic efficiency and selectivity [430, 422, 416].
- **Dynamic Effect on Reactivities:** Non-adiabatic effects, which coupled electronic and nuclear motions, are crucial in a wide range of chemical processes [465, 298].
- **Kinetic and Thermodynamic Properties:** Extreme temperatures and pressures that are often encountered in industrial settings influence reaction rates and equilibrium [307, 168, 167].
- **Surface and Interface Phenomena:** The role of surfaces and interfaces in catalyzing reactions, including adsorption and desorption processes and surface-induced catalytic activity [439, 266, 230].
- **Material Degradation and Stability:** Understanding how materials degrade over time under various conditions and strategies for improving the longevity and durability of catalysts [458, 115].

Though we only discussed the adiabatic QMD method in the following, the nonadiabatic molecular dynamics (NAMD) can also be applied to study the kinetics of catalysis with additional computation of excited states, nonadiabatic couplings, and propagation of electronic wavefunction [94, 299], which will be discussed in later applications. In particular, NAMD plays an essential role in modeling exciton migration and separation into charges (electrons and holes) [299] before they are utilized in catalysis.



## Computational catalysis for artificial photosynthesis

**Objectives** As discussed, dynamics simulations are crucial for revealing the complexity of chemical reactions, including both kinetics and dynamical effects. Unlike *Application 1*, which is limited to predefined reaction pathways, QMD simulations explore the most effective pathways by analyzing efficiency and reaction rates with various catalysts. Therefore, QMD improves the methodology for selecting appropriate catalysts for artificial photosynthesis. The catalyst selection process within the QMD framework involves determining the number of reacted trajectories ( $N_{\text{reacted}}$ ) out of the total trajectories ( $N_{\text{all}}$ ). The ratio of these trajectories determines the quantum yield or reaction efficiency ( $\Phi$ ), while reacted trajectories are examined to determine the reaction rate ( $k$ ) similar to that of in *Application 1*. The reaction rate is defined by the inverse of the average time ( $\langle t \rangle$ ) required for a reactant (R) to convert into a product (P) under specified reaction conditions. In this context, a “trajectory” refers to the path molecules follow on their PES over time. Each trajectory outlines the evolution of the molecule, beginning with a specific set of initial conditions, including the positions and velocities of all particles. A trajectory is categorized as a reacted trajectory if it transforms the reactant into the desired product.

For a down-selected candidate catalyst from *Application 1* and specific reaction mechanism, such as water oxidation or CO<sub>2</sub> reduction, the reaction efficiency or quantum yield ( $Q$ ) can be estimated using the formula  $Q = \frac{N_{\text{reacted}}}{N_{\text{all}}}$ . This ratio measures the probability that reactants convert to products under given conditions. By calculating the average time for reacted trajectories,  $\langle t \rangle$ , the reaction rate can be defined as  $k \sim \frac{1}{\langle t \rangle}$ . This approach describes a reaction rate in kinetic terms, offering a quantifiable measure of the efficiency and effectiveness of a catalyst in facilitating a particular chemical reaction. Thus, QMD enables the design and optimization of catalysts for artificial photosynthesis under diverse conditions. Accurate QMD simulations require selecting appropriate quantum methods to estimate Potential Energy Surfaces (PES) and forces alongside a classical approach for modeling nuclear motion. Determining the ideal simulation parameters, such as the time step and total simulation time, is also crucial. Additionally, it is essential to select appropriate initial conditions for reaction trajectories. This involves sampling from a distribution of initial velocities and positions representing a wide range of possible reactant states.

**End-to-end computational workflow** **Computational Workflow:** Figure 6-3 shows a process for performing QMD simulations to identify the most effective catalysts for water oxidation and various CO<sub>2</sub> reduction reactions. Analogous to *Application 1*, this workflow involves choosing a reaction for artificial photosynthesis (either oxidation or reduction) and a set of down-selected catalyst candidates from *Application 1* (ranging from  $K_1$  to  $K_n$ ). Subsequently, it involves selecting the initial configuration for reactant (R) and catalyst (K). Unlike the previous workflow, this method does not require a predefined product (P) or reaction pathway. After assigning the initial velocity and coordinates for the molecular system, the next steps, akin to *Application 1*, involve selecting the appropriate valence orbitals within the system and choosing the active space for simulation. Subsequently, the electronic Hamiltonian is determined to achieve a balance between high accuracy and computational efficiency. The Hamiltonian and wavefunction for initial configuration are mapped onto a computational circuit. Further, the workflow maps the state of the initial configuration onto a computer to estimate the ground state energies. Next, the quantum circuit that represents the converged ground state Wavefunction is used to measure the forces (gradient of energies with respect to atomic coordinates). Using the computed force, the coordinate and velocity are updated, and the system is then propagated along the PES by Newton’s equation of Motion [96].

Next, for estimating the quantum yield ( $\Phi$ ), the workflow determines the “reacted” trajectories that result in the creation of desired products. For example, for a water oxidation reaction, electrons

## Computational catalysis for artificial photosynthesis

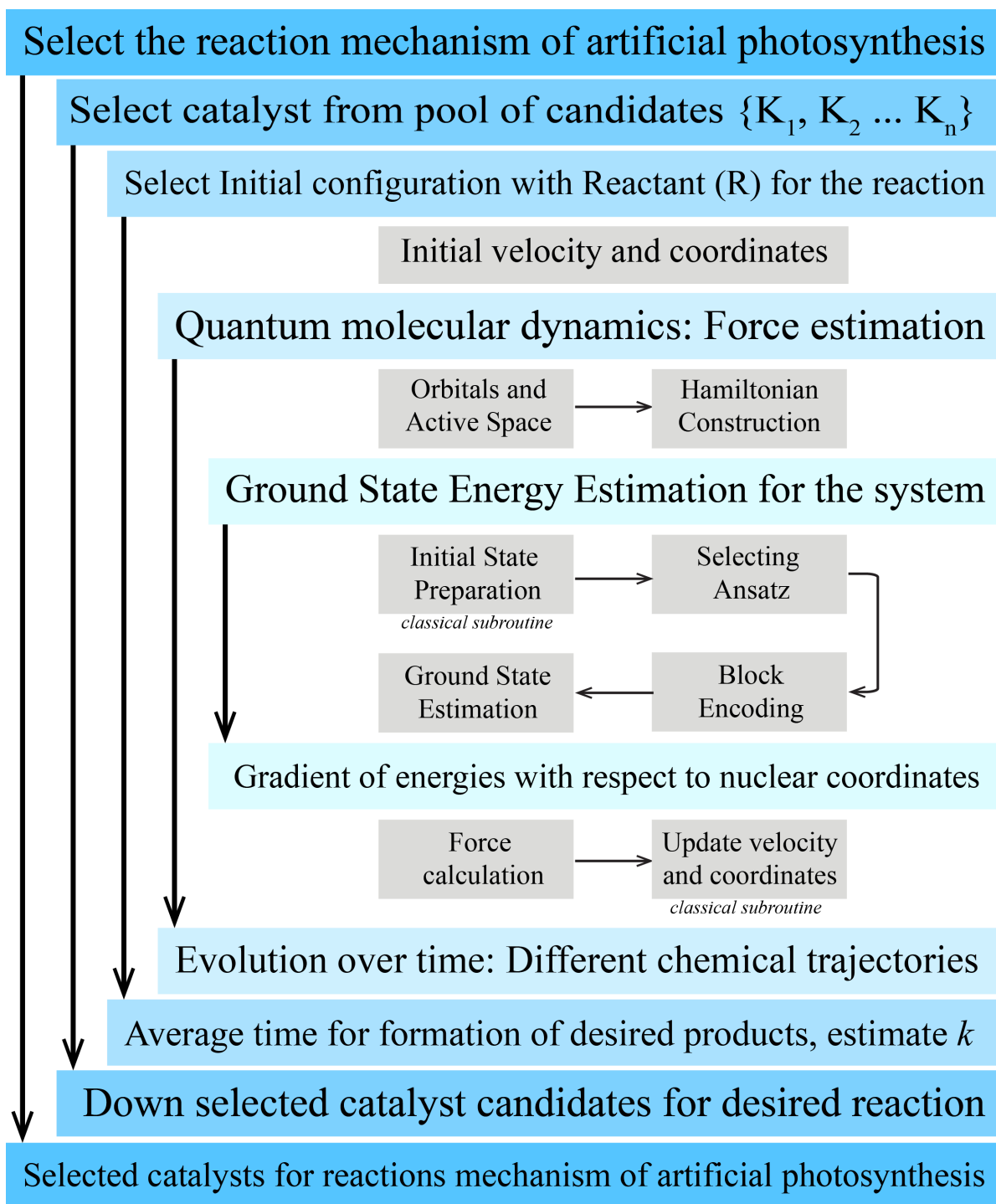


Figure 6-3: Flowchart of selecting catalysts for different reaction mechanisms of artificial photosynthesis using QMD.

## Computational catalysis for artificial photosynthesis

and protons are the desired product, while for a CO<sub>2</sub> reduction reaction, CO or other fuels are the desired product. The inverse of the average time for the ‘reacted’ trajectories is used to calculate the reaction rate ( $k$ ). In the next step, following the comparison of reaction rates for various catalysts ( $K_1$  through  $K_n$ ), the workflow selects the most effective catalyst based on its efficiency and selectivity in driving the reactions (higher quantum yield and faster rates). This selected catalyst is anticipated to enhance the efficiency and viability of artificial photosynthesis. As illustrated in Figure 6-3, this procedure includes chemistry, quantum chemistry, and both quantum and classical modeling. This workflow helps advance artificial photosynthesis by identifying catalysts for different reaction mechanisms.

**Hard Computational Module:** The initial “hard computational module” of QMD simulation is the computationally demanding task of estimating the ground state energy (similar to *Application 1*). Quantum computing is a pivotal solution to these challenges, offering a pathway to solve problems involving electron correlations with high accuracy and efficiency. The complexity of this task is particularly pronounced in QMD simulations, which require dynamic updates to the system’s state. Each update of coordinates necessitates a subsequent estimation of the ground state energy to reflect the system’s current state. This emphasizes both the computational intensity and the necessity for precise capture of quantum mechanical behaviors of interacting electrons.

The other challenge in performing large-scale QMD simulations is accurately estimating the forces during the simulation. The difficulty in computing forces lies in calculating the gradients of the ground state wavefunction with respect to nuclear coordinates. The numerical gradients, which require  $6N$  computational of ground states with a finite difference (where  $N$  is a number of atoms), make it almost impossible to propagate the QMD. Analytical gradient, while much more efficient than its numerical counterpart, is hard to develop due to the nested chain rule of derivatives of intermediates parameters. The derivatives are further complicated by the exponentially large wavefunctions in some cases, which impede efficient computation on classical computers. Thus, quantum computing holds the potential to revolutionize QMD simulations, enabling significant advancements in quantum chemistry.

The whole workflow shown in Figure 6-3 can be summarized as follows:

1. **Select Reaction Mechanism:** Begin by choosing the reaction mechanism involved in artificial photosynthesis, water oxidation reaction, or CO<sub>2</sub> reduction reactions.
2. **Select Catalyst from Pool of Candidates:** Accordingly choose the potential catalysts,  $K_1, K_2, \dots, K_n$ .
3. **Select Initial configuration:** Select initial configuration with reactant and catalyst. For the water oxidation reaction, H<sub>2</sub>O is the reactant, and for the CO<sub>2</sub> reduction, CO<sub>2</sub> is the reactant.
  - (a) **Initial velocity and coordinates:** Determine the initial condition for molecular structures of the reactant and catalyst.
4. **Quantum Molecular Dynamics:** Calculate forces using ground state energies and update the velocity and coordinates for the system. For which -
  - (a) **Orbital and Active Space:** Determine the relevant orbital and select active space to define the scope of the Hamiltonian.

## Computational catalysis for artificial photosynthesis

- (b) **Hamiltonian Construction:** Construct the electronic Hamiltonian for the molecular system.
  - i. **Ground State Energy Estimation:** Employ quantum algorithms to approximate the ground state energies and eigenfunctions.
    - A. **Initial State Preparation:** Prepare initial states or wavefunctions for each molecular structure.
    - B. **Selecting Ansatz:** Selecting the initial quantum state to efficiently navigate the solution space of a problem on the computer.
    - C. **Block Encoding:** Encode the state Ansatz (including the initial states and unitaries for uncovering the correlations) of the molecules onto a computer.
    - D. **Ground State Energy:** Perform the ground state energy estimation on computers, for example, on quantum computers, by measuring each individual Pauli string in the qubit Hamiltonian.
  - (c) **Force Calculation:** Compute forces by taking the gradient of energies with respect to nuclear coordinate using ground state energy computed in the previous step.
  - (d) **Update the Velocity and Coordinate:** The system with catalyst is then propagated along the potential energy surface (PES) by Newton's equation of Motion.
5. **Evolution Over Time:** Identify reaction trajectories that result in the formation of diverse products.
6. **Reaction rate Calculation ( $k$ ):** Estimation of the average time for the formation of the desired products, facilitating the computation of reaction rate ( $k$ ).
7. **Catalyst Selection for Reactions:** From the initial pool of candidates, select the ideal catalyst that best facilitates the reaction.
8. **Selected Catalysts for Artificial Photosynthesis:** List all promising catalysts for reactions, both water oxidation reaction and CO<sub>2</sub> reduction reactions.

### Why classical methods are not sufficient to perform the hard computational module

Ab initio QMD method treats the electrons and nuclei quantum mechanically and classically, respectively, within the Born-Oppenheimer approximation. Within the Ab initio QMD, nuclei then propagated along the potential energy surface (PES) by propagating Newton's equation of Motions [96]

$$M_I \dot{\mathbf{R}} = \mathbf{P}_I, \quad \dot{\mathbf{P}}_I = \mathbf{F}_I = -\nabla_{\mathbf{R}_I} [E_g(\mathbf{R}) + V_{NN}(\mathbf{R})]. \quad (73)$$

where  $\mathbf{R}_I$ ,  $\mathbf{P}_I$ ,  $M_I$ , and  $\mathbf{F}_I$  are positions, momenta, masses, and forces of the  $I$ -th atom.  $E_g(\mathbf{R})$  and  $V_{NN}(\mathbf{R})$  are the ground state electronic and nuclear repulsive energies, respectively. Therefore, in the propagation of classical trajectories, energy and forces (negative gradient of energies with respect to nuclear coordinates) are computed "on-the-fly" at each MD step through the solution of the time-independent Schrödinger equation for the electrons. Since integrating Newton's equation is cheap on classical computers (compared to the quantum mechanical solution to the Schrödinger equation), the fundamental complexity of ab initio QMD simulation is twofold: 1) the intrinsic complexity of computing energy (which has been discussed in application 1) and forces and 2) the larger number

# Computational catalysis for artificial photosynthesis

of time steps to accurately simulate the dynamics of reactions over long time scale ( $> \text{ps}$  or even ns).

**Larger number of time steps.** Take a typical reaction with a picosecond time scale as an example; a QMD simulation with 1 fs time step requires at least  $10^3$  calculations of energies and forces. Even if each energy/force calculation only takes 1 CPU second, a QMD simulation in a nanosecond time scale needs 280 CPU hours. Consequently, the majority of current QMD simulations can only handle small systems, and semiempirical quantum mechanical (SQM) methods (that simplify the first-principles calculations parameterizing one-body and Coulomb integrals) [299] are usually used.

**Complexity of quantum forces.** Since we have discussed the complexity of energy calculations, here we focus on the discussion of force calculations. In general, the energy  $E$  explicitly depends on  $\mathbf{R}$  and  $\theta$  (parameters of the Ansatz). Gradients of ground state energy with respect to nuclear coordinates are given by

$$\nabla_{I\alpha} E = \langle \Phi | \nabla_{I\alpha} \hat{H} | \Phi \rangle + \left[ \langle \Phi | \hat{H} | \nabla_{I\alpha} \Phi \rangle + h.c. \right] = \frac{\partial E}{\partial \hat{H}} \frac{d\hat{H}}{d\mathbf{R}} + \frac{\partial E}{\partial \theta} \frac{d\theta}{d\mathbf{R}}. \quad (74)$$

The last two terms are Pulay forces, which do not vanish when  $\Phi(\theta)$  varies with respect to nuclear coordinates (because the wavefunction or the parameterized Ansatz are dependent on  $\mathbf{R}$ ). Hence, the complexity of computing forces on classical computers mainly are two-fold: 1)  $\nabla_{I\alpha} \hat{H}$  requires the gradients of one-body and two-body integrals; 2)  $|\nabla_{I\alpha} \Phi\rangle$  accounts the "orbital relaxation" effect on gradients, its analytical form can be derived from the widely used "Lagrangian formalism" or "Z-vector" techniques [173, 171]).

**Concrete problem instantiations** Though substantial advancements have been achieved in the development of quantum algorithms for solving electronic structure problems, the majority of this work has been predominantly focused on the static ground state properties as shown in *Application 1*, with only a limited number of studies addressing the challenge of computing forces using quantum computers. In our application, we specifically explore the use of transition metal complexes as catalysts (illustrated in Figure 6-2) to showcase the potential of quantum computing in the ab initio QMD simulations of catalysts.

**Measuring forces on quantum computers.**  $\frac{d\hat{H}}{d\mathbf{R}}$  in Eq. 74 contains the derivatives of one-electron and two-electron integrals, which can be efficiently computed on classical computers with a computational complexity of  $O(N^4)$ .  $\frac{\partial E}{\partial \hat{H}}$  involves the "unrelaxed" one- and two-body reduced density matrix (1-RDM and 2-RDM), which can be readily measured on QC once the quantum circuits for the ground state wavefunction are converged,

$$\rho_{pq}^1 \equiv \frac{\partial E}{\partial h_{pq}} = \langle \Phi(\theta) | a_q^\dagger a_p | \Phi(\theta) \rangle$$

$$\rho_{pqrs}^2 \equiv \frac{\partial E}{\partial h_{pqrs}} = \langle \Phi(\theta) | a_q^\dagger a_p^\dagger a_r a_s | \Phi(\theta) \rangle.$$

Though the "orbital relaxation" part ( $\frac{\partial E}{\partial \theta} \frac{d\theta}{d\mathbf{R}}$ ) is nontrivial, the analytical formalism can be derived via the Lagrangian formalism [229, 313], ending up with a formula that is functional of 1- and 2-RDMs. As a result, the number of terms that need to be measured on quantum computers also scales as  $O(N^4)$ . Since the force measurements adapt the same quantum circuits as the ground state energy

## Computational catalysis for artificial photosynthesis

estimation, there is no additional phase estimation, introducing only a very low computational overhead compared to energy estimation [304, 305].

**Sampling of initial conditions.** In Ab Initio QMD simulation of chemical reactions, the initial conditions of reactants are sampled to reflect thermal fluctuations. Then, the QMD simulates how these conditions evolve over time, specifically focusing on the trajectories that lead to product formation. The quantum yield, representing the efficiency of the reaction, is calculated by the proportion of successful transitions to product states among all trajectories. Achieving a statistically converged quantum yield requires sampling a sufficient number of trajectories to accurately represent the thermodynamic ensemble of initial states. The exact number needed depends on the reaction complexity and the variability introduced by thermal fluctuations. Typically, hundreds of trajectories ( $\sim 300$ , for example [299]) may be necessary to ensure that the calculated quantum yield is robust and reflective of the true reaction dynamics under study.

It should be noted that MD trajectories can be trivially paralleled over a larger number of processors as each trajectory is independent. In addition, the expensive measurement of energies and forces at each MD step can be bypassed by the recently proposed quantum-classical Liouvillian dynamics methods. Based on the Koopman–von Neumann formulation of classical mechanics, the Liouville equation of motion for nuclei can be implemented as unitary dynamics on quantum computers, and the resulting framework is able to propagate electronic and nuclear DOFs with quantum and classical dynamics, respectively [386].

**List of candidate systems where a similar process is relevant?** A similar workflow can be used for cases where the dynamical evolution of the system is required. For example,

- Designing catalysts for other chemical reactions [258, 448, 441].
- Mechanochemistry: Initiation of reactions under mechanical influence [307, 168, 167].
- In materials science: Ion diffusion for battery applications [445, 259] and exfoliation of layered materials [394, 393, 292].
- Nuclear fusion reaction. In fusion reactions, the nuclei need to overcome the Coulomb barrier to trigger the fusion reaction. The reaction is very similar to the chemical reactions, though the energy, time, and length scales are different [15].

### 6.3 Requirements summary

This section summarizes the application requirements for all the applications described in this chapter.

## Computational catalysis for artificial photosynthesis

### **Application 1: Energetics of Reaction Pathways for Down Selection of Catalysts for Artificial Photosynthesis**

<b>Workload:</b>	Total time limit	1 week per catalyst candidate (screening of 100 catalysts in 2 years)
	Number of subroutine calls required	100 = 20 (transition states) × 5 (reaction pathways per catalyst)
	Maximum subroutine time limit	1.6 hours
	Model type	Fermionic Hamiltonian
<b>Problem specifications:</b>	Size	minimum 64 spin-orbitals target 650 spin-orbitals
	Interaction Structure	Sparse irregular
	Computational target	ground state
	Accuracy requirement	1 mHartree

### **Application 2: Reaction Dynamics through Quantum Molecular Dynamics Simulations**

<b>Workload:</b>	Total time limit	1 month per catalyst candidate (most promising screened candidates)
	Number of subroutine calls required	100,000 = 1000 (molecular dynamics steps) × 100 (initial conditions per catalyst)
	Maximum subroutine time limit	0.5 minute (progress on the classical side required)
	Model type	Fermionic Hamiltonian
<b>Problem specifications:</b>	Size	minimum 64 spin-orbitals target 650 spin-orbitals
	Interaction Structure	Sparse irregular
	Computational target	ground state and forces
	Accuracy requirement	1 mHartree

## 6.4 Quantum implementation

Example of the workflow explained in Application 1 using an example of water oxidation reaction with 8 transition states and an active space of 28 electrons in 19 orbitals (38 spin orbitals) with quantum implementation and resource estimation can be found in [289].

## 7 Simulations of quantum chromodynamics and nuclear astrophysics

This chapter presents applications relevant to nuclear physics. We focus on applications that probe extreme regimes which are experimentally or observationally accessible, but not simulable by known classical methods. Relevant experiments range from the Relativistic Heavy-Ion Collider (an experimental facility at Brookhaven National Laboratory) to IceCube (a neutrino observatory in Antarctica supervised by the University of Wisconsin-Madison, and the largest neutrino telescope in the world). The computational capability required is quantum Hamiltonian simulation: the Hamiltonians used are lattice discretizations of field theory Hamiltonians (QCD and an effective theory of neutrinos). Current classical approaches in all cases suffer from severe systematic errors of unknown magnitude; these systematics come from approximations that must be made in order to render the calculations classically tractable. The potential benefit of quantum computers lies in their ability to perform the simulations with all systematics under control.

**Hamiltonian Type:** Neutrino Effective Field Theory and QCD Hamiltonian.

**Quantum Computational Kernel:** Hamiltonian Simulation.



# Simulations of quantum chromodynamics and nuclear astrophysics

## 7.1 Application area overview

Nuclear physics concerns itself with the many-body dynamics of the Standard Model of physics. The dynamics of the Standard Model is inherently quantum mechanical with many degrees of freedom, as particles can be freely created and annihilated at high energies. Thus a fully error-corrected large-scale quantum computer will be required to predict the exotic states of matter which emerge from quantum field theory. While essentially every sub-domain of nuclear physics can profit from a quantum computer for at least some range of its problems, two important examples addressed here are the behavior of the dense gas of neutrinos created in a core-collapse supernova and the properties of the quark-gluon plasma, a state of matter that formed and dominated the universe early in cosmological history. Both of these examples connect to world-leading experiments that have been built or are under construction by the United States. In the case of supernovae, the neutrino experiments DUNE and IceCube act as supernova neutrino observatories, capable of measuring the neutrino output of a supernova, while the Facility for Rare Isotope Beams (FRIB) (see [174]) will provide important insight into the r-Process of Nucleosynthesis, which in astrophysical environments can radically modify the momentum and flavor distribution of the neutrino gas. In the case of the quark-gluon plasma, the Relativistic Heavy Ion Collider both established the existence of this state of matter, and has led the experimental investigation into its properties. Each of these facilities, while covering a myriad of physics applications (covered in [402]), hosts experiments that would benefit profoundly from the quantum calculations we describe in this section.

## 7.2 Problem and computational workflows

### 7.2.1 Application 1: Supernova neutrinos

Core-collapse supernovae are among the most catastrophic events in the universe, and play an important role in cosmological history, providing an engine by which elements heavier than iron can be synthesized. Supernovae simulations require understanding physics at many different scales [30, 194]. Although supernovae are ultimately driven by the microscopic mechanisms in nuclear physics, their simulation naively appears to be a problem of classical physics of transport and fluid dynamics. However, these supernovae generate a tremendous number of neutrinos, with the bulk of the energy of the supernova being carried away by the neutrinos. While generally a weakly interacting particle, the neutrino densities in a supernova are such that the flavor and momentum distributions can be significantly impacted by their quantum mechanical self-interactions, and new dynamical phenomena may occur beyond the well-understood vacuum oscillations of neutrino flavor (see review [420]). For a complete treatment of the physics of a supernova, a critical question to answer is the exact momentum and flavor distribution of the neutrinos during the course of the supernova. At such large densities, traditional classical computational methods of kinetic theory become impractical, as it is necessary to determine the time-evolution of the full many-body density matrix, and recently, much effort in the field has been devoted to using quantum computation and quantum information science as a way forward [17].

**Specific background of the application** Tracing out a static nuclear and electron background that the neutrinos are embedded in, the hamiltonian for the neutrinos is given by [385] (see also [420])

## Simulations of quantum chromodynamics and nuclear astrophysics

and further references therein):

$$\hat{H} = \hat{H}_1 + \hat{H}_2, \quad (75)$$

$$\hat{H}_1 = \sum_{f,f'} \sum_{s,s'} \int d^3\vec{p} B_{ff',ss'}(t,\vec{p}) \hat{a}_{f,s}^\dagger(\vec{p}) \hat{a}_{f',s'}(\vec{p}), \quad (76)$$

$$\begin{aligned} \hat{H}_2 = \sum_{f_1,f_2,f_3,f_4} \sum_{s_1,s_2,s_3,s_4} \int d^3\vec{p}_1 d^3\vec{p}_2 d^3\vec{p}_3 d^3\vec{p}_4 C(\vec{p}_1^{f_1 s_1}, \vec{p}_2^{f_2 s_2}, \vec{p}_3^{f_3 s_3}, \vec{p}_4^{f_4 s_4}) \delta^{(3)}\left(\sum_i \vec{p}_i\right) \\ \times \hat{a}_{f_3,s_3}^\dagger(\vec{p}_3) \hat{a}_{f_1,s_1}(\vec{p}_1) \hat{a}_{f_4,s_4}^\dagger(\vec{p}_4) \hat{a}_{f_2,s_2}(\vec{p}_2). \end{aligned} \quad (77)$$

The operators  $\hat{a}_{f,s,\vec{p}}^\dagger, \hat{a}_{f,s,\vec{p}}$  are fermionic creation and annihilation operators with anti-commutation relations that create and annihilate states of flavor  $f$ , spin  $s$  and momentum  $\vec{p}$  (above  $f_i$  and  $s_i$  refer to flavor and spin labels of the operators):

$$[\hat{a}_{f,s}(\vec{p}), \hat{a}_{f',s'}(\vec{q})]_+ = 0, \quad (78)$$

$$[\hat{a}_{f,s}^\dagger(\vec{p}), \hat{a}_{f',s'}^\dagger(\vec{q})]_+ = 0, \quad (79)$$

$$[\hat{a}_{f,s}^\dagger(\vec{p}), \hat{a}_{f',s'}(\vec{q})]_+ = 2(2\pi)^3 E_f(\vec{k}) \delta_{ff'} \delta_{ss'} \delta^{(3)}(\vec{p} - \vec{q}), \quad (80)$$

$$E_f(\vec{k}) = \sqrt{\vec{k}^2 + m_f^2}. \quad (81)$$

In the notation of Ref. [111], the coefficient  $C$  for relativistic neutrinos is easily expressed in terms of helicity projected 2-spinors, as helicity and chirality dependence become identical, and is given as:

$$C(\vec{p}_1^f, \vec{p}_2^{\bar{f}}, \vec{p}_3^{\bar{f}'}, \vec{p}_4^{f'}) = \frac{G_F}{\sqrt{2}} \langle p_1 | \gamma^\mu | p_3 \rangle \langle p_2 | \gamma_\mu | p_4 \rangle. \quad (82)$$

For neutrino-anti-neutrino annihilation we have:

$$C(\vec{p}_1^f, \vec{p}_2^{\bar{f}}, \vec{p}_3^{f'}, \vec{p}_4^{\bar{f}'}) = \frac{G_F}{\sqrt{2}} \langle p_1 | \gamma^\mu | p_2 \rangle \langle p_3 | \gamma_\mu | p_4 \rangle. \quad (83)$$

The hamiltonians  $\hat{H}_1$  and  $\hat{H}_2$  represent the one and two-body neutrino hamiltonians.  $G_F$  is the low energy coupling constant from the 4-Fermi effective theory of the standard model that results from integrating out the Z-boson. The one body hamiltonian includes the neutrino kinetic energy terms, the mass mixing matrix, and the interactions of neutrinos against any fixed background of nuclear or electron matter.

Another simplifying assumption we can impose is that the neutrinos are relativistic in momenta. Given that typical nuclear reactions producing the neutrinos have an energy scale on the order of a few MeV, and the neutrino mass is less than 0.1eV, this is a safe assumption for the neutrinos as they travel through the supernova. Treating the neutrinos as massless then forces all neutrinos to have left-handed chirality, and anti-neutrino's right-handed chirality, and we need not keep track of the spin degree of freedom. Eventually vacuum oscillations will prove important at length scales on the order of a few kilometers, but for neutrino-neutrino scattering, this is a higher order effect.

The primary goal of the theorist analyzing the problem is to calculate the final distribution of momenta and flavors of the neutrinos given a specific initial distribution. If  $\hat{\rho}$  is the initial density matrix of all the neutrinos, this is the asymptotic flavor-dependent momentum spectrum:

$$N_f(t,\vec{p}) = \text{tr}[\hat{a}_f^\dagger(\vec{p}) \hat{a}_f(\vec{p}) e^{it\hat{H}} \hat{\rho} e^{-it\hat{H}}], \text{ as } t \gg T_{sn}. \quad (84)$$

## Simulations of quantum chromodynamics and nuclear astrophysics

We note that vacuum oscillations prohibit the neutrinos from have a fixed momentum distribution per flavor asymptotically. Physically, of course, infinite time evolution is not needed for the full hamiltonian. On a certain time scale, which we call  $T_{sn}$ ,<sup>4</sup> we can expect the neutrinos will escape the supernova, and the neutrino-neutrino ( $\hat{H}_2$  above) and neutrino-matter (included in  $\hat{H}_1$  above) interactions will become irrelevant, as the matter and neutrino densities plummet. From this time forward, only vacuum oscillations of the neutrinos would matter, included in the one-body term above, and are straightforward to calculate.

**Overview of the value of the application** Scientifically, supernova challenge our capabilities to model complex thermonuclear explosions, requiring the incorporation of microscopic nuclear physics reactions, neutrino dynamics, and fluid modelling into a physically coherent and predictive package. Given that neutrinos carry  $\sim 90\%$  of the energy released in such an event, proper handling of their dynamics is critical to correct modeling of the supernova. Moreover, these neutrinos can be directly observed in dedicated science experiments that are either on-going or under constructions [376].

While not the sole reason for these experiments, some of the science goals for the U.S. led and funded neutrino experiments IceCube (via the National Science Foundation,  $\sim$  \$242 million) and the Deep Underground Neutrino Experiment (DUNE, funded via the Department of Energy, Office of Science, High Energy Physics, projected total  $\sim$  \$5 billion), see [233, 2], is the detection of neutrinos from a supernova occurring in the Milky-Way galaxy. These can be expected to occur one to three times every hundred years, with the 1987a supernova event being the last nearby core-collapse supernova. The observation of neutrinos from this event has been a critical source of information used to constrain both stellar collapse models as well as beyond the Standard Model physics.

DUNE will be able to provide both directionality information on the neutrinos origin, count the number of neutrinos, as well as measure their energy. Given accurate neutrino cross-sections for the DUNE detector, all this information will directly constrain the predicted spectrum of neutrinos from the core-collapse supernova, and direct experimental measurements for Eq. (84) can be performed for  $f = e$ , the electron neutrino.

**Concrete utility estimation** Within Los Alamos National Laboratory, the supernova neutrino problem has been worked on for well over a decade, with an expenditure varying between \$400K to \$1 million annually. Moreover, supernova simulation which requires the correct characterization of the neutrino background has been a long-standing problem of interest to the Laboratory as a test bed for fluid dynamics simulations and multi-scale, multi-physics modeling. It has received an average investment of \$2-5 million, though the exact number is hard to estimate due to its spread over many programs and the underlying multi-use functionality of the developed code and models. From a physics point of view, these simulations are deficient without a proper understanding of the underlying neutrino background, and will not be fully capable of claiming a definitive understanding of core-collapse supernova without a solution to the neutrino scattering problem.

**Objectives** The primary objective would be to produce a quantitative prediction for the time-scale when Eq. (84) reaches an equilibrium value, given physically reasonable initial density matrices and matter profiles. More generally, one would like to answer the question whether the density matrix thermalizes in an appropriate sense before  $T_{sn}$ , the time it takes for the supernova to end. An

---

<sup>4</sup>This is expected to be around 10s [194].

## Simulations of quantum chromodynamics and nuclear astrophysics

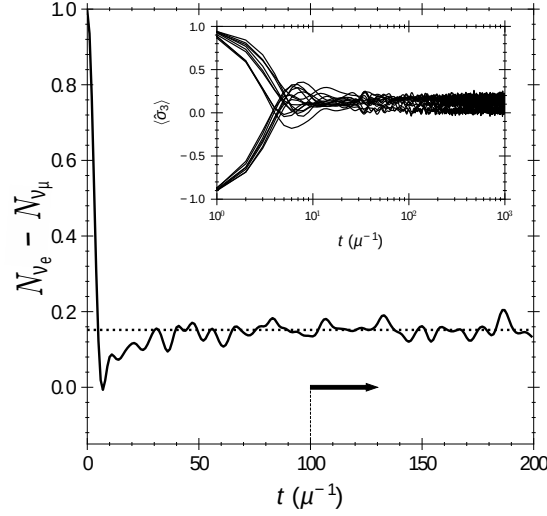


Figure 7-1: We plot the evolution of the difference in flavor occupation,  $N_{\nu_e} - N_{\nu_\mu}$ , for neutrino in momentum mode  $i = 1$  compared to the prediction utilizing the grand-canonical partition function (black dotted line), which represents the equilibrated long-time answer. The calculation is performed for a toy model of the full neutrino problem where the number of momentum modes equals the number of neutrinos, with an unphysically small number of neutrinos. The momentum modes are not allowed to change, only the flavor occupation in the simplified model. Thus each neutrino is labeled by its specific fixed momentum mode  $i = 1, \dots, 16$ , and  $N_{\nu_e}(i) - N_{\nu_\mu}(i)$  captures the flavor distribution of that mode. The line and arrow indicate when the time-averaging begins for comparison against the grand canonical prediction. *Inset:*  $N_e(i) - N_\mu(i)$  as a function of time for every neutrino on the entire considered time domain. Adapted from [277].

example of such a calculation of the thermalization time for a small system in a simplified model of neutrino-neutrino scattering is given in figure 7-1; see [277] for details.

**End-to-end computational workflow** Direct time evolution of the second-quantized hamiltonian for the initial  $\sim 10^{38}$  per cubic meter of neutrinos would be hopeless to calculate, and unnecessary. One simply would need to show that Eq. (84) reaches a stable distribution as the number of neutrinos grows large. The desired work-flow would proceed as follows, with the steps requiring quantum computational methods being explicitly indicated, and all other steps can be assumed to be a classical workload.

1. Discretize the number of momentum modes into a fixed set  $\mathcal{P} = \{\vec{p}_i\}_{i=1}^K$ , and we can associate each momentum mode with a specific quantum state specifying whether or not the momentum mode is occupied and by what flavor of (anti)neutrino. More explicitly, for two flavors of neutrinos+anti-neutrinos, we have a set of labels denoting the occupation of a state:

$$\mathcal{F} = \{0, \nu_e, \nu_\mu, \nu_e + \nu_\mu, \bar{\nu}_e, \bar{\nu}_\mu, \bar{\nu}_e + \bar{\nu}_\mu, \nu_e + \bar{\nu}_e, \nu_\mu + \bar{\nu}_\mu, \nu_e + \bar{\nu}_\mu, \bar{\nu}_e + \nu_\mu\}. \quad (85)$$

Where 0 denotes no occupation. Then we write any state of the discretized system as:

$$|\psi\rangle = \sum_{\phi_1 \in \mathcal{F}, \phi_2 \in \mathcal{F}, \dots} c(\phi_1, \dots, \phi_K) \otimes_{i=1}^K |\phi_i\rangle_{\vec{p}_i}. \quad (86)$$

Thus for a two flavor example, we need 4 qubits per momentum mode to represent the occupation of the system. We note that this first quantized formalism can neglect the pair

## Simulations of quantum chromodynamics and nuclear astrophysics

creation of neutrinos, as this process is not density enhanced, and is suppressed by the weak coupling constant  $G_F$ . Two-body scattering processes that preserve the total number of neutrinos minus anti-neutrinos will be most relevant. However, nothing precludes the inclusion of pair creation, though the number of momentum modes needed for an accurate description of the dynamics may grow so that artificial discretization effects are sufficiently suppressed. An example of this implementation, albeit on a small, unphysical scale, can be found in [83].

2. Fix number of momentum modes  $K$ , and total number of neutrinos  $N$  and anti-neutrinos  $\bar{N}$ .  $K$  will specify the qubit requirements of the quantum computer.
3. Initiate a physically reasonable set of initial states: these are product states, which for each neutrino is Gaussian distributed over momenta, with the momentum peaked at the nuclear scales at which the neutrinos are generated, i.e., 1 – 10 MeV. Product states suffice due to the uncorrelated production of the neutrinos, and the gaussian distribution localizes the neutrinos to specific regions of the supernova. The simulation will be performed with no matter background or vacuum oscillations at all, neglecting  $\hat{H}_1$ .
4. Perform quantum evolution until the required momentum spectra reaches an equilibrium value. The equilibrium value can be deduced as a steady state value in time of the momentum spectrum, where moment to moment fluctuations are small relative to the long-time averaged observable [392, 261]. For an example of such an plot, see Fig. 7-1, where the flavor distribution of a fixed momentum mode is plotted as a function of time.
5. Repeat steps 2-4, increasing  $K, N$ , and  $\bar{N}$  until discretization effects are negligible, and one can estimate the momenta spectra for the large  $N/\bar{N}$  limit.
6. Now repeat the calculation (steps 1-5) for more sophisticated matter backgrounds informed by classical supernova simulations (such effects are reviewed in [336]) and with vacuum oscillations induced by masses, which will result in the inclusion of the  $\hat{H}_1$  term.

### Why classical methods are not sufficient to perform the hard computational module

In general, calculating time-dependent quantities with classical methods is exponentially hard in the time-frame needed to be resolved, see [436]. Since the question we wish to resolve is the needed thermalization time for the observables of the system, barring special insights into the specific problem, full exploration of the thermalization time would be classically expensive. Aside from the classically tractable solutions to the classical limit of the equations of motion for the forward scattering neutrino interactions (itself a simplified model of the full neutrino scattering problem), no attempt has been made to classically calculate the quantum hamiltonian for neutrino scattering for any sort of realistic system sizes, as it would be impossible to do so on current hardware.

**Notes on quantum implementation and resource estimation** We can easily give a lower bound to the computational quantum gate complexity of our hamiltonian by considering a simplified case of the neutrino scattering hamiltonian known as the coherent forward scattering model of [16]. In the integrals over all possible momenta, one only considers the cases where  $\vec{p}_1 = -\vec{p}_3$  and  $\vec{p}_2 = -\vec{p}_4$ , or  $\vec{p}_1 = -\vec{p}_4$  and  $\vec{p}_2 = -\vec{p}_3$ , which represent the forward/back-scattering scenarios. Further, one neglects anti-neutrinos, and restricts to a two-flavor model. From the point of view of the first-quantized formalism, un-occupied momentum modes cannot become occupied, and all that can happen is that the flavor swaps between the momentum modes. It is straightforward to

## Simulations of quantum chromodynamics and nuclear astrophysics

see then that the forward scattering model fixes the number of momentum modes to be the number of neutrinos,  $N = K$ , and the hamiltonian will take a form that is analyzed in [226]. Further, the forward scattering model is a strict subset of the full problem, and thus any gate count and qubit requirements for the forward scattering problem lower bounds the difficulty of the full problem.

Within the forward scattering model, then, we can write the hamiltonian as an all-to-all Heisenberg model, yielding:

$$\hat{H} = \sum_{i=1}^N \vec{b}_i \cdot \hat{\sigma}_i + \frac{G_F \mu}{\sqrt{2}N} \sum_{1 \leq i < j \leq N} p_i \cdot p_j \hat{\sigma}_i \cdot \hat{\sigma}_j. \quad (87)$$

Where now  $N$  is the number of neutrinos or equivalently momentum modes, and  $\vec{b}_i$  is the one-body coupling matrix,  $\vec{p}_i$  is the momentum of the  $i$ -th neutrino,  $\mu$  is density of neutrinos, which we can take to be 1 with a redefinition of time after setting the one-body terms to zero, and  $\hat{\sigma}_i$  is a Pauli matrix operating on the flavor space of the  $i$ -th momentum mode. Ignoring the one-body terms in the hamiltonian, and focusing on the two-body interactions, the Heisenberg interactions can easily be written in terms a swap gate, and the exponentiation of a term in the Hamiltonian is again a sum of a swap gate with the identity. With an all-to-all connected architecture, the simplest Trotterization of this Hamiltonian yields a circuit with  $N$  depth for a single Trotter step. Following [165, 226] we can estimate the computational gate complexity assuming a linear connectivity for the qubit architecture, which now yields an order  $N^2$  circuit for a single Trotter step.

**Concrete problem instantiations** The simplest case that can prove to be of scientific use will be to consider a gas of momentum plane-wave neutrinos, undergoing two-body interactions without a complicating matter background, in the relativistic limit. Then the one-body hamiltonian reduces to the identity, being the conserved total kinetic energy of the system. Then the goal will be to see how equilibration is reached for flavor distribution of single momentum mode in Eq. (84) for a given distribution of initial neutrino momenta and flavors. Actual equilibration of single-body observables can happen with relatively small system sizes in simplified models [277]. Thus it is reasonable to start with system sizes with  $\sim 100$  momentum modes. Multiple questions must be explored, whose answer is not known a priori:

1. Fixing  $K$ ,  $N$  and  $\bar{N}$ , what is the time scale  $t_{\text{eq.}}(N, \bar{N}, K)$  for equilibration? If the time-scale is power-law dependent on these quantities, this can be deduced from only a few runs of the quantum computer with a linear progression in the number of neutrinos and momentum modes. Constant or logarithmic dependence would require scanning an order of magnitude.
2. Fixing  $N$  and  $\bar{N}$ , what are the number of momentum modes  $K$  needed before discretization effects are negligible, i.e., order 1%, for the late time value of Eq. (84)? We denote this number as  $K(N, \bar{N})$ , and now the time scale  $t_{\text{eq.}}$  will simply be a function of  $N$  &  $\bar{N}$ .
3. Deduce the behavior of  $t_{\text{eq.}}$  as  $N$  &  $\bar{N}$  grow, to order 1% accuracy.

As we do not expect to be close to any phase transitions or critical points of the system for *generic* initial conditions, it is reasonable to expect that we do not need large system sizes to "extrapolate to infinity."<sup>5</sup> Of course, this would easily be verified in the course of the calculation. Depending

---

<sup>5</sup>Being at a phase transition is very sensitive to system size, as a true phase transition can only occur at infinite system size. Finite size effects will smooth out the expected singularities associated to the phase transition.

## Simulations of quantum chromodynamics and nuclear astrophysics

on the behavior of the time-scale with the system size, then, starting with system sizes of order  $\sim 100$  momentum modes (or 400 qubits), and scaling to  $\sim 1000$  modes (or 4000 qubits), would be sufficient to determine if anything *unusual* is happening for order 100 neutrinos. Thus the largest quantum computer we would need should have order 4000 logical qubits, capable of running circuits with order 4000 gates for multiple Trotter time-steps. Note that for finding the equilibrium value, we can expect a single shot should be sufficient, as the system can be expected to be self-averaging. Again, this is the expectation that the system will equilibrate to an effective thermal system at high temperatures for generic initial conditions [391, 107, 392].

### 7.2.2 Application 2: Hydrodynamics of hot and dense matter

Theoretical predictions of the behavior of the quark-gluon plasma require the calculation of a small number of *transport coefficients*, of which the most significant is the shear viscosity of the plasma. This computation is not possible with current classical algorithms, nor with those that are foreseeable in the near term; however a straightforward quantum algorithm is known.

**Specific background of the application** The Relativistic Heavy-Ion Collider (RHIC) at Brookhaven National Laboratory performs high-energy collisions of gold nuclei. (CERN's Large Hadron Collider spends around one-tenth of its time performing similar experiments, albeit with lead instead of gold.) The immediate result of each such collision is a rapidly expanding ball of hot, dense matter known as the quark-gluon plasma (QGP). Investigating the QGP's properties has been a major goal of nuclear physics in the U.S. since its discovery in the early 2000s.

The quark-gluon plasma is a state of matter obtained at temperatures in excess of  $\sim 10^{12}$  Kelvin. It is well described by quantum chromodynamics (QCD); however simulating a full heavy-ion collision directly from QCD is prohibitively expensive, even with a quantum computer. Modern modeling of the QGP is centered around the belief that at large scales (larger than  $10^{-15}$  meters) it behaves as a fluid, and can therefore be treated with (relativistic) hydrodynamics. This belief comes from both theoretical work (see [353]) and evidence for hydrodynamic behavior in experiments [232].

The central object of relativistic hydrodynamics [353] is the *energy-momentum tensor*  $T^{\mu\nu}$ . This is a conserved quantity, obeying

$$\partial_\mu T^{\mu\nu} = 0. \quad (88)$$

This equation has no content without the definition of  $T$ . This tensor is obtained from a gradient expansion and expressed in terms of the local velocity and density fields. Certain components of  $T$  have simple physical interpretation: in particular  $T^{00}$  is the energy density, and  $T^{0i} = p^i$  is the momentum density.

Relativistic hydrodynamics is a somewhat exotic theory. It has a far more familiar non-relativistic limit: the Navier-Stokes equation. This is a partial differential equation describing the behavior of a fluid with pressure  $p$ , density  $\rho$ , and velocity  $u$ :

$$\rho \left( \frac{\partial u_i}{\partial t} + u_j \nabla_j u_i \right) + \nabla p = \eta \partial_j (\partial_i u_j + \partial_j u_i) + \left( \zeta - \frac{2}{3} \eta \right) \partial_i \partial_j u_j. \quad (89)$$

The coefficients  $\eta$  and  $\zeta$ , referred to respectively as the shear and bulk viscosities, are free parameters of the model. They appear as free parameters in this equation because they are free parameters in the mapping from the density and velocity fields to the energy-momentum tensor. They must be determined either by a fit to data, or by microscopic (i.e. non-hydrodynamic) calculations.

## Simulations of quantum chromodynamics and nuclear astrophysics

Physically, these terms represent dissipation—they cause macroscopic disturbances to decay, with the energy of those disturbances converted into heat.

Full relativistic hydrodynamics has more free parameters, but it remains the case that shear viscosity is expected to be the dominant dissipative term (see e.g. [339] for a comparison of shear and bulk viscosities, and [353] for a discussion of higher-order coefficients). The simulation of relativistic hydrodynamics is a well studied problem; a modern simulation code used for heavy-ion collisions is MUSIC [372, 373, 311].

Such simulators require the viscosities as inputs. In the case of the QGP, no reliable microscopic calculation of the viscosities is available—they can be determined only by fits to data, and then somewhat imprecisely. A large-scale quantum computer would rectify this, allowing first-principles determination of the transport coefficients. This calculation proceeds by simulating the time-evolution of hot and dense matter under a lattice discretization of the QCD Hamiltonian. The simplest such discretization is [231]

$$H_{\text{QCD}} = -\frac{1}{g^2 a} \sum_P \text{Re Tr} \left[ \prod_{\langle ij \rangle \in P} U_{ij} \right] + \frac{4g^2}{a} \sum_{\langle ij \rangle} \pi_{ij}^2 + m \sum_i \bar{\psi}_i \psi_i + \sum_{\langle ij \rangle} \bar{\psi}_i U_{ij} \psi_j. \quad (90)$$

This Hamiltonian addresses continuous objects (the gauge fields  $U$ ) not suitable for direct implementation on a qubit-based quantum computer. A large and rapidly growing literature seeks the most efficient “qubitization” of the Hamiltonian (of which a small sample is [197, 196, 4, 82]); this question will not be addressed further here, but rather in the spirit of [243] we will treat the qubitization as a subroutine, any implementation of which can be used by the higher-level algorithm for studying hydrodynamics.

Our focus is on the shear viscosity, which is believed to be the dominant dissipative force in the QGP. The shear viscosity may be understood as a constant determining the rate of decay of a shear wave. A shear wave is a particular (low-energy) excitation of a fluid in which one component of the velocity, say  $v_1(x)$ , depends on a separate coefficient of the position. As a simplest example we might have

$$v_1(x, t) = A(t) \sin kx_3 \quad (91)$$

with  $v_2 = v_3 = 0$ . The coefficient  $A$  is the amplitude of the shear wave, and at late times has an exponential decay proportional to  $\eta$ .

In order to measure the shear viscosity we will need to measure correlation functions of  $T^{0i}$ . This operator is defined in the continuum, not on the lattice. We must find a sequence of lattice operators, constructed in terms of the fundamental operators used to construct the Hamiltonian of Eq. (90), that converge to  $T^{0i}$  in the continuum. One such calculation is described in [87]; a more careful nonperturbative calculation (done classically via lattice QCD) may improve the convergence of the quantum calculation.

**Overview of the value of the application** The QGP is the central object of study at BNL’s Relativistic Heavy-Ion Collider, see for example [346], which highlights the study of the low-viscosity quark-gluon-plasma at RHIC. RHIC’s original construction cost was around \$617 million [415], and in 2006 its yearly operational budget was estimated at the level of \$115.5 million [343].

The ability to *reliably* calculate transport coefficients—particularly the shear viscosity—is of theoretical interest independent from the behavior of the standard model and QCD. A long-standing conjecture holds that the shear viscosity of a fluid can never fall below the *KSS bound*  $\eta \geq \frac{1}{4\pi} s$ ,



## Simulations of quantum chromodynamics and nuclear astrophysics

where  $s$  is the entropy density [237]. The bound itself is now widely believed invalid in general [93]; however comparatively little is known about field theories exhibiting low ratios  $\frac{\eta}{s}$ , and it is not known whether or not QCD in particular violates the bound.

**Concrete utility estimation** To further emphasize the importance of QGP studies at RHIC, and the importance of viscosity to the QGP, we offer the following statistics, gleaned from theoretical physics articles posted to the arxiv through January 20, 2024:

- Of 5582 articles mentioning RHIC or LHC in the title or abstract, a total of 503 also mention the QGP (9%).
- Of 5582 articles mentioning RHIC or LHC in the title or abstract, a total of 259 also mention viscosity (5%).
- Specifically with regards to RHIC: of 2976 articles mentioning RHIC in the title or abstract, a total of 215 (7%) mention viscosity.
- Of 1302 articles mentioning the QGP in the title or abstract, a total of 182 also mention viscosity (14%).

Taking these crude measures at face value, it appears that viscosity is deeply relevant to at least 7% of the scientific work of RHIC, corresponding to \$43 million of the construction cost or to \$8 million of yearly operational cost (based on the 2006 estimation [343]).

**Objectives** To predict the angle-dependent distribution of energy produced in heavy-ion collisions at RHIC and LHC.

**End-to-end computational workflow** There are three large-scale steps to this calculation: a classical pre-processing step for determining lattice parameters, the core step utilizing the quantum processor, and a classical post-processing step in which hydrodynamic simulations are performed:

1. Determine a suitable set of lattice parameters of a qubitized Hamiltonian. This determines the free parameters to be used in the quantum circuit for the second step.
2. Estimate transport coefficients (and other thermodynamic properties) of QCD matter, using this Hamiltonian as an approximation to continuum QCD, across a range of chemical potentials and temperatures.
3. Using these coefficients, perform hydrodynamics simulations of the sort being performed today, to predict the distribution of energy yields in a collision at RHIC.

In what follows we will, for concreteness, assume that the gauge fields are qubitized as described in [4]. The quark fields are unaffected by this qubitization, and no additional free parameters are introduced in the fermionic part of the Hamiltonian  $H_f$ . The bosonic fields are significantly restricted: each link is now associated to a 1080-dimensional Hilbert space formally spanned by the elements of the Valentiner subgroup of  $SU(3)$ . To permit a closer approach to the continuum limit, the Hamiltonian to be used has an additional free parameter  $\gamma$ :

$$H_{\text{QCD}} = -\frac{1}{g^2 a} \sum_P \text{Re Tr} \left[ \prod_{\langle ij \rangle \in P} U_{ij} + \gamma \left( \prod_{\langle ij \rangle \in P} U_{ij} \right)^2 \right] + \frac{4g^2}{a} \sum_{\langle ij \rangle} \pi_{ij}^2 + H_f. \quad (92)$$

## Simulations of quantum chromodynamics and nuclear astrophysics

The parameter  $\gamma$  has been determined [4] and validated [5] for pure gauge fields in the action formalism. These values are likely to be approximately correct for gauge fields coupled to fermions in the Hamiltonian formalism, but not exactly. We describe now a procedure for determining these values, simultaneously with the fermion mass parameter, via classical lattice calculations (see [142] for an introductory reference). The entire procedure takes place at a fixed desired lattice spacing  $a$ .

1. For a given set of parameters  $g^2, a, \gamma, m$ , perform HMC sampling (as described in [142] or similar) to collect  $\sim 100$  statistically independent samples.
2. Measure the pion mass and string tension.
3. If the error bars on the above measurements exceed 10%, return to step 1 and collect more samples.
4. Repeat the above for a grid of parameters  $(g^2, \gamma, m)$  to identify those with pion mass and string tension matching the physical values.
5. Via the transfer matrix formalism [95], convert these parameters in the action to Hamiltonian parameters.

With this procedure complete, we have determined a Hamiltonian system that is a good approximation to continuum QCD. The approximation can be improved by various means; the most important (here elided) is to repeat the above procedure for a somewhat finer lattice spacing (a difference of 25% is reasonable), and then perform the same simulations on both lattices. The difference between the two simulations provides an estimate of the error due to lattice artifacts, and the two can be used to extrapolate to the physical ( $a = 0$ ) point.

We now turn to the second step above; that is, the computation of the shear viscosity. The outline of this procedure is simple, crudely resembling a physical experiment. We must first prepare a sample of the material to be studied (hot, dense QCD), and then we inspect the behavior of shear fluctuations, brought into existence by the finite temperature, over time. This procedure is repeated for each sample of interest—that is, each number and energy density.

The preparation of the sample is the least obvious step—unlike Hamiltonian evolution (which is more-or-less a one-size-fits-all algorithm, at least for local lattice theories), state preparation is awash with system-specific complications. Happily the states we are interested in are at relatively high temperature, where state preparation is much easier. A variety of algorithms for this sort of state preparation have been discussed in the literature [85, 86, 87]; here we make use of a heat bath, which leads to an algorithm with a particular conceptual simplicity. We need one addition to the QCD Hamiltonian above:

$$H_{\text{coupled}} = H_{\text{QCD}} + \sum_{\langle ij \rangle} \frac{1}{2} (\phi_i - \phi_j)^2 + \sum_i \left( \frac{1}{2} \pi_i^2 \lambda \phi_i^4 \right) + g' \sum_i \bar{\psi}_i \psi_i \phi_i \quad (93)$$

The scalar fields  $\phi$  constitute the heat bath, coupled to the fermions by a Yukawa coupling. The single-index  $\pi_i$  operator is canonically conjugate to  $\phi_i$ , not to be confused with the two-index (and conceptually similar)  $\pi_{ij}$  of the QCD Hamiltonian. The simulation of strongly coupled scalar fields has been carefully described in [204], including the preparation of the vacuum. Therefore we are able to cool the QCD system by preparing a zero-temperature heat bath (with strong self-coupling  $\lambda$ ) and turning on a weak Yukawa coupling to drain energy. Note that bringing the heat bath into

## Simulations of quantum chromodynamics and nuclear astrophysics

the continuum limit is unimportant, so we can simply choose  $\lambda = 0.1$  from the outset and disregard the hypothetical  $\phi^2$  term.

In detail, the computation of the shear viscosity proceeds as follows [87]:

1. Prepare (on a quantum processor, with appropriate lattice couplings) a QCD state with the desired fermion density  $n$ . The state prepared does not matter: for concreteness let it be a product state, with all gauge fields in their strong-coupling ground state. Preparation of this sort of state is detailed in [247]. Note that this is not the ground state of any Hamiltonian we are interested in—it is in fact a very high-temperature state of the Hamiltonian under which we will evolve.
2. On a separate set of qubits prepare, following [204], the ground state of the strongly coupled scalar field. From this point on the two sets of qubits are to be considered one system.
3. Perform one step of time-evolution under the coupled Hamiltonian of Eq. (93), with Yukawa coupling  $g' \sim 0.01$ . The coupling is chosen to not substantially change the thermodynamics of the QCD system, while allowing equilibration to take place in a reasonable number of time-steps.
4. Measure the energy in the QCD fields ( $\langle H_{\text{QCD}} \rangle$ ). Return to step 3 and repeat as long as the energy density  $\epsilon$  is above the desired value.
5. Turn off the Yukawa coupling. Evolve for a short time additional ( $\sim 10 \text{ fm } c^{-1}$  will suffice) to equilibrate.
6. The simulated system is now in equilibrium, with the desired energy and fermion density. We now measure the amplitude of the shear wave; that is, the expectation value of the operator

$$\hat{A}_k = \int dx \sin kx_3 \hat{T}^{01}(x), \quad (94)$$

where the integral is taken over spatial positions  $x$  (after lattice discretization [87] this is a sum). The most interesting wavevector  $k$  to consider is the largest one available in the simulated system. The operator  $\hat{T}^{ij}$  is the energy-momentum tensor; the component  $T^{01}$  represents momentum density along the  $x_1$  direction, and an expression for it in terms of fundamental lattice operators is given in [87].

7. Continue to time-evolve according to an appropriate qubitization of Eq. (90), while periodically measuring the amplitude of the shear wave. Due to thermal fluctuations this is not a constant, but rather a random walk with some autocorrelation time. Evolve for  $\sim 5 \text{ fm } c^{-1}$ .
8. Inspect the autocorrelator  $\langle A(0)A(t) \rangle$  and fit to an exponential decay at  $t = 4 \text{ fm } c^{-1}$ . The decay coefficient yields an estimate of the shear viscosity.
9. The error bars on this extraction are likely too large. Return to step 7 and repeat until relative error on  $\eta$  is within 20%.
10. Repeat 1-9 for each pair  $(\epsilon, n)$  of energy and fermion density of interest.

The result of this procedure is a first-principles estimate of the rate of decay of shear waves in hot, dense QCD. Several approximations have been made (finite lattice size and so on), but all are in principle controllable by following the same procedure with different coefficients. In short: the calculation above is novel and of substantial physical interest.

## Simulations of quantum chromodynamics and nuclear astrophysics

**A note on limits.** In “concrete problem instantiation” below, a reasonable set of parameters is listed for obtaining a first estimate of the shear viscosity. Moreover, byproducts of this calculation (particularly the measurement of the shear correlator as a function of time) are of interest even without a high-precision estimate of the shear viscosity.

Nevertheless it is worth mentioning what is necessary in order to attain a higher precision calculation of the shear viscosity itself, beyond this first calculation. Several extrapolations must be performed. For the purpose of illustration (that is, with no guarantee of completeness), the limits which are to be considered are:

- The continuum limit: the lattice spacing is taken to zero, and the bare parameters in the Hamiltonian are tuned to achieve the physical meson and baryon masses.
- The infinite-volume limit: finite-volume effects are expected to be algebraic in  $mL$ , where  $L$  is the physical side-length of the lattice and  $m$  is a characteristic mass scale.
- The long-wavelength limit: the shear viscosity described the decay of a mode with asymptotically low wavenumber  $k$ .
- The long-time limit: the shear viscosity is defined from the *asymptotic* behavior of the correlator discussed above.
- The high-statistics limit: the determination of shear viscosity can only be done when the measured correlator is sufficiently free from statistical noise.

Not all of these limits commute, and where they do not, physical considerations select the correct order of limits. Schematically this order is:

$$\lim_{k \rightarrow 0} \lim_{t \rightarrow 0} \lim_{L \rightarrow \infty} \lim_{a \rightarrow 0} \lim_{\text{statistics}} . \quad (95)$$

In practice these limits are accomplished by performing calculations close enough to the asymptotic regime that the scaling (and therefore systematic errors) can be estimated from one or two data points. For example, one might perform one calculation at a lattice spacing of 0.15 fm, and another at a lattice spacing of 0.12 fm; the difference between the two offers a reasonable estimate of the systematic error induced by the finite lattice spacing.

### Why classical methods are not sufficient to perform the hard computational module

The hard computational piece is the determination of shear viscosity from QCD. Shear viscosities have been computed via perturbation theory for weakly-coupled fields theories [195]. However, at the energy scales probed by RHIC, QCD is strongly coupled—by definition, perturbation theory is a very poor approximation. (This is a large part of what makes RHIC physics so interesting.) Indeed, perturbative estimates of the shear viscosity of the quark-gluon plasma have historically varied over multiple orders of magnitude.

This leaves nonperturbative methods, which in the context of quantum chromodynamics means lattice QCD. Classical computational methods for quantum systems are most successful when computing thermodynamic (static) properties of matter at vanishing chemical potential—that is, when there is an equal number of fermions and antifermions. The resource scaling of these methods is a low-order polynomial for such systems. When dynamical quantities are desired, the resource scaling becomes exponential in the size of the system being simulated. Similarly, when there is a strong

## Simulations of quantum chromodynamics and nuclear astrophysics

fermion-antifermion imbalance, the resource scaling of known algorithms is again exponential due to the famous “fermion sign problem”. This latter problem is exceptionally well-studied, and has been the target of intense research for three decades. A solution for QCD remains elusive.

**Concrete problem instantiation** To concretely instantiate the above algorithm we need to pick precise physical parameters to be simulated. There are three sets of physical parameters: those defining the Hamiltonian, those defining the matter to be simulated, and those defining the estimation of shear viscosity. Our recommendation for a valuable initial calculation is:

Category	Parameter	Value	Justification
Hamiltonian	$a$	0.2 fm	$aT \ll 1$
	$L$	2 fm	$LT \gg 1$
Matter	$T$	160 MeV	Pseudocritical temperature [319]
	$n$	0	Previous estimates available
Fit	$k$	$2\pi/L$	Fits in box
	$t$	$4 \text{ fm } c^{-1}$	Heavy-ion timescale

The final column in the table above summarizes the primary consideration justifying the choice of parameter. Note also that the above table reports a temperature rather than an energy density—it is readily converted to an energy density via the equation of state (see [319]).

The above calculation is physically informative and would on its own represent a major advance in our understanding of the hydrodynamics of QCD matter. However, to perform a hydrodynamic simulation we need not just one value of the shear viscosity, but measurements across a range of energy and number densities. Happily, at least away from the conjectured QCD critical point, the transport coefficients may be expected to vary smoothly with temperature and chemical potential. Therefore, a sensible initial task is to compute the shear viscosity as described above on a coarse grid of temperatures and chemical potentials. A  $10 \times 10$  grid with dimensions set by the largest energy and number density occurring in a current hydrodynamic calculation should be sufficient. For concreteness, take the peak energy density to be  $T_{\max} = 3 \text{ GeV fm}^{-3}$  [33] and the peak number density to be  $n_{\max} = 3\rho_0 = 0.45 \text{ fm}^{-3}$ .

### 7.3 Requirements summary

This section summarizes the application requirements for all the applications described in this chapter.

## Simulations of quantum chromodynamics and nuclear astrophysics

### Application 1: Supernova neutrinos

	Total time limit	5 years (order of magnitude related to the lifespan of the corresponding experiments)
<b>Workload:</b>	Number of subroutine calls required	1000 = 10 (coupling to supernova sims.) × 100 (iterations over $K, N, \bar{N}$ )
	Maximum subroutine time limit	N/A
<b>Problem specifications:</b>	Model type	Fermionic Hamiltonian
	Size	1000 momenta modes
	Interaction Structure	Fully connected
	Computational target	Flavor occupation numbers
	Accuracy requirement	1% relative on flavor occupation numbers

### Application 2: Hydrodynamics of hot and dense matter

	Total time limit	5 years (order of magnitude related to the lifespan of the corresponding experiments)
<b>Workload:</b>	Number of subroutine calls required	200 = 10 (energies) × 10 (densities) × 2 (lattice spacings)
	Maximum subroutine time limit	N/A
<b>Problem specifications:</b>	Model type	Qubitized QCD Hamiltonian
	Size	36,000 = 10 × 10 × 10 (lattice sites) × 11 (Valentiner qubitization) × 3 (links per site) + 3000 (fermions)
	Interaction Structure	Sparse regular (3D lattice)
	Computational target	Shear viscosity
	Accuracy requirement	20% relative on shear viscosity

## **8 End Notes**

### **8.1 Author Contributions**

The design and oversight of this document was contributed by Carleton Coffrin, Stephan Eidenbenz, Andrey Lokhov, Sidhant Misra and Marc Vuffray. Contributions on quantum algorithms were provided by Andreas Bärtzchi and Abhijith Jayakumar. Implementations of quantum algorithms and related supplementary materials were prepared by Jonhas Colina, Zachary Morrell and Zain Mughal. The MAGLAB user facility application chapter was lead by Minseong Lee and Sidhant Misra. The high-temperature super conductivity application chapter was lead by Francesco Caravelli and Marc Vuffray. The driven-dissipative Dicke model application chapter was lead by Andrei Piryatinski and Marc Vuffray. The exotic phases of magnetic materials application chapter was lead by Allen Scheie and Sidhant Misra. The catalysis for artificial photosynthesis application chapter was lead by Avanish Mishra, Yu Zhang and Andrey Lokhov. The nuclear physics and astrophysics applications chapter was lead by Duff Neill, Scott Lawrence and Andrey Lokhov.

### **8.2 Acknowledgements**

The contributors of this manuscript kindly thank: Dr. Joe Altepeter for making this research possible; Dr. Dave Clader, Dr. Rachael Al-Saadon and Dr. Yeuan-Ming Sheu for technical feedback on early drafts of this document; Dr. Jian-Xin Zhu for helpful discussions on modeling superconductivity in materials; Ms. Anna Trujillo for project management support of this research; Los Alamos National Laboratory's High Performance Computing Division for institutional computing workload data and discussions. This research was developed with funding from the Defense Advanced Research Projects Agency (DARPA). The views, opinions and/or findings expressed are those of the authors and should not be interpreted as representing the official views or policies of the Department of Defense or the U.S. Government.

### **8.3 Change Log**

- v0.1.0 - First document version. Application chapters on experimental magnetic materials, Fermi-Hubbard materials, dissipative Dicke model, magnetic material phases, artificial photosynthesis, and nuclear physics and astrophysics.

## References

- [1] Scott Aaronson. “Read the fine print”. In: *Nature Physics* 11.4 (2015), pp. 291–293.
- [2] Abi, B., et. al. “Supernova neutrino burst detection with the deep underground neutrino experiment”. In: *European Physical Journal C* 81.5, 423 (May 2021), p. 423. DOI: 10.1140/epjc/s10052-021-09166-w. arXiv: 2008.06647 [hep-ex].
- [3] Tameem Albash and Daniel A Lidar. “Adiabatic quantum computation”. In: *Reviews of Modern Physics* 90.1 (2018), p. 015002.
- [4] Andrei Alexandru et al. “Gluon Field Digitization for Quantum Computers”. In: *Phys. Rev. D* 100.11 (2019), p. 114501. DOI: 10.1103/PhysRevD.100.114501. arXiv: 1906.11213 [hep-lat].
- [5] Andrei Alexandru et al. “Spectrum of digitized QCD: Glueballs in a S(1080) gauge theory”. In: *Phys. Rev. D* 105.11 (2022), p. 114508. DOI: 10.1103/PhysRevD.105.114508. arXiv: 2112.08482 [hep-lat].
- [6] Andris Ambainis and Oded Regev. “An elementary proof of the quantum adiabatic theorem”. In: *arXiv preprint quant-ph/0411152* (2004).
- [7] P W Anderson. “The resonating valence bond state in La<sub>2</sub>CuO<sub>4</sub> and superconductivity”. en. In: *Science* 235.4793 (Mar. 1987), pp. 1196–1198.
- [8] Philip W Anderson. “An approximate quantum theory of the antiferromagnetic ground state”. In: *Physical Review* 86.5 (1952), p. 694.
- [9] Francesco Aquilante et al. “Modern quantum chemistry with [Open]Molcas”. en. In: *J. Chem. Phys.* 152.21 (June 2020), p. 214117.
- [10] Marcelo Arlego and Wolfram Brenig. “Plaquette order in the  $J_1 - J_2 - J_3$  model: Series expansion analysis”. In: *Phys. Rev. B* 78 (22 Dec. 2008), p. 224415. DOI: 10.1103/PhysRevB.78.224415. URL: <https://link.aps.org/doi/10.1103/PhysRevB.78.224415>.
- [11] Daniel P Arovas et al. “The Hubbard model”. en. In: *Annu. Rev. Condens. Matter Phys.* 13.1 (Mar. 2022), pp. 239–274.
- [12] N. W. Ashcroft and N. D. Mermin. *Solid State Physics*. Holt-Saunders, 1976.
- [13] Nikita Astrakhantsev et al. “Broken-Symmetry Ground States of the Heisenberg Model on the Pyrochlore Lattice”. In: *Phys. Rev. X* 11 (4 Oct. 2021), p. 041021. DOI: 10.1103/PhysRevX.11.041021. URL: <https://link.aps.org/doi/10.1103/PhysRevX.11.041021>.
- [14] Harry A Atwater. “Artificial photosynthesis: A pathway to solar fuels”. In: *Physics Today* 76.12 (2023), pp. 32–39.
- [15] B. B. Back et al. “Recent developments in heavy-ion fusion reactions”. In: *Rev. Mod. Phys.* 86.1 (Mar. 2014), pp. 317–360. DOI: 10.1103/RevModPhys.86.317. URL: <https://link.aps.org/doi/10.1103/RevModPhys.86.317>.
- [16] A. B. Balantekin and Y. Pehlivan. “Neutrino-Neutrino Interactions and Flavor Mixing in Dense Matter”. In: *J. Phys. G* 34 (2007), pp. 47–66. DOI: 10.1088/0954-3899/34/1/004. arXiv: astro-ph/0607527.
- [17] A. B. Balantekin et al. “Quantum information and quantum simulation of neutrino physics”. In: *Eur. Phys. J. A* 59.8 (2023), p. 186. DOI: 10.1140/epja/s10050-023-01092-7. arXiv: 2305.01150 [nucl-th].



## References

- [18] A Banerjee et al. “Proximate Kitaev quantum spin liquid behaviour in a honeycomb magnet”. In: *Nature materials* 15.7 (2016), pp. 733–740.
- [19] Arnab Banerjee et al. “Neutron scattering in the proximate quantum spin liquid  $\text{RuCl}_3$ ”. In: *Science* 356.6342 (2017), pp. 1055–1059. DOI: 10.1126/science.aah6015. eprint: <https://www.science.org/doi/pdf/10.1126/science.aah6015>. URL: <https://www.science.org/doi/abs/10.1126/science.aah6015>.
- [20] James Barber and Phong D Tran. “From natural to artificial photosynthesis”. In: *Journal of The Royal Society Interface* 10.81 (2013), p. 20120984.
- [21] Rodney J. Bartlett and Monika Musiał. “Coupled-cluster theory in quantum chemistry”. In: *Rev. Mod. Phys.* 79.1 (Feb. 2007), pp. 291–352. DOI: 10.1103/RevModPhys.79.291. URL: <https://link.aps.org/doi/10.1103/RevModPhys.79.291>.
- [22] Bela Bauer et al. “Quantum Algorithms for Quantum Chemistry and Quantum Materials Science”. In: *Chem. Rev.* 120.22 (Nov. 2020), pp. 12685–12717. DOI: 10.1021/acs.chemrev.9b00829. URL: <https://doi.org/10.1021/acs.chemrev.9b00829>.
- [23] K. S. D. Beach. “Master equation approach to computing RVB bond amplitudes”. In: *Phys. Rev. B* 79 (22 June 2009), p. 224431. DOI: 10.1103/PhysRevB.79.224431. URL: <https://link.aps.org/doi/10.1103/PhysRevB.79.224431>.
- [24] Axel D. Becke. “Perspective: Fifty years of density-functional theory in chemical physics”. In: *J. Chem. Phys.* 140.18 (Apr. 2014), 18A301. ISSN: 0021-9606. DOI: 10.1063/1.4869598. eprint: [https://pubs.aip.org/aip/jcp/article-pdf/doi/10.1063/1.4869598/15480507/18a301\\_1\\_online.pdf](https://pubs.aip.org/aip/jcp/article-pdf/doi/10.1063/1.4869598/15480507/18a301_1_online.pdf). URL: <https://doi.org/10.1063/1.4869598>.
- [25] Andrew C Benniston and Anthony Harriman. “Artificial photosynthesis”. In: *Materials Today* 11.12 (2008), pp. 26–34.
- [26] Owen Benton et al. “A spin-liquid with pinch-line singularities on the pyrochlore lattice”. In: *Nature Communications* 7 (2016), p. 11572. DOI: 10.1038/ncomms11572.
- [27] Serena Berardi et al. “Molecular artificial photosynthesis”. In: *Chem. Soc. Rev.* 43 (22 2014), pp. 7501–7519. DOI: 10.1039/C3CS60405E. URL: <http://dx.doi.org/10.1039/C3CS60405E>.
- [28] Dominic W Berry et al. “Efficient quantum algorithms for simulating sparse Hamiltonians”. In: *Communications in Mathematical Physics* 270 (2007), pp. 359–371.
- [29] Dominic W Berry et al. “Simulating Hamiltonian dynamics with a truncated Taylor series”. In: *Physical review letters* 114.9 (2015), p. 090502.
- [30] H. A. Bethe. “Supernova mechanisms”. In: *Rev. Mod. Phys.* 62 (4 Oct. 1990), pp. 801–866. DOI: 10.1103/RevModPhys.62.801.
- [31] Hans Bethe. “Zur theorie der metalle: I. Eigenwerte und eigenfunktionen der linearen atomkette”. In: *Zeitschrift für Physik* 71.3-4 (1931), pp. 205–226.
- [32] Uwe Birkenheuer et al. “Model density approach to the Kohn–Sham problem: Efficient extension of the density fitting technique”. In: *Int. Quantum Chem.* 102.5 (2005), pp. 743–761.
- [33] J. D. Bjorken. “Highly Relativistic Nucleus-Nucleus Collisions: The Central Rapidity Region”. In: *Phys. Rev. D* 27 (1983), pp. 140–151. DOI: 10.1103/PhysRevD.27.140.

## References

- [34] R Blankenbecler, D J Scalapino, and R L Sugar. “Monte Carlo calculations of coupled boson-fermion systems. I”. en. In: *Phys. Rev. D Part. Fields* 24.8 (Oct. 1981), pp. 2278–2286.
- [35] P E Blöchl. “Projector augmented-wave method”. en. In: *Phys. Rev. B Condens. Matter* 50.24 (Dec. 1994), pp. 17953–17979.
- [36] Sergio Boixo, Emanuel Knill, and Rolando D Somma. “Fast quantum algorithms for traversing paths of eigenstates”. In: *arXiv preprint arXiv:1005.3034* (2010).
- [37] Xavier Bonet-Monroig, Ryan Babbush, and Thomas E. O’Brien. “Nearly Optimal Measurement Scheduling for Partial Tomography of Quantum States”. In: *Phys. Rev. X* 10 (3 Sept. 2020), p. 031064. DOI: 10.1103/PhysRevX.10.031064. URL: <https://link.aps.org/doi/10.1103/PhysRevX.10.031064>.
- [38] Michael Bonitz and Dirk Semkat, eds. *Introduction to computational methods in many body physics*. Rinton Press, Feb. 2006.
- [39] Andrew T Boothroyd. *Principles of neutron scattering from condensed matter*. Oxford University Press, 2020.
- [40] M. Born and R. Oppenheimer. “Zur Quantentheorie der Molekeln”. In: *Annalen der Physik* 389.20 (1927), pp. 457–484. DOI: <https://doi.org/10.1002/andp.19273892002>. eprint: <https://onlinelibrary.wiley.com/doi/pdf/10.1002/andp.19273892002>. URL: <https://onlinelibrary.wiley.com/doi/abs/10.1002/andp.19273892002>.
- [41] Sergey B Bravyi and Alexei Yu Kitaev. “Fermionic quantum computation”. In: *Annals of Physics* 298.1 (2002), pp. 210–226.
- [42] Sergey B. Bravyi and Alexei Yu. Kitaev. “Fermionic Quantum Computation”. In: *Ann. Phys.* 298.1 (2002), pp. 210–226. ISSN: 0003-4916. DOI: <https://doi.org/10.1006/aphy.2002.6254>. URL: <http://www.sciencedirect.com/science/article/pii/S0003491602962548>.
- [43] C Broholm et al. “Quantum spin liquids”. In: *Science* 367.6475 (2020), eaay0668.
- [44] Henrik Bruus and Karsten Flensburg. *Many-body quantum theory in condensed matter physics*. en. Oxford Graduate Texts. London, England: Oxford University Press, Sept. 2004.
- [45] Finn Lasse Buessen and Simon Trebst. “Competing magnetic orders and spin liquids in two- and three-dimensional kagome systems: Pseudofermion functional renormalization group perspective”. In: *Phys. Rev. B* 94 (23 Dec. 2016), p. 235138. DOI: 10.1103/PhysRevB.94.235138. URL: <https://link.aps.org/doi/10.1103/PhysRevB.94.235138>.
- [46] Ralf Bulla, Theo A Costi, and Thomas Pruschke. “Numerical renormalization group method for quantum impurity systems”. en. In: *Rev. Mod. Phys.* 80.2 (Apr. 2008), pp. 395–450.
- [47] Vera von Burg et al. “Quantum computing enhanced computational catalysis”. In: *Phys. Rev. Res.* 3.3 (2021), p. 033055.
- [48] I J Bush et al. “Parallel implementation of the ab initio CRYSTAL program: electronic structure calculations for periodic systems”. en. In: *Proc. Math. Phys. Eng. Sci.* 467.2131 (July 2011), pp. 2112–2126.
- [49] Earl Campbell. “Random compiler for fast Hamiltonian simulation”. In: *Physical review letters* 123.7 (2019), p. 070503.
- [50] Yudong Cao et al. “Quantum Chemistry in the Age of Quantum Computing”. In: *Chem. Rev.* 119.19 (2019), pp. 10856–10915. DOI: 10.1021/acs.chemrev.8b00803.

## References

- [51] Yudong Cao et al. “Quantum chemistry in the age of quantum computing”. In: *Chem. Rev.* 119.19 (2019), pp. 10856–10915.
- [52] Luca Capriotti and Sandro Sorella. “Spontaneous Plaquette Dimerization in the  $J_1 - -J_2$  Heisenberg Model”. In: *Phys. Rev. Lett.* 84 (14 Apr. 2000), pp. 3173–3176. DOI: 10.1103/PhysRevLett.84.3173. URL: <https://link.aps.org/doi/10.1103/PhysRevLett.84.3173>.
- [53] Luca Capriotti et al. “Resonating Valence Bond Wave Functions for Strongly Frustrated Spin Systems”. In: *Phys. Rev. Lett.* 87 (9 Aug. 2001), p. 097201. DOI: 10.1103/PhysRevLett.87.097201. URL: <https://link.aps.org/doi/10.1103/PhysRevLett.87.097201>.
- [54] R. Car and M. Parrinello. “Unified Approach for Molecular Dynamics and Density-Functional Theory”. In: *Phys. Rev. Lett.* 55 (22 Nov. 1985), pp. 2471–2474. DOI: 10.1103/PhysRevLett.55.2471. URL: <https://link.aps.org/doi/10.1103/PhysRevLett.55.2471>.
- [55] E W Carlson et al. “Concepts in high temperature superconductivity”. In: (2002).
- [56] Troy Carter et al. “Powering the Future: Fusion & Plasmas”. In: (Dec. 2020). DOI: 10.2172/1995209. URL: <https://www.osti.gov/biblio/1995209>.
- [57] *Catalyst Market Size Research Report [2023-2030] | 116 Pages — linkedin.com*. <https://www.linkedin.com/pulse/catalyst-market-size-research-report-gxae/>. [Accessed 08-04-2024].
- [58] M. Cerezo et al. “Challenges and opportunities in quantum machine learning”. In: *Nature Computational Science* 2.9 (Sept. 2022). ISSN: 2662-8457. DOI: 10.1038/s43588-022-00311-3. URL: <https://doi.org/10.1038/s43588-022-00311-3>.
- [59] M. Cerezo et al. *Does provable absence of barren plateaus imply classical simulability? Or, why we need to rethink variational quantum computing*. 2023. eprint: arXiv:2312.09121.
- [60] M. Cerezo et al. “Variational quantum algorithms”. In: *Nature Reviews Physics* 3.9 (Sept. 2021), pp. 625–644. ISSN: 2522-5820. DOI: 10.1038/s42254-021-00348-9. URL: <https://doi.org/10.1038/s42254-021-00348-9>.
- [61] Marco Cerezo et al. “Variational quantum algorithms”. In: *Nature Reviews Physics* 3.9 (2021), pp. 625–644.
- [62] P B Chakraborty, P J H Denteneer, and R T Scalettar. “Determinant quantum Monte Carlo study of the screening of the one-body potential near a metal-insulator transition”. In: *Phys. Rev. B Condens. Matter Mater. Phys.* 75.12 (Mar. 2007).
- [63] Garnet Kin-Lic Chan and Sandeep Sharma. “The Density Matrix Renormalization Group in Quantum Chemistry”. In: *Annual Review of Physical Chemistry* 62.1 (2024/01/30 2011), pp. 465–481. DOI: 10.1146/annurev-physchem-032210-103338. URL: <https://doi.org/10.1146/annurev-physchem-032210-103338>.
- [64] P. Chandra and B. Douçot. “Possible spin-liquid state at large  $S$  for the frustrated square Heisenberg lattice”. In: *Phys. Rev. B* 38 (13 Nov. 1988), pp. 9335–9338. DOI: 10.1103/PhysRevB.38.9335. URL: <https://link.aps.org/doi/10.1103/PhysRevB.38.9335>.
- [65] K A Chao, J Spałek, and A M Oleś. “Canonical perturbation expansion of the Hubbard model”. In: *Phys. Rev. B Condens. Matter* 18.7 (Oct. 1978), pp. 3453–3464.
- [66] Benjamin W. J. Chen, Lang Xu, and Manos Mavrikakis. “Computational Methods in Heterogeneous Catalysis”. In: *Chem. Rev.* 121.2 (2021), pp. 1007–1048. DOI: 10.1021/acs.chemrev.0c01060.

## References

- [67] Benjamin W. J. Chen, Lang Xu, and Manos Mavrikakis. “Computational Methods in Heterogeneous Catalysis”. In: *Chemical Reviews* 121.2 (2021), pp. 1007–1048. DOI: 10.1021/acs.chemrev.0c01060.
- [68] Chi-Fang Chen, Michael J Kastoryano, and András Gilyén. “An efficient and exact noncommutative quantum Gibbs sampler”. In: *arXiv preprint arXiv:2311.09207* (2023).
- [69] Chi-Fang Chen et al. “Concentration for random product formulas”. In: *PRX Quantum* 2.4 (2021), p. 040305.
- [70] Chi-Fang Chen et al. “Quantum thermal state preparation”. In: *arXiv preprint arXiv:2303.18224* (2023).
- [71] Sang-Wook Cheong and Maxim Mostovoy. “Multiferroics: a magnetic twist for ferroelectricity”. In: *Nature materials* 6.1 (2007), pp. 13–20.
- [72] Li Ern Chern and Yong Baek Kim. “Theoretical study of quantum spin liquids in  $S = \frac{1}{2}$  hyper-hyperkagome magnets: Classification, heat capacity, and dynamical spin structure factor”. In: *Phys. Rev. B* 104 (9 Sept. 2021), p. 094413. DOI: 10.1103/PhysRevB.104.094413. URL: <https://link.aps.org/doi/10.1103/PhysRevB.104.094413>.
- [73] Andrew M Childs. “On the relationship between continuous-and discrete-time quantum walk”. In: *Communications in Mathematical Physics* 294 (2010), pp. 581–603.
- [74] Andrew M Childs, Aaron Ostrander, and Yuan Su. “Faster quantum simulation by randomization”. In: *Quantum* 3 (2019), p. 182.
- [75] Andrew M Childs et al. “Theory of trotter error with commutator scaling”. In: *Physical Review X* 11.1 (2021), p. 011020.
- [76] Andrew M Childs et al. “Toward the first quantum simulation with quantum speedup”. In: *Proceedings of the National Academy of Sciences* 115.38 (2018), pp. 9456–9461.
- [77] Andrew M. Childs and Robin Kothari. “Limitations on the simulation of non-sparse hamiltonians”. In: *Quantum Info. Comput.* 10.7 (July 2010), pp. 669–684. ISSN: 1533-7146.
- [78] Andrew M. Childs and Tongyang Li. “Efficient simulation of sparse Markovian quantum dynamics”. In: *Quantum Information & Computation* 17.11&12 (2017), pp. 901–947. DOI: 10.26421/QIC17.11-12.
- [79] Chung-Pin Chou and Hong-Yi Chen. “Simulating a two-dimensional frustrated spin system with fermionic resonating-valence-bond states”. In: *Phys. Rev. B* 90 (4 July 2014), p. 041106. DOI: 10.1103/PhysRevB.90.041106. URL: <https://link.aps.org/doi/10.1103/PhysRevB.90.041106>.
- [80] Anirban Narayan Chowdhury and Rolando D. Somma. “Quantum algorithms for Gibbs sampling and hitting-time estimation”. In: *Quantum Information & Computation* 17.1&2 (2017), pp. 41–64. DOI: 10.26421/QIC17.1-2.
- [81] Andrey V. Chubukov and Th. Jolicoeur. “Dimer stability region in a frustrated quantum Heisenberg antiferromagnet”. In: *Phys. Rev. B* 44 (21 Dec. 1991), pp. 12050–12053. DOI: 10.1103/PhysRevB.44.12050. URL: <https://link.aps.org/doi/10.1103/PhysRevB.44.12050>.
- [82] Anthony Ciavarella, Natalie Klco, and Martin J. Savage. “Trailhead for quantum simulation of SU(3) Yang-Mills lattice gauge theory in the local multiplet basis”. In: *Phys. Rev. D* 103.9 (2021), p. 094501. DOI: 10.1103/PhysRevD.103.094501. arXiv: 2101.10227 [quant-ph].

## References

- [83] Vincenzo Cirigliano, Srimoyee Sen, and Yukari Yamauchi. “Neutrino many-body flavor evolution: the full Hamiltonian”. In: (). arXiv: 2404.16690.
- [84] Richard Cleve and Chunhao Wang. “Efficient quantum algorithms for simulating Lindblad evolution”. In: *arXiv preprint arXiv:1612.09512* (2016).
- [85] Thomas D. Cohen and Hyunwoo Oh. “Efficient vacuum-state preparation for quantum simulation of strongly interacting local quantum field theories”. In: *Phys. Rev. A* 109.2 (2024), p. L020402. DOI: 10.1103/PhysRevA.109.L020402. arXiv: 2310.19229 [hep-lat].
- [86] Thomas D. Cohen and Hyunwoo Oh. “Optimizing the rodeo projection algorithm”. In: *Phys. Rev. A* 108.3 (2023), p. 032422. DOI: 10.1103/PhysRevA.108.032422. arXiv: 2305.19952 [quant-ph].
- [87] Thomas D. Cohen et al. “Quantum algorithms for transport coefficients in gauge theories”. In: *Phys. Rev. D* 104.9 (2021), p. 094514. DOI: 10.1103/PhysRevD.104.094514. arXiv: 2104.02024 [hep-lat].
- [88] Michael A Collins. “Molecular potential-energy surfaces for chemical reaction dynamics”. In: *Theoretical Chemistry Accounts* 108 (2002), pp. 313–324.
- [89] Coalition for the Commercial Application of Superconductors (CCAS). “Superconductivity Present and Future Applications”. In: IEEE council on Superconductivity, 2014.
- [90] US Congress. “High-temperature superconductivity in perspective”. In: *Office of Technology Assessment*. US Government Printing Office, 1990.
- [91] Cyrille Costentin, Marc Robert, and Jean-Michel Savéant. “Catalysis of the electrochemical reduction of carbon dioxide”. In: *Chem. Soc. Rev.* 42.6 (2013), pp. 2423–2436.
- [92] Jordan Cotler and Frank Wilczek. “Quantum overlapping tomography”. In: *Physical review letters* 124.10 (2020), p. 100401.
- [93] Sera Cremonini. “The Shear Viscosity to Entropy Ratio: A Status Report”. In: *Mod. Phys. Lett. B* 25 (2011), pp. 1867–1888. DOI: 10.1142/S0217984911027315. arXiv: 1108.0677 [hep-th].
- [94] Rachel Crespo-Otero and Mario Barbatti. “Recent Advances and Perspectives on Nonadiabatic Mixed Quantum–Classical Dynamics”. In: *Chem. Rev.* 118.15 (2018), pp. 7026–7068. DOI: 10.1021/acs.chemrev.7b00577.
- [95] Michael Creutz. “Gauge Fixing, the Transfer Matrix, and Confinement on a Lattice”. In: *Phys. Rev. D* 15 (1977). Ed. by J. Julve and M. Ramón-Medrano, p. 1128. DOI: 10.1103/PhysRevD.15.1128.
- [96] Basile F. E. Curchod and Todd J. Martínez. “Ab Initio Nonadiabatic Quantum Molecular Dynamics”. In: *Chem. Rev.* 118.7 (2018), pp. 3305–3336. ISSN: 0009-2665. DOI: 10.1021/acs.chemrev.7b00423. (Visited on 10/17/2020).
- [97] Elbio Dagotto. “Correlated electrons in high-temperature superconductors”. In: *Rev. Mod. Phys.* 66.3 (July 1994), pp. 763–840.
- [98] Elbio Dagotto. “Correlated electrons in high-temperature superconductors”. In: *Rev. Mod. Phys.* 66.3 (July 1994), pp. 763–840.

## References

- [99] Elbio Dagotto and Adriana Moreo. “Phase diagram of the frustrated spin-1/2 Heisenberg antiferromagnet in 2 dimensions”. In: *Phys. Rev. Lett.* 63 (19 Nov. 1989), pp. 2148–2151. DOI: 10.1103/PhysRevLett.63.2148. URL: <https://link.aps.org/doi/10.1103/PhysRevLett.63.2148>.
- [100] Elbio Dagotto et al. “Properties of the multiorbital Hubbard models for the iron-based superconductors”. en. In: *Front. Phys.* 6.4 (Dec. 2011), pp. 379–397.
- [101] Peng-Ling Dai et al. “Spinon Fermi Surface Spin Liquid in a Triangular Lattice Antiferromagnet NaYbSe<sub>2</sub>”. In: *Phys. Rev. X* 11 (2 May 2021), p. 021044. DOI: 10.1103/PhysRevX.11.021044. URL: <https://link.aps.org/doi/10.1103/PhysRevX.11.021044>.
- [102] Alexander M Dalzell et al. “Quantum algorithms: A survey of applications and end-to-end complexities”. In: *arXiv preprint arXiv:2310.03011* (2023).
- [103] Andrea Damascelli, Zahid Hussain, and Zhi-Xun Shen. “Angle-resolved photoemission studies of the cuprate superconductors”. In: *Rev. Mod. Phys.* 75.2 (Apr. 2003), pp. 473–541.
- [104] R. Darradi et al. “Ground state phases of the spin-1/2  $J_1 - -J_2$  Heisenberg antiferromagnet on the square lattice: A high-order coupled cluster treatment”. In: *Phys. Rev. B* 78 (21 Dec. 2008), p. 214415. DOI: 10.1103/PhysRevB.78.214415. URL: <https://link.aps.org/doi/10.1103/PhysRevB.78.214415>.
- [105] Holger Dau, Etsuko Fujita, and Licheng Sun. “Artificial photosynthesis: Beyond mimicking nature”. In: *ChemSusChem* 10.22 (2017), pp. 4228–4235.
- [106] Holger Dau et al. “The Mechanism of Water Oxidation: From Electrolysis via Homogeneous to Biological Catalysis”. In: *ChemCatChem* 2.7 (2010), pp. 724–761. DOI: <https://doi.org/10.1002/cctc.201000126>. eprint: <https://chemistry-europe.onlinelibrary.wiley.com/doi/pdf/10.1002/cctc.201000126>. URL: <https://chemistry-europe.onlinelibrary.wiley.com/doi/abs/10.1002/cctc.201000126>.
- [107] J. M. Deutsch. “Quantum statistical mechanics in a closed system”. In: *Phys. Rev. A* 43 (4 Feb. 1991), pp. 2046–2049. DOI: 10.1103/PhysRevA.43.2046. URL: <https://link.aps.org/doi/10.1103/PhysRevA.43.2046>.
- [108] Bernard Dieny et al. “Opportunities and challenges for spintronics in the microelectronics industry”. In: *Nature Electronics* 3.8 (2020), pp. 446–459.
- [109] Lexin Ding, Stefan Knecht, and Christian Schilling. “Quantum Information-Assisted Complete Active Space Optimization (QICAS)”. In: *J. Phys. Chem. Lett.* 14.49 (Dec. 2023), pp. 11022–11029. DOI: 10.1021/acs.jpcllett.3c02536. URL: <https://doi.org/10.1021/acs.jpcllett.3c02536>.
- [110] Zhiyan Ding and Lin Lin. “Even shorter quantum circuit for phase estimation on early fault-tolerant quantum computers with applications to ground-state energy estimation”. In: *PRX Quantum* 4.2 (2023), p. 020331.
- [111] Lance J. Dixon. “Calculating scattering amplitudes efficiently”. In: *Theoretical Advanced Study Institute in Elementary Particle Physics (TASI 95): QCD and Beyond*. Jan. 1996, pp. 539–584. arXiv: [hep-ph/9601359](https://arxiv.org/abs/hep-ph/9601359).

## References

- [112] R. L. Doretto. “Plaquette valence-bond solid in the square-lattice  $J_1$ - $J_2$  antiferromagnet Heisenberg model: A bond operator approach”. In: *Phys. Rev. B* 89 (10 Mar. 2014), p. 104415. DOI: 10.1103/PhysRevB.89.104415. URL: <https://link.aps.org/doi/10.1103/PhysRevB.89.104415>.
- [113] F W Dorr. “Experience with the CRAY-1 computer at the Los Alamos Scientific Laboratory”. In: (Jan. 1977). URL: <https://www.osti.gov/biblio/7081495>.
- [114] Markus Drescher et al. “Dynamical signatures of symmetry-broken and liquid phases in an  $S = \frac{1}{2}$  Heisenberg antiferromagnet on the triangular lattice”. In: *Phys. Rev. B* 108 (22 Dec. 2023), p. L220401. DOI: 10.1103/PhysRevB.108.L220401. URL: <https://link.aps.org/doi/10.1103/PhysRevB.108.L220401>.
- [115] Jane Edgington and Linsey C Seitz. “Advancing the Rigor and Reproducibility of Electrocatalyst Stability Benchmarking and Intrinsic Material Degradation Analysis for Water Oxidation”. In: *ACS Catalysis* 13.5 (2023), pp. 3379–3394.
- [116] Wilma Eerenstein, ND Mathur, and James F Scott. “Multiferroic and magnetoelectric materials”. In: *nature* 442.7104 (2006), pp. 759–765.
- [117] T. Einarsson and H. J. Schulz. “Direct calculation of the spin stiffness in the  $J_1$ - $J_2$  Heisenberg antiferromagnet”. In: *Phys. Rev. B* 51 (9 Mar. 1995), pp. 6151–6154. DOI: 10.1103/PhysRevB.51.6151. URL: <https://link.aps.org/doi/10.1103/PhysRevB.51.6151>.
- [118] V. J. Emery, S. A. Kivelson, and J. M. Tranquada. “Stripe phases in high-temperature superconductors”. In: *Proceedings of the National Academy of Sciences* 96.16 (Aug. 1999), pp. 8814–8817. ISSN: 1091-6490. DOI: 10.1073/pnas.96.16.8814. URL: <http://dx.doi.org/10.1073/pnas.96.16.8814>.
- [119] Department of Energy. *E3SM - Energy Exascale Earth System Model*. <https://e3sm.org/>. [Accessed 15-04-2024]. 2014.
- [120] Department of Energy. *FY 2023 Congressional Budget*. <https://www.energy.gov/sites/default/files/2022-04/doe-fy-23-budget-stat-by-org-v2.pdf>. [Accessed 14-04-2024]. 2022.
- [121] Department of Energy. *Supercomputing and Exascale*. <https://www.energy.gov/supercomputing-and-exascale>. [Accessed 15-04-2024]. 2019.
- [122] F H Essler, V E Korepin, and K Schoutens. “Complete solution of the one-dimensional Hubbard model”. en. In: *Phys. Rev. Lett.* 67.27 (Dec. 1991), pp. 3848–3851.
- [123] Siyuan Fang et al. “Photocatalytic CO<sub>2</sub> reduction”. In: *Nature Reviews Methods Primers* 3.1 (2023), p. 61. DOI: 10.1038/s43586-023-00243-w. URL: <https://doi.org/10.1038/s43586-023-00243-w>.
- [124] Patrik Fazekas. In: *Lecture Notes on Electron Correlation and Magnetism*. WORLD SCIENTIFIC, Jan. 1999, pp. 1–16.
- [125] Amendra Fernando and Christine M. Aikens. “Reaction Pathways for Water Oxidation to Molecular Oxygen Mediated by Model Cobalt Oxide Dimer and Cubane Catalysts”. In: *J. Phys. Chem. C* 119.20 (2015), pp. 11072–11085. DOI: 10.1021/jp511805x.

## References

- [126] Francesco Ferrari and Federico Becca. “Gapless spin liquid and valence-bond solid in the  $J_1$ - $J_2$  Heisenberg model on the square lattice: Insights from singlet and triplet excitations”. In: *Phys. Rev. B* 102 (1 July 2020), p. 014417. DOI: 10.1103/PhysRevB.102.014417. URL: <https://link.aps.org/doi/10.1103/PhysRevB.102.014417>.
- [127] Richard P Feynman. “Simulating Physics with Computers”. In: *International Journal of Theoretical Physics* 21.6/7 (1982).
- [128] Richard P Feynman, Robert B Leighton, and Matthew Sands. *The Feynman lectures on physics*. Vol. 2. California Institute of Technology, 1964.
- [129] Richard P. Feynman. “Simulating physics with computers”. In: *International Journal of Theoretical Physics* 21.6 (June 1982), pp. 467–488. ISSN: 1572-9575. DOI: 10.1007/BF02650179. URL: <https://doi.org/10.1007/BF02650179>.
- [130] Richard P. Feynman. “Simulating physics with computers”. In: *Int. J. Theor. Phys.* 21.6 (1982), pp. 467–488. ISSN: 1572-9575. DOI: 10.1007/BF02650179. URL: <https://doi.org/10.1007/BF02650179>.
- [131] F. Figueirido et al. “Exact diagonalization of finite frustrated spin-(1/2 Heisenberg models”. In: *Phys. Rev. B* 41 (7 Mar. 1990), pp. 4619–4632. DOI: 10.1103/PhysRevB.41.4619. URL: <https://link.aps.org/doi/10.1103/PhysRevB.41.4619>.
- [132] Randy S Fishman, Jaime A Fernandez-Baca, and Toomas Rõõm. *Spin-wave theory and its applications to neutron scattering and THz spectroscopy*. Morgan & Claypool Publishers, 2018.
- [133] P Forn-Díaz et al. “Ultrastrong coupling regimes of light-matter interaction”. In: *Reviews of Modern Physics* 91.2 (2019), p. 025005.
- [134] W. M. C. Foulkes et al. “Quantum Monte Carlo simulations of solids”. In: *Rev. Mod. Phys.* 73 (1 Jan. 2001), pp. 33–83. DOI: 10.1103/RevModPhys.73.33. URL: <https://link.aps.org/doi/10.1103/RevModPhys.73.33>.
- [135] National Science Foundation. *NSF to sustain the world’s most powerful magnet lab through 2027*. <https://new.nsf.gov/news/nsf-sustain-worlds-most-powerful-magnet-lab>. [Accessed 13-03-2024]. 2022.
- [136] Fabio Franchini. *An introduction to integrable techniques for one-dimensional quantum systems*. en. 1st ed. Lecture notes in physics. Cham, Switzerland: Springer International Publishing, May 2017.
- [137] Irénée Frérot and Tommaso Roscilde. “Quantum variance: A measure of quantum coherence and quantum correlations for many-body systems”. In: *Phys. Rev. B* 94 (7 Aug. 2016), p. 075121. DOI: 10.1103/PhysRevB.94.075121. URL: <https://link.aps.org/doi/10.1103/PhysRevB.94.075121>.
- [138] Irénée Frérot and Tommaso Roscilde. “Reconstructing the quantum critical fan of strongly correlated systems using quantum correlations”. In: *Nat. Commun.* 10 (2019), p. 577. DOI: 10.1038/s41467-019-08324-9.
- [139] Anton Frisk Kockum et al. “Ultrastrong coupling between light and matter”. In: *Nature Reviews Physics* 1.1 (2019), pp. 19–40.
- [140] Masaki Fujita et al. “Progress in neutron scattering studies of spin excitations in high-TcCuprates”. en. In: *J. Phys. Soc. Jpn.* 81.1 (Jan. 2012), p. 011007.



## References

- [141] Junqi Gao et al. “Review of magnetoelectric sensors”. In: *Actuators*. Vol. 10. 6. MDPI. 2021, p. 109.
- [142] Christof Gatttringer and Christian Lang. *Quantum chromodynamics on the lattice: an introductory presentation*. Vol. 788. Springer Science & Business Media, 2009.
- [143] Michel Gaudin. *The Bethe wavefunction*. en. Cambridge, England: Cambridge University Press, Apr. 2014.
- [144] Florian Gebhard. *The Mott metal-insulator transition*. en. 1997th ed. Springer Tracts in Modern Physics. Berlin, Germany: Springer, Mar. 1997.
- [145] Paolo Giannozzi et al. “QUANTUM ESPRESSO: a modular and open-source software project for quantum simulations of materials”. en. In: *J. Phys. Condens. Matter* 21.39 (Sept. 2009), p. 395502.
- [146] András Gilyén. “Quantum Singular Value Transformation & Its Algorithmic Applications”. PhD thesis. University of Amsterdam, 2019. URL: <https://hdl.handle.net/11245.1/20e9733e-6014-402d-afa9-20f3cc4a0568>.
- [147] András Gilyén et al. “Quantum singular value transformation and beyond: exponential improvements for quantum matrix arithmetics”. In: *Proceedings of the 51st Annual ACM SIGACT Symposium on Theory of Computing*. 2019, pp. 193–204.
- [148] Dylan Girodat et al. “Geometric alignment of aminoacyl-tRNA relative to catalytic centers of the ribosome underpins accurate mRNA decoding”. In: *Nature Communications* 14.1 (Sept. 2023), p. 5582. ISSN: 2041-1723. DOI: 10.1038/s41467-023-40404-9. URL: <https://doi.org/10.1038/s41467-023-40404-9>.
- [149] Shou-Shu Gong et al. “Global phase diagram and quantum spin liquids in a spin- $\frac{1}{2}$  triangular antiferromagnet”. In: *Phys. Rev. B* 96 (7 Aug. 2017), p. 075116. DOI: 10.1103/PhysRevB.96.075116. URL: <https://link.aps.org/doi/10.1103/PhysRevB.96.075116>.
- [150] Shou-Shu Gong et al. “Plaquette Ordered Phase and Quantum Phase Diagram in the Spin- $\frac{1}{2}$   $J_1 - J_2$  Square Heisenberg Model”. In: *Phys. Rev. Lett.* 113 (2 July 2014), p. 027201. DOI: 10.1103/PhysRevLett.113.027201. URL: <https://link.aps.org/doi/10.1103/PhysRevLett.113.027201>.
- [151] Lev P Gor’kov and Vladimir Z Kresin. “Colloquium : High pressure and road to room temperature superconductivity”. In: *Rev. Mod. Phys.* 90.1 (Jan. 2018).
- [152] Pallab Goswami, Predrag Nikolic, and Qimiao Si. “Superconductivity in multi-orbital t-J 1 -J 2 model and its implications for iron pnictides”. In: *EPL* 91.3 (Aug. 2010), p. 37006.
- [153] Richard L Greene et al. “The strange metal state of the electron-doped cuprates”. en. In: *Annu. Rev. Condens. Matter Phys.* 11.1 (Mar. 2020), pp. 213–229.
- [154] Peter A Grünberg. “Nobel Lecture: From spin waves to giant magnetoresistance and beyond”. In: *Reviews of Modern Physics* 80.4 (2008), p. 1531.
- [155] Shouzhen Gu, Rolando D Somma, and Burak Şahinoğlu. “Fast-forwarding quantum evolution”. In: *Quantum* 5 (2021), p. 577.
- [156] James Gubernatis, Naoki Kawashima, and Philipp Werner. *Quantum Monte Carlo Methods: Algorithms for Lattice Models*. Cambridge University Press, Jan. 2016. ISBN: 9780511902581. DOI: 10.1017/cbo9780511902581. URL: <http://dx.doi.org/10.1017/CB09780511902581>.

## References

- [157] Martin C Gutzwiller. “Effect of correlation on the ferromagnetism of transition metals”. In: *Phys. Rev. Lett.* 10.5 (Mar. 1963), pp. 159–162.
- [158] Jeongwan Haah et al. “Quantum algorithm for simulating real time evolution of lattice Hamiltonians”. In: *SIAM Journal on Computing* 52.6 (2021), FOCS18–250.
- [159] Jeongwan Haah et al. “Sample-optimal tomography of quantum states”. In: *Proceedings of the forty-eighth annual ACM symposium on Theory of Computing*. 2016, pp. 913–925.
- [160] Jürgen Hafner. “Ab-initio simulations of materials using VASP: Density-functional theory and beyond”. en. In: *J. Comput. Chem.* 29.13 (Oct. 2008), pp. 2044–2078.
- [161] R. Haghshenas and D. N. Sheng. “ $U(1)$ -symmetric infinite projected entangled-pair states study of the spin-1/2 square  $J_1 - J_2$  Heisenberg model”. In: *Phys. Rev. B* 97 (17 May 2018), p. 174408. DOI: 10.1103/PhysRevB.97.174408. URL: <https://link.aps.org/doi/10.1103/PhysRevB.97.174408>.
- [162] Imre Hagymási et al. “Possible Inversion Symmetry Breaking in the  $S = 1/2$  Pyrochlore Heisenberg Magnet”. In: *Phys. Rev. Lett.* 126 (11 Mar. 2021), p. 117204. DOI: 10.1103/PhysRevLett.126.117204. URL: <https://link.aps.org/doi/10.1103/PhysRevLett.126.117204>.
- [163] Yu-Long Hai et al. “Superconductivity Above 100 K Predicted in Carbon-Cage Network”. In: *Advanced Science* 10.33 (Oct. 2023). ISSN: 2198-3844. DOI: 10.1002/advs.202303639. URL: <http://dx.doi.org/10.1002/advs.202303639>.
- [164] F Duncan M Haldane. “Continuum dynamics of the 1-D Heisenberg antiferromagnet: Identification with the O (3) nonlinear sigma model”. In: *Physics letters a* 93.9 (1983), pp. 464–468.
- [165] Benjamin Hall et al. “Simulation of collective neutrino oscillations on a quantum computer”. In: *Phys. Rev. D* 104.6, 063009 (Sept. 2021), p. 063009. DOI: 10.1103/PhysRevD.104.063009. arXiv: 2102.12556 [quant-ph].
- [166] David Oakley Hall and Krishna Rao. *Photosynthesis*. Cambridge University Press, 1999.
- [167] Brenden W Hamilton, Matthew P Kroonblawd, and Alejandro Strachan. “Extemporaneous mechanochemistry: Shock-wave-induced ultrafast chemical reactions due to intramolecular strain energy”. In: *J. Phys. Chem. Lett.* 13.29 (2022), pp. 6657–6663.
- [168] Gao-Feng Han et al. “Mechanochemistry for ammonia synthesis under mild conditions”. In: *Nat. Nano.* 16.3 (2021), pp. 325–330.
- [169] Jiaxiu Han et al. “Experimental simulation of open quantum system dynamics via trotterization”. In: *Physical Review Letters* 127.2 (2021), p. 020504.
- [170] Tian-Heng Han et al. “Fractionalized excitations in the spin-liquid state of a kagome-lattice antiferromagnet”. In: *Nature* 492.7429 (2012), pp. 406–410. URL: <https://doi.org/10.1038/nature11659>.
- [171] Nicholas C. Handy and III Schaefer Henry F. “On the evaluation of analytic energy derivatives for correlated wave functions”. In: *The Journal of Chemical Physics* 81.11 (Apr. 1984), pp. 5031–5033. DOI: 10.1063/1.447489. URL: <https://doi.org/10.1063/1.447489>.
- [172] Markus Hauke Philipp and Heyl, Luca Tagliacozzo, and Peter Zoller. “Measuring multipartite entanglement through dynamic susceptibilities”. In: *Nat. Phys.* 12.8 (2016), pp. 778–782. ISSN: 1745-2481. DOI: 10.1038/nphys3700. URL: <https://doi.org/10.1038/nphys3700>.

## References

- [173] Trygve Ulf Helgaker. “Simple derivation of the potential energy gradient for an arbitrary electronic wave function”. In: *International Journal of Quantum Chemistry* 21.5 (2024/04/23 1982), pp. 939–940. DOI: <https://doi.org/10.1002/qua.560210520>. URL: <https://doi.org/10.1002/qua.560210520>.
- [174] C J Horowitz et al. “r-process nucleosynthesis: connecting rare-isotope beam facilities with the cosmos”. In: *Journal of Physics G: Nuclear and Particle Physics* 46.8 (July 2019), p. 083001. DOI: 10.1088/1361-6471/ab0849. URL: <https://dx.doi.org/10.1088/1361-6471/ab0849>.
- [175] “<https://nationalmaglab.org>”. In: ().
- [176] “<https://nationalmaglab.org/about-the-maglab/facts-figures/world-records/>”. In: ().
- [177] Shijie Hu et al. “Dirac Spin Liquid on the Spin-1/2 Triangular Heisenberg Antiferromagnet”. In: *Phys. Rev. Lett.* 123 (20 Nov. 2019), p. 207203. DOI: 10.1103/PhysRevLett.123.207203. URL: <https://link.aps.org/doi/10.1103/PhysRevLett.123.207203>.
- [178] Wen-Jun Hu et al. “Competing spin-liquid states in the spin- $\frac{1}{2}$  Heisenberg model on the triangular lattice”. In: *Phys. Rev. B* 92 (14 Oct. 2015), p. 140403. DOI: 10.1103/PhysRevB.92.140403. URL: <https://link.aps.org/doi/10.1103/PhysRevB.92.140403>.
- [179] Wen-Jun Hu et al. “Direct evidence for a gapless  $Z_2$  spin liquid by frustrating Néel antiferromagnetism”. In: *Phys. Rev. B* 88 (6 Aug. 2013), p. 060402. DOI: 10.1103/PhysRevB.88.060402. URL: <https://link.aps.org/doi/10.1103/PhysRevB.88.060402>.
- [180] Wen-Jun Hu et al. “Nematic spin liquid phase in a frustrated spin-1 system on the square lattice”. In: *Phys. Rev. B* 100 (16 Oct. 2019), p. 165142. DOI: 10.1103/PhysRevB.100.165142. URL: <https://link.aps.org/doi/10.1103/PhysRevB.100.165142>.
- [181] Hsin-Yuan Huang, Richard Kueng, and John Preskill. “Predicting many properties of a quantum system from very few measurements”. In: *Nature Physics* 16.10 (2020), pp. 1050–1057.
- [182] Hsin-Yuan Huang, Richard Kueng, and John Preskill. “Predicting many properties of a quantum system from very few measurements”. In: *Nat. Phys.* 16.10 (2020), pp. 1050–1057. DOI: 10.1038/s41567-020-0932-7. URL: <https://doi.org/10.1038/s41567-020-0932-7>.
- [183] Kerson Huang. *Introduction to statistical physics, second edition*. 2nd ed. Philadelphia, PA: Chapman & Hall/CRC, Sept. 2009.
- [184] J Hubbard. “Electron correlations in narrow energy bands”. en. In: *Proc. R. Soc. Lond.* 276.1365 (Nov. 1963), pp. 238–257.
- [185] Philipp Hyllus et al. “Fisher information and multiparticle entanglement”. In: *Phys. Rev. A* 85 (2 2012), p. 022321. DOI: 10.1103/PhysRevA.85.022321. URL: <https://link.aps.org/doi/10.1103/PhysRevA.85.022321>.
- [186] James T Hynes. “Chemical reaction dynamics in solution”. In: *Annual Review of Physical Chemistry* 36.1 (1985), pp. 573–597.
- [187] V. I. Iglovikov, E. Khatami, and R. T. Scalettar. “Geometry dependence of the sign problem in quantum Monte Carlo simulations”. In: *Phys. Rev. B* 92 (4 July 2015), p. 045110. DOI: 10.1103/PhysRevB.92.045110. URL: <https://link.aps.org/doi/10.1103/PhysRevB.92.045110>.
- [188] Yasir Iqbal et al. “Quantum and Classical Phases of the Pyrochlore Heisenberg Model with Competing Interactions”. In: *Phys. Rev. X* 9 (1 Jan. 2019), p. 011005. DOI: 10.1103/PhysRevX.9.011005. URL: <https://link.aps.org/doi/10.1103/PhysRevX.9.011005>.

## References

- [189] Yasir Iqbal et al. “Spin liquid nature in the Heisenberg  $J_1 - J_2$  triangular antiferromagnet”. In: *Phys. Rev. B* 93 (14 Apr. 2016), p. 144411. DOI: 10.1103/PhysRevB.93.144411. URL: <https://link.aps.org/doi/10.1103/PhysRevB.93.144411>.
- [190] L. Isaev, G. Ortiz, and J. Dukelsky. “Hierarchical mean-field approach to the  $J_1 - J_2$  Heisenberg model on a square lattice”. In: *Phys. Rev. B* 79 (2 Jan. 2009), p. 024409. DOI: 10.1103/PhysRevB.79.024409. URL: <https://link.aps.org/doi/10.1103/PhysRevB.79.024409>.
- [191] N. B. Ivanov and P. Ch. Ivanov. “Frustrated two-dimensional quantum Heisenberg antiferromagnet at low temperatures”. In: *Phys. Rev. B* 46 (13 Oct. 1992), pp. 8206–8213. DOI: 10.1103/PhysRevB.46.8206. URL: <https://link.aps.org/doi/10.1103/PhysRevB.46.8206>.
- [192] George Jackeli and Giniyat Khaliullin. “Mott insulators in the strong spin-orbit coupling limit: from Heisenberg to a quantum compass and Kitaev models”. In: *Physical review letters* 102.1 (2009), p. 017205.
- [193] J. Jakli č and P. Prelov šek. “Lanczos method for the calculation of finite-temperature quantities in correlated systems”. In: *Phys. Rev. B* 49 (7 Feb. 1994), pp. 5065–5068. DOI: 10.1103/PhysRevB.49.5065. URL: <https://link.aps.org/doi/10.1103/PhysRevB.49.5065>.
- [194] H. -Th. Janka et al. “Theory of core-collapse supernovae”. In: *Phys. Rep.* 442.1-6 (Apr. 2007), pp. 38–74. DOI: 10.1016/j.physrep.2007.02.002. arXiv: astro-ph/0612072 [astro-ph].
- [195] Sangyong Jeon. “Hydrodynamic transport coefficients in relativistic scalar field theory”. In: *Phys. Rev. D* 52 (1995), pp. 3591–3642. DOI: 10.1103/PhysRevD.52.3591. arXiv: hep-ph/9409250.
- [196] Yao Ji, Henry Lamm, and Shuchen Zhu. “Gluon digitization via character expansion for quantum computers”. In: *Phys. Rev. D* 107.11 (2023), p. 114503. DOI: 10.1103/PhysRevD.107.114503. arXiv: 2203.02330 [hep-lat].
- [197] Yao Ji, Henry Lamm, and Shuchen Zhu. “Gluon Field Digitization via Group Space Decimation for Quantum Computers”. In: *Phys. Rev. D* 102.11 (2020), p. 114513. DOI: 10.1103/PhysRevD.102.114513. arXiv: 2005.14221 [hep-lat].
- [198] Hong-Chen Jiang, Hong Yao, and Leon Balents. “Spin liquid ground state of the spin- $\frac{1}{2}$  square  $J_1$ - $J_2$  Heisenberg model”. In: *Phys. Rev. B* 86 (2 July 2012), p. 024424. DOI: 10.1103/PhysRevB.86.024424. URL: <https://link.aps.org/doi/10.1103/PhysRevB.86.024424>.
- [199] Michelle Johannes. “The iron age of superconductivity”. en. In: *Physics (College Park Md.)* 1.28 (Oct. 2008).
- [200] KM Johansen et al. “Aluminum migration and intrinsic defect interaction in single-crystal zinc oxide”. In: *Phys. Rev. Applied* 3.2 (2015), p. 024003.
- [201] J Robert Johansson, Paul D Nation, and Franco Nori. “QuTiP: An open-source Python framework for the dynamics of open quantum systems”. In: *Computer Physics Communications* 183.8 (2012), pp. 1760–1772.
- [202] Roger D Johnson et al. “Monoclinic crystal structure of  $\alpha$ -RuCl<sub>3</sub> and the zigzag antiferromagnetic ground state”. In: *Physical Review B* 92.23 (2015), p. 235119.
- [203] P. Jordan and E. Wigner. “Über das Paulische Äquivalenzverbot”. In: *Zeitschrift für Physik* 47.9 (1928), pp. 631–651. ISSN: 0044-3328. DOI: 10.1007/BF01331938. URL: <https://doi.org/10.1007/BF01331938>.

## References

- [204] Stephen P. Jordan, Keith S. M. Lee, and John Preskill. “Quantum Algorithms for Quantum Field Theories”. In: *Science* 336 (2012), pp. 1130–1133. DOI: 10.1126/science.1217069. arXiv: 1111.3633 [quant-ph].
- [205] Jaewoon Jung et al. “Scaling molecular dynamics beyond 100,000 processor cores for large-scale biophysical simulations”. In: *Journal of Computational Chemistry* 40.21 (2019), pp. 1919–1930. DOI: <https://doi.org/10.1002/jcc.25840>. eprint: <https://onlinelibrary.wiley.com/doi/pdf/10.1002/jcc.25840>. URL: <https://onlinelibrary.wiley.com/doi/abs/10.1002/jcc.25840>.
- [206] Yoichi Kamihara et al. “Iron-based layered superconductor: LaOFeP”. en. In: *J. Am. Chem. Soc.* 128.31 (Aug. 2006), pp. 10012–10013.
- [207] Junjiro Kanamori. “Electron correlation and ferromagnetism of transition metals”. In: *Prog. Theor. Phys.* 30.3 (Sept. 1963), pp. 275–289.
- [208] Matthew W. Kanan and Daniel G. Nocera. “In Situ Formation of an Oxygen-Evolving Catalyst in Neutral Water Containing Phosphate and  $\text{Co}^{2+}$ ”. In: *Science* 321.5892 (2008), pp. 1072–1075. DOI: 10.1126/science.1162018. eprint: <https://www.science.org/doi/pdf/10.1126/science.1162018>. URL: <https://www.science.org/doi/abs/10.1126/science.1162018>.
- [209] Yao-Tai Kang et al. “Single-orbital realization of high-temperature  $s_{\pm}$  superconductivity in the square-octagon lattice”. en. In: *Phys. Rev. B.* 99.18 (May 2019).
- [210] Markus D. Kärkäs et al. “Artificial Photosynthesis: Molecular Systems for Catalytic Water Oxidation”. In: *Chem. Rev.* 114.24 (Dec. 2014), pp. 11863–12001. DOI: 10.1021/cr400572f. URL: <https://doi.org/10.1021/cr400572f>.
- [211] Y Kasahara et al. “Majorana quantization and half-integer thermal quantum Hall effect in a Kitaev spin liquid”. In: *Nature* 559.7713 (2018), pp. 227–231.
- [212] B Keimer et al. “From quantum matter to high-temperature superconductivity in copper oxides”. en. In: *Nature* 518.7538 (Feb. 2015), pp. 179–186.
- [213] B Keimer et al. “From quantum matter to high-temperature superconductivity in copper oxides”. en. In: *Nature* 518.7538 (Feb. 2015), pp. 179–186.
- [214] Julia Kempe, Alexei Kitaev, and Oded Regev. “The complexity of the local Hamiltonian problem”. In: *Siam journal on computing* 35.5 (2006), pp. 1070–1097.
- [215] Mária Kieferová, Artur Scherer, and Dominic W Berry. “Simulating the dynamics of time-dependent Hamiltonians with a truncated Dyson series”. In: *Physical Review A* 99.4 (2019), p. 042314.
- [216] Dohyung Kim et al. “Artificial Photosynthesis for Sustainable Fuel and Chemical Production”. In: *Angew. Chem., Int. Ed.* 54.11 (2024/01/18 2015), pp. 3259–3266. DOI: <https://doi.org/10.1002/anie.201409116>. URL: <https://doi.org/10.1002/anie.201409116>.
- [217] Heung-Sik Kim, Andrei Catuneanu, Hae-Young Kee, et al. “Kitaev magnetism in honeycomb  $\text{RuCl}_3$  with intermediate spin-orbit coupling”. In: *Physical Review B* 91.24 (2015), p. 241110.
- [218] Itamar Kimchi, Adam Nahum, and T. Senthil. “Valence Bonds in Random Quantum Magnets: Theory and Application to  $\text{YbMgGaO}_4$ ”. In: *Phys. Rev. X* 8 (3 July 2018), p. 031028. DOI: 10.1103/PhysRevX.8.031028. URL: <https://link.aps.org/doi/10.1103/PhysRevX.8.031028>.

## References

- [219] Peter Kirton et al. “Introduction to the Dicke model: From equilibrium to nonequilibrium, and vice versa”. In: *Advanced Quantum Technologies* 2.1-2 (2019), p. 1800043.
- [220] A Yu Kitaev. “Fault-tolerant quantum computation by anyons”. In: *Annals of physics* 303.1 (2003), pp. 2–30.
- [221] A Yu Kitaev. “Quantum measurements and the Abelian stabilizer problem”. In: *arXiv preprint quant-ph/9511026* (1995).
- [222] Alexei Kitaev. “Anyons in an exactly solved model and beyond”. In: *Annals of Physics* 321.1 (2006), pp. 2–111.
- [223] Charles Kittel. *Introduction to Solid State Physics*. 8th ed. Wiley, 2004. ISBN: 9780471415268. URL: [http://www.amazon.com/Introduction-Solid-Physics-Charles-Kittel/dp/047141526X/ref=dp\\_ob\\_title\\_bk](http://www.amazon.com/Introduction-Solid-Physics-Charles-Kittel/dp/047141526X/ref=dp_ob_title_bk).
- [224] S A Kivelson, E Fradkin, and V J Emery. “Electronic liquid-crystal phases of a doped Mott insulator”. en. In: *Nature* 393.6685 (June 1998), pp. 550–553.
- [225] Ian D Kivlichan et al. “Improved fault-tolerant quantum simulation of condensed-phase correlated electrons via trotterization”. In: *Quantum* 4 (2020), p. 296.
- [226] Ian D. Kivlichan et al. “Quantum Simulation of Electronic Structure with Linear Depth and Connectivity”. In: *Phys. Rev. Lett.* 120.11, 110501 (Mar. 2018), p. 110501. DOI: 10.1103/PhysRevLett.120.110501. arXiv: 1711.04789 [quant-ph].
- [227] Martin Kliesch et al. “Dissipative quantum church-turing theorem”. In: *Physical review letters* 107.12 (2011), p. 120501.
- [228] Alexey Klimov et al. “Magnetoelectric write and read operations in a stress-mediated multi-ferroic memory cell”. In: *Applied Physics Letters* 110.22 (2017).
- [229] Henrik Koch et al. “Coupled cluster energy derivatives. Analytic Hessian for the closed-shell coupled cluster singles and doubles wave function: Theory and applications”. In: *J. Chem. Phys.* 92.8 (Apr. 1990), pp. 4924–4940. ISSN: 0021-9606. DOI: 10.1063/1.457710. eprint: [https://pubs.aip.org/aip/jcp/article-pdf/92/8/4924/18986340/4924\\_1\\_online.pdf](https://pubs.aip.org/aip/jcp/article-pdf/92/8/4924/18986340/4924_1_online.pdf). URL: <https://doi.org/10.1063/1.457710>.
- [230] Per Kofstad. “Reactions at Surfaces and Interfaces”. In: *Reactivity of Solids*. Ed. by John Wood et al. Boston, MA: Springer US, 1977, pp. 15–42. DOI: 10.1007/978-1-4684-2340-2\_2.
- [231] John B. Kogut and Leonard Susskind. “Hamiltonian Formulation of Wilson’s Lattice Gauge Theories”. In: *Phys. Rev. D* 11 (1975), pp. 395–408. DOI: 10.1103/PhysRevD.11.395.
- [232] Peter F. Kolb and Ulrich W. Heinz. “Hydrodynamic description of ultrarelativistic heavy ion collisions”. In: (May 2003). Ed. by Rudolph C. Hwa and Xin-Nian Wang, pp. 634–714. arXiv: nucl-th/0305084.
- [233] Lutz Köpke and IceCube Collaboration. “Improved Detection of Supernovae with the Ice-Cube Observatory”. In: *Journal of Physics Conference Series*. Vol. 1029. Journal of Physics Conference Series. May 2018, 012001, p. 012001. DOI: 10.1088/1742-6596/1029/1/012001. arXiv: 1704.03823 [astro-ph.HE].
- [234] Robin Kothari. “Efficient algorithms in quantum query complexity”. PhD thesis. University of Waterloo, 2014. URL: <http://hdl.handle.net/10012/8625>.

## References

- [235] G Kotliar and A E Ruckenstein. “New functional integral approach to strongly correlated Fermi systems: The Gutzwiller approximation as a saddle point”. en. In: *Phys. Rev. Lett.* 57.11 (Sept. 1986), pp. 1362–1365.
- [236] Gabriel Kotliar et al. “Cellular dynamical mean field approach to strongly correlated systems”. In: *Phys. Rev. Lett.* 87.18 (Oct. 2001).
- [237] P. Kovtun, Dan T. Son, and Andrei O. Starinets. “Viscosity in strongly interacting quantum field theories from black hole physics”. In: *Phys. Rev. Lett.* 94 (2005), p. 111601. DOI: 10.1103/PhysRevLett.94.111601. arXiv: hep-th/0405231.
- [238] Jakub A Koza et al. “Electrodeposition of Crystalline  $\text{Co}_3\text{O}_4$  A Catalyst for the Oxygen Evolution Reaction”. In: *Chemistry of Materials* 24.18 (2012), pp. 3567–3573.
- [239] Fabian B Kugler et al. “Strongly correlated materials from a numerical renormalization group perspective: How the Fermi-liquid state of  $\text{Sr}_{-}\{2\}\text{RuO}_{-}\{4\}$  emerges”. en. In: *Phys. Rev. Lett.* 124.1 (Jan. 2020), p. 016401.
- [240] Los Alamos National Laboratory. *Trinity supercomputer, August 2015 Trinity: Advanced Technology System*. <https://mission.lanl.gov/advanced-simulation-and-computing/platforms/trinity/>. [Accessed 15-04-2024]. 2015.
- [241] National High Magnetic Field Laboratory. *National MagLab - MagLab — nationalmaglab.org*. <https://nationalmaglab.org/>. [Accessed 14-04-2024]. 2024.
- [242] Ville Lahtinen and Jiannis Pachos. “A short introduction to topological quantum computation”. In: *SciPost Physics* 3.3 (2017), p. 021.
- [243] Henry Lamm, Scott Lawrence, and Yukari Yamauchi. “General Methods for Digital Quantum Simulation of Gauge Theories”. In: *Phys. Rev. D* 100.3 (2019), p. 034518. DOI: 10.1103/PhysRevD.100.034518. arXiv: 1903.08807 [hep-lat].
- [244] Nathan K Langford et al. “Experimentally simulating the dynamics of quantum light and matter at deep-strong coupling”. In: *Nature Communications* 8.1 (2017), p. 1715.
- [245] Pontus Laurell et al. “Magnetic excitations, nonclassicality, and quantum wake spin dynamics in the Hubbard chain”. In: *Phys. Rev. B* 106 (8 Aug. 2022), p. 085110. DOI: 10.1103/PhysRevB.106.085110. URL: <https://link.aps.org/doi/10.1103/PhysRevB.106.085110>.
- [246] Pontus Laurell et al. “Quantifying and Controlling Entanglement in the Quantum Magnet  $\text{Cs}_2\text{CoCl}_4$ ”. In: *Phys. Rev. Lett.* 127 (3 July 2021), p. 037201. DOI: 10.1103/PhysRevLett.127.037201. URL: <https://link.aps.org/doi/10.1103/PhysRevLett.127.037201>.
- [247] Scott Lawrence. “Sign Problems in Quantum Field Theory: Classical and Quantum Approaches”. PhD thesis. Maryland U., 2020. arXiv: 2006.03683 [hep-lat].
- [248] Alexandre Le Boité. “Theoretical methods for ultrastrong light–matter interactions”. In: *Advanced Quantum Technologies* 3.7 (2020), p. 1900140.
- [249] Eric Kin-Ho Lee et al. “Heisenberg-Kitaev model on the hyperhoneycomb lattice”. In: *Physical Review B* 89.4 (2014), p. 045117.
- [250] Patrick A Lee, Naoto Nagaosa, and Xiao-Gang Wen. “Doping a Mott insulator: Physics of high-temperature superconductivity”. en. In: *Rev. Mod. Phys.* 78.1 (Jan. 2006), pp. 17–85.

## References

- [251] Seunghoon Lee et al. “Evaluating the evidence for exponential quantum advantage in ground-state quantum chemistry”. en. In: *Nat. Commun.* 14.1 (Apr. 2023), p. 1952. ISSN: 2041-1723. DOI: 10.1038/s41467-023-37587-6. URL: <https://www.nature.com/articles/s41467-023-37587-6> (visited on 12/19/2023).
- [252] Nicholas Lewis and Whitney Spivey. *Computing on the mesa*. <https://discover.lanl.gov/publications/national-security-science/2020-winter/computing-on-the-mesa/>. [Accessed 15-04-2024]. 2020.
- [253] Dandan Li et al. “Photocatalytic CO<sub>2</sub> reduction over metal-organic framework-based materials”. In: *Coordination Chemistry Reviews* 412 (2020), p. 213262. DOI: <https://doi.org/10.1016/j.ccr.2020.213262>. URL: <https://www.sciencedirect.com/science/article/pii/S0010854520300461>.
- [254] Xiangzhi Li et al. “Proximity-induced chiral quantum light generation in strain-engineered WSe<sub>2</sub>/NiPS<sub>3</sub> heterostructures”. In: *Nature Materials* 22.11 (2023), pp. 1311–1316.
- [255] Yan-Chao Li et al. “Multipartite entanglement serves as a faithful detector for quantum phase transitions”. In: *New Journal of Physics* 26.2 (Feb. 2024), p. 023031. DOI: 10.1088/1367-2630/ad273a. URL: <https://dx.doi.org/10.1088/1367-2630/ad273a>.
- [256] Yuesheng Li et al. “Gapless quantum spin liquid ground state in the two-dimensional spin-1/2 triangular antiferromagnet YbMgGaO<sub>4</sub>”. In: *Scientific reports* 5.1 (2015), p. 16419.
- [257] Elliott H Lieb and F Y Wu. “Absence of Mott transition in an exact solution of the short-range, one-band model in one dimension”. In: *Phys. Rev. Lett.* 20.25 (June 1968), pp. 1445–1448.
- [258] Jin Soo Lim et al. “Evolution of metastable structures at bimetallic surfaces from microscopy and machine-learning molecular dynamics”. In: *J. Am. Chem. Soc.* 142.37 (2020), pp. 15907–15916.
- [259] Joonhyung Lim et al. “Two-dimensional infrared spectroscopy and molecular dynamics simulation studies of nonaqueous lithium ion battery electrolytes”. In: *J. Phys. Chem. B* 123.31 (2019), pp. 6651–6663.
- [260] Lin Lin. “Lecture notes on quantum algorithms for scientific computation”. In: *arXiv preprint arXiv:2201.08309* (2022).
- [261] Noah Linden et al. “Quantum mechanical evolution towards thermal equilibrium”. In: *Phys. Rev. E* 79.6, 061103 (June 2009), p. 061103. DOI: 10.1103/PhysRevE.79.061103. arXiv: 0812.2385 [quant-ph].
- [262] Wen-Yuan Liu et al. *Deconfined quantum criticality with emergent symmetry in the extended Shastry-Sutherland model*. 2023. arXiv: 2309.10955 [cond-mat.str-el]. URL: <https://doi.org/10.48550/arXiv.2309.10955>.
- [263] Wen-Yuan Liu et al. “Gapless quantum spin liquid and global phase diagram of the spin-1/2 J<sub>1</sub>-J<sub>2</sub> square antiferromagnetic Heisenberg model”. In: *Science Bulletin* 67.10 (2022), pp. 1034–1041. ISSN: 2095-9273. DOI: <https://doi.org/10.1016/j.scib.2022.03.010>. URL: <https://www.sciencedirect.com/science/article/pii/S2095927322001001>.
- [264] Wen-Yuan Liu et al. “Gapless spin liquid ground state of the spin- $\frac{1}{2}$  J<sub>1</sub> – J<sub>2</sub> Heisenberg model on square lattices”. In: *Phys. Rev. B* 98 (24 Dec. 2018), p. 241109. DOI: 10.1103/PhysRevB.98.241109. URL: <https://link.aps.org/doi/10.1103/PhysRevB.98.241109>.



## References

- [265] Yingshuo Liu and Charles C. L. McCrory. “Modulating the mechanism of electrocatalytic CO<sub>2</sub> reduction by cobalt phthalocyanine through polymer coordination and encapsulation”. In: *Nat. Commun.* 10.1 (2019), p. 1683. DOI: 10.1038/s41467-019-09626-8. URL: <https://doi.org/10.1038/s41467-019-09626-8>.
- [266] Z-P Liu. “Chemical reactions at surfaces and interfaces from first principles: Theory and application”. In: *Pure and applied chemistry* 76.12 (2004), pp. 2069–2083.
- [267] Alois Loidl, Peter Lunkenheimer, and Vladimir Tsurkan. “On the proximate Kitaev quantum-spin liquid  $\alpha$ -RuCl<sub>3</sub>: thermodynamics, excitations and continua”. In: *Journal of Physics: Condensed Matter* 33.44 (2021), p. 443004.
- [268] Guang Hao Low and Isaac L Chuang. “Hamiltonian simulation by qubitization”. In: *Quantum* 3 (2019), p. 163.
- [269] Guang Hao Low and Isaac L Chuang. “Optimal Hamiltonian simulation by quantum signal processing”. In: *Physical review letters* 118.1 (2017), p. 010501.
- [270] Guang Hao Low and Nathan Wiebe. “Hamiltonian simulation in the interaction picture”. In: *arXiv preprint arXiv:1805.00675* (2018).
- [271] Qiang Luo et al. “Gapless quantum spin liquid in a honeycomb  $\Gamma$  magnet”. In: *npj Quantum Materials* 6.1 (June 2021), p. 57. ISSN: 2397-4648. DOI: 10.1038/s41535-021-00356-z. URL: <https://doi.org/10.1038/s41535-021-00356-z>.
- [272] Dingshun Lv et al. “Quantum simulation of the quantum Rabi model in a trapped ion”. In: *Physical Review X* 8.2 (2018), p. 021027.
- [273] Danya Lyu, Jinchang Xu, and Zhenyou Wang. “Time-resolved in situ vibrational spectroscopy for electrocatalysis: challenge and opportunity”. In: *Frontiers in Chemistry* 11 (2023).
- [274] T Maier et al. “D-wave superconductivity in the hubbard model”. en. In: *Phys. Rev. Lett.* 85.7 (Aug. 2000), pp. 1524–1527.
- [275] Matthieu Mambrini et al. “Plaquette valence-bond crystal in the frustrated Heisenberg quantum antiferromagnet on the square lattice”. In: *Phys. Rev. B* 74 (14 Oct. 2006), p. 144422. DOI: 10.1103/PhysRevB.74.144422. URL: <https://link.aps.org/doi/10.1103/PhysRevB.74.144422>.
- [276] Daniel Manzano. “A short introduction to the Lindblad master equation”. In: *Aip Advances* 10.2 (2020).
- [277] Joshua D. Martin et al. “Equilibration of quantum many-body fast neutrino flavor oscillations”. In: *Phys. Rev. D* 108.12 (2023), p. 123010. DOI: 10.1103/PhysRevD.108.123010. arXiv: 2307.16793 [hep-ph].
- [278] Dominik Marx and Jurg Hutter. “Ab initio molecular dynamics: Theory and implementation”. In: *Modern methods and algorithms of quantum chemistry* 1.301-449 (2000), p. 141.
- [279] Nicola Marzari et al. “Maximally localized Wannier functions: Theory and applications”. en. In: *Rev. Mod. Phys.* 84.4 (Oct. 2012), pp. 1419–1475.
- [280] Sam McArdle et al. “Quantum computational chemistry”. In: *Rev. Mod. Phys.* 92.1 (Mar. 2020), pp. 015003–. DOI: 10.1103/RevModPhys.92.015003. URL: <https://link.aps.org/doi/10.1103/RevModPhys.92.015003>.

## References

- [281] James P McEvoy and Gary W Brudvig. “Water-splitting chemistry of photosystem II”. In: *Chem. Rev.* 106.11 (2006), pp. 4455–4483.
- [282] Varun Menon et al. “Multipartite entanglement in the one-dimensional spin- $\frac{1}{2}$  Heisenberg antiferromagnet”. In: *Phys. Rev. B* 107 (5 Feb. 2023), p. 054422. DOI: 10.1103/PhysRevB.107.054422. URL: <https://link.aps.org/doi/10.1103/PhysRevB.107.054422>.
- [283] Walter Metzner et al. “Functional renormalization group approach to correlated fermion systems”. en. In: *Rev. Mod. Phys.* 84.1 (Mar. 2012), pp. 299–352.
- [284] Thomas J Meyer. “Chemical approaches to artificial photosynthesis”. In: *Acc. Chem. Res.* 22.5 (1989), pp. 163–170.
- [285] Fabio Mezzacapo. “Ground-state phase diagram of the quantum  $J_1 - J_2$  model on the square lattice”. In: *Phys. Rev. B* 86 (4 July 2012), p. 045115. DOI: 10.1103/PhysRevB.86.045115. URL: <https://link.aps.org/doi/10.1103/PhysRevB.86.045115>.
- [286] Gregory Mills, Hannes Jónsson, and Gregory K. Schenter. “Reversible work transition state theory: application to dissociative adsorption of hydrogen”. In: *Surface Science* 324.2 (1995), pp. 305–337. ISSN: 0039-6028. DOI: [https://doi.org/10.1016/0039-6028\(94\)00731-4](https://doi.org/10.1016/0039-6028(94)00731-4). URL: <https://www.sciencedirect.com/science/article/pii/0039602894007314>.
- [287] Avانش Mishra et al. “Atomistic origin of phase stability in oxygen-functionalized MXene: a comparative study”. In: *J. Phys. Chem. C* 121.34 (2017), pp. 18947–18953.
- [288] Satoshi Morita, Ryui Kaneko, and Masatoshi Imada. “Quantum Spin Liquid in Spin 1/2 J<sub>1</sub>-J<sub>2</sub> Heisenberg Model on Square Lattice: Many-Variable Variational Monte Carlo Study Combined with Quantum-Number Projections”. In: *Journal of the Physical Society of Japan* 84.2 (2015), p. 024720.
- [289] Zachary Morrell et al. *Quantum Computing Applications Specifications*. <https://github.com/lanl-ansi/qc-applications>. 2023.
- [290] Arash A Mostofi et al. “An updated version of wannier90: A tool for obtaining maximally-localised Wannier functions”. In: *Comput. Phys. Commun.* 185.8 (Aug. 2014), pp. 2309–2310.
- [291] N F Mott and R Peierls. “Discussion of the paper by de Boer and Verwey”. In: *Proc. Phys. Soc.* 49.4S (Aug. 1937), pp. 72–73.
- [292] Titas Kumar Mukhopadhyay and Ayan Datta. “Deciphering the role of solvents in the liquid phase exfoliation of hexagonal boron nitride: A molecular dynamics simulation study”. In: *J. Phys. Chem. C* 121.1 (2017), pp. 811–822.
- [293] V. Murg, F. Verstraete, and J. I. Cirac. “Exploring frustrated spin systems using projected entangled pair states”. In: *Phys. Rev. B* 79 (19 May 2009), p. 195119. DOI: 10.1103/PhysRevB.79.195119. URL: <https://link.aps.org/doi/10.1103/PhysRevB.79.195119>.
- [294] Rahul Nandkishore, L S Levitov, and A V Chubukov. “Chiral superconductivity from repulsive interactions in doped graphene”. en. In: *Nat. Phys.* 8.2 (Feb. 2012), pp. 158–163.
- [295] Rahul Nandkishore, Ronny Thomale, and Andrey V Chubukov. “Superconductivity from weak repulsion in hexagonal lattice systems”. In: *Phys. Rev. B Condens. Matter Mater. Phys.* 89.14 (Apr. 2014).
- [296] Joji Nasu, Masafumi Udagawa, and Yukitoshi Motome. “Thermal fractionalization of quantum spins in a Kitaev model: Temperature-linear specific heat and coherent transport of Majorana fermions”. In: *Physical Review B* 92.11 (2015), p. 115122.

## References

- [297] Chetan Nayak et al. “Non-Abelian anyons and topological quantum computation”. In: *Rev. Mod. Phys.* 80 (3 Sept. 2008), pp. 1083–1159. DOI: 10.1103/RevModPhys.80.1083. URL: <https://link.aps.org/doi/10.1103/RevModPhys.80.1083>.
- [298] Tammie R Nelson et al. “Non-adiabatic excited-state molecular dynamics: Theory and applications for modeling photophysics in extended molecular materials”. In: *Chemical reviews* 120.4 (2020), pp. 2215–2287.
- [299] Tammie R. Nelson et al. “Non-adiabatic Excited-State Molecular Dynamics: Theory and Applications for Modeling Photophysics in Extended Molecular Materials”. In: *Chem. Rev.* 120.4 (2020), pp. 2215–2287. DOI: 10.1021/acs.chemrev.9b00447.
- [300] Michael A. Nielsen and Isaac L. Chuang. *Quantum Computation and Quantum Information: 10th Anniversary Edition*. 10th. USA: Cambridge University Press, 2011. ISBN: 1107002176.
- [301] Yusuke Nomura and Masatoshi Imada. “Dirac-Type Nodal Spin Liquid Revealed by Refined Quantum Many-Body Solver Using Neural-Network Wave Function, Correlation Ratio, and Level Spectroscopy”. In: *Phys. Rev. X* 11 (3 Aug. 2021), p. 031034. DOI: 10.1103/PhysRevX.11.031034. URL: <https://link.aps.org/doi/10.1103/PhysRevX.11.031034>.
- [302] M. R. Norman. “Colloquium: Herbertsmithite and the search for the quantum spin liquid”. In: *Rev. Mod. Phys.* 88 (4 Dec. 2016), p. 041002. DOI: 10.1103/RevModPhys.88.041002. URL: <https://link.aps.org/doi/10.1103/RevModPhys.88.041002>.
- [303] M. R. Norman et al. “Phenomenological models for the gap anisotropy of Bi2Sr2CaCu2O8 as measured by angle-resolved photoemission spectroscopy”. In: *Physical Review B* 52.1 (1995), pp. 615–622. ISSN: 1095-3795. DOI: 10.1103/physrevb.52.615. URL: <http://dx.doi.org/10.1103/PhysRevB.52.615>.
- [304] Thomas E O’Brien et al. “Efficient quantum computation of molecular forces and other energy gradients”. In: *Physical Review Research* 4.4 (2022), p. 043210.
- [305] Thomas E O’Brien et al. “Calculating energy derivatives for quantum chemistry on a quantum computer”. In: *npj Quantum Information* 5.1 (2019), p. 113.
- [306] Masao Ogata and Hidetoshi Fukuyama. “Thet–J model for the oxide high-Tc superconductors”. In: *Rep. Prog. Phys.* 71.3 (Mar. 2008), p. 036501.
- [307] Mitchell T Ong et al. “First principles dynamics and minimum energy pathways for mechanochemical ring opening of cyclobutene”. In: *J. Am. Chem. Soc.* 131.18 (2009), pp. 6377–6379.
- [308] Lars Onsager. “Crystal statistics. I. A two-dimensional model with an order-disorder transition”. In: *Physical Review* 65.3-4 (1944), p. 117.
- [309] Joseph AM Paddison et al. “Continuous excitations of the triangular-lattice quantum spin liquid YbMgGaO4”. In: *Nature Physics* 13.2 (2017), pp. 117–122.
- [310] D A Papaconstantopoulos and M J Mehl. “The Slater Koster tight-binding method: a computationally efficient and accurate approach”. In: *J. Phys. Condens. Matter* 15.10 (Mar. 2003), R413–R440.
- [311] Jean-François Paquet et al. “Production of photons in relativistic heavy-ion collisions”. In: *Phys. Rev. C* 93.4 (2016), p. 044906. DOI: 10.1103/PhysRevC.93.044906. arXiv: 1509.06738 [hep-ph].

## References

- [312] Shayani Parida et al. “Vertically stacked 2H-1T dual-phase MoS<sub>2</sub> microstructures during lithium intercalation: a first principles study”. In: *Journal of the American Ceramic Society* 103.11 (2020), pp. 6603–6614.
- [313] Robert M. Parrish, Gian-Luca R. Anselmetti, and Christian Gogolin. “Analytical Ground- and Excited-State Gradients for Molecular Electronic Structure Theory from Hybrid Quantum/Classical Methods”. Version 1. In: *arXiv:2110.05040 [quant-ph]* (2021). DOI: 10.48550/arXiv.2110.05040. arXiv: 2110.05040 [quant-ph]. URL: <https://doi.org/10.48550/arXiv.2110.05040>.
- [314] Eva Pavarini, ed. *The LDA+DMFT approach to strongly correlated materials*. en. Forschungszentrum Jülich, Sept. 2011.
- [315] M. C. Payne et al. “Iterative minimization techniques for ab initio total-energy calculations: molecular dynamics and conjugate gradients”. In: *Rev. Mod. Phys.* 64 (4 Oct. 1992), pp. 1045–1097. DOI: 10.1103/RevModPhys.64.1045. URL: <https://link.aps.org/doi/10.1103/RevModPhys.64.1045>.
- [316] Dan-Ni Pei et al. “Defective titanium dioxide single crystals exposed by high-energy {001} facets for efficient oxygen reduction”. In: *Nat. Commun.* 6.1 (2015), p. 8696.
- [317] David R Penn. “Stability theory of the magnetic phases for a simple model of the transition metals”. In: *Phys. Rev.* 142.2 (Feb. 1966), pp. 350–365.
- [318] GA Peterson et al. “Ultrastrong parametric coupling between a superconducting cavity and a mechanical resonator”. In: *Physical Review Letters* 123.24 (2019), p. 247701.
- [319] Owe Philipsen. “The QCD equation of state from the lattice”. In: *Prog. Part. Nucl. Phys.* 70 (2013), pp. 55–107. DOI: 10.1016/j.pnpnp.2012.09.003. arXiv: 1207.5999 [hep-lat].
- [320] M. Pineda and M. Stamatakis. “Kinetic Monte Carlo simulations for heterogeneous catalysis: Fundamentals, current status, and challenges”. In: *The Journal of Chemical Physics* 156.12 (Apr. 2022), p. 120902. DOI: 10.1063/5.0083251. URL: <https://doi.org/10.1063/5.0083251>.
- [321] Andrei Piryatinski et al. “Nonequilibrium states of a plasmonic Dicke model with coherent and dissipative surface-plasmon–quantum-emitter interactions”. In: *Physical Review Research* 2.1 (2020), p. 013141.
- [322] KW Plumb et al. “Continuum of quantum fluctuations in a three-dimensional S= 1 Heisenberg magnet”. In: *Nature Physics* 15.1 (2019), pp. 54–59. URL: <https://doi.org/10.1038/s41567-018-0317-3>.
- [323] Rico Pohle, Nic Shannon, and Yukitoshi Motome. “Spin nematics meet spin liquids: Exotic quantum phases in the spin-1 bilinear-biquadratic model with Kitaev interactions”. In: *Phys. Rev. B* 107 (14 Apr. 2023), p. L140403. DOI: 10.1103/PhysRevB.107.L140403. URL: <https://link.aps.org/doi/10.1103/PhysRevB.107.L140403>.
- [324] Rico Pohle, Youhei Yamaji, and Masatoshi Imada. *Ground state of the S=1/2 pyrochlore Heisenberg antiferromagnet: A quantum spin liquid emergent from dimensional reduction*. 2023. arXiv: 2311.11561 [cond-mat.str-el]. URL: [arxiv.org/abs/2311.11561](https://arxiv.org/abs/2311.11561).
- [325] Didier Poilblanc and Matthieu Mambrini. “Quantum critical phase with infinite projected entangled paired states”. In: *Phys. Rev. B* 96 (1 July 2017), p. 014414. DOI: 10.1103/PhysRevB.96.014414. URL: <https://link.aps.org/doi/10.1103/PhysRevB.96.014414>.

## References

- [326] Didier Poilblanc, Matthieu Mambrini, and Sylvain Capponi. “Critical colored-RVB states in the frustrated quantum Heisenberg model on the square lattice”. In: *SciPost Physics* 7.4 (2019), p. 041.
- [327] Didier Poilblanc et al. “Static and dynamical correlations in a spin-1/2 frustrated antiferromagnet”. In: *Phys. Rev. B* 43 (13 May 1991), pp. 10970–10983. DOI: 10.1103/PhysRevB.43.10970. URL: <https://link.aps.org/doi/10.1103/PhysRevB.43.10970>.
- [328] David Poulin and Pawel Wocjan. “Sampling from the thermal quantum Gibbs state and evaluating partition functions with a quantum computer”. In: *Physical review letters* 103.22 (2009), p. 220502.
- [329] David Poulin et al. “Quantum Algorithm for Spectral Measurement with a Lower Gate Count”. In: *Physical Review Letters* 121 (1 July 2018), p. 010501. DOI: 10.1103/PhysRevLett.121.010501. URL: <https://link.aps.org/doi/10.1103/PhysRevLett.121.010501>.
- [330] David Poulin et al. “Quantum simulation of time-dependent Hamiltonians and the convenient illusion of Hilbert space”. In: *Physical review letters* 106.17 (2011), p. 170501.
- [331] John Preskill. “Quantum Computing in the NISQ era and beyond”. In: *Quantum* 2 (Aug. 2018), p. 79. ISSN: 2521-327X. DOI: 10.22331/q-2018-08-06-79. URL: <https://doi.org/10.22331/q-2018-08-06-79>.
- [332] Tom Preston-Werner. *Semantic Versioning 2.0.0*. <https://semver.org/>. [Accessed 21-04-2024]. 2013.
- [333] *Private communication with Vivien Zapf and Minseong Lee*.
- [334] Yang Qi and Zheng-Cheng Gu. “Continuous phase transition from Néel state to  $Z_2$  spin-liquid state on a square lattice”. In: *Phys. Rev. B* 89 (23 June 2014), p. 235122. DOI: 10.1103/PhysRevB.89.235122. URL: <https://link.aps.org/doi/10.1103/PhysRevB.89.235122>.
- [335] Xiangjian Qian and Mingpu Qin. “Absence of spin liquid phase in the  $J_1 - J_2$  Heisenberg model on the square lattice”. In: *Phys. Rev. B* 109 (16 Apr. 2024), p. L161103. DOI: 10.1103/PhysRevB.109.L161103. URL: <https://link.aps.org/doi/10.1103/PhysRevB.109.L161103>.
- [336] David Radice et al. “Turbulence in core-collapse supernovae”. In: *Journal of Physics G: Nuclear and Particle Physics* 45.5 (2018), p. 053003.
- [337] Patrick Rall, Chunhao Wang, and Pawel Wocjan. “Thermal state preparation via rounding promises”. In: *Quantum* 7 (2023), p. 1132.
- [338] X Rao et al. “Survival of itinerant excitations and quantum spin state transitions in YbMg-GaO<sub>4</sub> with chemical disorder”. In: *Nature communications* 12.1 (2021), p. 4949.
- [339] Shubhalaxmi Rath and Binoy Krishna Patra. “Viscous properties of hot and dense QCD matter in the presence of a magnetic field”. In: *Eur. Phys. J. C* 81.2 (2021), p. 139. DOI: 10.1140/epjc/s10052-021-08931-1. arXiv: 2010.02886 [hep-ph].
- [340] Jeffrey G Rau, Eric Kin-Ho Lee, and Hae-Young Kee. “Generic spin model for the honeycomb iridates beyond the Kitaev limit”. In: *Physical review letters* 112.7 (2014), p. 077204.
- [341] Jeffrey G Rau, Eric Kin-Ho Lee, and Hae-Young Kee. “Spin-orbit physics giving rise to novel phases in correlated systems: Iridates and related materials”. In: *Annual Review of Condensed Matter Physics* 7 (2016), pp. 195–221.

## References

- [342] Markus Reiher et al. “Elucidating reaction mechanisms on quantum computers”. In: *Proc. Natl. Acad. Sci.* 114.29 (2017), pp. 7555–7560.
- [343] *Relativistic Heavy Ion Collider*. [Online; accessed 23-Apr-2024]. 2024. URL: [https://en.wikipedia.org/wiki/Relativistic\\_Heavy\\_Ion\\_Collider](https://en.wikipedia.org/wiki/Relativistic_Heavy_Ion_Collider).
- [344] Stephan Reschke et al. “Sub-gap optical response in the Kitaev spin-liquid candidate  $\alpha$ -RuCl<sub>3</sub>”. In: *Journal of Physics: Condensed Matter* 30.47 (2018), p. 475604.
- [345] Edgar A Reyes Cruz et al. “Molecular-Modified Photocathodes for Applications in Artificial Photosynthesis and Solar-to-Fuel Technologies”. In: *Chem. Rev.* 122.21 (2022), pp. 16051–16109.
- [346] *RHIC: A New Area of Physics*. URL: <https://www.bnl.gov/rhic/new-physics.php>.
- [347] J Richter and J Schulenburg. “The spin-1/2 J<sub>1</sub>–J<sub>2</sub> Heisenberg antiferromagnet on the square lattice: Exact diagonalization for N= 40 spins”. In: *The European Physical Journal B* 73.1 (2010), pp. 117–124.
- [348] Johannes Richter, Ronald Zinke, and Damian JJ Farnell. “The spin-1/2 square-lattice J<sub>1</sub>–J<sub>2</sub> model: the spin-gap issue”. In: *The European Physical Journal B* 88 (2015), pp. 1–6.
- [349] Jörg Rissler, Reinhard M. Noack, and Steven R. White. “Measuring orbital interaction using quantum information theory”. In: *Chem. Phys* 323 (2006), pp. 519–531. URL: <https://www.sciencedirect.com/science/article/pii/S0301010405005069>.
- [350] Wesley Roberts, Michael Vogl, and Gregory A Fiete. “Fidelity of the Kitaev honeycomb model under a quench”. In: *arXiv preprint arXiv:2208.07732* (2022).
- [351] Dario Rocca et al. “Reducing the Runtime of Fault-Tolerant Quantum Simulations in Chemistry through Symmetry-Compressed Double Factorization”. In: *arXiv:2403.03502 [quant-ph]* (2024). URL: <https://doi.org/10.48550/arXiv.2403.03502>.
- [352] Jérémie Roland and Nicolas J Cerf. “Quantum search by local adiabatic evolution”. In: *Physical Review A* 65.4 (2002), p. 042308.
- [353] Paul Romatschke and Ulrike Romatschke. *Relativistic Fluid Dynamics In and Out of Equilibrium*. Cambridge Monographs on Mathematical Physics. Cambridge University Press, May 2019. ISBN: 978-1-108-48368-1, 978-1-108-75002-8. DOI: 10.1017/9781108651998. arXiv: 1712.05815 [nucl-th].
- [354] Aldo H Romero et al. “ABINIT: Overview and focus on selected capabilities”. en. In: *J. Chem. Phys.* 152.12 (Mar. 2020), p. 124102.
- [355] Adam Justin Rondinone. “CINT 2026 Strategic Plan”. In: (Feb. 2021). DOI: 10.2172/1764870. URL: <https://www.osti.gov/biblio/1764870>.
- [356] Tommaso Roscilde et al. “Studying Quantum Spin Systems through Entanglement Estimators”. In: *Phys. Rev. Lett.* 93 (16 Oct. 2004), p. 167203. DOI: 10.1103/PhysRevLett.93.167203. URL: <https://link.aps.org/doi/10.1103/PhysRevLett.93.167203>.
- [357] Manolis M Roubelakis et al. “Proton-coupled electron transfer kinetics for the hydrogen evolution reaction of hangman porphyrins”. In: *Energy & Environmental Science* 5.7 (2012), pp. 7737–7740.
- [358] A N Rubtsov, V V Savkin, and A I Lichtenstein. “Continuous-time quantum Monte Carlo method for fermions”. en. In: *Phys. Rev. B Condens. Matter Mater. Phys.* 72.3 (July 2005).

## References

- [359] S. N. Saadatmand and I. P. McCulloch. “Symmetry fractionalization in the topological phase of the spin- $\frac{1}{2}$   $J_1 - J_2$  triangular Heisenberg model”. In: *Phys. Rev. B* 94 (12 Sept. 2016), p. 121111. DOI: 10.1103/PhysRevB.94.121111. URL: <https://link.aps.org/doi/10.1103/PhysRevB.94.121111>.
- [360] Subir Sachdev and R. N. Bhatt. “Bond-operator representation of quantum spins: Mean-field theory of frustrated quantum Heisenberg antiferromagnets”. In: *Phys. Rev. B* 41 (13 May 1990), pp. 9323–9329. DOI: 10.1103/PhysRevB.41.9323. URL: <https://link.aps.org/doi/10.1103/PhysRevB.41.9323>.
- [361] Subir Sachdev and Debanjan Chowdhury. “The novel metallic states of the cuprates: Topological Fermi liquids and strange metals”. en. In: *Prog. Theor. Exp. Phys.* 2016.12 (Dec. 2016), p. 12C102.
- [362] Subir Sachdev and Bernhard Keimer. “Quantum criticality”. In: *Physics Today* 64.2 (2011), pp. 29–35.
- [363] Lucile Savary and Leon Balents. “Quantum spin liquids: a review”. In: *Reports on Progress in Physics* 80.1 (2016), p. 016502.
- [364] D. J. Scalapino. *Numerical Studies of the 2D Hubbard model, Numerical in Handbook of High-Temperature Superconductivity (Ed. Schrieffer)*. Springer New York, 2007. ISBN: 9780387350714. DOI: 10.1007/978-0-387-68734-6. URL: <http://dx.doi.org/10.1007/978-0-387-68734-6>.
- [365] Robin Schäfer et al. “Abundance of Hard-Hexagon Crystals in the Quantum Pyrochlore Antiferromagnet”. In: *Phys. Rev. Lett.* 131 (9 Aug. 2023), p. 096702. DOI: 10.1103/PhysRevLett.131.096702. URL: <https://link.aps.org/doi/10.1103/PhysRevLett.131.096702>.
- [366] A. Scheie et al. “Witnessing entanglement in quantum magnets using neutron scattering”. In: *Phys. Rev. B* 103 (22 June 2021), p. 224434. DOI: 10.1103/PhysRevB.103.224434. URL: <https://link.aps.org/doi/10.1103/PhysRevB.103.224434>.
- [367] A. O. Scheie et al. “Nonlinear magnons and exchange Hamiltonians of the delafossite proximate quantum spin liquid candidates KYbSe<sub>2</sub> and NaYbSe<sub>2</sub>”. In: *Phys. Rev. B* 109 (1 Jan. 2024), p. 014425. DOI: 10.1103/PhysRevB.109.014425. URL: <https://link.aps.org/doi/10.1103/PhysRevB.109.014425>.
- [368] A. O. Scheie et al. “Proximate spin liquid and fractionalization in the triangular antiferromagnet KYbSe<sub>2</sub>”. In: *Nature Physics* 20.1 (Jan. 2024), pp. 74–81. ISSN: 1745-2481. DOI: 10.1038/s41567-023-02259-1. URL: <https://doi.org/10.1038/s41567-023-02259-1>.
- [369] Allen Scheie et al. “Multiphase magnetism in Yb<sub>2</sub>Ti<sub>2</sub>O<sub>7</sub>”. In: *Proceedings of the National Academy of Sciences* 117.44 (2020), pp. 27245–27254.
- [370] Allen Scheie et al. “Quantum wake dynamics in Heisenberg antiferromagnetic chains”. In: *Nature Communications* 13.1 (2022), p. 5796. DOI: 10.1038/s41467-022-33571-8. URL: <https://doi.org/10.1038/s41467-022-33571-8>.
- [371] Allen Scheie et al. “Reconstructing the spatial structure of quantum correlations”. In: *arXiv preprint arXiv:2306.11723* (2023).
- [372] Bjoern Schenke, Sangyong Jeon, and Charles Gale. “(3+1)D hydrodynamic simulation of relativistic heavy-ion collisions”. In: *Phys. Rev. C* 82 (2010), p. 014903. DOI: 10.1103/PhysRevC.82.014903. arXiv: 1004.1408 [hep-ph].

## References

- [373] Bjorn Schenke, Sangyong Jeon, and Charles Gale. “Elliptic and triangular flow in event-by-event (3+1)D viscous hydrodynamics”. In: *Phys. Rev. Lett.* 106 (2011), p. 042301. DOI: 10.1103/PhysRevLett.106.042301. arXiv: 1009.3244 [hep-ph].
- [374] H. Bernhard Schlegel. “Exploring potential energy surfaces for chemical reactions: An overview of some practical methods”. In: *Journal of Computational Chemistry* 24.12 (2003), pp. 1514–1527. DOI: <https://doi.org/10.1002/jcc.10231>. eprint: <https://onlinelibrary.wiley.com/doi/pdf/10.1002/jcc.10231>. URL: <https://onlinelibrary.wiley.com/doi/abs/10.1002/jcc.10231>.
- [375] D. Schmalfuß et al. “Quantum  $J_1 - J_2$  Antiferromagnet on a Stacked Square Lattice: Influence of the Interlayer Coupling on the Ground-State Magnetic Ordering”. In: *Phys. Rev. Lett.* 97 (15 Oct. 2006), p. 157201. DOI: 10.1103/PhysRevLett.97.157201. URL: <https://link.aps.org/doi/10.1103/PhysRevLett.97.157201>.
- [376] Kate Scholberg. “Supernova Neutrino Detection”. In: *Annual Review of Nuclear and Particle Science* 62 (Nov. 2012), pp. 81–103. DOI: 10.1146/annurev-nucl-102711-095006. arXiv: 1205.6003 [astro-ph.IM].
- [377] U. Schollwöck. “The density-matrix renormalization group”. In: *Rev. Mod. Phys.* 77 (1 Apr. 2005), pp. 259–315. DOI: 10.1103/RevModPhys.77.259. URL: <https://link.aps.org/doi/10.1103/RevModPhys.77.259>.
- [378] HJ Schulz and TAL Ziman. “Finite-size scaling for the two-dimensional frustrated quantum Heisenberg antiferromagnet”. In: *Europhysics Letters* 18.4 (1992), p. 355.
- [379] HJ Schulz, TAL Ziman, and Didier Poilblanc. “Magnetic order and disorder in the frustrated quantum Heisenberg antiferromagnet in two dimensions”. In: *Journal de Physique I* 6.5 (1996), pp. 675–703.
- [380] Jacob T. Seeley, Martin J. Richard, and Peter J. Love. “The Bravyi-Kitaev transformation for quantum computation of electronic structure”. In: *J. Chem. Phys.* 137.22 (2012), p. 224109. DOI: 10.1063/1.4768229. URL: <https://doi.org/10.1063/1.4768229>.
- [381] John Shalf. “The future of computing beyond Moore’s Law”. In: *Philosophical Transactions of the Royal Society A* 378.2166 (2020), p. 20190061.
- [382] Yao Shen et al. “Evidence for a spinon Fermi surface in a triangular-lattice quantum-spin-liquid candidate”. In: *Nature* 540.7634 (2016), pp. 559–562.
- [383] Nicholas E. Sherman, Maxime Dupont, and Joel E. Moore. “Spectral function of the  $J_1 - J_2$  Heisenberg model on the triangular lattice”. In: *Phys. Rev. B* 107 (16 Apr. 2023), p. 165146. DOI: 10.1103/PhysRevB.107.165146. URL: <https://link.aps.org/doi/10.1103/PhysRevB.107.165146>.
- [384] Qimiao Si, Rong Yu, and Elihu Abrahams. “High-temperature superconductivity in iron pnictides and chalcogenides”. In: *Nature Reviews Materials* 1.4 (Mar. 2016). ISSN: 2058-8437. DOI: 10.1038/natrevmats.2016.17. URL: <http://dx.doi.org/10.1038/natrevmats.2016.17>.
- [385] G. Sigl and G. Raffelt. “General kinetic description of relativistic mixed neutrinos”. In: *Nuclear Physics B* 406.1 (1993), pp. 423–451. ISSN: 0550-3213. DOI: [https://doi.org/10.1016/0550-3213\(93\)90175-0](https://doi.org/10.1016/0550-3213(93)90175-0). URL: <https://www.sciencedirect.com/science/article/pii/0550321393901750>.



## References

- [386] Sophia Simon et al. “Improved Precision Scaling for Simulating Coupled Quantum-Classical Dynamics”. In: *PRX Quantum* 5 (1 Mar. 2024), p. 010343. DOI: 10.1103/PRXQuantum.5.010343. URL: <https://link.aps.org/doi/10.1103/PRXQuantum.5.010343>.
- [387] Rajiv R. P. Singh et al. “Dimer order with striped correlations in the  $J_1$ – $J_2$  Heisenberg model”. In: *Phys. Rev. B* 60 (10 Sept. 1999), pp. 7278–7283. DOI: 10.1103/PhysRevB.60.7278. URL: <https://link.aps.org/doi/10.1103/PhysRevB.60.7278>.
- [388] J. Sirker et al. “ $J_1$  –  $J_2$  model: First-order phase transition versus deconfinement of spinons”. In: *Phys. Rev. B* 73 (18 May 2006), p. 184420. DOI: 10.1103/PhysRevB.73.184420. URL: <https://link.aps.org/doi/10.1103/PhysRevB.73.184420>.
- [389] José M Soler et al. “The SIESTA method for ab initio order-N materials simulation”. In: *J. Phys. Condens. Matter* 14.11 (Mar. 2002), pp. 2745–2779.
- [390] Ivo Souza, Nicola Marzari, and David Vanderbilt. “Maximally localized Wannier functions for entangled energy bands”. In: *Phys. Rev. B Condens. Matter* 65.3 (Dec. 2001).
- [391] Mark Srednicki. “Chaos and quantum thermalization”. In: *Phys. Rev. E* 50 (2 Aug. 1994), pp. 888–901. DOI: 10.1103/PhysRevE.50.888. URL: <https://link.aps.org/doi/10.1103/PhysRevE.50.888>.
- [392] Mark Srednicki. “Thermal fluctuations in quantized chaotic systems”. In: *Journal of Physics A: Mathematical and General* 29.4 (Feb. 1996), p. L75. DOI: 10.1088/0305-4470/29/4/003. URL: <https://dx.doi.org/10.1088/0305-4470/29/4/003>.
- [393] Vishnu Sresht, Agilio AH Padua, and Daniel Blankschtein. “Liquid-phase exfoliation of phosphorene: design rules from molecular dynamics simulations”. In: *ACS nano* 9.8 (2015), pp. 8255–8268.
- [394] Pooja Srivastava et al. “Mechanistic insight into the chemical exfoliation and functionalization of Ti<sub>3</sub>C<sub>2</sub> MXene”. In: *ACS applied materials & interfaces* 8.36 (2016), pp. 24256–24264.
- [395] Christopher J. Stein and Markus Reiher. “Automated Selection of Active Orbital Spaces”. In: *Journal of Chemical Theory and Computation* 12.4 (Apr. 2016), pp. 1760–1771. DOI: 10.1021/acs.jctc.6b00156. URL: <https://doi.org/10.1021/acs.jctc.6b00156>.
- [396] Yuan Su et al. “Fault-tolerant quantum simulations of chemistry in first quantization”. In: *PRX Quantum* 2.4 (2021), p. 040332.
- [397] SV Syzranov and AP Ramirez. “Eminiscent phase in frustrated magnets: a challenge to quantum spin liquids”. In: *Nature Communications* 13.1 (2022), p. 2993. DOI: 10.1038/s41467-022-30739-0. URL: <https://doi.org/10.1038/s41467-022-30739-0>.
- [398] Ken’ichi Takano et al. “Nonlinear  $\sigma$  Model Method for the  $J_1$  –  $J_2$  Heisenberg Model: Disordered Ground State with Plaquette Symmetry”. In: *Phys. Rev. Lett.* 91 (19 Nov. 2003), p. 197202. DOI: 10.1103/PhysRevLett.91.197202. URL: <https://link.aps.org/doi/10.1103/PhysRevLett.91.197202>.
- [399] O Tanaka et al. “Thermodynamic evidence for a field-angle-dependent Majorana gap in a Kitaev spin liquid”. In: *Nature Physics* 18.4 (2022), pp. 429–435.
- [400] Kristan Temme et al. “Quantum metropolis sampling”. In: *Nature* 471.7336 (2011), pp. 87–90.
- [401] Barbara M Terhal and David P DiVincenzo. “Problem of equilibration and the computation of correlation functions on a quantum computer”. In: *Physical Review A* 61.2 (2000), p. 022301.

## References

- [402] The 2023 Nuclear Science Advisory Committee. *A New Era of Discovery, the 2023 Long-Range Plan for Nuclear Physics*. 2023. URL: [https://science.osti.gov/-/media/np/nsac/pdf/reports/2024/2023-NSAC-LRP-Report\\_Final.pdf](https://science.osti.gov/-/media/np/nsac/pdf/reports/2024/2023-NSAC-LRP-Report_Final.pdf).
- [403] J. D. Thompson et al. “Quasiparticle Breakdown and Spin Hamiltonian of the Frustrated Quantum Pyrochlore  $\text{Yb}_2\text{Ti}_2\text{O}_7$  in a Magnetic Field”. In: *Phys. Rev. Lett.* 119 (5 Aug. 2017), p. 057203. DOI: 10.1103/PhysRevLett.119.057203. URL: <https://link.aps.org/doi/10.1103/PhysRevLett.119.057203>.
- [404] Jules Tilly et al. “The variational quantum eigensolver: a review of methods and best practices”. In: *Physics Reports* 986 (2022), pp. 1–128.
- [405] Tom Timusk and Bryan Statt. “The pseudogap in high-temperature superconductors: an experimental survey”. In: *Reports on Progress in Physics* 62.1 (Jan. 1999), pp. 61–122. ISSN: 1361-6633. DOI: 10.1088/0034-4885/62/1/002. URL: <http://dx.doi.org/10.1088/0034-4885/62/1/002>.
- [406] Nikolay V Tkachenko et al. “Correlation-Informed Permutation of Qubits for Reducing Ansatz Depth in the Variational Quantum Eigensolver”. In: *PRX Quantum* 2.2 (2021), p. 020337.
- [407] Nikolay V. Tkachenko et al. *Quantum Davidson Algorithm for Excited States*. arXiv:2204.10741 [quant-ph]. Apr. 2022. URL: <http://arxiv.org/abs/2204.10741> (visited on 07/29/2023).
- [408] Yoshinori Tokura, Masashi Kawasaki, and Naoto Nagaosa. “Emergent functions of quantum materials”. In: *Nature Physics* 13.11 (2017), pp. 1056–1068. URL: <https://doi.org/10.1038/nphys4274>.
- [409] J M Tranquada et al. “Evidence for stripe correlations of spins and holes in copper oxide superconductors”. en. In: *Nature* 375.6532 (June 1995), pp. 561–563.
- [410] Andrew Tranter et al. “A comparison of the Bravyi–Kitaev and Jordan–Wigner transformations for the quantum simulation of quantum chemistry”. In: *Journal of chemical theory and computation* 14.11 (2018), pp. 5617–5630.
- [411] Simon Trebst and Ciarán Hickey. “Kitaev materials”. In: *Physics Reports* 950 (2022), pp. 1–37.
- [412] Norm M Tubman et al. “Postponing the orthogonality catastrophe: efficient state preparation for electronic structure simulations on quantum devices”. In: *arXiv preprint arXiv:1809.05523* (2018).
- [413] Norm M. Tubman et al. *Postponing the orthogonality catastrophe: efficient state preparation for electronic structure simulations on quantum devices*. arXiv:1809.05523 [cond-mat, physics:physics, physics:quant-ph]. Sept. 2018. URL: <http://arxiv.org/abs/1809.05523> (visited on 12/19/2023).
- [414] Mark E Tuckerman. “Ab initio molecular dynamics: basic concepts, current trends and novel applications”. In: *Journal of Physics: Condensed Matter* 14.50 (2002), R1297.
- [415] OFFICE OF AUDIT SERVICES U.S. DEPARTMENT OF ENERGY OFFICE OF INSPECTOR GENERAL. *Audit Report: Relativistic Heavy-Ion Collider Project*. URL: <https://www.energy.gov/sites/default/files/igprod/documents/CalendarYear2002/ig-0543.pdf>.

## References

- [416] Priscila Vensaus et al. “Enhancement of electrocatalysis through magnetic field effects on mass transport”. In: *Nature Communications* 15.1 (2024), p. 2867.
- [417] Frank Verstraete and J Ignacio Cirac. “Mapping local Hamiltonians of fermions to local Hamiltonians of spins”. In: *Journal of Statistical Mechanics: Theory and Experiment* 2005.09 (2005), P09012.
- [418] Valerio Vitale et al. “Automated high-throughput wannierisation”. en. In: *Npj Comput. Mater.* 6.1 (June 2020).
- [419] D Vollhardt and A I Lichtenstein. “Dynamical mean-field approach with predictive power for strongly correlated materials”. en. In: *Eur. Phys. J. Spec. Top.* 226.11 (July 2017), pp. 2439–2443.
- [420] M. Cristina Volpe. “Neutrinos from dense environments : Flavor mechanisms, theoretical approaches, observations, and new directions”. In: (Jan. 2023). arXiv: 2301.11814 [hep-ph].
- [421] Hui Wang et al. “Hydrogen-rich superconductors at high pressures”. In: *WIREs Computational Molecular Science* 8.1 (Sept. 2017). ISSN: 1759-0884. DOI: 10.1002/wcms.1330. URL: <http://dx.doi.org/10.1002/wcms.1330>.
- [422] Kun Wang et al. “Recent advances in catalyst design and activity enhancement induced by a magnetic field for electrocatalysis”. In: *Journal of Materials Chemistry A* 11.15 (2023), pp. 7802–7832.
- [423] Ling Wang and Anders W. Sandvik. “Critical Level Crossings and Gapless Spin Liquid in the Square-Lattice Spin-1/2  $J_1 - J_2$  Heisenberg Antiferromagnet”. In: *Phys. Rev. Lett.* 121 (10 Sept. 2018), p. 107202. DOI: 10.1103/PhysRevLett.121.107202. URL: <https://link.aps.org/doi/10.1103/PhysRevLett.121.107202>.
- [424] Ling Wang et al. “Constructing a Gapless Spin-Liquid State for the Spin-1/2  $J_1 - J_2$  Heisenberg Model on a Square Lattice”. In: *Phys. Rev. Lett.* 111 (3 July 2013), p. 037202. DOI: 10.1103/PhysRevLett.111.037202. URL: <https://link.aps.org/doi/10.1103/PhysRevLett.111.037202>.
- [425] Ling Wang et al. “Tensor-product state approach to spin- $\frac{1}{2}$  square  $J_1 - J_2$  antiferromagnetic Heisenberg model: Evidence for deconfined quantum criticality”. In: *Phys. Rev. B* 94 (7 Aug. 2016), p. 075143. DOI: 10.1103/PhysRevB.94.075143. URL: <https://link.aps.org/doi/10.1103/PhysRevB.94.075143>.
- [426] Samson Wang et al. “Noise-induced barren plateaus in variational quantum algorithms”. In: *Nature Communications* 12.1 (Nov. 2021), p. 6961. ISSN: 2041-1723. DOI: 10.1038/s41467-021-27045-6. URL: <https://doi.org/10.1038/s41467-021-27045-6>.
- [427] Xiaoyu Wang et al. “Strong-coupling expansion of multi-band interacting models: Mapping onto the transverse-field J1-J2 Ising model”. en. In: *Ann. Phys. (N. Y.)* 435.168522 (Dec. 2021), p. 168522.
- [428] Michael R Wasielewski. “Photoinduced electron transfer in supramolecular systems for artificial photosynthesis”. In: *Chem. Rev.* 92.3 (1992), pp. 435–461.
- [429] Dave Wecker et al. “Solving strongly correlated electron models on a quantum computer”. In: *Physical Review A* 92.6 (2015), p. 062318.

## References

- [430] Valerie Vaissier Welborn, Luis Ruiz Pestana, and Teresa Head-Gordon. “Computational optimization of electric fields for better catalysis design”. In: *Nature Catalysis* 1.9 (2018), pp. 649–655.
- [431] Xiao-Gang Wen. “Quantum orders and symmetric spin liquids”. In: *Physical Review B* 65.16 (2002), p. 165113.
- [432] S R White and R M Noack. “Real-space quantum renormalization groups”. en. In: *Phys. Rev. Lett.* 68.24 (June 1992), pp. 3487–3490.
- [433] Steven R White and D J Scalapino. “Density matrix renormalization group study of the striped phase in the 2Dt-J Model”. In: *Phys. Rev. Lett.* 80.6 (Feb. 1998), pp. 1272–1275.
- [434] Nathan Wiebe et al. “Higher order decompositions of ordered operator exponentials”. In: *Journal of Physics A: Mathematical and Theoretical* 43.6 (2010), p. 065203.
- [435] Alexander Wietek and Andreas M. Läuchli. “Chiral spin liquid and quantum criticality in extended  $S = \frac{1}{2}$  Heisenberg models on the triangular lattice”. In: *Phys. Rev. B* 95 (3 Jan. 2017), p. 035141. DOI: 10.1103/PhysRevB.95.035141. URL: <https://link.aps.org/doi/10.1103/PhysRevB.95.035141>.
- [436] Dominik S. Wild and Álvaro M. Alhambra. “Classical Simulation of Short-Time Quantum Dynamics”. In: *PRX Quantum* 4.2, 020340 (June 2023), p. 020340. DOI: 10.1103/PRXQuantum.4.020340. arXiv: 2210.11490 [quant-ph].
- [437] Muwei Wu, Dao-Xin Yao, and Han-Qing Wu. “Exact diagonalization study of the anisotropic Heisenberg model related to  $\text{YbMgGaO}_4$ ”. In: *Phys. Rev. B* 103 (20 May 2021), p. 205122. DOI: 10.1103/PhysRevB.103.205122. URL: <https://link.aps.org/doi/10.1103/PhysRevB.103.205122>.
- [438] Tao Wu et al. “Magnetic-field-induced charge-stripe order in the high-temperature superconductor  $\text{YBa}_2\text{Cu}_3\text{O}_y$ ”. en. In: *Nature* 477.7363 (Sept. 2011), pp. 191–194.
- [439] Chenlu Xie et al. “Surface and interface control in nanoparticle catalysis”. In: *Chemical reviews* 120.2 (2019), pp. 1184–1249.
- [440] Tao Xie et al. “Complete field-induced spectral response of the spin-1/2 triangular-lattice antiferromagnet  $\text{CsYbSe}_2$ ”. In: *npj Quantum Materials* 8.1 (Sept. 2023), p. 48. ISSN: 2397-4648. DOI: 10.1038/s41535-023-00580-9. URL: <https://doi.org/10.1038/s41535-023-00580-9>.
- [441] Cong-Qiao Xu et al. “Structural rearrangement of Au–Pd nanoparticles under reaction conditions: An ab initio molecular dynamics study”. In: *ACS nano* 11.2 (2017), pp. 1649–1658.
- [442] Ravi Yadav et al. “Kitaev exchange and field-induced quantum spin-liquid states in honeycomb  $\alpha\text{-RuCl}_3$ ”. In: *Scientific reports* 6.1 (2016), p. 37925.
- [443] Youhei Yamaji et al. “Clues and criteria for designing a Kitaev spin liquid revealed by thermal and spin excitations of the honeycomb iridate  $\text{Na}_2\text{IrO}_3$ ”. In: *Physical Review B* 93.17 (2016), p. 174425.
- [444] Han Yan et al. “Theory of multiple-phase competition in pyrochlore magnets with anisotropic exchange with application to  $\text{Yb}_2\text{Ti}_2\text{O}_7$ ,  $\text{Er}_2\text{Ti}_2\text{O}_7$ , and  $\text{Er}_2\text{Sn}_2\text{O}_7$ ”. In: *Phys. Rev. B* 95 (9 Mar. 2017), p. 094422. DOI: 10.1103/PhysRevB.95.094422. URL: <https://link.aps.org/doi/10.1103/PhysRevB.95.094422>.

## References

- [445] Jianjun Yang and John S Tse. “Li ion diffusion mechanisms in LiFePO<sub>4</sub>: an ab initio molecular dynamics study”. In: *J. Phys. Chem. A* 115.45 (2011), pp. 13045–13049.
- [446] Ke R Yang, Gregory W Kyro, and Victor S Batista. “The landscape of computational approaches for artificial photosynthesis”. In: *Nature Computational Science* 3.6 (2023), pp. 504–513.
- [447] Ke R Yang, Gregory W Kyro, and Victor S Batista. “The landscape of computational approaches for artificial photosynthesis”. In: *Nature Computational Science* 3.6 (2023), pp. 504–513.
- [448] Yongpeng Yang, Xiangjian Shen, and Yi-Fan Han. “Diffusion mechanisms of metal atoms in PdAu bimetallic catalyst under CO atmosphere based on ab initio molecular dynamics”. In: *Applied Surface Science* 483 (2019), pp. 991–1005.
- [449] Zhengning Yang et al. “Experimental demonstration of quantum overlapping tomography”. In: *Physical Review Letters* 130.5 (2023), p. 050804.
- [450] Sheng Ye et al. “Water Oxidation Catalysts for Artificial Photosynthesis”. In: *Adv. Mat.* 31.50 (2024/01/18 2019), p. 1902069. DOI: <https://doi.org/10.1002/adma.201902069>. URL: <https://doi.org/10.1002/adma.201902069>.
- [451] Tzu-Ching Yen and Artur F. Izmaylov. “Cartan Subalgebra Approach to Efficient Measurements of Quantum Observables”. In: *PRX Quantum* 2 (4 Oct. 2021), p. 040320. DOI: 10.1103/PRXQuantum.2.040320. URL: <https://link.aps.org/doi/10.1103/PRXQuantum.2.040320>.
- [452] R Au-Yeung et al. “Quantum algorithms for scientific applications”. In: *arXiv preprint arXiv:2312.14904* (2023).
- [453] Ji-Feng Yu and Ying-Jer Kao. “Spin-1/2  $J_1$ - $J_2$  Heisenberg antiferromagnet on a square lattice: A plaquette renormalized tensor network study”. In: *Phys. Rev. B* 85 (9 Mar. 2012), p. 094407. DOI: 10.1103/PhysRevB.85.094407. URL: <https://link.aps.org/doi/10.1103/PhysRevB.85.094407>.
- [454] Rong Yu et al. “Superconductivity at the border of electron localization and itinerancy”. In: *Nat. Commun.* 4.1 (2013), p. 2783.
- [455] F C Zhang and T M Rice. “Effective Hamiltonian for the superconducting Cu oxides”. In: *Phys. Rev. B Condens. Matter* 37.7 (Mar. 1988), pp. 3759–3761.
- [456] Guang-Ming Zhang, Hui Hu, and Lu Yu. “Valence-Bond Spin-Liquid State in Two-Dimensional Frustrated Spin-1/2 Heisenberg Antiferromagnets”. In: *Phys. Rev. Lett.* 91 (6 Aug. 2003), p. 067201. DOI: 10.1103/PhysRevLett.91.067201. URL: <https://link.aps.org/doi/10.1103/PhysRevLett.91.067201>.
- [457] Hao Zhang and Cristian D. Batista. “Classical spin dynamics based on  $SU(N)$  coherent states”. In: *Phys. Rev. B* 104 (10 Sept. 2021), p. 104409. DOI: 10.1103/PhysRevB.104.104409. URL: <https://link.aps.org/doi/10.1103/PhysRevB.104.104409>.
- [458] J Zhang et al. “Fuel cells—proton-exchange membrane fuel cells| catalysts: life-limiting considerations”. In: (2009).
- [459] Shang-Shun Zhang et al. “Schwinger boson theory of ordered magnets”. In: *Phys. Rev. B* 105 (22 June 2022), p. 224404. DOI: 10.1103/PhysRevB.105.224404. URL: <https://link.aps.org/doi/10.1103/PhysRevB.105.224404>.

## References

- [460] Shengzhi Zhang et al. “Electronic and magnetic phase diagrams of the Kitaev quantum spin liquid candidate  $\text{Na}_2\text{Co}_2\text{TeO}_6$ ”. In: *Physical Review B* 108.6 (2023), p. 064421.
- [461] Shiwei Zhang, J Carlson, and J E Gubernatis. “Constrained path Monte Carlo method for fermion ground states”. In: *Phys. Rev. B Condens. Matter* 55.12 (Mar. 1997), pp. 7464–7477.
- [462] Shu Zhang et al. “Dynamical Structure Factor of the Three-Dimensional Quantum Spin Liquid Candidate  $\text{NaCaNi}_2\text{F}_7$ ”. In: *Phys. Rev. Lett.* 122 (16 Apr. 2019), p. 167203. DOI: 10.1103/PhysRevLett.122.167203. URL: <https://link.aps.org/doi/10.1103/PhysRevLett.122.167203>.
- [463] Xing Zhang et al. “Highly selective and active  $\text{CO}_2$  reduction electrocatalysts based on cobalt phthalocyanine/carbon nanotube hybrid structures”. In: *Nat. Commun.* 8.1 (2017), p. 14675. DOI: 10.1038/ncomms14675. URL: <https://doi.org/10.1038/ncomms14675>.
- [464] Xinshu Zhang et al. “A magnetic continuum in the cobalt-based honeycomb magnet  $\text{BaCo}_2(\text{AsO}_4)_2$ ”. In: *Nature Materials* 22.1 (2023), pp. 58–63.
- [465] Yu Zhang, Tammie Nelson, and Sergei Tretiak. “Non-adiabatic molecular dynamics of molecules in the presence of strong light-matter interactions”. In: *The Journal of Chemical Physics* 151.15 (2019).
- [466] Yu Zhang et al. “Variational Quantum Eigensolver with Reduced Circuit Complexity”. In: *Npj Quantum Inf.* 8 (1 2022), p. 96.
- [467] Bo-Xiao Zheng et al. “Stripe order in the underdoped region of the two-dimensional Hubbard model”. en. In: *Science* 358.6367 (Dec. 2017), pp. 1155–1160.
- [468] REN Zhi-An et al. “Superconductivity at 55K in Iron-Based F-Doped Layered Quaternary Compound  $\text{Sm}[\text{O}_{1-x}\text{F}_x]\text{FeAs}$ ”. In: *Chinese Physics Letters* 25.6, 2215–2216 (2008), pp. 2215–2216. URL: [https://cpl.iphy.ac.cn/EN/abstract/article\\_43504.shtml](https://cpl.iphy.ac.cn/EN/abstract/article_43504.shtml).
- [469] M. E. Zhitomirsky and Kazuo Ueda. “Valence-bond crystal phase of a frustrated spin-1/2 square-lattice antiferromagnet”. In: *Phys. Rev. B* 54 (13 Oct. 1996), pp. 9007–9010. DOI: 10.1103/PhysRevB.54.9007. URL: <https://link.aps.org/doi/10.1103/PhysRevB.54.9007>.
- [470] Xingjiang Zhou et al. “High-temperature superconductivity”. en. In: *Nat. Rev. Phys.* 3.7 (May 2021), pp. 462–465.
- [471] Yi Zhou, Kazushi Kanoda, and Tai-Kai Ng. “Quantum spin liquid states”. In: *Reviews of Modern Physics* 89.2 (2017), p. 025003.
- [472] Yi Zhou et al. “ $\text{Na}_4\text{Ir}_3\text{O}_8$  as a 3D Spin Liquid with Fermionic Spinons”. In: *Phys. Rev. Lett.* 101 (19 Nov. 2008), p. 197201. DOI: 10.1103/PhysRevLett.101.197201. URL: <https://link.aps.org/doi/10.1103/PhysRevLett.101.197201>.
- [473] Jian-Xin Zhu. *Bogoliubov-de Gennes Method and Its Applications*. Springer International Publishing, 2016. ISBN: 9783319313146. DOI: 10.1007/978-3-319-31314-6. URL: <http://dx.doi.org/10.1007/978-3-319-31314-6>.
- [474] Jian-Xin Zhu et al. “Fourier-transformed local density of states and tunneling into a d-wave superconductor with bosonic modes”. In: *Physical Review B* 73.1 (Jan. 2006). ISSN: 1550-235X. DOI: 10.1103/physrevb.73.014511. URL: <http://dx.doi.org/10.1103/PhysRevB.73.014511>.

## References

- [475] Zhenyue Zhu and Steven R. White. “Spin liquid phase of the  $S = \frac{1}{2}/J_1 - J_2$  Heisenberg model on the triangular lattice”. In: *Phys. Rev. B* 92 (4 July 2015), p. 041105. DOI: 10.1103/PhysRevB.92.041105. URL: <https://link.aps.org/doi/10.1103/PhysRevB.92.041105>.